Abstract

Title of Dissertation: Investigations of
the Earth's Magnetosphere with
Global Magnetohydrodynamic Simulations

Xi Shao, Doctor of Philosophy, 2001

Dissertation directed by: Professor Dennis Papadopoulos
Departments of Astronomy and Physics

Variations in the solar wind plasma density, flow velocity, and, most important, the direction of the interplanetary magnetic field (IMF) cause significant changes throughout the Earth's magnetosphere, ionosphere and on the ground [*Baker et al.*, 1998]. These changes can cause disruption to power distribution systems, wired and wireless communications. With more satellites launched in space and more ground-based measurements, understanding and predicting the geospace environment becomes more and more important and feasible.

In the recent past, the Lyon-Fedder-Mobarry (LFM) three-dimensional global magnetohydrodynamic (MHD) code has became a powerful approach for studying the magnetosphere-ionosphere system driven by the solar wind. In this thesis, we use the LFM code, originally developed by J. G. Lyon, J. A. Fedder, and C.

Mobarry and commonly called the LFM, to study the Earth's magnetosphere. The code couples a 3D MHD magnetospheric model with a 2D electrostatic ionospheric model and is then driven by solar wind input provided by either satellites or physics-based models.

The goal of this thesis is to use the global MHD model to investigate and understand the physical properties of the Earth's magnetosphere, its coupling with the ionosphere and to further expand the capability of the model in real event simulations. We have studied three topics in magnetospheric physics:

- **Earth's magnetosphere with steady northward IMF:**

  The structure and magnetic topology of the magnetosphere with steady northward IMF is one of the fundamental problems in magnetospheric physics. Global MHD simulations play an important role in this study. The community of global MHD modeling has long disagreed about whether the magnetosphere with steady northward IMF has a long or short tail for the nominal conditions (steady state with constant solar wind number density= 5 1/cc, B_Z= 5 nT and V_{SW}= 400 km/s). We find here a short tail configuration (tail length $\sim$ 40 R_E), which is consistent with the results of [*Gombosi et al.* [1998] and *Bargatze et al.* [1999]. The long tail configuration obtained by *Raeder et al.* [1995] is discussed. The differences between the present work and the earlier results of *Fedder and Lyon* [1995] are clarified by addressing the issue of transients and plasma preconditioning. Simulations clearly show cusp region reconnection and ionospheric four-cell convection pattern. Our simulation observes the concave shape of the steady magnetosphere, which was predicted by the phenomenological analysis of *Song et al.* [2000].

To understand the magnetosphere with steady northward IMF and its scaling with input parameters, we vary the magnitude of the solar wind magnetic field B_{IMF} and the velocity V_{SW}. We demonstrate that the ionospheric conductance is a minor effect in determining the steady magnetotail size. Only, the transient behavior is influenced by the conductance. Based on conservation of flux and force balance, simple analytical models are derived to interpret the parametric dependences of the scaling of the tail on solar wind conditions. The parametric dependence of 1D cuts of various tail plasma and field quantities along the X and Z axes are analyzed. The simulations show that during steady state, inside the tail (in the region x<-20 R_E on the equatorial plane), the tail field B_z is comparable to the solar wind magnetic field B_z and the tail field B_x is nearly 0. The modeled steady 3D current sheet profiles are also presented.

After searching the satellite observations over an 8 year period, we found one quiet-time northward IMF event, during which the Geotail satellite is inside the tail. A real northward IMF event, which occurred on Feb. 9, 1995, is simulated and the results are compared with the observations. The simulated time scale for the temporal evolution and magnitude of various components of the magnetic field agree well with observations. This supports our model of the evolution of the magnetosphere to steady state. Thus the simulation provides a reliable comparison of the northward IMF steady state.

- **Magnetospheric substorms:**

Because of their relevance to massive global energy loading and unloading,

lots of observations and studies have been made for magnetic substorm events. In this thesis, we simulate and analyze an ideal substorm with the MHD model. The ideal substorm is initiated by a sudden northward-southward IMF turning. This study serves as a pictorial review of the typical behavior of the magnetosphere and ionosphere during substorms. The results show auroral onset and expansion, AL index dipping, dipolarization, current sheet disruption, formation of the substorm current wedge, and formation and ejection of plasmoid. There are flow channels connecting the mid-tail and inner-tail region, which supports the observations that auroral activities originate from the inner magnetotail.

Then, using nonlinear dynamical techniques, we statistically investigate whether the simulated substorms from global MHD models have the non-equilibrium phase transition-like features revealed by *Sitnov et al.* [2000]. We simulate 6 intervals of total duration of 240 hours from the same data set used in *Sitnov et al.* [2000]. We analyze the input-output (vB_s–pseudo-AL index) system obtained from the global MHD model and compare the results to those in *Sitnov et al.* [2000, 2001].

The statistical analysis of the coupled vB_s–pseudo-AL index system shows the first-order phase transition map, which is consistent with the map obtained for the vB_s–observed-AL index system from *Sitnov et al.* [2000]. Although, the comparison between observations and global MHD simulations for individual events may vary, the overall global transition pattern during the substorm cycle revealed by Singular Spectrum Analysis (SSA) is statistically consistent between simulations and observations.

The coupled vB_s–pseudo-AL index system shows multi-scale behavior (scale-

invariant power-law dependence) in singular power spectrum. We find critical exponents of the non-equilibrium transitions in the magnetosphere, which reflect the multi-scale aspect of the substorm activity, different from power-law frequency of autonomous systems. The exponents relate input and output parameters of the magnetosphere. We also discuss the limitations of the global MHD model in reproducing the multi-scale behavior when compared to the real system. The behavior of the systems formed by coupling vB_s with other ionospheric and magnetospheric response is also analyzed and discussed.

- **Magnetosphere-ionosphere coupling:**

Models using the global MHD model output to simulate riometer and magnetometer observations are developed. The models are applied to the January 10, 1997 magnetospheric storm event and the results are compared with the observations. Modeling ionospheric measurements and comparisons with observations are important in understanding magnetosphere-ionosphere coupling and help to validate and improve the LFM model.

Riometers measure the changes in the absorption of very high frequency (VHF) radio signals of galactic origin passing through the ionosphere [*Rosenberg et al.*, 1991]. We develop a model to simulate riometer observations using global MHD simulation output. We find that turbulent heating due to electrojet instabilities is important in calculating the ionospheric absorption. A model that describes the temporally and spatially averaged electron temperature is developed and compares with available radar observations of the electron heating. The model including turbulent heating

agrees well with the riometer observations.

Magnetometers monitor the perturbations of the ground magnetic field produced by the ionospheric currents and the induced imaging ground currents. The model simulating magnetometer data uses the computed ionospheric current density distribution and the height dependence of the electrojet (determined by the precipitating electron energy), to calculate the perturbed magnetic field by implementing Biot-Savart's law. The model including height dependence of the current sheet reduces by 10 percent the error compared to the fixed height model. The limitations of the global MHD model in calculating ground observed perturbed magnetic field are also discussed.

These three topics provide a comprehensive coverage for using global MHD model to study magnetospheric physics. Through extensive studies of the Earth's magnetosphere, the overall conclusion is that the LFM model is an invaluable tool in studying magnetospheric sciences and predicting space weather.

Investigations of
the Earth's Magnetosphere with
Global Magnetohydrodynamic Simulations

by

Xi Shao

Dissertation submitted to the Faculty of the Graduate School
of the University of Maryland in partial fulfillment
of the requirements for the degree of
Doctor of Philosophy
2001

Advisory Committee:

Professor Dennis Papadopoulos, Chairman/Advisor
Professor Michael A'Hearn
Dr. Charles C. Goodrich
Dr. Parvez N. Guzdar
Professor Adil B. Hassam
Professor Chuan-Sheng Liu
Professor James M. Stone

Dedication

To My Parents and My Wife Who Made It All Possible

Acknowledgements

TABLE OF CONTENTS

V   Summary   207

7   Summary   208

VI   Appendices   222

A   Computational Model for Simulating Riometer Observations   223

B   Computational Model for Simulating Magnetometer Observations   231

LIST OF TABLES

LIST OF FIGURES

Investigations of
the Earth's Magnetosphere with
Global Magnetohydrodynamic Simulations

Xi Shao

November 30, 2001

This comment page is not part of the dissertation.

Part I

Introduction

Chapter 1

Background and Directions

1.1   Introduction to Magnetospheric Physics and Its Relevance to Our Life

The sun has two major outputs, radiation (photons) and the solar wind. The solar wind is the tenuous ionized gas streaming outward from the sun and approaching the speed of hundreds of kilometers per second at 1 AU. These outputs affect geospace (region surrounding the Earth) in different ways. Radiation couples mainly in the atmosphere, driving our weather. The solar wind couples at higher altitudes, the magnetosphere and ionosphere. The latter coupling is electrodynamic. Figure 1.1 (from *Kivelson and Russell* [1995]) shows the schematic three dimensional view of the Earth's magnetosphere and the associated currents, fields and plasma regions.

Magnetopheric physics is a young research subject that studies the coupled system formed by the solar wind, the magnetosphere and the ionosphere. A
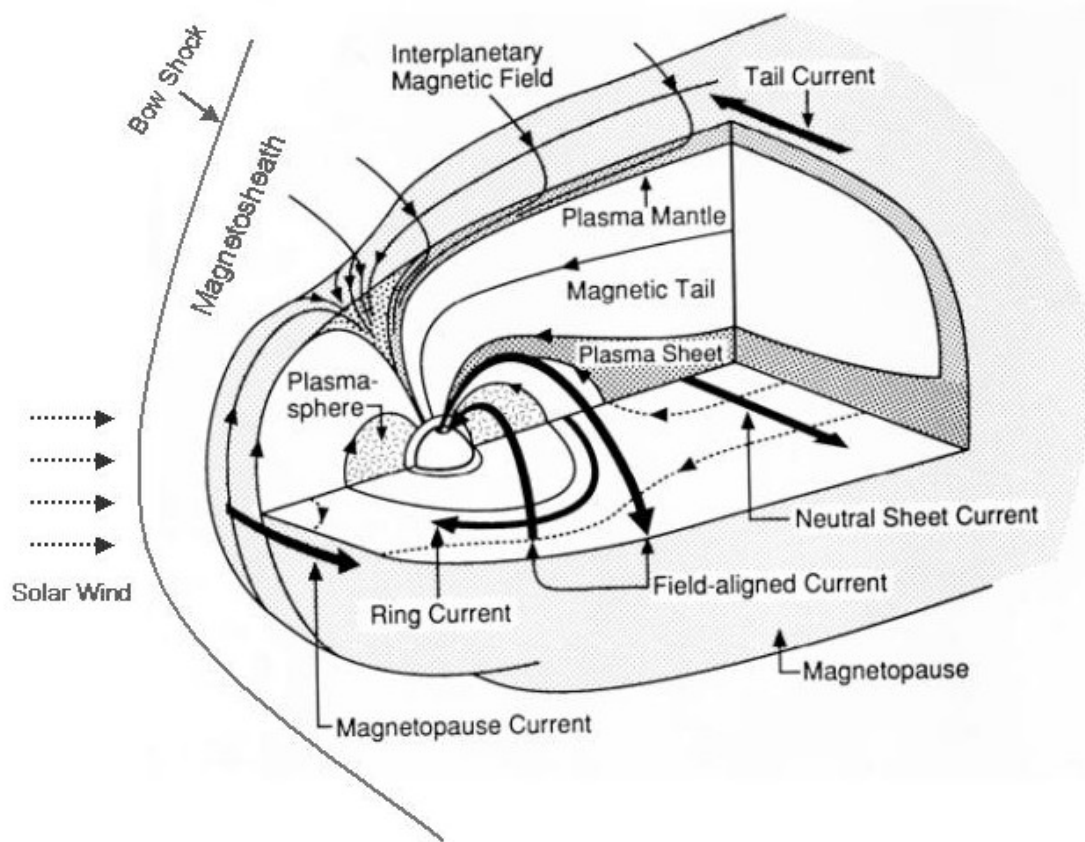
Figure 1.1: Three dimensional view of the Earth's magnetosphere and the associated currents, fields and plasma regions. (From *Kivelson and Russell* [1995].)

fascinating and easily observed manifestation of magnetospheric physics is the aurora. Figure 1.2 shows a picture of an auroral display taken above Alaska. Earth's magnetic field acts as "wires" to transmit the solar wind energy to the ionosphere, where the energy is dissipated mainly as heat, and to accelerate charged particles circling fairly close to the Earth. The ionosphere in the northern and southern regions acts as the primary resistor. This circuit is responsible for the aurora. The auroral radiation is emitted by atmospheric constituents that are excited by precipitating particles.

Figure 1.2: Picture of an auroral display taken above Alaska (From www.webshots.com).

Variations in the solar wind plasma density, flow velocity and most important, the direction of the interplanetary magnetic field (IMF), cause significant changes throughout the Earth's magnetosphere, ionosphere, and on the ground with serious, practical consequences [*Baker et al.*, 1998]. These changes have been called "space weather". Changes in the currents flowing through the ionosphere can cause disruption to power distribution systems, long-line telephone networks, radio communications, and corrosion of pipelines on the ground. Changes in the radiation environment near Earth can seriously affect satellite operations through spacecraft charging and generation of false commands [*Baker et al.*, 1987, 1994].

We have just passed the peak of the solar cycle. With more satellites launched into space, more reliance on wired and wireless communication, the impact of this solar maximum to everyday life is quite different from previous cycles. The increased activity level within the 3 years around the peak will bring more and stronger events capable of disrupting geospace, the space environment in the vicinity of Earth. Thus, understanding and predicting the geospace environment is more and more important and feasible in space age. This has become the focus of the study of magnetospheric physics.

In the following sections, we first introduce the global configuration of the Earth's magnetosphere with emphasis on the critical role of the orientation of the solar wind magnetic field on the interaction between the solar wind and the magnetosphere, and the important phenomenon of the magnetospheric substorm. These will be followed by a general introduction on studies of the coupling between the solar wind, the magnetosphere and the ionosphere using global, numerical, MHD simulations. The focus of this thesis is to understand the Earth's magnetosphere with steady northward IMF, statistical features of magnetospheric substorms and magnetosphere-ionosphere coupling through global MHD modeling. The objectives and directions of the thesis are presented in section 1.7. In the last section of this chapter, we present the outline of the thesis.

1.2 Global Configuration of the Earth's Magnetosphere

Figure 1.1 illustrates the global configuration of the Earth's magnetosphere. The presence of the Earth's magnetic field prevents direct entry of the solar wind through the outer boundary of the magnetosphere, the magnetopause; the solar wind is deflected around it after having been slowed down to subsonic velocities at the Earth's bow shock (e.g. [*Kivelson and Russell*, 1995]). The Earth's magnetic field is sufficiently strong that it can usually keep the solar wind from approaching closer than about 10 Earth radii (R_E). The region between the bow shock and the magnetopause is the magnetosheath. The kinetic pressure of the shocked solar wind compresses the dipolar terrestrial magnetic field and, on the nightside of the Earth, transforming it into a long, tail-like structure, the magnetotail. The magnetotail consists of two lobe regions with nearly antiparallel magnetic fields. The transition region between the lobes is called the neutral sheet. The central part of the magnetotail, in the neighborhood of the neutral sheet, is populated with plasma with energies of several KeV. This region, the plasma sheet, is connected to the auroral ionosphere along magnetic field lines. Closer to the Earth, energetic ions with energies of some tens of KeV oscillate between the converging magnetic fields in the northern and southern magnetosphere and drift westward under the influence of gradient and curvature drift. The westward drift

constitutes a considerable current encircling the Earth. This region at radial distance of several R_E is called the ring current. [*Kamide and Baumjohann*, 1993; *Lyon*, 2000]

Following Maxwell's Law, the distortion of the terrestrial dipole field into the typical magnetospheric shape is accompanied by electrical currents [*Kamide and Baumjohann*, 1993]. As shown in Figure 1.1, the compression of the terrestrial magnetic field on the dayside is caused by currents flowing perpendicular to the magnetic field lines across the magnetopause surface. These currents are called the "Chapman-Ferraro" currents. The tail-like field of the nightside magneto-sphere is formed by the tail current flowing on the tail surface and the neutral sheet current in the central plasma sheet. Both of them are connected and form a Θ-like current system. The ring current is another large scale system which influences the configuration of the inner magnetosphere. The greatest contribu-tion to the ring current energy density comes from $\sim$ 20-200 keV ions [*Jursa*, 1985]. The outer portions of the ring current merge with the tail current in the plasma sheet. In addition to these purely magnetospheric currents that flow per-pendicular to the ambient magnetic field, there is another set of currents which flows along the magnetic field lines. These field-aligned currents connect the current systems in the magnetosphere and its boundaries to those flowing in the polar ionosphere. The field-aligned currents are essential for the electrodynamic exchange of energy and momentum between these regions.

Interplanetary Field Northward

(a)

Interplanetary Field Southward

(b)
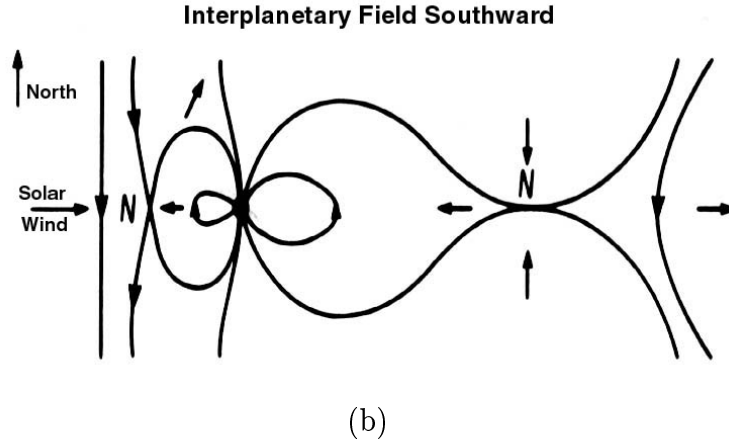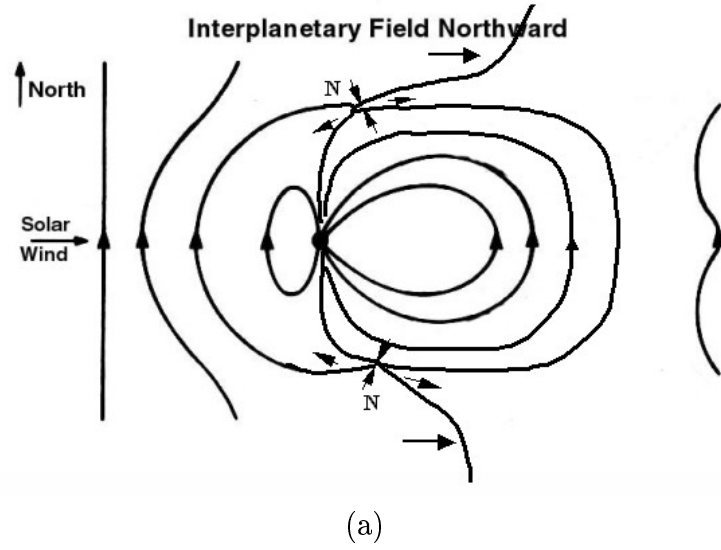
Figure 1.3: Topology of the magnetosphere in north-south plane for northward and southward interplanetary field, according to J. W. Dungey in the early 1960s. In the steady state, the plasma flows as indicated by the short arrows. Symbol "N" refers to the neutral point of the magnetic reconnection. (a) With northward IMF. (b) With southward IMF. (From *Dungey* [1963]; *Kivelson and Russell* [1995])

Observations have shown that the direction of solar wind interplanetary magnetic field (IMF) has a controlling influence in the configuration of the Earth's magnetosphere. The coupling between the solar wind and the magnetosphere

is mediated and controlled by the magnetic field in the solar wind through the process of magnetic reconnection. When regions with differently directed magnetic fields come in contact, it is possible for magnetic field lines to break and reconnect. *Dungey* [1963] first sketched the topology of the magnetosphere for northward and southward IMF. Figure 1.3 (from *Dungey* [1963]; *Kivelson and Russell* [1995]) shows the schematic plots of the magnetospheric topology. For steady northward IMF, magnetic reconnection occurs in the cusp region, where oppositely directed field lines of solar wind and terrestrial origin, respectively, join. For steady southward IMF, magnetic reconnection occurs on the dayside subsolar line, turning closed field into open field lines (that is one end connected to the Earth and the other in the solar wind). The reconnected, open field lines take part in the antisunward motion of the solar wind and get dragged to the nightside where the tail lobe field is enhanced. To maintain steady state, reconnection must occur on the nightside that feeds magnetic flux back to the dayside through magnetospheric convection. Geomagnetic substorms occur due to the imbalance of subsolar and tail reconnection. Lots of studies have been focused on magnetospheric substorms [*Baker et al.*, 1996; *Lui*, 1991].

Thus, in the next two sections, we discuss the general aspects of the Earth's magnetosphere with northward IMF and magnetopheric substorms.

1.3 The Earth's Magnetosphere with Northward IMF

For Earth's magnetosphere with northward IMF, the observational features are summarized as following:

1. *Dungey* [1963] first introduced the concept of reconnection at the night side of the cusps (shown in Figure 1.3). *Burch et al.* [1980] reported AE-D measurements of reverse ion dispersion together with sunward convection near the poleward boundary of the cusp during a period of northward interplanetary field. Later, Burch et al. [1986] interpreted a similar event in terms of cusp region reconnection. Impulsive Alfven waves were also observed by polar orbit satellites at the polarward edge of the dayside cusp region when cusp region reconnection is active [*Kennel, 1995*].

2. In the ionosphere, two reverse convection cells on the open field lines are added to direct convection cells at lower latitudes, making four cells in all. Figure 1.4 shows the schematic plot of the four-cell ionospheric convection pattern for northward IMF (from *Kennel* [1995]). The NBZ current (field-aligned current) system [*Iijima et al.,* 1984; *Zanetti and Potemra,* 1986] is responsible for forming the two inner reverse cells opposite to the sense of cells (outer cell) produced by region 1 current system. The auroral is brightest in regions of upward field-aligned current, since precipitating electrons stream into ionosphere

along upward field-aligned current. Two broad sun-aligned arcs are expected when there are four convection cells. More complex patterns are also observed. During extended northward IMF, the cross polar potential is much smaller than for southward IMF conditions [*Reiff and Burch,* 1985].
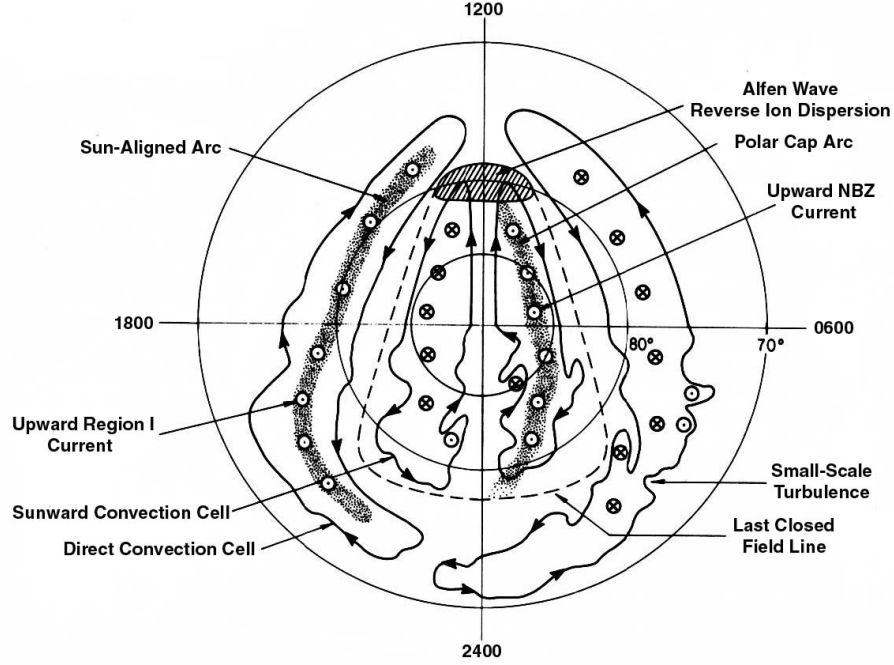
Figure 1.4: Polar cap four-cell convection pattern for northward IMF (From *Kennel* [1995]). Two reverse convection cells on the open field lines are added to direct convection cells at lower latitudes, making four cells in all.

3. A statistical study of the boundary between polar rain and auroral precipitation suggested that the open part of the polar cap shrinks to a small region above 80 degrees (geomagnetic latitude) in northward field conditions [*Makita and Meng,* 1983]. *Fairfield* [1993] reported the apparent dissappearance of the magnetotail at the observation site X= -225 R_E during the period of strongly

northward IMF.

4. Observations [*Clauer and Friis-Christensen,* 1988] have also shown that after northward IMF turning, the convection in the dayside ionosphere started to respond within minutes, but that it took about 20 minutes for the ionospheric current and flow pattern to achieve its new configuration.

5. Recently [*Huang et al.,* 2000, 2001] reported observations of 40-60 minutes quasi-periodic oscillation in the ionospheric velocity, ground magnetic field perturbation and magnetospheric magnetic field observed by GOES8 satellite for northward IMF. They attributed the magnetospheric-ionospheric perturbations to the excitation of standing magneto-sonic wave inside the magnetospheric cavity.

Earth's magnetosphere with northward IMF is relatively quiet and the magnetosphere is less stressed compared to the magnetosphere with southward IMF. It is often called the quiet-time magnetosphere. Therefore, it is a good case to study with the global magnetospheric models.

1.4   Magneospheric Substorms

The magnetospheric substorm is a dynamic reconfiguration of the magnetosphere accompanied by strong energy dissipation, with the magnetosphere returning from a high to a low energy state. Observations show that the kinetic energy flux of the solar wind impinging on the dayside magnetopause with its cross-section

of about 30 R_E (Earth radii) is about 10^4GW for typical solar wind conditions. During a typical substorm event, about 10^{15} joule of energy is deposited into the ionosphere on a 30 minutes timescale [*Kamide and Baumjohann*, 1993].

The substorm is a global phenomenon whose manifestation can be noted in nearly all regions of the magnetosphere and ionosphere. Based on auroral observations, the magnetospheric substorm goes through three phases: the growth phase, the expansion phase and the recovery phase. In the growth phase, energy from the solar wind is stored in the magnetosphere, resulting in a stressed tail-like configuration. This is 'broken' during the expansion phase. After the release of energy, the system slowly returns to 'normal' (ground state before the growth phase) during the recovery phase. The following observational features are summarized in several papers [e.g. *Kamide and Baumjohann*, 1993; *Lui*, 1990; *Kivelson and Russell*, 1995; *Wiltberger*, 1998].

1. Growth phase: Following a southward IMF turning, magnetic reconnection occurs at the dayside magnetopause. Newly reconnected field lines couple to the solar wind and are carried towards the night side to pile up on the tail lobe. The tail lobe field is stretched and the plasma sheet thins. The lobe flux increases resulting in enhanced cross tail current. In the ionosphere, the polar cap area increases and the auroral oval expands equatorward and becomes more oval shaped. The electrojet currents are enhanced. A two cell convection pattern forms and the cross-polar cap potential increases. This process lasts for several

tens of minutes to an hour before substorm onset.
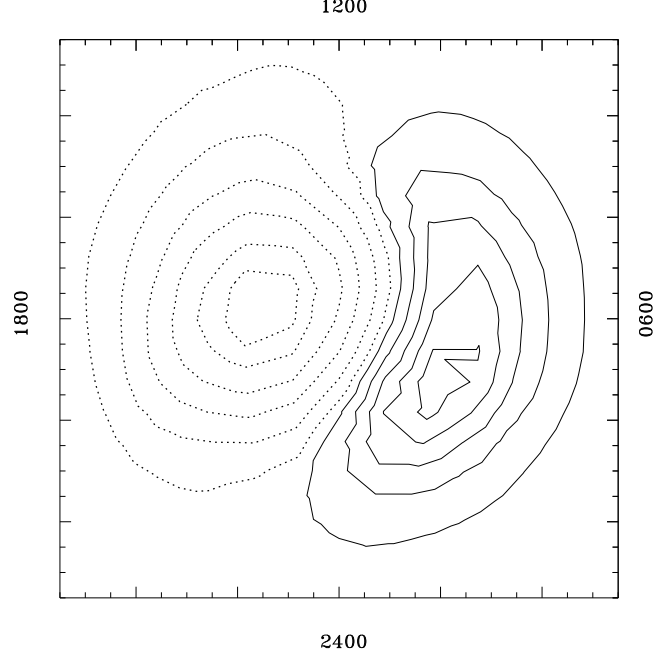
Figure 1.5: Polar cap electric potential contour for southward IMF. The dashed lines depict the negative potential cell and the solid lines show the positive potential cell.

Figure 1.5 (from LFM global MHD simulation) shows the ionospheric electric potential contour for southward IMF. The cross polar cap potential is much higher than in the case with northward IMF. The contours of constant electrostatic potential are also streamlines of flow in the ionosphere. The dayside reconnected field lines drives the ionospheric convection while it travels to the nightside.

2. Expansion phase: The name expansion phase comes from the auroral observations. The substorm onset marks the start of the expansion phase. The triggering factors for the substorm onset are still controversial [*Baker et al.,*

14

1996; *Lui,* 1991; *Kivelson and Russell,* 1995]. The major difficulties are to sequence the events in the inner and mid tail and map them to the ionospheric observations. In the tail, tail magnetic field reconnection occurs. Down the tail $5 \leq |x| \leq 15R_E$, a substorm current wedge (SCW) forms. Observations also show particle injection, magnetic field dipolarization and impulsive electric field penetration. Figure 1.6 (from *Kamide and Baumjohann* [1993]) shows a
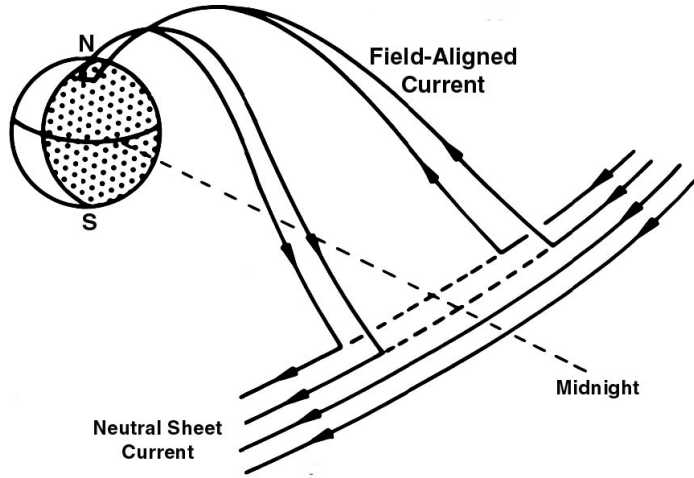
Figure 1.6: Schematic plot of substorm current wedge which short-circuits the neutral sheet current in the magnetotail. (From *Kamide and Baumjohann* [1993])

schematic plot of the substorm current wedge, that short-circuits the neutral sheet current in the magnetotail. The tail-lobe magnetic field line dipolarizes from the tail-like configuration. In the midtail ($15 \leq |x| \leq 80R_E$), observations show plasma sheet thinning, transient fast flows, and occasionally large fluctuating E-fields. In the ionosphere, at the expansion onset, the equatorward discrete

auroral arc brightens. Pi 2 (irregular pulse of duration 40-150 seconds) bursts accompany each intensification. A westward traveling surge and auroral bulge are formed. Figure 1.7 shows a schematic plot of the westward current surge. The
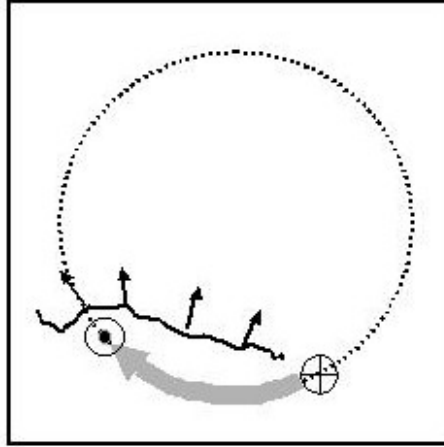
Figure 1.7: Substorm electrojet (westward traveling current).The circles with dot and cross, respectively, depict the field-aligned current closure of the substorm current wedge (shown in Figure 1.6). The auroral bulge expands poleward, westward and eastward.

circles with dot and cross, respectively, depict the field-aligned current closure of the substorm current wedge (shown in Figure 1.6). The auroral bulge typically expands poleward, westward and eastward following onset. Bright structure appeared in the diffuse auroral. Observational AL index is derived from the H component of the magnetic field monitored at 12 stations distributed in longitude. It is obtained from the lower envelope of the single combined plot of the deviations at all stations of the component H from its quiet-time value [*Jursa*, 1985], and is a measure of the strength of the auroral electrojet. During ex-

16

pansion phase, the AL index has an obvious negative bay. Observations also show further enhancement of the eletrojets and outflow of ionospheric ions. The time-scale of this phase is typically 30 minutes to 1 hour.

3. Recovery phase: The distinction between the end of the expansion phase and the beginning of the recovery phase is not so clear as the separation between the growth and the expansion phase. During this phase, in the near tail region ($5 \leq |x| \leq 15R_E$), geosynchronous satellites observe drift echoes of particles injected at substorm onset, while in the midtail, the plasma sheet thickens, typically by a factor of 2. Fast field-aligned flow appear at the plasma sheet boundary layer. In the far-tail ($|x| > 80R_E$) region, fast flows of plasmoids (bundle of magnetic field lines) are observed [*Hones, 1979*]. Plasmoids have a bipolar B_z feature. The Bz perturbation consists of a positive Bz that gradually decreases and becomes negative as the loop magnetic flux passing the spacecraft. In the ionosphere, the auroral bulge size and luminosity is reduced and the auroral oval moves into the morning sector and reaches the most poleward extension.

To account for different magnetospheric and ionospheric phenomena during magnetospheric substroms, many models have been developed [*Kivelson and Russell,* 1995]. Currently, the most favored ones are the Near-Earth Neutral-Line (NENL) model [*Baker et al.,* 1996]and the Current-Disruption (CD) model [*Lui,* 1991]. In this thesis, we attempt to develop an understanding of magnetospheric

substorms as seen in global magnetospheric modeling.

Applying statistical and nonlinear dynamical techniques to large amount of observational data, studies of *Sharma* [1995], *Klimas et al.* [1996], *Tsurutani et al.* [1990], *Takalo et al.* [1993], *Ohtani et al.* [1995, 1998] and *Lui* [1998] showed that during substorms the Earth's magnetosphere exhibits a number of characteristic features of low effective dimension and a power law spectra of fluctuations on different scales. A self-organization model was developed to explain the low effective dimension behavior [*Sharma*, 1995; *Klimas et al.*, 1996] and a self-organized criticality model was developed to explain the multi-scale behavior [*Sergeev et al.*, 1996; *Consilini*, 1997; *Chapman et al.*, 1998; *Lui et al.*, 2000]. However, the self-organization model can not explain the multi-fractal behavior of the substorms. The typical self-organized criticality model is essentially independent of the driver and thus is autonomous, which is not the case with the Earth's magnetosphere. In this thesis, we investigate statistical features of magnetospheric substorms as seen in global magnetospheric modeling and compare to those features derived from observations.

1.5 Ionosphere-Magnetosphere Coupling

The Earth's magnetosphere is dominated by a collision-free plasma, while the ionosphere is the region where the effects of collisions of charged particles cannot be neglected and electrical conductivities transverse to the geomagnetic field

maximize. The magnetic field connects electrodynamically the ionosphere and the magnetosphere, causing an exchange or coupling of energy and momentum between the two regions. A strong coupling occurs since the two regions are connected by the same magnetic field lines. This interaction is important for many phenomena such as plasma convection in both the magnetosphere and the polar ionosphere, magnetospheric substorms, the formation of auroral potential structure through which the acceleration of auroral particles and the corresponding generation of auroral forms occur, the penetration of high-latitude electric fields into low latitudes and the flow of field-currents [*Kamide and Baumjohann*, 1993]. An extensive database of substorm activity is obtained from ground-based networks of various instruments. High-latitude ground magnetometers, riometers and photometers are among these instruments. Therefore, in modeling the magnetosphere-ionosphere coupling, comparison with the ionospheric observations is of critical importance in developing "ground truth".

1.6 Global Magnetospheric Modeling

Today, with multiple satellites in space and the advances in super-computing, spacecraft and ground data combined with multiscale computer models developed by International Space-Terrestrial Program (ISTP) provide a new and coherent understanding of the magnetospheric physics. Global MHD simulations that include the ionospheric response and are dynamically driven by upstream

satellite data allow for direct comparison with the field and flow quantities measured by magnetospheric satellites, ground data and images from the POLAR satellite.

Several major global magnetospheric modeling codes [*Fedder and Lyon,* 1987, 1995; *Raeder,* 1999; *Berchem,* 1995; *Bargatze,* 1999; *Gambosi,* 1998] exist. The Lyon-Fedder-Mobarry (LFM) global magnetospheric model is one of the leading MHD codes in use today for numerical simulation of the coupled solar wind - magnetosphere - ionosphere system. The LFM global magnetohydrodynamic (MHD) simulations have proven to be a powerful approach for the study of the solar wind-magnetosphere-ionosphere system of the Earth [*Fedder and Lyon,* 1987; *Fedder et al.,* 1991; *Mobarry et al.,* 1996; *Slinker et al.,* 1995]. This technique is best used to understand how the energy, mass, and momentum transfer from the solar wind to the magnetosphere occurs and determine the magnetic field topology of the magnetosphere [*Fedder and Lyon,* 1987, 1995]. Recently, quantitative prediction of the magnetospheric and ionospheric response to the solar wind was achieved. In this thesis, we use the LFM model to investigate the the dynamical properties of the Earth's magnetosphere under different solar wind conditions. The details of LFM model are introduced in chapter 2.

Global MHD models have been applied in two ways. In the first method, the model is driven with actual satellite observed solar wind input to reproduce the observed salient features of the substorm phenomenon both qualitatively and

quantitatively. The second method is a theoretical approach which investigates physics based issues with this code by specifying simple upstream solar wind conditions, e.g. time-independent or simple time-dependent conditions.

1.7 Objectives and Directions of this Work

The goal of this thesis is to use the global MHD model to investigate and understand the physical properties of the Earth's magnetosphere, its coupling with the ionosphere and to further expand the capability of the global MHD model in actual event simulations. Specifically, this thesis consists of three major parts covering three topics in magnetospheric physics:

- **Steady state Earth's magnetosphere with northward IMF** (Chapter 3)

- **Magnetospheric substorms** (Chapter 4 and 5)

- **Magnetosphere-ionosphere coupling** (Chapter 6).

This thesis applies the global MHD model to both theoretical and actual-event simulations. In what follows, we present the objectives and directions for each of the three topics, respectively.

1.7.1 Steady State Earth's Magnetosphere with Northward IMF

- **Standard Case Study**

  The structure and magnetic topology of the magnetosphere under northward IMF is one of the fundamental problems in magnetospheric physics. Due to the three dimensional nature of the problem, numerical modeling plays an important role in quantitative studies of the Earth's magnetosphere with steady northward IMF, while simple analytical models help to validate the numerical results. Numerical models [*Raeder et al.* [1995]; *Gombosi et al.*, 1998; *Song et al.*, 1999; *Bargatze et al.*, 1999], relying on three-dimensional global MHD simulations, all showed cusp region reconnection.

  The community of global MHD modeling has long disagreed about the tail length of the Earth's magnetosphere with steady northward IMF for nominal conditions: solar wind velocity=400 km/sec, magnetic field B_z= 5 nT, number density= 5 cc^{-1} and constant ionospheric Pedersen conductance= 5 mhos. Here, the magnetotail length of the steady state magnetosphere is defined as the position of the last closed field line along x axis antisunward in the Noon-Midnight meridian. In this thesis, we call the steady state under these solar wind conditions as the standard case. If the mag-

netotail length is less than 60 R_E, the steady Earth's magnetosphere with northward IMF is regarded as having a short closed tail. Whereas if the magnetotail length is larger than 140 R_E or the tail is open, the steady state magnetosphere is regarded as having a long tail. No cases of the simulated tail length which are in between are reported.

Gombosi et al. [1998], *Song et al.* [1999] and *Bargatze et al.* [1999] found a short closed tail $\sim (40 - 60)R_E$ for the standard case. Simulations of *Berchem et al.* [1995] and *Raeder et al.* [1995] indicated a long tail, with the magnetotail never fully closed after several hours of constant northward IMF. *Fedder and Lyon* [1995], using the same code as that in this thesis, showed a quasi-equilibrium state of the magnetosphere for northward IMF. The quasi-equilibrium state was reached in 2 hours and 20 min after the northward turning. The tail length at this stage was 155 R_E.

A key result of this thesis is the resolution of the long vs. short tail controversy, by focusing on the evolution time scale of the magnetospheric steady state configuration. The present work found a short tail configuration (tail length $\sim (40)R_E$) for the standard case. The 3D configuration of the steady state was examined. Cusp region reconnection and ionospheric four-cell convection pattern are clearly seen in our simulations. The concave shape of the steady state magnetosphere predicted by *Song et al.* [2000] is observed in our simulation.

- **Parametric Dependence on Solar Wind Condition**

  The parametric dependence and scaling of the steady state magnetosphere with northward IMF on the solar wind conditions were studied by *Song and Russel* [1992] and *Song et al.* [1999]. These simple (mainly one dimension) analytical models can't fully explain the parametric dependence revealed by global MHD simulations and overemphasize the role of the ionospheric conductance in determining the tail size.

  In this thesis, we examine the quiet time steady magnetosphere and its scaling with input parameters. The parameters varied during northward IMF are (1) the magnitude of the interplanetary magnetic field B_{IMF} and (2) the magnitude of the solar wind velocity V_{SW}. We demonstrate that the ionospheric conductance is a minor effect in determining the steady magnetotail size. Only the transient behavior is influenced by the conductance. We determined numerically the dependence of the characteristic magnetospheric spatial scale sizes on the strength of the solar wind and the IMF. Based on conservation of flux and force balance, simple analytical models are used to interpret the scaling of the tail on solar wind conditions.

  Finally, the structure of the magnetosphere and its dependence on different solar wind conditions was studied. The parametric dependences of 1D cuts of various tail plasma and field quantities along X axis and Z direction (in SM (solar-magnetospheric) coordinates) are analyzed. The simulations

show that inside the tail during the steady state, in the region x<-20 R_E on the equatorial plane, the magnetotail field B_z is comparable to the solar wind magnetic field B_z and the field B_x is nearly 0.

- **Comparison between Simulation and Observation**

Although the controversies about the short and long tail configuration of the steady state existed for more than 5 years, before this study, there was no direct comparison between observation and simulation for quiet time magnetosphere with northward IMF. Our simulations show that it takes hours for the magnetosphere to reach steady state. Whether the magnetosphere has a long or short tail depends on whether the solar wind driver varies on time scale shorter or longer than the relaxation time. The actual solar wind is rarely quiet for several hours and it is even rarer that there is a satellite traveling inside the tail far away enough from the Earth to record the tail field during the quiet-time interval. This is why there was no direct comparison between the simulation and observation for quiet-time northward IMF event before this study.

After searching the satellite observations during the 8 year period from 1992 to 2000, we find one quiet-time northward IMF event, during which the Geotail satellite is inside the magneto-tail. We simulate this actual northward IMF event which occurred on Feb. 9, 1995, and compare the

results with the Geotail satellite observations. We find that the time scale for the temporal evolution and magnitude of the various components of the tail field from our simulation were in excellent agreement with those observed by the Geotail satellite. This supports our model of the evolution of the magnetosphere to steady state during northward IMF.

1.7.2 Magnetospheric Substorms

- **Global MHD Simulation of an Ideal Magnetospheric Substorm**

  Global MHD simulations have often been applied to simulate and understand magnetospheric substorms [*Fedder et al.*, 1995b; *Goodrich et al.*, 1998; *Lopez et al.*, 1998; *Lyon et al.*, 1998; *Pulkkinen et al.*, 1998; *Wiltberger*, 1998; *Papadopoulos et al.*, 1999; *Wiltberger et al.*, 2000; *Slinker et al.*, 2001; *Raeder et al.*, 2001]. They were quite successful in reproducing the observed substorm activities in both the magnetosphere and the ionosphere. In this thesis, an ideal magnetospheric substorm was simulated with the LFM global MHD model and comprehensively analyzed. The substorm is initiated by a sudden northward-southward IMF turning. This study serves as a pictorial review of the typical behavior of the Earth's magnetosphere and ionosphere during substorms as simulated with the global MHD model. The results show auroral onset and expansion, AL index dipping, dipolarization, current sheet disruption, formation of the

substorm current wedge and formation and ejection of a plasmoid created by the neutral line. There are flow channels penetrating into the inner magnetosphere and connecting the mid-tail and inner-tail region, which supports the observations that auroral activities originate from the inner magnetotail. However, it is not easy to characterize the time sequence of all the events in the inner magnetotail, especially since their occurrence varies with position in the magnetotail.

- **Phase Transition-like Behavior of Magnetospheric Substorms**

  Sitnov et al. [2000] proposed that during substorms, the global coherent and multi-scale aspects of the magnetospheric behavior exhibit features of non-equilibrium phase transition, consistent with earlier phenomenological models of substorm activity [*Sergeev et al.,* 1996] and magnetospheric convection [*Chen and Wolf,* 1993]. In particular, the global low-dimensional image of substorm dynamics resembles the characteristic temperature-pressure-density diagram of equilibrium water-steam transition system. On the other hand, the multi-scale behavior may be explained by deviations from this low-dimensional picture close to the critical point, where the conventional second-order phase transition take place [*Stanley,* 1971]. More recently, *Sitnov et al.* [2001] found a critical exponent of the non-equilibrium transitions in the magnetosphere, that corresponds to the multi-scale aspect of the substorm activity, different from a power-law frequency depen-

dence and the scale spectra in autonomous systems. This exponent relates input and output parameters of the magnetosphere and is quite consistent with a second-order phase transition.

In the past, the global MHD studies focused on simulation of individual substorm events and comparison with satellite and ground observations. In this thesis, we investigate whether the simulated substorms produced in global MHD model have non-equilibrium phase transition-like features revealed by the statistical study of *Sitnov et al.* [2000], based upon simulations of large amount of substorm events. We use the LFM global MHD model to simulate 6 intervals of total duration of 240 hours from the same data set used in [*Sitnov et al.*, 2000, 2001]. Applying the nonlinear dynamical techniques used by *Sitnov et al.* [2000, 2001], we analyze statistically the input-output (vB_s–pseudo-AL index) system using the data obtained from the global MHD model and compare the results to those in *Sitnov et al.* [2000, 2001]. Pseudo-AL index is produced from the maximum westward Hall current searched in the ionosphere model. One advantage of the global MHD model is that, within the model, it provides a large amount of information on the magnetospheric and ionospheric response to the solar wind. Therefore, besides the simulated AL index, we also analyze the behavior of the ionospheric cross polar potential, ionospheric total Joule heating, magnetospheric tail field B_Z and field aligned current at selected

locations in the magnetotail.

The analysis of the coupled vB_s–pseudo-AL index system derived from the global MHD simulations show the first-order phase transition map, which is consistent with similar map obtained for the vB_s–observed-AL index system by *Sitnov et al.* [2000, 2001]. Although, the comparison between observations and global MHD simulations for individual events may vary, the overall global transition pattern during the substorm cycle revealed by Singular Spectrum Analysis (SSA) is consistent in simulations and observations. The procedure of phase transition analysis using SSA has revealed essentially the same features of global configuration change both in the actual system and in the global MHD simulations.

The coupled vB_s–pseudo-AL index system derived from global MHD simulations shows multi-scale behavior (scale-invariant power-law dependence). We also find critical exponents of the non-equilibrium transitions in the magnetosphere, that reflect the multi-scale aspect of the substorm activity, different from power-law frequency and the scale spectra of autonomous systems. The exponents relate input and output parameters of the magnetosphere and distinguish the second order phase transition model from the self-organized criticality model. The limitations of the global MHD model in reproducing the multi-scale behavior are discussed. The behavior of the systems formed by coupling vB_s with other ionospheric and magneto-

spheric response is also analyzed and discussed.

1.7.3   Magnetosphere-Ionosphere Coupling

The magnetospheric response to the solar wind is often measured in the iono-
sphere, using networks of magnetometers, riometers, and radars. An extensive
database on substorm activities is obtained from ground-based measurements.
Modeling the magnetosphere-ionosphere coupling and comparison with iono-
spheric observations plays an important role in understanding how the solar
wind drives the magnetosphere and the ionosphere to produce phenomena ob-
served by means of ground measurements. In LFM global MHD model, [*Fedder
et al.*, 1995b], the inner boundary condition for the MHD solution is determined
from the ionospheric simulation. The solution in the ionosphere is performed
by solving a 2 dimensional height integrated electrostatic potential equation
driven by the field aligned currents within the magnetosphere. The ionospheric
model output gives the electrostatic potential, the precipitating electron energy
and flux, the 2D height integrated Hall and Pedersen conductance [*Jursa*, 1985]
and the ionospheric current and allows for comparison with measurements. An
important test of the models is how well they reproduce the ionospheric measure-
ments. In this thesis, we present the models used for simulating the observations
of riometers and magnetometers from the output of the global MHD simulations.
The model results are then compared with riometer and magnetometer network

data for the January 10, 1997 event.

- **Modeling Riometer Observations**

  Riometers measure the changes in the absorption of very high frequency (VHF) radio signals of galactic origin passing through the ionosphere [*Rosenberg et al.*, 1991]. We develop a model to simulate the ionospheric absorption from the output of the global MHD simulations. It is found that the preliminary model results of the code are inconsistent with the riometer data. This leads us to further research, to identify the causes for the discrepancy and to improve the appropriate part of the model. It is found that turbulent heating due to electrojet instabilities is important in calculating the ionospheric absorption. In view of this, we develop a model that describes the temporally and spatially averaged electron temperature, based on non-linear physics considerations and comparison with available radar observations of the electron heating. The model gives a much better agreement with the riometer observations.

- **Modeling Magnetometer Observations**

  Magnetometers monitor the perturbations of the ground magnetic field produced by the ionospheric currents and the induced imaging ground current (since the Earth's surface is a good conductor). For the simulations of magnetometer data, the model uses the computed ionospheric current den-

sity distribution and the height dependence of the electrojet (determined by the energy of precipitating electrons), to calculate the perturbed magnetic field by implementing Biot-Savart's law. The model including height dependence of the current layer on precipitating electron energy reduces by 10 percent the error compared to the model with fixed current sheet height.

The development of the models for simulating riometer and magnetometer data and comparison with the actual observations guide us to validate and improve our model and achieve better understanding of the magnetosphere-ionosphere coupling.

Chapter 2

Introduction to Global Magnetospheric Modeling–The Lyon-Fedder-Mobarry (LFM) Model

The Lyon-Fedder-Mobarry (LFM) 3-D global magnetospheric model is one of the leading MHD codes in use today for numerical simulation of the coupled solar wind - magnetosphere - ionosphere system. The detailed introduction and documentation about this model can be found in [*Fedder et al.*, 1995a; *Fedder and Lyon*, 1995; *Mobbary*, 1996 and *Wiltberger*, 1998]. The major part of the introduction in this chapter has referenced Wiltberger's thesis [*Wiltberger*, 1998]. LFM model consists of two interlinked simulations for modeling the magnetosphere and ionosphere. The solar wind and magnetospheric plasmas are modeled via the ideal MHD equations. In section 2.1, we discuss the general aspects of global MHD modeling. Then, the numerical techniques used in LFM model

33

are presented. In section 2.3, we discuss the actual grid used within the MHD simulation and the typical resolution it provides. This section also discusses the MHD boundary conditions including the techniques employed for allowing a temporally varying B_x to be input along the front boundary. The ionosphere is simulated by solving a height integrated electrostatic model that has been coupled to the magnetospheric solution. The ionospheric module is discussed in section 2.4.

2.1 Global MHD Modeling

The magnetosphere is composed of several distinct regions. An examination of the typical plasma parameters and scale lengths leads us to conclude that collisionless MHD has a regime of validity that includes solar wind, magnetosheath, tail lobe, and plasma sheet. The magnetopause and neutral sheet have scale lengths that require a kinetic description of the plasma. Furthermore the typical parameters range over several orders of magnitude throughout the magnetosphere.

In global modeling, we strive to capture the large scale physics in an attempt to understand the interactions between the regions that compose the entire coupled system. A fully kinetic description of the plasma has a regime of validity that includes all regions, but it has very high computational cost. This approach requires a significant number of numerical particles per cell (10-100) be

maintained throughout a system with several orders of magnitude in density variations. Also, a full particle simulation requires the use of very small time-steps to resolve the small time-scales. Both of the factors make particle simulation over a computational domain large enough to model the magnetosphere infeasible with currently available computational resources and techniques. Although MHD is not strictly valid throughout the magnetospheric system, we can utilize the partial coherence preserving properties of the magnetic field to extend the technique into this regime with some credibility in the results. The length scales that are produced by a global MHD simulation will generally be larger than the actual ones (e.g. tail current sheet), but the general behavior may be well represented. Furthermore, there exist well developed numerical methods for solving these equations, and current computational resources allow for realistic simulations to be produced over the entire range of parameters present in the solar wind - magnetosphere - ionosphere system. The validity of using this approach to model the entire magnetosphere has been justified by qualitative and quantitative comparisons to in situ observations and basic physical simulations [*Fedder and Lyon,* 1987; *Fedder et al.,* 1991; *Mobarry et al.,* 1996; *Slinker et al.,* 1995; *Song et al.,* 1999; *Raeder,* 1994, 1999; *Berchem et al.,* 1995, 1998; *Fedder et al.,* 1995b; *Goodrich et al.,* 1998; *Lopez et al.,* 1998; *Lyon et al.,* 1998; *Pulkkinen et al.,* 1998].

Ideal magnetohydrodynamics (MHD) treats the plasma as a collisionless mag-

netofluid [*Sturrock.* 1994]. The ideal MHD equations are

$$\frac{\partial \rho}{\partial t} + \nabla \bullet (\rho \vec{v}) = 0 \tag{2.1}$$

$$\rho \frac{d\vec{v}}{dt} = -\nabla \left(p + \frac{B^2}{8\pi} \right) + \frac{1}{4\pi} \vec{B} \bullet \nabla \vec{B} \tag{2.2}$$

$$\frac{d}{dt} \left(\frac{p}{\rho^\gamma} \right) = 0 \tag{2.3}$$

$$\frac{\partial \vec{B}}{\partial t} = \nabla \times (\vec{u} \times \vec{B}) \tag{2.4}$$

$$\nabla \bullet \vec{B} = 0 \tag{2.5}$$

The derivation of these equations relies upon the assumption that response frequencies of the plasma are much smaller than the collision and ion cyclotron frequencies and the length scales are much larger than the ion and electron larmor radii. The magnetic fields allow the MHD approach to be utilized when the plasma is collisionless especially when considering a cold plasma.

The magnetosphere is electromagnetically coupled to the ionosphere via the field aligned current systems. Closed field lines connect the ionosphere with the magnetosphere while open field lines connect the ionosphere to the solar wind. The high conductivity parallel to the magnetic field in the magnetospheric and solar wind plasma results in a mapping of electric fields from these regions into the ionosphere. In general, the high latitude ionosphere can be modeled using an electrostatic electric field and an anisotropic conductivity model which is coupled to the magnetosphere and solar wind by current conservation of the field aligned currents [*Kelly,* 1989].

2.2   Numerical Techniques in LFM Model

In this section we discuss, in general terms, the techniques that are used to solve the MHD equations within the Lyon-Fedder-Mobarry global magnetospheric code. Detailed discussion of the numerical techniques used in LFM can be found in Wiltberger's thesis [*Wiltberger,* 1998]. These numerical techniques are: finite volume method, Partial Interface Method (PIM) developed by John G. Lyon and staggered mesh technique for the treatment of the magnetic field.

2.2.1   The Finite Volume Method

The finite volume method is a numerical technique designed for computing the solution to a set of conservation laws. Its greatest strength is that it deals directly with the conservation laws, and so it conserves the fundamental quantities, e.g. mass, momentum, and energy, on the discrete level. In fact it was shown by *lax* [1954] that only a discretization of the conservative formulation of the flow equations maintains the correct behavior of discontinuities within the solution.

The MHD equations is recasted in conservative form,

$$\frac{\partial \rho}{\partial t} + \nabla \bullet (\rho \vec{v}) = 0 \tag{2.6}$$

$$\frac{\partial \rho \vec{v}}{\partial t} + \nabla \bullet \left[\rho \vec{v} \vec{v} + \left(p + \frac{B^2}{8\pi} \right) \bar{I} - \frac{\vec{B}\vec{B}}{4\pi} \right] = 0 \tag{2.7}$$

$$\frac{\partial \vec{B}}{\partial t} + \nabla \bullet (\vec{v}\vec{B} - \vec{B}\vec{v}) = 0 \tag{2.8}$$

$$\frac{\partial \rho E}{\partial t} + \nabla \bullet \left[\vec{v}\left(\rho E + p + \frac{B^2}{8\pi} \right) - \vec{B}(\vec{v} \bullet \vec{B}) \right] = 0. \qquad (2.9)$$

The total energy, E, in Eq. (2.9) is defined as

$$E \equiv \frac{1}{2}\rho v^2 + \frac{p}{\gamma + 1} + \frac{B^2}{8\pi} \qquad (2.10)$$

As an illustration of the numerical techniques, we consider solutions to a single one dimensional conservation law,

$$\frac{\partial u}{\partial t} + \frac{\partial F(u)}{\partial x} = 0. \qquad (2.11)$$

In Eq. (2.11) $F(u)$ is the flux of u that enters or leaves a given cell. Discretizing this equation over a single cell yields,

$$\frac{\partial \bar{u}_i}{\partial t} = \frac{1}{\Delta x}\left[F(u_{i-\frac{1}{2}}) - F(u_{i+\frac{1}{2}}) \right] \qquad (2.12)$$

where $\bar{u}_i$ is the cell average and $F(u_{i\pm\frac{1}{2}})$ is the flux at the cell interfaces. Everything in Eq. (2.12) is known except for the interface values of u. The accuracy of the finite volume approach is therefore completely determined by the accuracy from which the interface values are determined.

2.2.2 Partial Interface Method (PIM)

The challenge of numerical simulation is to develop a stable scheme that balances and minimizes the competing sources of error that arise from the discretization process. Numerical diffusion causes structures, e.g. contact discontinuities and

local maximums, to spread out over time. Dispersion causes errors in the propagation velocities that depend on wave number and lead to the development of unphysical oscillations near discontinuities. *Godunov* [1959] showed that any linear scheme of second order accuracy or higher will produce these unphysical oscillations. On the other hand first order schemes generally have an unacceptably high level of diffusion. Hybrid schemes, of which PIM is one of many, are a solution to this dilemma; they maintain a monotonic solution, one with no new extrema, by selectively adding diffusion to a high order scheme.

The first order finite volume technique is commonly called donor cell method. Applying to the 1D problem in Eq. (2.12), the algorithm,

$$
\begin{aligned}
u_i^{n+1} &= u_i^n + \frac{\Delta t}{\Delta x} \left(F_{i-\frac{1}{2}} - F_{i+\frac{1}{2}} \right) \\
&= u_i^n + \frac{\Delta t}{\Delta x} \left(F_{i-1}^n - F_i^n \right)
\end{aligned}
\tag{2.13}
$$

has the numerical flux at the interface, $F_{i\pm\frac{1}{2}}$, as the value of the cell in the 'upwind' direction. The donor cell method is diffusive and is prevented from being very useful, especially in cases where we need to consider the long time behavior of systems with discontinuities.

The second order technique is,

$$
\begin{aligned}
u_i^{n+1} &= u_i^n + \frac{\Delta t}{\Delta x} \left(F_{i-\frac{1}{2}} - F_{i+\frac{1}{2}} \right) \\
&= u_i^n + \frac{\Delta t}{\Delta x} \left(\frac{1}{2}(F_{i-1}^n + F_i^n) - \frac{1}{2}(F_i^n + F_{i+1}^n) \right).
\end{aligned}
\tag{2.14}
$$

In this case the numerical flux at the interface is the average value of states on

either side of the interface. The form can be slightly different for different second order method. The second techniques produce profile which has oscillations trailing behind the discontinuities. Furthermore these oscillations result in the development of negative values which can be problematic for quantities, e.g. mass and energy, that are positive definite.

The Partial Interface Method achieves a compromise between the first and second order finite volume technique by combining the approaches in a nonlinear fashion to produce a hybrid scheme. The general expression of this approach is

$$
\begin{aligned}
u_i^{n+1} &= u_i^n + \frac{\Delta t}{\Delta x}\left(F_{i-\frac{1}{2}} - F_{i+\frac{1}{2}}\right) \\
F_{i+\frac{1}{2}} &= F_{i+\frac{1}{2}}^L + C_{i+\frac{1}{2}}\left(F_{i+\frac{1}{2}}^H - F_{i+\frac{1}{2}}^L\right),
\end{aligned}
\tag{2.15}
$$

where $C_{i+\frac{1}{2}}$ is the flux limiter and is determined by the local conditions to be a number between zero and one which determines the amount of mixing between the high order, $F_{i+\frac{1}{2}}^H$, and low order, $F_{i+\frac{1}{2}}^L$, fluxes. Using the second order algorithm to provide the high order fluxes, the PIM for the problem in Eq. (2.12) is

$$
\begin{aligned}
u_i^{n+1} &= u_i^n + \frac{v\Delta t}{\Delta x}\left(F_{i-\frac{1}{2}} - F_{i+\frac{1}{2}}\right) \\
F_{i+\frac{1}{2}} &= \frac{1}{2}(u_i^n + u_{i+1}^n) - \frac{1}{2}sign(u_{i+1}^n - u_i^n)\ \bullet \\
&\qquad \bullet max\left(0, \left|u_{i+1}^n - u_i^n\right| - Bs_i\left|u_i^n - u_{i-1}^n\right|\right) \tag{2.16} \\
s_i &= \frac{1}{2}\left|sign(u_{i+1}^n - u_i^n) + sign(u_i^n - u_{i-1}^n)\right| \tag{2.17}
\end{aligned}
$$

The function s_i is an extremum detector and forces the method to use the donor

cell flux when the upwind cell is an extremum. The parameter, B, is a magic number, which has been found from experience to provide the best results when set between one and ten.

The LFM uses an eighth order flux formulae, [*Zalesak,* 1979], to determine the high order fluxes on the cell interfaces. The limiter is essentially the same limiter presented in Eq. (2.15). There are two key features of the PIM. First, it is a finite volume technique and when applied to the MHD equations it will maintain the correct properties described by the Rankine-Hugoniot relations. Secondly, it will place the shocks in the correct location, but the detailed microphysics of the discontinuities will not be captured. This approach implicitly assumes the macroscale physics is driving the microscale physics and that we need not examine the solution on microscale lengths.

Since the LFM uses a hybrid scheme which applies diffusion based in a non-linear fashion upon local conditions, it is not possible to define a global value for thes numerical viscosity or resistivity of the algorithm. The essential physics of the technique is that it will apply just enough diffusion to sharp gradients within the solution that they will be supported by the grid without introducing extraneous oscillations. This means that quantities like the reconnection rate will be controlled by the global character of the solution and the boundary conditions.

2.2.3 Treatment of the Magnetic Field

One of the greatest difficulties in solving the MHD equations numerically is presented by the constraint that the magnetic field must remain divergence free, $\nabla \bullet \vec{B} = 0$, at all times. Failure to conserve the divergence free of the magnetic field results in solutions with unphysical features such as field aligned forces.

The LFM uses a staggered mesh technique first developed for electromagnetic problems by *Yee* [1966] and later, independent from Yee's work, applied to TVD schemes for the MHD equations by *Lyon* [1983]; *Evans and Hawley* [1988] and *Stone and Norman* [1992]. The staggered mesh relies upon the fact that the magnetic flux is a conserved quantity determined from a line integral of the electric field. The magnetic field components, actually the magnetic fluxes, are placed at the center of the cell faces. The electric fields, which determine the advancement of the magnetic field, are placed along the cell edges. As long as there is monotonic determination of the electric fields along the cell edges for each time step, the solenoidal nature of the magnetic field is preserved to machine roundoff throughout the calculation and the advancement of the magnetic field at the cell interface.

In essence, using the staggered mesh reduces the $\nabla \bullet \vec{B} = 0$ problem to an accurate calculation of the electric fields at the cell corners. In ideal MHD the electric fields are

$$\vec{E} = -\frac{1}{c}(\vec{u} \times \vec{B}). \qquad (2.18)$$

Thus, we need to calculate the magnetic field at the cell corners. In the LFM, an eighth order interpolation algorithm is used to determine the magnetic field at the cell corners from the average value at the cell interface. Before the PIM is used to determine the numerical fluxes, the values from the interpolation are bounded by the average magnetic field in the surrounding cells. This approach means that the numerical resistivity used within the code will depend upon the local conditions.

Magnetic merging is important in our simulations, even though the MHD equations are nondissipative. Magnetic reconnection is allowed by averaging within localized regions. This averaging occurs when oppositely directed flux convect into a single computational cell [*Fedder et al.,* 1995a]. The reconnection rate is not determined by the cell size or the strength of the numerical dissipation. This is because the strong solar wind flows dictate the global timescales by convecting field lines to any resolvable distance where nonideal processes can then break the field line topology.

2.3   The LFM Grid and MHD Boundary Conditions

The Lyon-Fedder-Mobarry three-dimensional (3-D) MHD simulation code [e.g., *Fedder et al.,* 1995a, 1995b; *Fedder and Lyon,* 1995; *Mobarry et al.,* 1996] models

the solar wind, the magnetopshere beyond 2-3.5 R_E, and the coupling of the MHD solutions to an electrostatic model for the ionosphere. The code solves the MHD equations within a large cylindrical region 60 R_E in radius and 330 R_E in length. The front inflow boundary is at x=30 R_E. The inner boundary is at $(x^2 + y^2 + z^2) = 2 - 3.5 R_E$, where x, y and z are the solar magnetospheric coordinates. The distorted spherical mesh is designed to have the maximum resolution near the bow magnetopause, in the ionosphere and geomagnetic tail. Figure 2.1 shows the global and amplified view of the 2D cut of the magnetospheric grid for the MHD simulation. The smallest grid size is $\sim 1/3\ R_E$. The resolution far from the Earth in the solar wind and magnetosheath near the outer boundary is poorer.

Solar wind conditions are imposed on the upstream and side boundaries. A simple supersonic outflow condition is used at the back boundary. This boundary has been located far enough downstream that the plasma is once again super Alfvenic, and thus the boundary is electromagnetically disconnected from the ionosphere and upstream plasma. A geocentric sphere of 2-3.5 R_E in radius is removed to form the inner boundary condition at which the magnetospheric solution is matched to an ionospheric simulation. Field-aligned currents are mapped along dipole field from the inner boundary to the ionsphere, where a convection electric field is computed. The electric field is then mapped to the inner boundary, where it is used to compute boundary conditions on the magnetic field and on the plasma momentum [*Fedder and Lyon,* 1987].
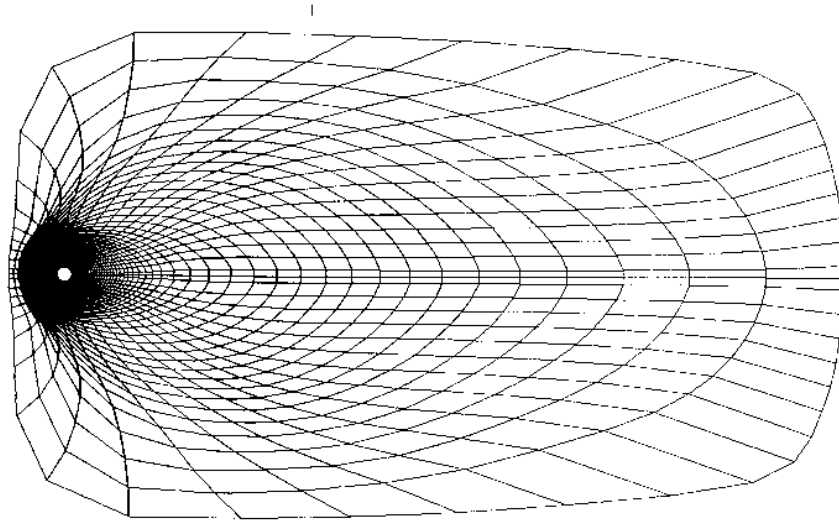
(a)
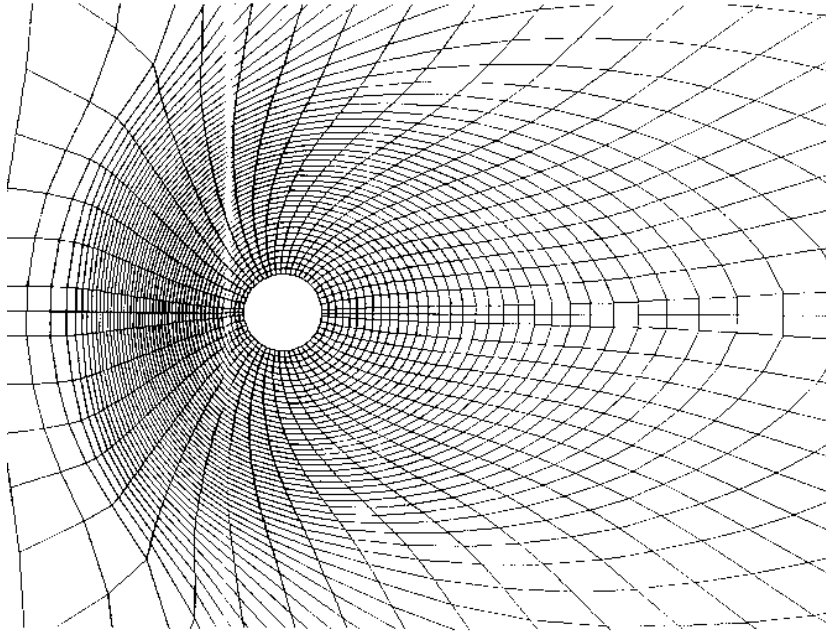
(b)

Figure 2.1: A 2d cut showing the magnetospheric grid for the MHD simulation. (a) The global view. (b) The amplified view. The resolution inside the nominal bow shock position and the inner magnetotail is the highest. The 3d grid consists of multiple copies of this 2d grid at uniformly spaced azimuthal angles.

Two kinds of inputs can be used to drive the LFM code. One is basic physical simulation with simple prescribed solar wind condition. The other one is the actual event simulation.

In this thesis, for the basic physical simulation, the solar wind conditions imposed on the front boundary are simple in the sense that solar wind magnetic field B_x and B_y are 0 and B_z is uniform in the front boundary. Therefore, divergence free of the magnetic field is maintained. Also, the symmetry of the model is preserved by letting solar wind $V_y=0$ and $V_z = 0$ and applying constant Perdersen conductance (=5 mho) and zero Hall conductance for the ionosphere model.

For actual event simulation, the simulation is performed in the Solar Magnetic (SM) coordinate system allowing for the tilt of the Earth's magnetic dipole relative to the solar wind flow direction to be included. Outflow conditions are imposed on the downstream boundary. Elsewhere, external boundary conditions were specified using satellite (WIND or ACE) observed solar wind data which have been propagated appropriately to the front and cylindrical sides of the grid.

The propagation of the satellite observed solar wind data to the front side of the grid in the LFM model is described in detail in [*Wiltberger et al.*, 2000]. In general, the structure of Faraday's law for ideal MHD prevents advection of components for the magnetic field that are not transverse to the flow direction. If the observed magnetic field can be fit to $B_X(t) = a + bB_Y(t) + cB_Z(t)$, then we

46

can effectively creat a new normal direction $\overrightarrow{n} = (\frac{1}{a}\overrightarrow{i} - \frac{b}{a}\overrightarrow{j} - \frac{c}{a}\overrightarrow{k})$ along which the normal magnetic field is constant. This allows a time dependent B_X to be introduced into the simulation by sweeping updates of the solar wind parameters across the front boundary.

LFM MHD code is supplemented with models receiving input from the LFM to address local problems. Extensive diagnostics and visualization tools were attached to the model for testing and validation. The overall architecture is shown in Figure 2.2.
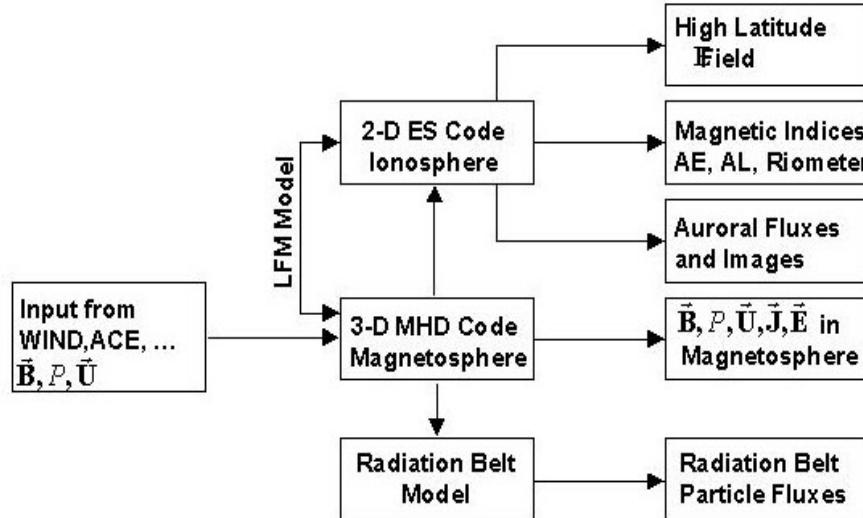
Figure 2.2: Capability of LFM model supplemented with RB code: input on the left, codes in the middle, output on the right. Output is tested against observations and metrics.

2.4 The Ionospheric Module

At the inner boundary located at $2 - 3.5$ R_E from the earth in the LFM Global MHD model [*Fedder et al.*, 1995b], the parallel current density $J_\parallel$ is computed at each time step. This parallel current is mapped into the ionosphere along unperturbed dipole magnetic field lines. The height-integrated current continuity equation relates the $J_\parallel$ to electric potential and conductances in the ionosphere. By using semi-empirical models for the conductances [*Robinson et al.*, 1987], the electrostatic potential Φ is computed. The basic 2D current continuity equation is

$$\nabla_\perp \bullet \Sigma \bullet \nabla_\perp \Phi = J_\parallel \tag{2.19}$$

with Φ the ionospheric potential, Σ the height-integrated anisotropic conductivity tensor and $J_\parallel$ the field aligned current. The ionospheric solution for $\vec{E}$ is mapped back to this boundary and used to define the boundary condition for the plasma velocity ($\vec{E} \times \vec{B}$ drift) via

$$\vec{v} = \frac{(-\nabla \Phi) \times \vec{B}}{B^2}. \tag{2.20}$$

For the ideal physics simulations in this thesis, to preserve the symmetry of the model, we apply constant Perdersen conductance (=5 mho) and zero Hall conductance for the ionosphere model.

For actual event simulations, the conductance tensor contains Pedersen and Hall components [*Kivelson and Russell*, 1995], whose values consist of two contri-

butions. The first contribution is from the steady solar EUV flux and the second

contribution is due to the particle precipitation in the auroral region. The latter

contribution is from the empirical model developed by *Robinson et al.* [1987].

The detailed empirical model for calculating the anisotropic conductance tensor

in LFM was presented in [*Fedder et al.,* 1995b]. Here, we restates the calculation

of the contribution to the conductance tensor from the particle precipitation in

the auroral region briefly.

Robinson et al. [1987] have developed an empirical method for determining

the auroral contributions to the Pedersen and Hall conductivities,

$$\delta\Sigma_P = \frac{5E^{\frac{3}{2}}\phi^{\frac{1}{2}}}{1 + 0.0625E^2} \tag{2.21}$$

$$\delta\Sigma_H = 0.45E^{0.85}\delta\Sigma_P \tag{2.22}$$

where E and ϕ are the energy and flux of the precipitating electrons.

The energy and flux of precipitating electrons in the LFM are determined

from the MHD quantities within the inner most grid cells. First a provisional

set of energy E_o and flux ϕ_o values are determined from thermal speed, c_s, and

density, ρ using

$$E_o = \alpha c_s^2 \tag{2.23}$$

$$\phi_o = \beta\rho E_o^{\frac{1}{2}}. \tag{2.24}$$

The parameters α and β are chosen constants which map the magnetospheric

plasma thermal flux and energy from the MHD inner boundary to the inner

ionosphere.

The field-aligned electric potential energy between the ionosphere and the innermost MHD mesh cell boundary is defined as

$$E_{\parallel} = \frac{R j_{\parallel} E_o^{\frac{1}{2}}}{\rho}, \tag{2.25}$$

where R is also a parameter.

The flux of precipitating electrons is modified to include the effects of field aligned potential drops and geomagnetic mirroring. It's defined as

$$\phi = \phi_o \left(8 - 7 \exp^{\frac{-E_{\parallel}}{7 E_o}} \right) \qquad E_{\parallel} > 0 \tag{2.26}$$

$$\phi = \phi_o \exp^{\frac{E_{\parallel}}{E_o}} \qquad E_{\parallel} < 0. \tag{2.27}$$

While the energy of precipitating electrons is simply

$$E = E_o + E_{\parallel} \tag{2.28}$$

The total ionospheric conductance is taken as the square root of the sum of the squares of the EUV conductance and the auroral conductance.

The ionospheric model incorporates the effects of magnetosphere - ionosphere coupling into the simulation results. It also provides the basis for computing a set of ionospheric diagnostics, e.g. convection patterns (equi-electric-potential contours), AL indices, and total energy flux, that can be compared with in situ measurements. Since the model instantaneously maps the quantities along field lines, it does not include the effects of Alfven wave propagation between these regions, which may be important.

Part II

Global MHD Simulation of the

Earth's Magnetosphere during

Steady Northward IMF

Chapter 3

Steady State Earth's Magnetosphere during Northward IMF

3.1 Introduction to Studies of Earth's Magnetosphere during Steady Northward IMF

The steady state of the magnetosphere with strictly northward IMF have been studied by numerous authors since *Dungey* [1961]. *Dungey* [1961] proposed that reconnection between the IMF and the magnetospheric field will occur at certain regions in the nightside magnetopause. *Johnson* [1960], *Axford and Hines* [1961], and *Dungey* [1961] suggested that the Earth's magnetosphere can, at least for certain directions of the IMF, have a closed magnetic topology. In the magnetospheric convection theory of *Axford and Hines* [1961], plasma flow, in the outer regions of the magnetosphere, is mapped along the geomagnetic field to the po-

lar ionosphere by currents which interconnect the two regions. The convection, both in the magnetospheric boundary layer and in the ionosphere, can be driven mechanically by the transfer of solar wind plasma into the closed geomagnetic field in the vicinity of the polar magnetic cusps and by the expansion of that plasma tailward, both along and across the field, in response to the sunward directed plasma pressure gradient and the tailward decrease in the magnetic field strength [*Johnson,* 1978]. These are the early phenomenological understandings.

Space measurements provide observational features for strongly northward IMF. The NBZ (Northward Bz) current system [*Iijima,* 1984; *Zanetti and Potemra,* 1986] is responsible for changing the magnetospheric convection in the polar ionosphere into the form of a four-cell convection pattern. During extended northward IMF the cross-polar potential is much smaller than that for southward IMF conditions [*Reiff and Burch,* 1985]. *Fairfield* [1993] reported the apparent disappearance of the magnetotail at the observation site downtail 225 R_E during the period of strongly northward IMF.

Both theoretical and numerical models of the Earth's magnetosphere with steady northward IMF have been developed. Theoretical models focus on simple analytical scaling estimation. Due to the complexity of the dynamic three dimensional problem, numerical modeling plays an important role in quantitative studies of the Earth's magnetosphere with steady northward IMF.

3.1.1 Numerical Studies of the Standard Case

Over the last 15 years, several groups have published three-dimensional global
MHD simulations of the Earth's magnetosphere with steady northward IMF
[*Ogino and Walker*, 1984, *Usadi et al.*, 1993, *Fedder and Lyon*, 1995, *Raeder et
al.*, 1995, *Gambosi et al.*, 1998, *Song et al.*, 1999, *Bargatze et al.*, 1999, *Guzdar
et al.*, 2001]. While the models of *Ogino and Walker* [1984] and *Usadi et al.*
[1993] have no well-defined ionospheric boundary and only assume a resistive
shell as the inner boundary, the models of *Fedder and Lyon* [1995], *Raeder et
al.* [1995], *Gambosi et al.* [1998] and *Bargatze et al.* [1999] are well devel-
oped global MHD models. Although the numerical methods vary, all of them
show cusp region reconnection. An important controversial issue is whether the
Earth's Magnetosphere with steady northward IMF develops a long or short tail.
In this thesis, we define a standard case: the Earth's magnetosphere is driven
with constant solar wind velocity=400 km/sec, magnetic field B_z=5 nT, number
density= 5 cc^{-1} and ionospheric Pedersen conductance= 5 mhos. The resulting
magnetotail length (R_{OC}) of the steady magnetosphere, which is defined in Fig-
ure 3.1 as the position of the last closed field line along x axis anti-sunward in
the Noon-Midnight meridian, varies for different global MHD models.

As we introduced in Chapter 1, *Gombosi et al.* [1998], *Song et al.* [1999] and
Bargatze et al. [1999] found a short closed tail $\sim (40 - 60)R_E$ for the standard
case. Simulations of *Berchem et al.* [1995] and *Raeder et al.* [1995] found a
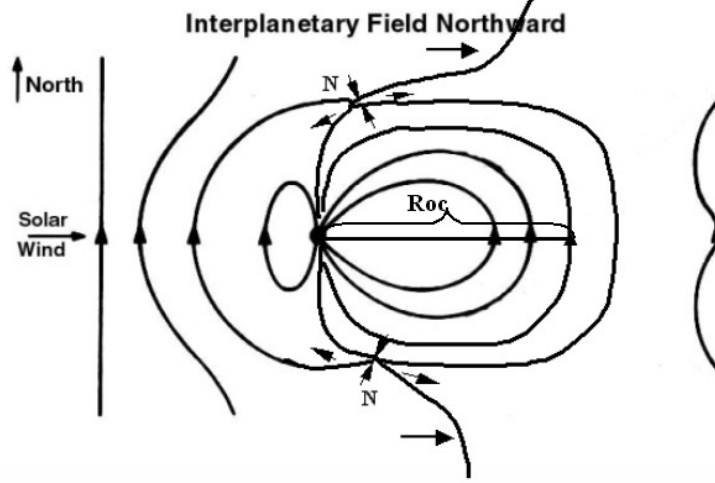
Figure 3.1: Illustration of the magnetotail length (R_{OC}) of the steady magnetosphere with northward IMF.

long tail, and the magnetotail is never fully closed even after several hours of constant northward IMF. *Fedder and Lyon* [1995], using the same code as that in this thesis, showed a quasi-equilibrium state of the Earth's magnetosphere for northward IMF. The tail length at this stage was 155 R_E.

The present work finds a short tail configuration (tail length $\sim 40R_E$) for the standard case. In this chapter, we focus on understanding the physical properties of the steady state Earth's magnetosphere for the standard case. We also discuss the long tail configuration obtained by *Berchem et al.* [1995] and *Raeder et al.* [1995]. The differences between the present work and the earlier results of *Fedder and Lyon* [1995] are clarified by addressing the issue of transients and plasma preconditioning.

3.1.2 The Development of Simple Analytical Model

Simple analytical models have been developed to estimate the global scales of the steady magnetosphere with northward IMF. Based on the model proposed by *Song and Russel* [1992] for the formation of the low-latitude boundary layer (LLBL) for strongly northward IMF, *Song et al.* [1999] find that the magneto-tail for steady northward IMF is closed and the tail length is determined by the solar wind driving force and the ionospheric drag force. They determine that the steady tail length is proportional to $\sqrt{\beta^2 + 1} + 1$, where $\beta = 2\mu_0 n_{SW} k T_{SW} / B_{\mathrm{IMF}}^2$ is the magnetosheath plasma beta near the magnetopause at local noon. They model the magnetic reconnection process at the cusp region by applying conservation of mass, flux, and energy to the cusp merging of flux tubes, and conclude that the total driving pressure (both thermal and magnetic) of a flux tube is propotional to $\sqrt{\beta^2 + 1} + 1$. In their model, the height $\sqrt{y^2 + z^2}$ of the reconnection site at the cusp region is assumed unchanged for different solar wind conditions. The drag force is due to the ionospheric conductance.

In this thesis, we find that the height of the reconnection site depends on the solar wind conditions. We demonstrate that the ionospheric conductance is a minor effect in determining the steady magnetotail size. Our work also shows that the global steady state structures are dictated by the strength of the solar wind and the IMF. We find that the dynamic pressure of the solar wind flow is more important than the plasma pressure. We systematically vary the strength

of the IMF field and the solar wind velocity. This allows us to map the change in the size of the steady state magnetosphere for different solar wind and IMF conditions.

3.1.3   Comparison between Observations and Simulations

Our simulation shows that to reach steady state in the standard case, the solar wind needs to be in steady northward IMF state for about 4 hours. The actual solar wind is rarely quiet for such a long time and the solar wind magnetic field always has $B_x \neq 0$ and $B_y \neq 0$ component, that might affect the topology of the magnetosphere. Also, there was no guidance on what kind of observation to look at. Therefore, there were no direct comparisons between observation and simulation for quiet time magnetosphere with northward IMF before this study.

In this thesis, we search for the signatures of the evolution of the magnetotail to steady state. Guided by the model we develop for the idealized case, we study the satellite observations, especially the local magnetic field, inside the tail during northward IMF. A actual northward IMF event that occurred on Feb. 9, 1995, is simulated and the results are compared with the Geotail satellite observations.

3.2 General Aspects of Steady State Magneto-sphere with Northward IMF–Standard Case

3.2.1 Global Magnetosphere Configuration

To reach a steady state, the solar wind with number density 5 cm^{-3} and velocity 400 km s^{-1} without interplanetary field was initiated from the upstream side and sustained for a period of 50 min; this was followed by 2.5 hours of upstream plasma flow with embedded southward IMF (5 nT) to allow for filling of the tailside magnetosphere with plasma; then the IMF was turned northward. The IMF was kept northward till a steady state was achieved. The time taken to reach steady is about 4 hours. To preserve the symmetry of the model, a constant Pedersen conductance (=5 mhos) and zero Hall conductance was used in the ionosphere model.

Panel (a) of Figure 3.2 shows the final steady state for the standard case in the north-south plane. The smallest grid size in this simulation is 1/3 R_E. Other simulation of double grid size shows the same final steady configuration. After ~4 hours the magnetosphere settles down to this steady state for which the boundary between the open and closed field line regions on the nightside is 40 R_E in the north-south plane. The simulations clearly show the reconnection process occurring in the cusp region and the reconnected field lines being swept towards the nightside. The large flow velocities in the region beyond $\pm$ 20 R_E in
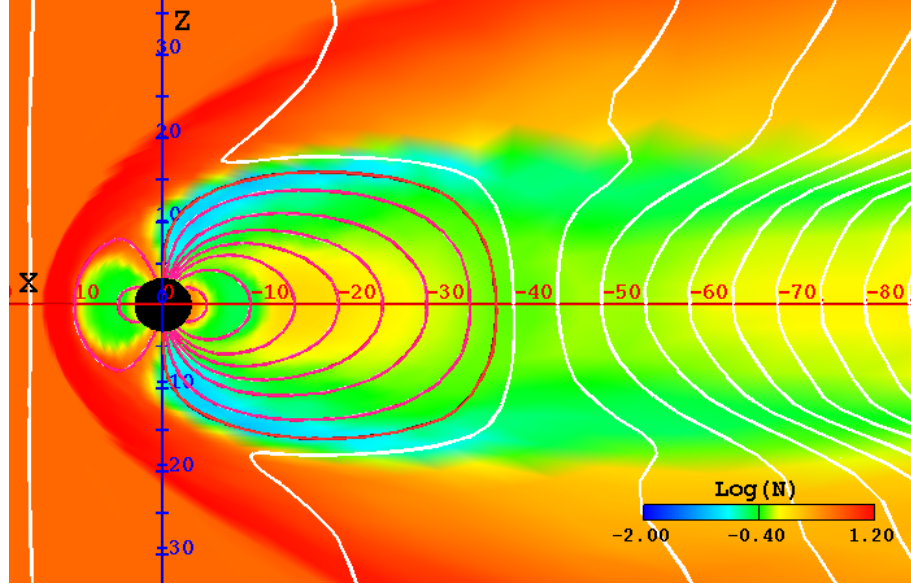
(a)
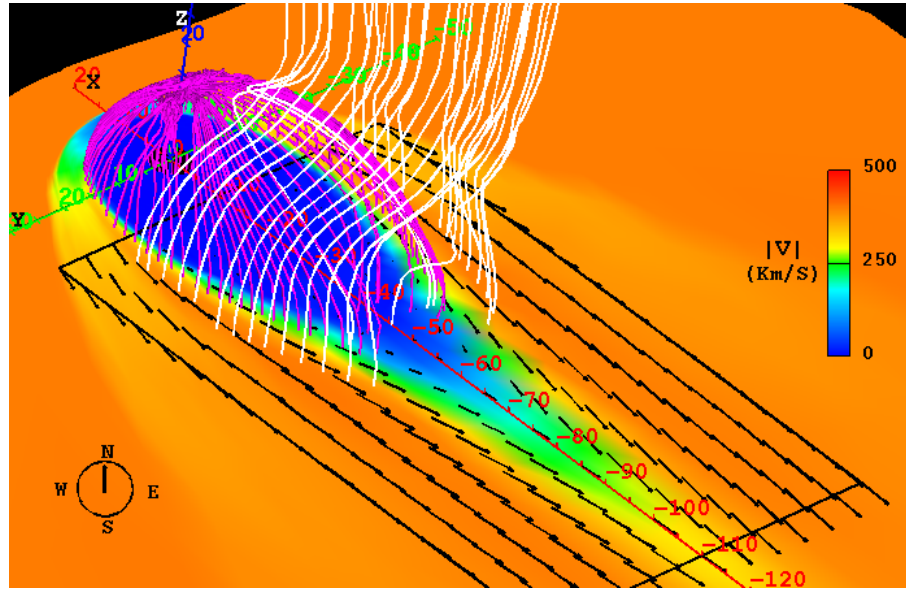
(b)

Figure 3.2: The steady state of the quiet time magnetosphere for $V_{SW} = 400$ km s^{-1} and $B_{\text{IMF}} = 5$ nT. (a) View in the north-south plane. The view point is from the west side of the Earth. The lines are magnetic field lines in the north-south plane. The x axis points toward the Sun and z axis points toward the north. The background is the log of density. (b) Three dimensional view of the quiet-time magnetosphere with an equatorial cut. The view point is from some position above the North Pole. In the background is the magnitude of the velocity, and black arrows are the velocity vectors in the equatorial plane. Red lines are the field lines on the last closed field line surface. White lines are open field lines.

the north-south direction (z axis), carries that portion of the field much faster onto the nightside compared to the segment of the field line in the midplane at x = -40 R_E and z = 0 R_E. As a consequence, a field line which initially had a curvature toward the Earth assumes a curvature away from the Earth on the downstream side. Also seen is the extended shock front associated with the density as the flow drapes around the Earth and its magnetic field.

The equatorial view of the steady state is shown in panel (b) of Figure 3.2. The classic flow of the solar wind past a solid Earth, draped with its magnetic field is clearly seen. The three-dimensional perspective of the magnetic field shows that the position of the last closed field line on the symmetry x axis (-40 R_E) is closer to the Earth than the position of the last closed field line off axis on either side at $y = \pm 10$ R_E. At these off axis locations the position of the last closed field line is approximately at x = -50 R_E. This is because flux from the dayside is convected to the nightside. The magnetic flux piles up and creates a boundary layer for the velocity flow. Across this boundary layer toward the midplane, the velocity decreases. The flow at the boundary layer drags the closed field line region flux to the downstream side. Correspondingly, the footprints of these field lines are convected in the ionosphere due to the $E \times B$ drift. The field lines inside the velocity transition boundary layer are convected into the region near $|y| < 10$ R_E and x= -40 R_E. During this process, the field lines are stretched and finally the condition at the cusp region matches the criterion for

reconnection; that is the local magnetic field reverses its direction within one cell. These reconnected field lines are peeled off and carried by the solar wind at the nightside. The concave shape of the open-closed field line boundary inside $|y| < 10\ R_E$ is formed by the decrease of the velocity across the boundary layer toward the midplane. All field lines on the closed surface inside the concave boundary map to the reconnection site in the cusp region. For those field lines in the mid-plane ($|y|=0$) the velocity of the field line is nearly zero, and hence those field lines are the least stretched. Therefore the boundary mapped from the reconnection site in the cusp is located nearest the Earth ($x=$ -40 R_E). For the field line at the outermost boundary the velocities are high, and the field lines are maximally stretched. Therefore, the point where reconnection occurs maps to the tips of the boundary at $|y|=10\ R_E$, that is the farthest from the Earth ($x=$ -50 R_E). In section 3.3 we will see that the concave structure exists persistently in all cases. *Song et al.* [1999] suggested the existence of the concave shape for the steady state quiet time magnetosphere. In their paper, panel b of Plate 3 presents the existence of the concave shape by shading the region beyond point a. Our simulation result confirms the concave shape for the steady state magnetosphere.
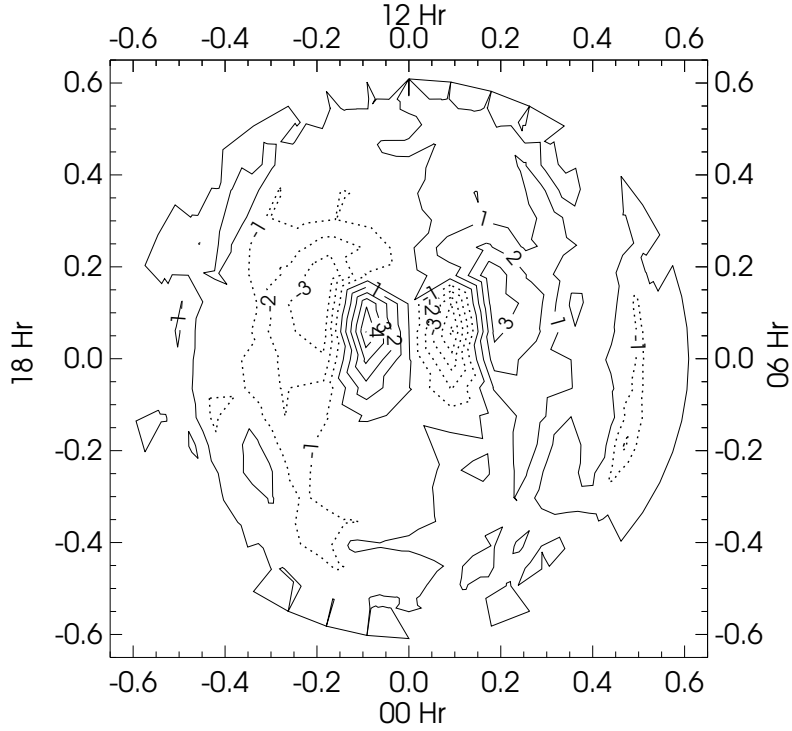
Figure 3.3: Contours of the potential in the ionosphere for steady state northward IMF with $B_{\mathrm{IMF}} = 5$ nT, $V_{SW} = 400$ km s^{-1} and ionospheric conductivity equals 5 mho. The interval between each contour is 1 kV.

3.2.2 Ionosphere Structure

In Figure 3.3 we plot the polar cap potential in the ionosphere for the standard case with B_{IMF}=5 nT, V_{SW}=400 km s^{-1} and the ionospheric conductivity $\Sigma = 5$ mho. One sees the characteristic four-cell convection pattern. The contours of constant electrostatic potential represent streamlines of flow in the ionosphere. As explained by *Song et. al.* [2000], the low-latitude boundary layer (LLBL) on the tailside acts as a generator, converting the flow energy into electromagnetic energy. Part of that energy is carried by the field-aligned Region 1 currents

into the ionosphere and drives the two outer convective cells. The tail reconnection and the associated NBZ currents, on the other hand, drive the reverse-flow convection cells in the high-latitude ionosphere. This qualitatively explains the formation of the ionospheric four-cell convection pattern and magnetosphere convection cell.

3.2.3   Discussion

Simulations of *Berchem et al.* [1995] and *Raeder et al.* [1995] maintain a long tail, and the magnetotail is never fully closed after several hours of constant northward IMF. This contradicts our results. More recently, *Raeder* [1999] investigated the effects of electrical resistivity on the tail length in global MHD simulations. *Raeder* [1999] uses a nonlinear anomalous resistivity function that is switched on when the local current density exceeds a certain threshold. He concludes that the short tail configuration results from the abnormal numerical resistivity. He suggests that the diffusion time scale due to realistic resistivity ($< 10^2 \Omega m$) for the reconnection process in the cusp region can only sustain a long tail. In arriving to this conclusion, the author neglects the $\nabla \times (\mathbf{V} \times \mathbf{B})$ term in the magnetic field convection-diffusion equation and only keeps the diffusion term due to resistivity when the scale size reaches 1 R_E. This leads to the over requirement on the local resistivity. Since the solar wind flow velocity is super-Alfvenic, its role in the overall timescale is important. It rapidly convects

the fields to any resolvable distance, and in the regions where it forms boundary layers with a field null, either resistivity or two-fluid effects (both of these are nonideal effects) facilitate reconnection. Also, from the recent work [*Shay et al.*, 1999] the reconnection rate is Alfvenic. Therefore it is our contention that the prescription used in the LFM MHD code (see section 2.2.3 in Chapter 2) to incorporate reconnection does not influence the global time scales. We do, however, agree that the timescale for the formation of the smaller-sized magnetosphere is of the order of hours, depending on the strength of the solar wind and the IMF.

3.3   Parametric Dependence on Solar Wind Condition

3.3.1   Parametric Dependence of Global Structure

The goal of this study is to understand the scaling of the steady state magnetosphere with input parameters. Two sets of parameters were varied and are (1) the magnitude of the interplanetary magnetic field B_{IMF} and (2) the magnitude of the solar wind velocity V_{SW}. The basic idea is to numerically develop the scaling of important magnetospheric characteristic spatial and temporal scale sizes with these fundamental parameters. The results can be used to guide simple

analytical models using global constraints and force balance conditions.

In all the cases, before northward turning, the solar wind conditions were the ones's we have described in section 3.2.1. During northward IMF the solar wind conditions for the two sets are listed in Table 3.1 and 3.2, respectively.

Solar Wind Condition	Set A (Different B_{IMF})				
	Case 1	Case 2	Case 3	Case 4	Case 5
B_{IMF} (nT)	4	5	10	15	20
V_{SW} (km/s)	400	400	400	400	400
Density (cm^{-3})	5	5	5	5	5

Table 3.1: Solar wind conditions for simulations of set A (different B_{IMF}).

Solar Wind Condition	Set B (Different V_{SW})				
	Case 1	Case 2	Case 3	Case 4	Case 5
B_{IMF} (nT)	5	5	5	5	5
V_{SW} (km/s)	200	300	400	500	600
Density (cm^{-3})	5	5	5	5	5

Table 3.2: Solar wind conditions for simulations of set B (different V_{SW}).

In order to specify the state of the magnetosphere quantitatively, we have defined and measured several parameters. The nightside's last closed field line surface is the surface inside which all the field lines are tied to the Earth, and outside which the field lines are connected to the solar wind IMF. This sur-
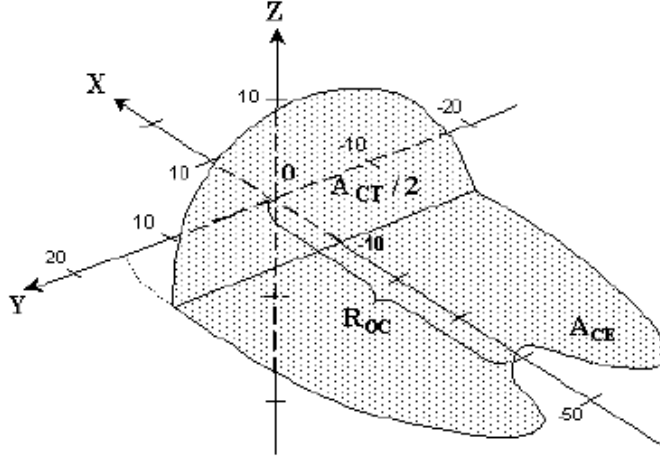
Figure 3.4:   Illustration of the definitions of R_{OC}, A_{CE}, and A_{CT}. The x axis points toward the sun and the z axis points toward the north.

face intersects the equatorial plane and forms a bounded area on the nightside. In Figure 3.4, A_{CE} (cross-equatorial area) is defined as the area of the region formed by this boundary and the $x=$ -10 R_E line in the equatorial plane. The inner boundary in our simulation is at 3.5 R_E. The cross-sectional area of the nightside's last closed field line surface at $x=$-10 R_E is defined as A_{CT} (cross-tail area). A value of $x=$-10 R_E is suitable for measuring the tail radius, because the major change of the tail occurs beyond this region and the tail radius is nearly unchanged around $x=$-10 R_E. The tail length R_{OC} is defined as the position of the last closed field line along the x axis at the $y=0$ plane. These definitions are depicted in Figure 3.4.

In the first set of simulations (set A in Table 3.1), we kept the flow speed constant, and varied the value of the B_{IMF} between 4 and 20 nT. Figure 3.5

66
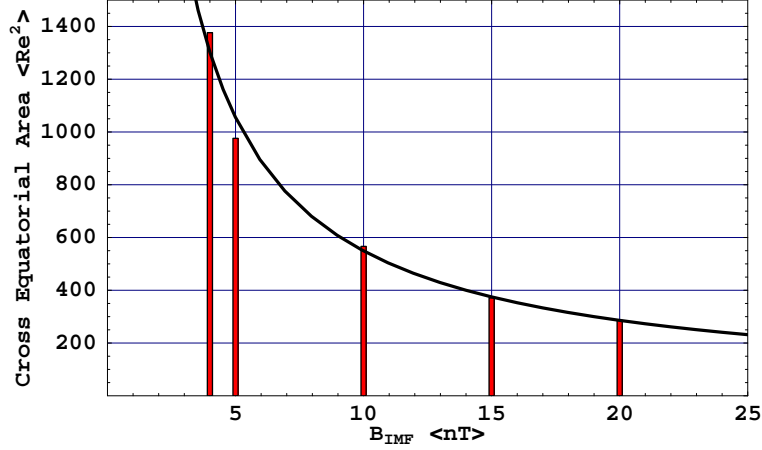
Figure 3.5: Closed field line cross-equatorial area A_{CE} versus B_{IMF} for the steady state magnetosphere for $V_{SW} = 400$ km s^{-1}.

shows the cross-equatorial area A_{CE} of the closed field line region on the night side measured from $x = -10$ R_E to the last closed flux surface as a function of the interplanetary magnetic field, B_{IMF}. For $B_{\mathrm{IMF}} = 4, 5, 10, 15,$ and 20 nT the MHD code was run until a steady state was achieved. By fitting the dependence to a scaling law, we find that $A_{CE} \propto B_{\mathrm{IMF}}^{-0.94}$.

This result can be qualitatively understood as follows: The conservation of the tail flux crossing the equatorial plane is a good approximation to the lowest order. To verify this we found from the code that as we increased B_{IMF} by a factor of 5, the flux decreased by $\sim 20\%$. For the five hundred percent change in the IMF the flux change is insignificant. The small change in flux is due to the nightside reconnection that occurs in the cusp region. This constancy of flux demands that $B_{\mathrm{Tail}} A_{CE}$ be a constant.

We next estimate the tail field. Inside the tail there is no flow, and the

plasma beta is very small. Beyond -20 R_E, the magnitude of the dipole field's contribution to the tail field is very small. From the force balance along the antisunward direction on the nightside ($y = 0$ and $x < -20$ R_E), since the magnetic field is primarily in the z direction in the equatorial plane, $\partial B_z^2/\partial x = 0$. This implies that the B_z field in the equatorial plane is constant. In the vicinity of the boundary between the open and closed field lines, continuity of magnetic pressure requires that the constant magnetic field be equal to B_{IMF}. This is because at the boundary the flow velocity is zero (being a stagnation point), and the only force in the x direction is due to B_{IMF}. Thus, for $x < -20$ R_E for $y = 0$ we expect the tail field in the equatorial plane to be constant and equal to B_{IMF}. This aspect is seen very clearly in Figure 3.6, where we have
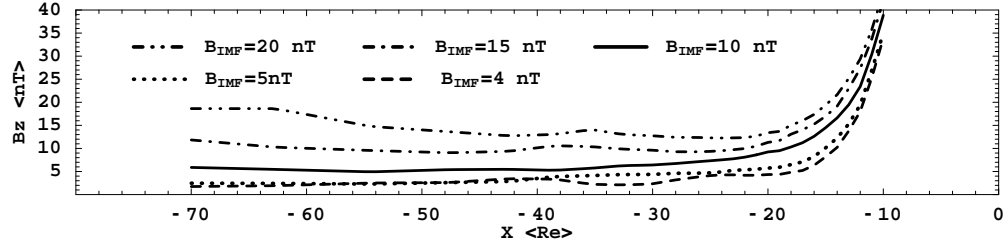
Figure 3.6: Steady state B_z versus x (≤ -10 R_E) at $y = 0$ and $z = 0$ for $B_{\text{IMF}} = 4, 5, 10, 15,$ and 20 nT.

plotted B_z as a function of x for $B_{\text{IMF}} = 4, 5, 10, 15,$ and 20 nT. What is clear is that for $x < -15$ R_E the field is constant in the tail.

We examine the force balance for $x < -20$ R_E in the y direction, since there is no flow and the plasma beta is small, we expect the magnetic field (predominantly in the z direction) to be uniform up to the boundary that separates the

open and closed field lines region. Thus, for a very significant area in the tail

in the equatorial plane, the tail field can be well approximated by B_{IMF}. This

gives a scaling $A_{CE} \propto B_{\text{IMF}}^{-1.0}$, which is in reasonable agreement with the nu-

merically computed scaling. The $1/B_{\text{IMF}}$ scaling of the tail length observed in

the simulations of *Gombosi et. al.* [1998] reduces to our scaling for constant tail

radius in the y direction direction R_y. Since, the tail area under consideration,

A_{CE} in the equatorial plane, has a complicated concave structure around y=0.

Thus we prefer to use the area rather than the tail length.
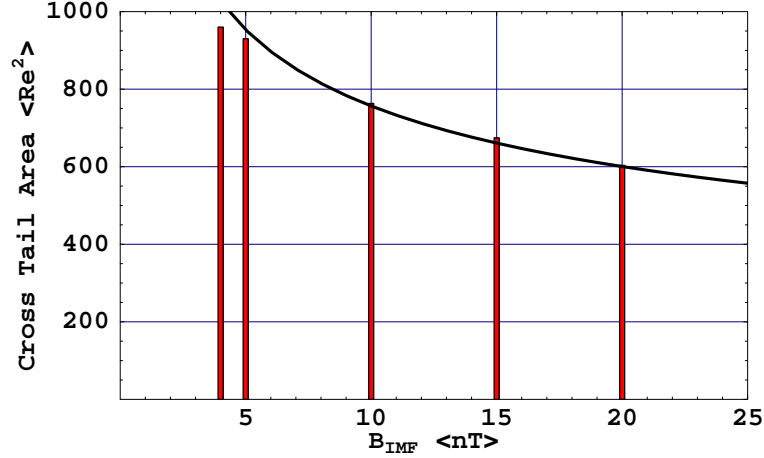
Figure 3.7:   Square root of cross-tail area of closed field line $(\sqrt{A_{CT}})$ versus B_{IMF} for the steady state magnetosphere for $V_{SW} = 400$ km s^{-1}.

Figure 3.7 shows the effective cross-tail area A_{CT} of the closed field region

on the nightside for $B_{\text{IMF}} = 4, 5, 10, 15$, and 20 nT measured at x=-10 R_E. The

solid line is based on the following theoretical model that for a simple dipole

field shows that $A_{CT} \propto 1/B_{\text{IMF}}^{1/3}$. The model considers that the cross-tail

area A_{CT} is proportional to the distance along the z axis (north-south) between

the reconnection points. This is because as B_{IMF} changes, the position of the reconnection height changes, but the distance in the east-west direction of the closed field line region does not change. Thus, if we were to view the region of the closed field line A_{CT} to be an ellipse, the minor radius along the z axis, R_z, changes as a function of B_{IMF}, but the major radius of the ellipse along the east-west y direction R_y does not. Hence the cross-tail area $A_{CT} \propto R_z$. For the reconnection to occur in the cusp region, it is necessary that the local magnetic field on the nightside be equal and opposite to the IMF. This implies that

$$\frac{B_s R_s{}^3}{R_z{}^3} = B_{\mathrm{IMF}}, \tag{3.1}$$

where B_s is the magnetic field at the field line foot point on the Earth and R_s is the radius of the Earth. We have used a simple dipole model for the Earth's magnetic field, which is justified well inside the tail. Now if we recall that the cross-tail area $A_{CT} \propto R_z$, we immediately find that $A_{CT} \propto 1/B_{\mathrm{IMF}}{}^{1/3}$. As can be seen from Figure 3.7, the agreement between the computed dependence of A_{CT} on B_{IMF} and the simple model is good.

In the second set of simulations (set B in Table 3.2), we kept the value of B_{IMF} constant and varied the flow speed. Figure 3.8 shows the scaling of the cross-tail area A_{CT} of the closed field line region on the nightside measured at -10 R_E as a function of the solar wind speed V_{SW}. For $V_{SW} = 200, 300, 400, 500,$ and 600 km s^{-1}, the MHD code was run until a steady state was achieved. Fitting the computed curve to a power law, we find that $A_{CT} \propto V_{SW}{}^{-0.4}$. This scaling
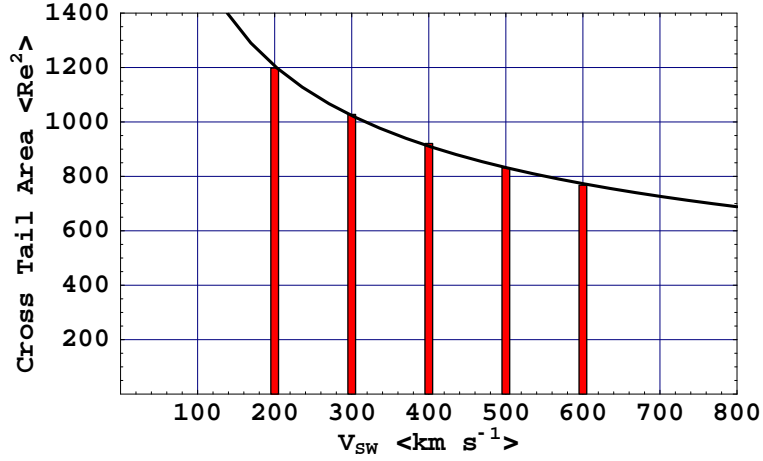
Figure 3.8: Closed field line cross-tail area A_{CE} versus V_{SW} for the steady state magnetosphere for $B_{\text{IMF}} = 5$ nT.

can be qualitatively understood as follows. From force balance the magnetic pressure is balanced by the kinematic pressure of the solar wind [*Klimas et al.*, 1992]:

$$\frac{\rho V_{SW}^2}{2L_V} \approx \frac{B_0^2}{8\pi L_B}. \tag{3.2}$$

Here L_V is the thickness of the velocity transition layer in which the velocity decreases from V_{SW} to several tens of km s^{-1}. L_B is the magnetic field scale length in which the magnetic field changes from the outer B_{IMF} to the major tail field around the x axis and is approximated as tail radius. Again, from flux conservation

$$B_0 L_B^2 = const, \tag{3.3}$$

where B_0 is the average tail field at the cross section x=-10 R_E. This together

71

with Eq. (3.2) implies that

$$\frac{\rho V_{SW}{}^2}{2L_V} \propto \frac{1}{L_B{}^5}. \tag{3.4}$$

The scale length L_V depends on the solar wind velocity V_{SW}. We find from our numerical studies that $V_{SW} \propto L_V$. Now the cross-tail area A_{CT} shrinks both in the north-south and the east-west direction owing to the dynamic pressure of the solar wind flow. As a result of Eq. (3.4) gives that $A_{CT} \propto L_B^2 \propto V_{SW}^{-0.4}$. This semi emperical scaling is in agreement with that obtained from the simulations.
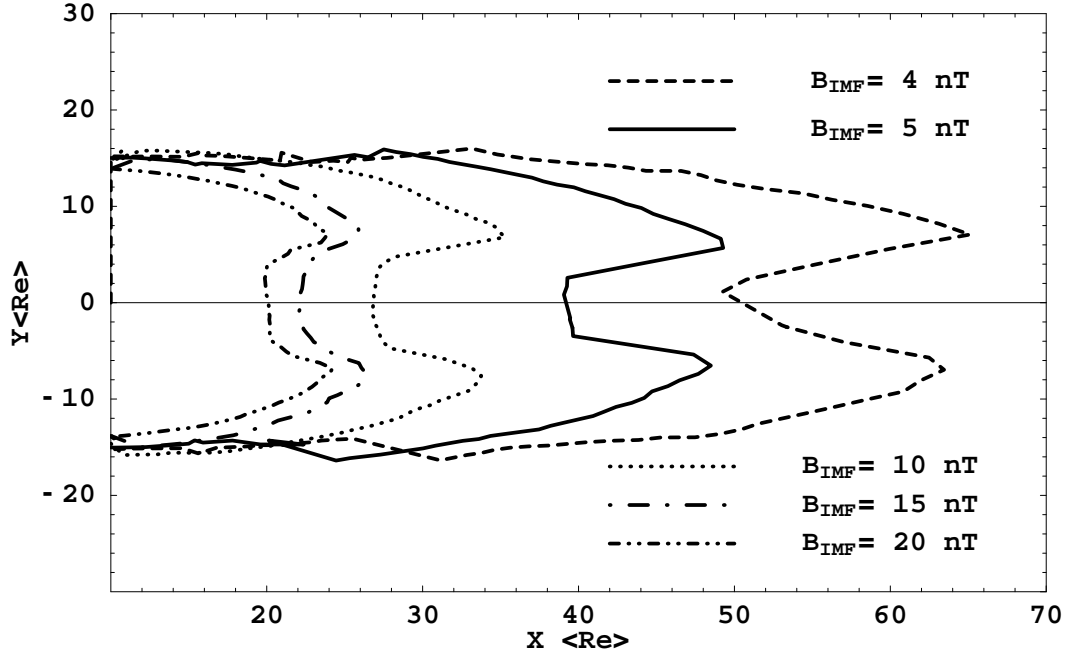
Figure 3.9: Boundary between the open and closed field lines for $B_{\mathrm{IMF}} = 4, 5, 10, 15,$ and 20 nT and $V_{SW} = 400$ km s^{-1}.

Figure 3.9 shows the location of the boundary between the open and closed field line region in the equatorial plane for $B_{\mathrm{IMF}} = 4, 5, 10, 15,$ and 20 nT, respectively, while Figure 3.10 shows the boundary between the open and closed
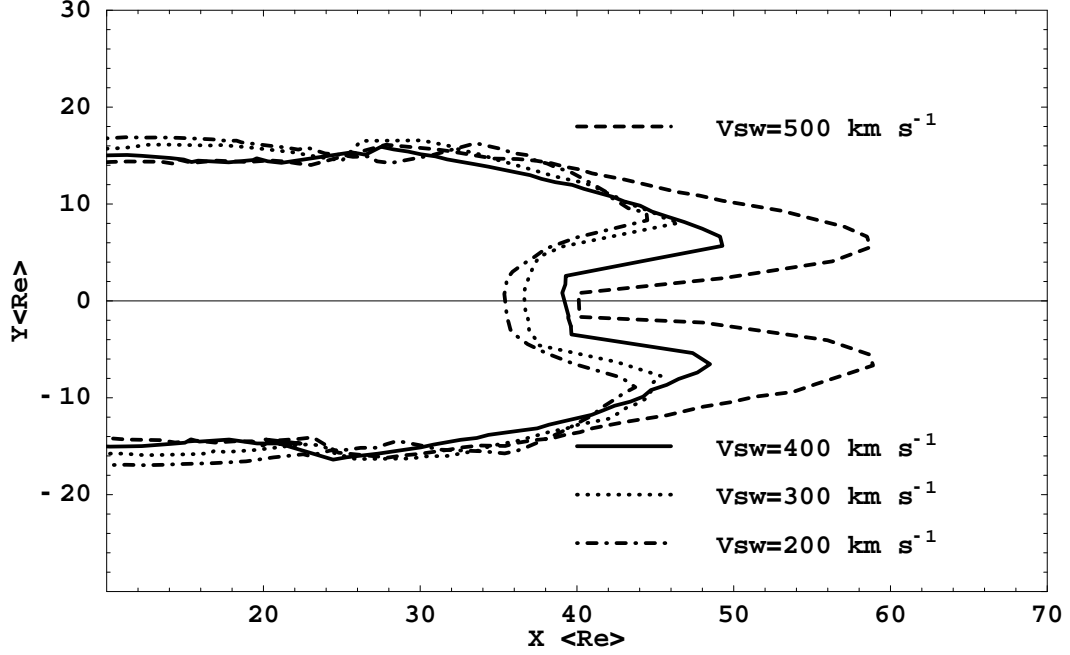
Figure 3.10: Boundary between the open and closed field lines for $V_{SW} = 200, 300, 400,$ and 500 km s^{-1} and $B_{\text{IMF}} = 5$ nT.

field line region in the equatorial plane for $V_{SW} = 200, 300, 400,$ and 500 km s^{-1}

for $B_{\text{IMF}} = 5$ nT. As mentioned in section 3.2.1, the concave structure persists in

all cases. We also see that the separation distance between the boundary point

at $y = 0$ and the farthest point at $y = \pm 10$ R_E, both of which are mapped from

the reconnection site, increases as B_{IMF} decreases. However, for different V_{SW},

the separation distance between the boundary point at $y = 0$ and the farthest

boundary point at $y \neq 0$ increases as V_{SW} increases.

To understand these dependences qualitatively, we treat the steady state of

the Earth's magnetosphere for northward IMF as a system in dynamical equi-

librium. The reconnection, which occurs in the cusp region, adds flux to the

73

dayside magnetosphere, and the solar wind grabs the newly reconnected field lines on the nightside and transports them downstream. The newly added flux on the dayside is convected along the low-latitude boundary layer to the night side. The corresponding ionospheric response is the inner convection cells of the four-cell ionospheric convection pattern shown in Figure 3.3. When the field lines arrive at the end of LLBL around $|y| < 10\ R_E$, the local magnetic field gradient at the cusp region is large enough for the reconnection to occur. For dynamic equilibrium, the timescale for adding flux at the dayside and peeling off of flux on the nightside should be equal. In the equatorial plane the flux-conservation can be stated as

$$B_d A_d = B_n A_n, \tag{3.5}$$

where $B_d(B_n)$ is the magnetic field for the newly added (peeled) flux at the dayside (nightside), and $A_d(A_n)$ is the area on the dayside (nightside) for the newly reconnected flux through the equatorial plane. B_n can be approximated by B_{IMF}; we also know that the dayside pressure balance gives

$$B_d^2 \propto \rho V_{SW}{}^2. \tag{3.6}$$

Combining Eq. (3.5) and Eq. (3.6), we have

$$\frac{A_n}{A_d} \propto \frac{\sqrt{\rho} V_{SW}}{B_{\mathrm{IMF}}}. \tag{3.7}$$

Assuming that the dayside area A_d is independent of B_{IMF} and V_{SW}, the scaling presented of Eq. (3.7) is consistent with the observed dependence of the closed

field line area in the equatorial plane as a function of B_{IMF} and V_{SW} as shown in Figures 3.9 and 3.10 respectively. The nightside area A_n increases with the increase of V_{SW} and decreases with the increase of B_{IMF}.

3.3.2 Structure of the Tail Plasma and Field

In this section, we study the structure of various tail plasma and field quantities for the steady state magnetosphere under different solar wind conditions. The parameters we varied for the solar wind condition are the same as in section 3.3.1, namely, the solar wind velocity and B_{IMF}. The final steady states are divided into two groups. One for the set A listed in Table 3.1 with solar wind B_{IMF}=4, 5, 10, 15, 20 nT; The second for the set B listed in Table 3.2 with V_{SW}= 200, 300, 400, 500, 600 km/sec.

Two kinds of 1D cut are applied to the steady state. One is along the X axis between x=-10 R_E and x=-70 R_E. The other is along the direction of the Z axis which intersects the equatorial plane at x=-10 R_E, y=0 R_E. This second cut is from z=-30 R_E to z=30 R_E. Both of the 1D cuts provide details about the structure of the magnetosphere in north-south plane. We have also studied the three dimensional structure of the shell current sheet and its dependence on different solar wind conditions.

3.3.2.1 Dependence of the Tail Plasma and Field on B_{IMF}

Figure 3.11 shows 1D-cuts of various steady state tail plasma and field quantities along the direction of Z axis at x=-10 R_E, y=0 R_E for different solar wind B_{IMF}. Due to the symmetry of the simulation, some quantities, such as V_y, B_z etc., are insignificant and have not been plotted.

The steady state tail density, velocity and electric field E_y are small in the region from z=-10 R_E to z=10 R_E. Outside this region, there is one layer (approximately inside 12 $R_E < |z| < 20 R_E$) across which B_x changes its direction. This corresponds to the kink of the magnetic field at the night side produced by the cusp region reconnection. V_x starts to increase in magnitude and matches the solar wind velocity when traverses the transition layer. The current density J_y shows a negative bump in the transition layer with magnitude of 10^{-9} A/m^2. The inner edge of the current density bump corresponds to the boundary of the closed magneto-tail. The magnetic field B_z matches the solar wind IMF at $|Z| > 20 R_E$. All the quantities are of even symmetry except V_z and B_x which as expected are of odd symmetry. V_z has significant magnitude around $|Z| = 20 R_E$, which shows the relaxation and expansion of the kinked magnetic field line.

The larger the B_{IMF} in the solar wind, the smaller the steady tail radius. This can be inferred from the inner edge of the bump of the current density J_y and the location of the transition layer of B_x. As we explained in section 3.3.1, the cross-tail area scales as $A_{CT} \propto 1/B_{\mathrm{IMF}}^{1/3}$. The increase of the solar
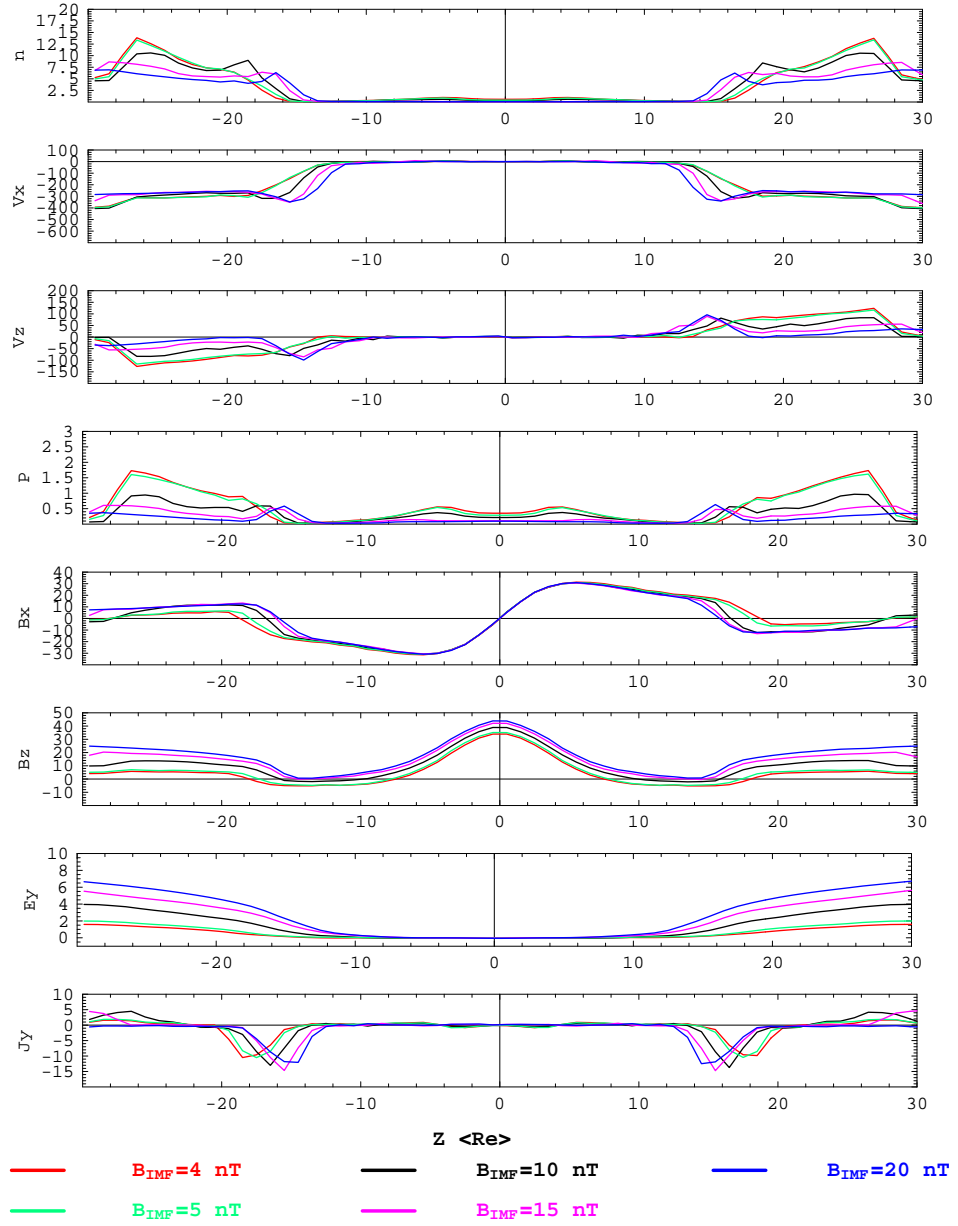
Figure 3.11: 1D-cuts of various tail plasma and field quantities along the direction of Z axis at x=-10 $R_{(}E)$, y=0 for the steady magnetosphere with solar wind B_{IMF}= 4, 5, 10, 15, 20 nT, V_{SW}=400 km/sec and n= 5 cm^{-3}. Different color of the curve represent steady states with different solar wind conditions. The colored labels at the bottom of the figure identify the solar wind condition with which the colored curve represents. Density n is of unit cm^{-3}; velocity is of unit km/sec; pressure is of unit $keV * cm^{-3}$; magnetic field is of unit nT; electric field is of unit $mV * m^{-1}$ and current density is of unit 10^{-10} $A * m^{-2}$.

magnetic field B_{IMF} leads to the increase of the steady magnetic field B_z inside the tail.

Next, Figure 3.12 shows the 1D-cuts of various steady state tail plasma and field quantities along the X axis for different B_{IMF}. The tail magnetic field B_z matches the magnitude of the B_{IMF} for x< -20 R_E. As expected, B_x is almost zero for x< -20 R_E. Inside the closed tail, the density is low and the velocity V_x is almost zero. Both the increase of the density and the velocity V_x mark the boundary of the closed magnetosphere. The slopes of the transition of the density and V_x are notably different for different B_{IMF}. The current density J_y varies from a positive to negative value and finally approaches 0 along the X axis in the anti-sunward direction. This corresponds the change in the curvature of the magnetic field from towards the Earth in the tail to anti-sunward in the open field line region near the tail boundary and finally merger with the solar wind magnetic field.

3.3.2.2 Dependence of the Tail Plasma and Field on V_{SW}

Figure 3.13 shows the 1D-cuts of various tail plasma and field quantities along the direction of Z axis at x=-10 R_E, y=0 R_E for the steady magnetosphere with solar wind V_{SW}=200, 300, 400, 500, 600 km/sec, B_{IMF}= 5 nT and n= 5 cm^{-3}. The dependence of the structure of the tail field along the Z direction on the solar wind velocity is different from the dependence on B_{IMF}. The tail velocity
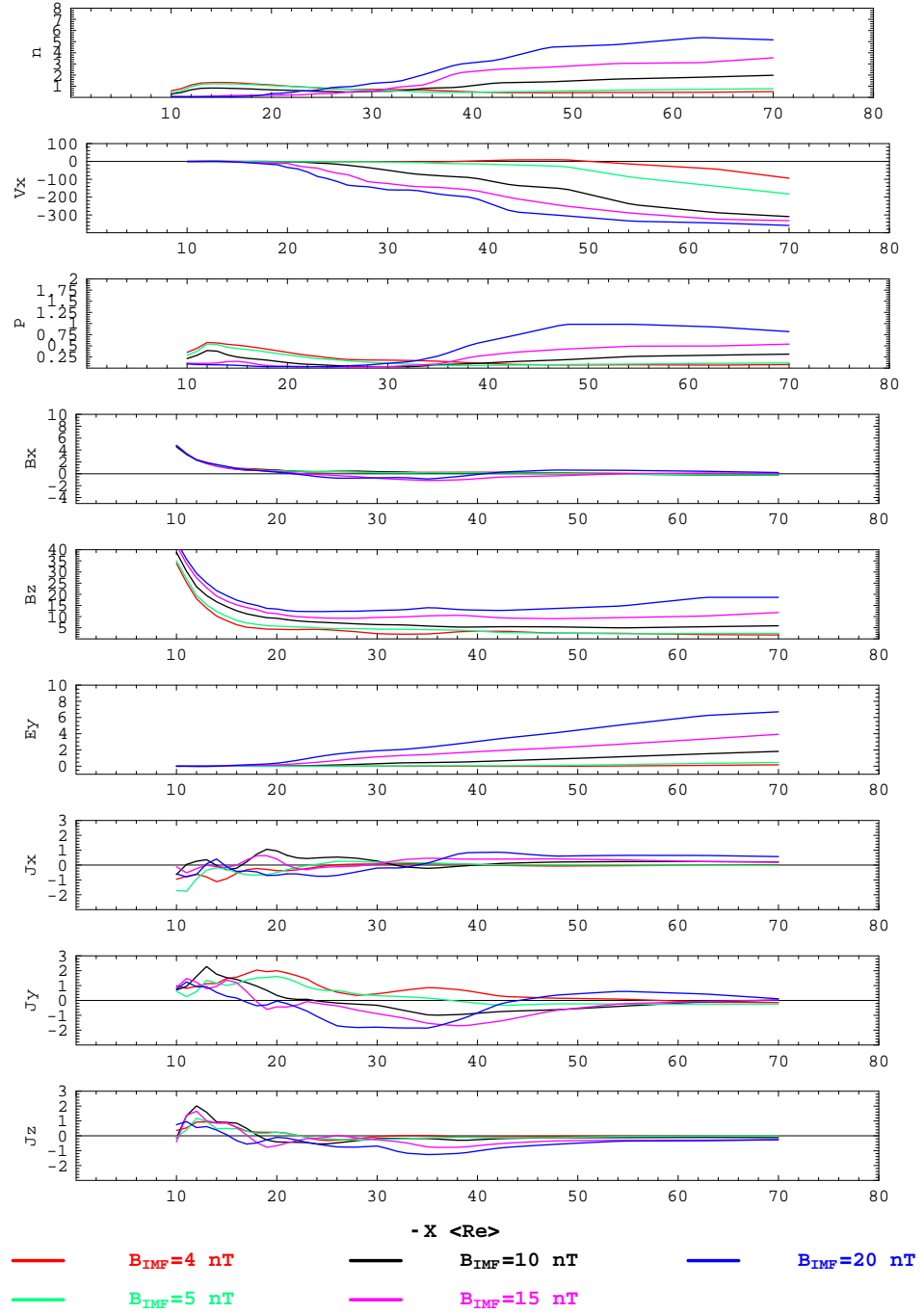
Figure 3.12: 1D-cuts of various tail plasma and field quantities along X axis for the steady magnetosphere with solar wind B_{IMF}= 4, 5, 10, 15, 20 nT, V_{SW}=400 km/sec and n= 5 cm^{-3}. Different color of the curve represent steady states with different solar wind conditions. The colored labels at the bottom of the figure identify the solar wind condition with which the colored curve represents. The units are the same as in Figure 3.11.
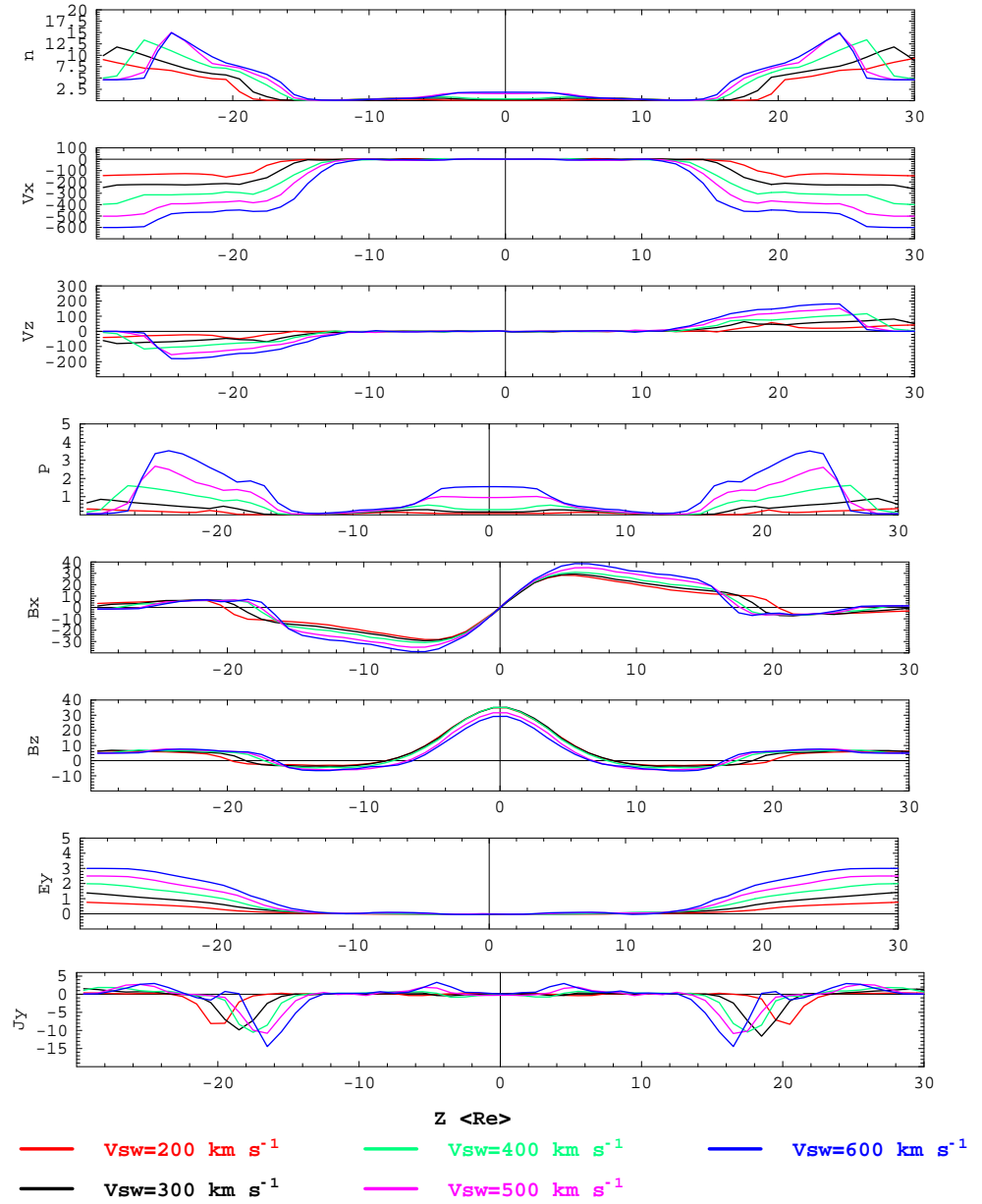
Figure 3.13: 1D-cut of various tail plasma and field quantities along the direction of Z axis at x=-10 $R_{(E)}$, y=0 for the steady magnetosphere with solar wind V_{SW}=200, 300, 400, 500, 600 km/sec, B_{IMF}= 5 nT and n= 5 cm^{-3}. Different color of the curve represent steady states with different solar wind conditions. The colored labels at the bottom of the figure identify the solar wind condition with which the colored curve represents. The units are the same as in Figure 3.11.

field V_x matches the appropriate solar wind velocity outside the tail and the distribution of the tail magnetic field B_z doesn't differ much for different solar wind velocities. The closed tail radius, which can be inferred from the increase in the density and the velocity V_x, varies notably for different solar wind velocity. This can also be inferred from the drift and the change in magnitude of the negative bump of the current density J_y. The tail magnetic field B_z matches the B_{IMF}= 5 nT for $|Z| > 20$ R_E. E_y which is mainly proportional to $V_x \times B_z$ shows similar variation as V_x.

Figure 3.14 shows the 1D-cuts of various tail plasma and field quantities along the X axis for the steady magnetosphere with different solar wind velocities. The overall dependence of the steady state structure of the tail field along the X axis on solar wind velocity is not as apparent as the dependence on solar wind magnetic field. This is mainly due to the fact that the B_{IMF} has more direct effect on the tail length than the solar wind velocity. With higher solar wind velocity, the stress on the tail side is larger. Therefore, the steady tail lobe thermal pressure and current density J_y is larger for higher solar wind velocity. With different solar wind velocity, the tail magnetic field B_z for x< -20 R_E converges to the same magnitude which is comparable to the solar wind IMF. This confirms our previous statement that the steady tail magnetic field in the equatorial plane is of the magnitude comparable to that of the solar wind IMF. The tail magnetic field B_x is almost 0 at x< -20 R_E for different solar wind
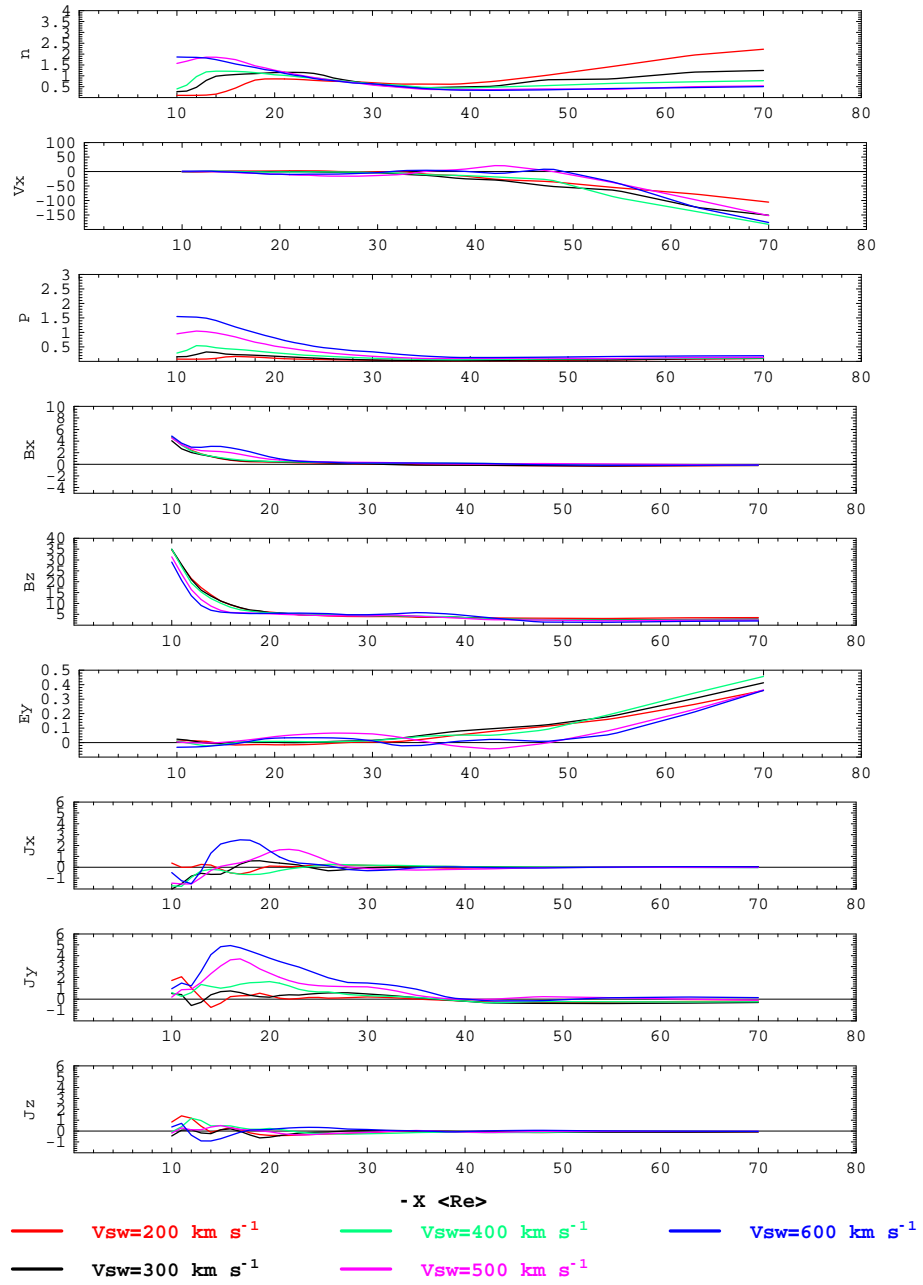
Figure 3.14: 1D-cut of various tail plasma and field quantities along X axis for the steady magnetosphere with solar wind V_{SW}=200, 300, 400, 500, 600 km/sec, B_{IMF}= 5 nT and n= 5 cm^{-3}. Different color of the curve represent steady states with different solar wind conditions. The colored labels at the bottom of the figure identify the solar wind condition with which the colored curve represents. The units are the same as in Figure 3.11.

velocity.

3.3.2.3 3D Shell-Current-Sheet Structure

Figure 3.15 shows the current profile for different solar wind conditions. The view point is from the side of the north-south (X-Z) plane. The background is the log of the magnitude of the total current density in the north-south (X-Z) plane. The white shell-like surface is the isosurface with total current density larger than 2.5×10^{-9} A/m^2.

In general, the dominant current structure is of shell-sheet shape. At the magnetopause on the dayside, the magnetic field is compressed and strengthened by the northward IMF. The magnetic pressure balances the solar wind dynamical pressure which has passed the shock front. Therefore, the shell current at the front centered on the X axis is mainly due to the gradient of the magnetic field. In the cusp region, the cusp reconnection is a dynamical steady state process and produces pairs of kinked magnetic field lines. One part of the newly reconnected field lines is tied to the Earth's ionosphere and adds flux to the dayside magnetosphere. The other part of the newly reconnected field line frozen into the solar wind is convected down stream in the anti-sunward direction. Therefore, the shell-current-sheet in the cusp region is mainly due to the curvature and X line structure of the magnetic field at the field null. Normally, the reconnected magnetic field lines, that are added to the dayside magneto-
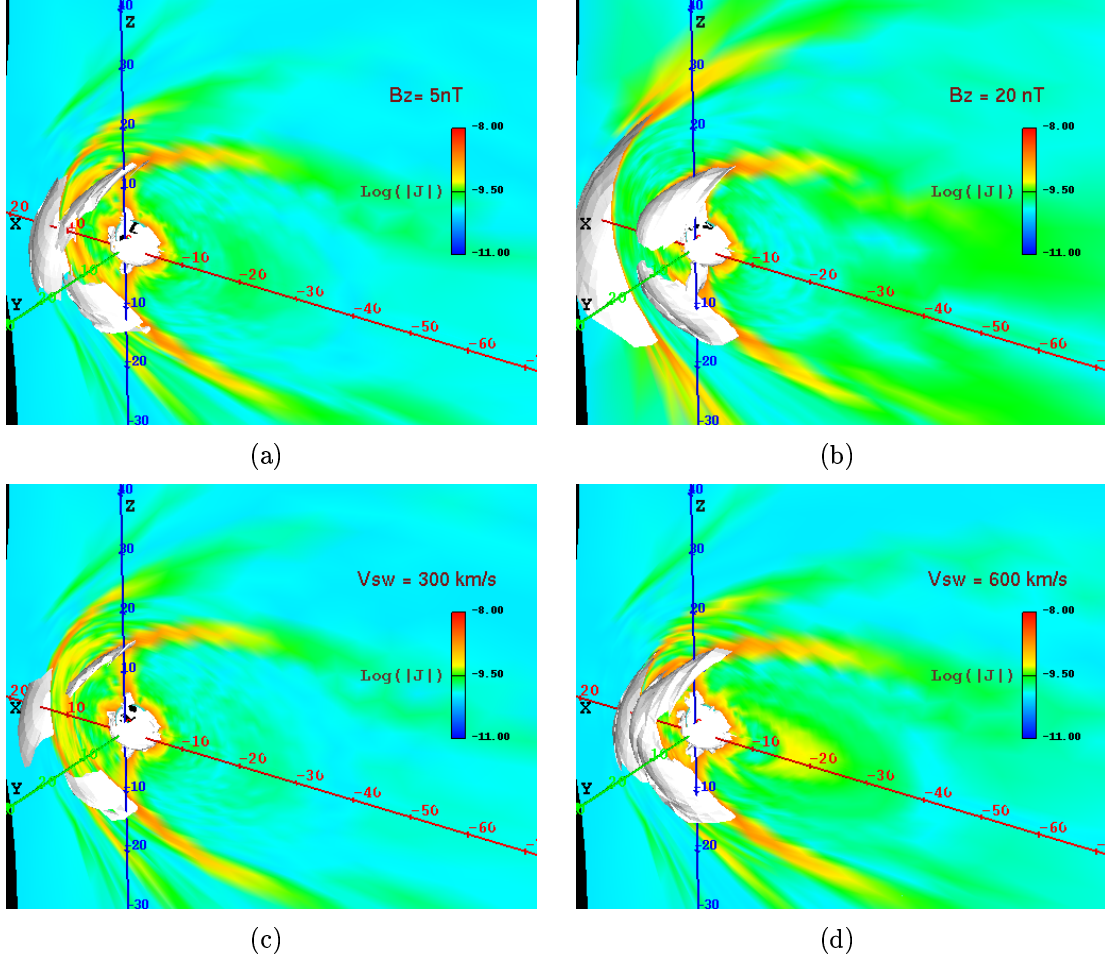
Figure 3.15: Steady 3D shell-current-sheet structure for different solar wind conditions. The view point is from the side of the north-south (X-Z) plane. The background is the log of the magnitude of the total current density in the north-south (X-Z) plane with color legend on the right. The white shell-like surface is the isosurface with total current density larger than 2.5×10^{-9} A/m^2. (a) Steady shell-current-sheet structure for Earth's magnetosphere with solar wind V_{SW}= 400 km/s, B_{IMF}=5 nT and density= 5 cm^{-3}. (b) Steady shell-current-sheet structure with solar wind V_{SW}= 400 km/s, B_{IMF}=10 nT and density= 5 cm^{-3}. (c) Steady shell-current-sheet structure with solar wind V_{SW}= 300 km/s, B_{IMF}=5 nT and density= 5 cm^{-3}. (d) Steady shell-current-sheet structure with solar wind V_{SW}= 600 km/s, B_{IMF}=5 nT and density= 5 cm^{-3}.

sphere assume sharper curvature than the reconnected magnetic field line which are convected away by the solar wind on the nightside. Thus, only the shell-shaped current sheet in the cusp region formed by the reconnected magnetic field line which are added to the dayside magnetosphere, is above the threshold current density and visible. The current due to the reconnected field line on the night-side still has significant magnitude. This can be seen in the red shaded area in the cusp region on the nightside. The tail current sheet around X axis is broad and of smaller magnitude compared to the current structure mentioned above.

Panels (a) and (b) of Figure 3.15 show the steady shell-current-sheet structures for B_{IMF}= 5, 20 nT, respectively. The solar wind V_{SW}= 400 km/s and density= 5 cm^{-3} are the same for the two cases. It can be seen that for higher interplanetary magnetic field B_{IMF}, the dayside current sheet at the magnetopause is further away from the Earth and covers more area. This is because the higher northward IMF strengthens the dayside magnetic field more and the magnetopause is formed further away from the Earth. The shell-current sheet at the cusp region is also broader with higher solar wind magnetic field B_{IMF}. With higher solar wind IMF, the magnetic field around the reconnection site is higher due to the reconnection criteria of opposite magnetic field line of similar magnitude. More magnetic flux is piled up at the cusp region. During steady stage, more reconnection needs to take place to dispose of the magnetic flux.

One direct consequence is the broader current sheet in the cusp region.

Panels (c) and (d) of Figure 3.15 show the steady shell-current-sheet structures for solar wind V_{SW}= 300, 600 km/sec, respectively. The solar wind B_{IMF}= 5 nT and density= 5 cm^{-3} are the same for the two panels. It can be seen that the dayside current sheet at the magnetopause is closer to the Earth. The higher solar wind ram pressure pushes the magnetopause closer to the Earth. The shell-current-sheet at the cusp region is also broader for higher solar wind velocity. With higher solar wind velocity, more solar wind magnetic flux are piled up at the cusp region and more reconnection is needed to dispose of these flux. Therefore, the shell-current-sheet at the cusp region is broader.

3.3.3   Time Evolution of the Magnetosphere to Steady State

A critical issue in understanding the magnetosphere for northward IMF, is the time required for the magnetosphere to reach steady state, as a function of the driving parameters.   Figure 3.16 shows the position of the last closed field line as measured on the nightside at $y = z = 0$ for different values of the B_{IMF}. $t = 0$ refers to the transition from southward IMF to northward IMF at the subpolar magnetopause. After the IMF turns from southward to northward, the stress on the tail is reduced and the tail starts to expand both in length and in radius. The last field line is convected downstream at the speed of the solar wind. As
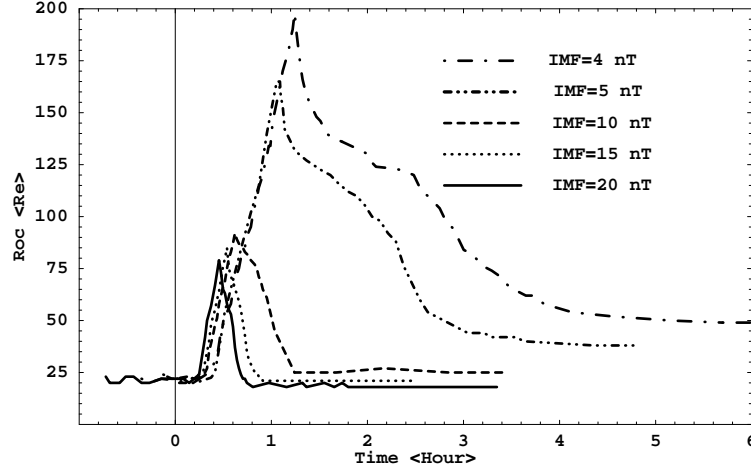
Figure 3.16: Time history of the last closed field line for $B_{\mathrm{IMF}} = 4, 5, 10, 15,$ and 20 nT and $V_{SW} = 400$ km s^{-1} at $y = z = 0$.

mentioned in section 3.2.1, when the condition in the cusp region matches the reconnection criterion, the field lines are reconnected and peeled off. Thus, at some instant of time, the tail reaches a maximum tail length. This maximum tail length scales as $1/B_{\mathrm{IMF}}^2$ and depends weakly on V_{SW} (not shown). Finally, the magnetosphere relaxes and reaches a state of minimum energy. The time taken to reach the steady state varies from 1 to 10 hours. With the preconditioning used in section 3.2.1, the time taken to reach a steady stage scales as $1/B_{\mathrm{IMF}}^2$. These studies imply that in reality the magnetosphere might not relax to a true quiet time steady state with northward IMF, since most of time the driving solar wind conditions vary on a faster timescale. However, in those rare cases when the northward IMF as well as the solar wind ram pressure is sustained for many hours such steady states may be realized.

We finally discuss the role of the ionospheric conductance on the tail size
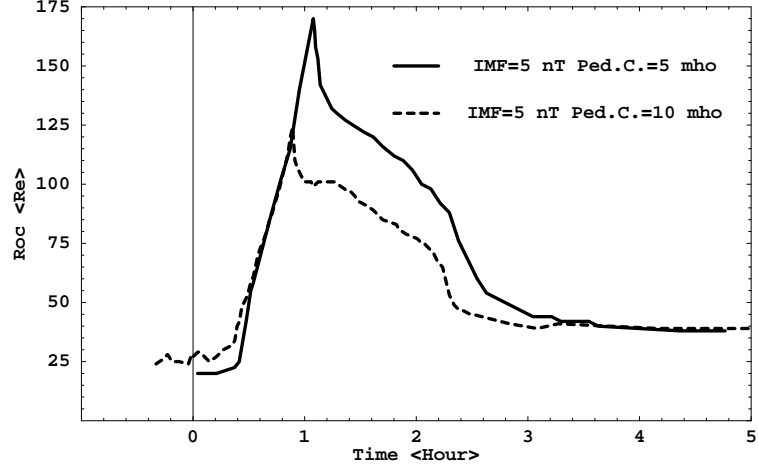
Figure 3.17: Time history of last closed field line for $B_{\mathrm{IMF}} = 5$ nT and $V_{SW} = 400$ km s^{-1} at $y = 0$ and $z = 0$ for ionospheric Pedersen conductance of 5 mho (solid line) and 10 mho (dashed line).

in steady state. Simulations with the same solar wind conditions, but different ionospheric Pedersen conductances of 5 and 10 mho in the ionosphere were performed. The evolution history of the tail length R_{OC} is plotted in Figure 3.17. Here $t = 0$ corresponds to the transition from southward IMF to northward IMF at the front of the magnetopause. We observe that the time evolution history of the tail length is different for the two cases, But the final steady state tail length is the same. As suggested by *Song et. al.* [2000], the ionospheric conductance controls the convection cell in the magnetosphere. During the evolution of the magnetosphere to steady state, the cross polar cap potential drops from 120 kV to about 15 kV and the ionospheric current is large. Higher ionospheric conductance allows for higher ionospheric convection velocity and the energy dissipation into the ionosphere is faster. Therefore, the relaxation of the tail

is quicker. However, the final steady state is the same because the ionospheric effects are negligible at this stage. Inside the magnetotail the convection velocity is much smaller than the velocity in the LLBL. Thus, in the steady state the ionosphere does not play a role in determining the magnetotail size. This conclusion is further affirmed by the fact that the simulations of *Ogino and Walker* [1984] and *Usadi et al.* [1993] indicated a short tail configuration ($\sim$ 40-60 R_E), although the inner boundary of these models is a simple resistive shell.

3.4   Comparison with Observations

Lack of direct satellite observations is the main reason that the controversy on long vs. short tail for steady state magnetosphere can not be resolved. It takes hours for the magnetosphere to reach steady state. It is rare that the solar conditions can maintain steady northward IMF for several hours and even rarer that there are satellites traveling inside the tail far away enough from the Earth to record the tail field during the quiet-time interval. Both of the factors make it difficult to resolve the problem. In this section, we present observational evidences of the tail relaxing from a long stretched configuration to a short-closed configuration during steady northward IMF and compare the observations with global MHD simulation results.

For the Earth's magnetotail to relax from a stretched long tail configuration and to reach a short-closed tail configuration, we expect the magnitude of tail

field B_x in the region of x<-20 R_E and around the equatorial plane decreases to reach very low values. Furthermore, the tail field B_z in the same region increases and becomes comparable to the steady solar wind magnetic field B_z component. The relaxation time is several hours. This is the type of evidence we seek for the relaxation of the tail to a short-closed tail configuration.
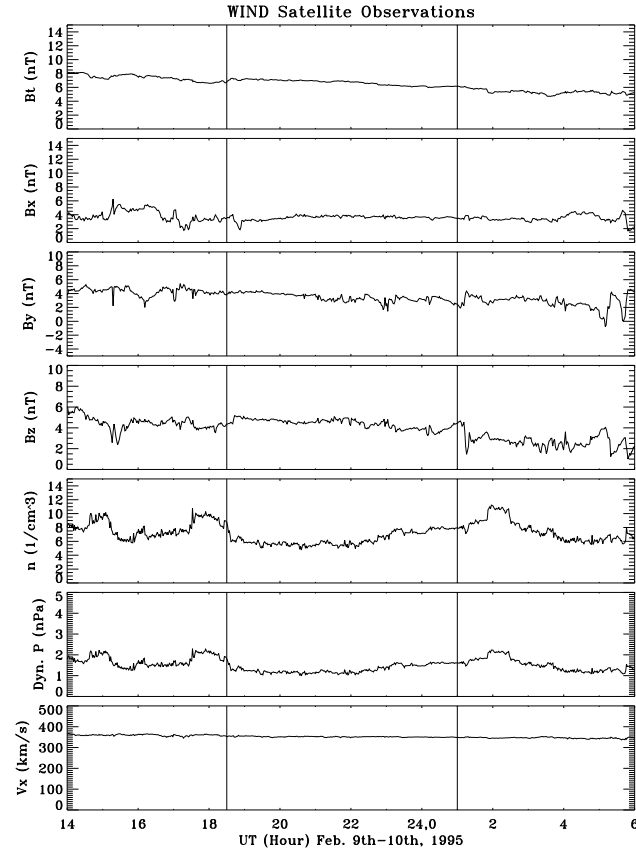
Figure 3.18: Solar wind condition as observed by the WIND satellite on Feb. 9-10, 1995.

On Feb. 9-10, 1995, the solar wind condition observed by the WIND satellite were quiet and maintained northward IMF for more than 10 hours. Figure 3.18

shows the solar wind condition on Feb. 9-10, 1995, observed by the WIND satellite. The data is obtained from CDAWeb. All the vector components are in geocentric solar-ecliptic (GSE) coordinates. The solar wind velocity V_x is around 350 km/sec and quite steady. The other two components of the solar wind velocity (V_y, V_z) are of much smaller magnitude and not plotted. The time interval of interest for WIND observations is between 18:30 UT on Feb. 9, 1995 and 1:00 UT on Feb. 10, 1995. The B_z component of the solar wind magnetic field is around 5 nT and quite steady in this interval. The B_x, B_y and ram pressure of the solar wind are also steady. Therefore, the solar wind maintained a steady northward IMF for at least 6 hours. The delay for the solar wind propagating from the WIND satellite to the Earth's magnetopause is about 50 minutes.

Geotail satellite is located down the Earth's magnetotail around x=-20R_E and near the equatorial plane. Figure 3.19 shows the trajectory of the geotail orbits in X-Y and X-Z plane in GSM coordinate. The time interval of interest is from 19:00 UT on Feb. 9, 1995 to 3:00 UT on Feb. 10, 1995. During this time interval, Geotail satellite is below and close to the equatorial plane. It traveled from (x=-24.55 R_E, y=-2.64 R_E, z=-3.02 R_E) to (x=-17.66 R_E, y=-7.19 R_E, z=-3.92 R_E) during the interval of 8 hours and the trajectory is inside the tail. The fact that it was inside the tail can be concluded on the basis of the simulation results where for the parameters of the solar wind cited above, the smallest size

91
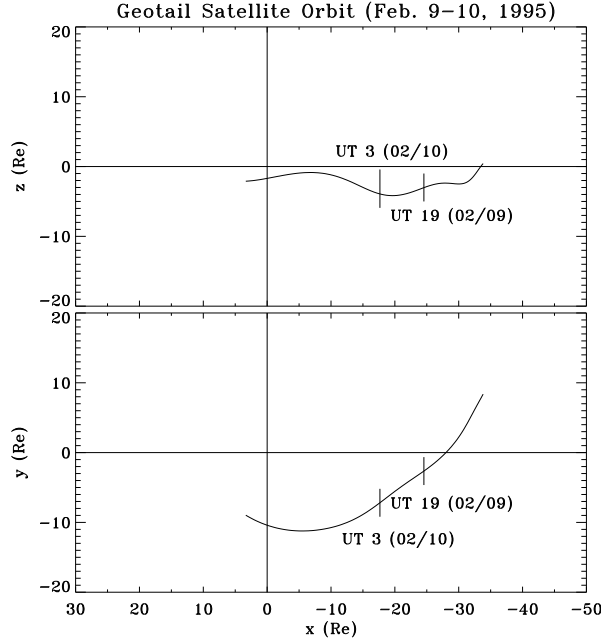
Figure 3.19: Geotail Satellite Orbit in GSM coordinate on Feb. 9-10, 1995.

of the tail length is about 45 to 50 R_E. Therefore, this is a good case to study the tail field evolution during steady northward IMF.

3.4.1 Observations

Figure 3.20 shows the tail magnetic field observed by the Geotail satellite (black curve) on Feb. 9-10, 1995. The magnetic field is in GSE coordinate. Between 14:00 UT and 19:00 UT on Feb. 9, the magnitude of tail field B_x is around 8 nT and B_z is around 1 nT. Starting from 19:00 UT, Feb. 9, the magnitude of B_x decreased and reached a steady value around 2nT after 23:00 UT on Feb. 9. Also starting from 19:00 UT, Feb. 9, B_z increased and reached a steady value
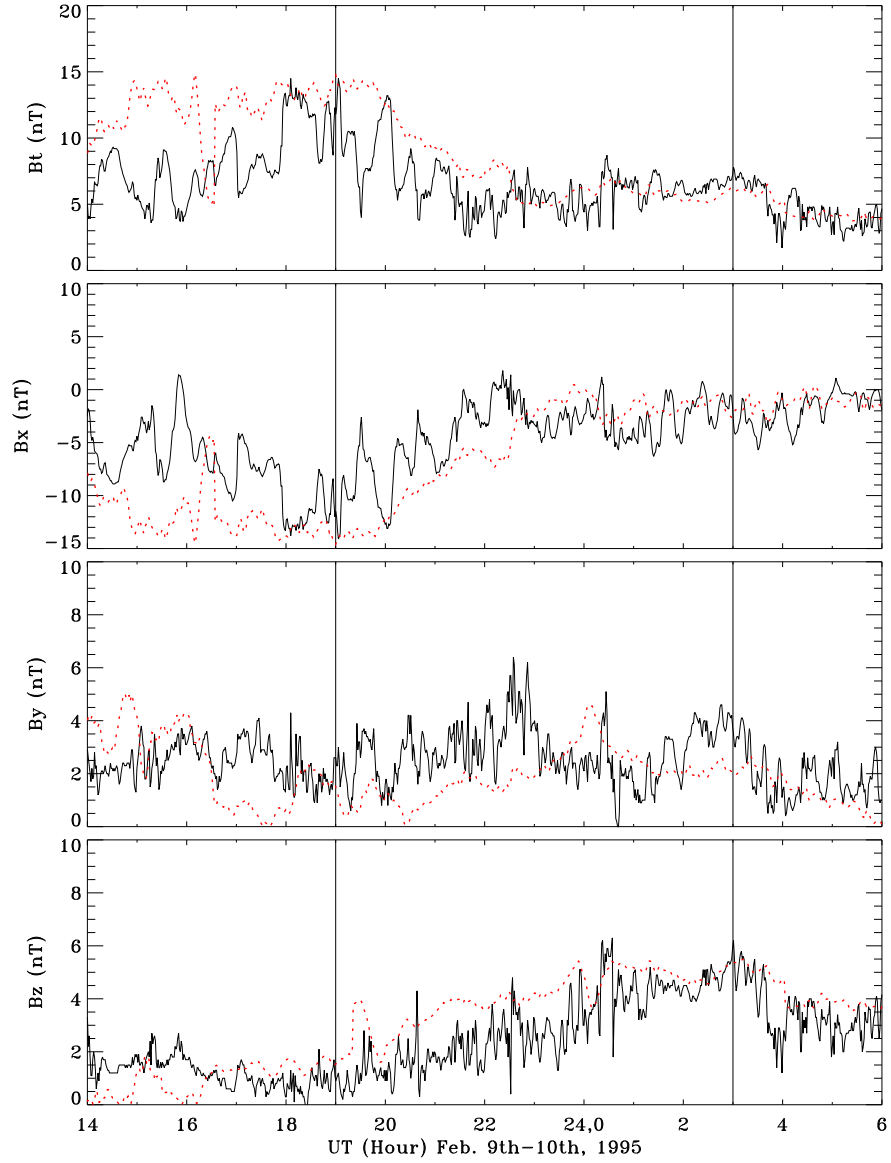
Figure 3.20: Comparison between Geotail observations and global MHD simulations on Feb. 9-10, 1995. The black curve is the magnetic field observed by the Geotail satellite and the red dotted curve is the modeled magnetic field from global MHD simulations. Both of the observed and modeled magnetic field are in GSE coordinate and of unit nT. Bt is the magnitude of the total magnetic field.

93

around 5 nT which is comparable to solar wind magnetic field B_z after 24:00, Feb. 9. Both B_x (nearly zero) and B_z (comparable to the magnitude of solar wind B_z) are quite steady in the interval between 00:30 UT, Feb. 10 and 3:00 UT, Feb. 10. During the whole time period, there is no obvious trend for the change in B_y.

The evolution of the magnetic field B_x from around 8 nT to 2 nT and B_z from nearly 0 nT to 5nT corresponds to the dipolarization of the magnetotail. This is the results of the transition from a long stretched tail configuration to a short-closed tail configuration. During the process of relaxation, our previous simulation shows the tail flux can be approximated as conserved. Therefore, the increase for the magnetic field B_z near the equatorial plane infers the decrease of the tail cross-equatorial-area which is the shortening of the magnetotail. As we have shown, the solar wind conditions are quite steady northward IMF with $B_z = 5$ nT for the time interval between 18:30 UT on Feb. 9 and 1:00 UT on Feb. 10. The dipolarization of the magnetotail or the evolution of the magnetosphere from a long tail to a short tail takes more than 4 hours, given that the solar wind is quite steady for more than 7 hours.

With only one satellite in the magnetotail, it is difficult to determine the tail length of the closed magnetotail. But we emphasize that during the steady state the magnetotail field B_z observed by the Geotail satellite is comparable to solar wind magnetic field B_z and lobe field B_x is nearly 0. This is what our

simulations of steady state magnetosphere with northward IMF in section 3.3 have predicted and the explanation is based on the fact that the continuity of magnetic pressure requires that the steady tail magnetic field be equal to solar wind magnetic field B_z. The detailed explanation can be found in section 3.3.

3.4.2 Comparison between observations and Simulations

In the previous section, during steady northward IMF, the observations show that magnetotail field shows the signature of the dipolarization of the magneto-tail. In this section, we present the results from global MHD simulation for the event occurred on Feb. 9-10, 1995. This helps us to have a better understanding of the evolution of the tail during the event.

The global MHD simulation is carried out with the model of the actual event simulation introduced in chapter 2. The WIND satellite observations are used as input and propagated to the front of our simulation grid. The time delay for the propagation is 50 minutes. The simulation was performed in the Solar Magnetic (SM) coordinate system allowing for the tilt of the Earth's magnetic dipole relative to the solar wind flow direction to be included. The full ionosphere model described in chapter 2 is used.

Figure 3.21 shows two panels of the three dimensional configuration of the Earth's magnetosphere from the simulation of the Feb. 9-10, 1995 event. In both of the panels, the background is a cut plane at z=-6 R_E and perpendicular to
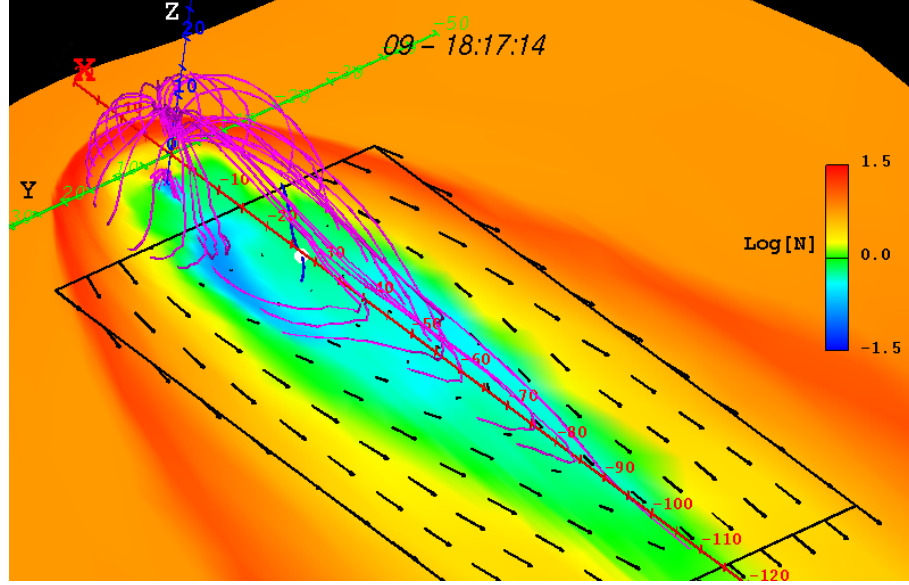
(a)
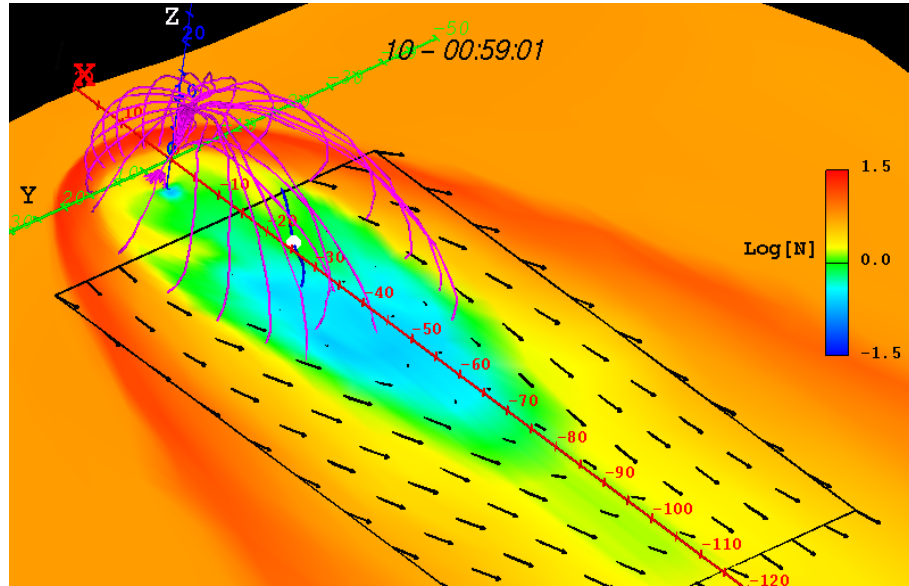
(b)

Figure 3.21: Three dimensional view of the Earth's magnetosphere from the global MHD simulation of the Feb. 9-10, 1995 event. In both of the panels, the view point is from some position above the North Pole. The coordinate system is in GSM. The black arrows are the velocity vectors in the cut plane. Pink lines are the field lines on the last closed field line surface. The blue curve inside the tail near x=-20 R_E is the trajectory of the Geotail satellite in GSM coordinate. The white ball on the blue curve represents the position of the Geotail Satellite. (a)Simulated magnetosphere configuration for 18:17 UT on Feb. 9, 1995. (b)Simulated magnetosphere configuration for 00:59 UT on Feb. 10, 1995.

the Z axis. The background color map is the log of density with color legend on the right. Pink lines are the field lines on the last closed field line surface. The blue curve inside the tail near x=-20 R_E is the trajectory of the Geotail satellite in GSM coordinate. The white ball on the blue curve represents the position of the Gaotail Satellite. During the time period of interest, the Geotail Satellite is below the equatorial plane. The last closed field lines are made sparse in the viewer's side to expose the trajectory of the Geotail satellite clearly. Panel (a) of Figure 3.21 shows the simulated magnetosphere configuration at 18:17 UT on Feb. 9. The magnetotail is of stretched long tail configuration and more than 100 R_E long. The low density region (green shaded) in the tail extends further than x=-120 R_E tailward. Panel (b) of Figure 3.21 shows the simulated magnetosphere configuration at 00:59 UT on Feb. 10. The tail extends to x$\simeq$-50 R_E and forms a short-closed tail configuration. The cross-tail area at x=-10 R_E in panel (b) is larger than the cross-tail area at x=-10 R_E in panel (a). The tail relaxes from a long stretched tail configuration to a short-closed tail configuration. Before 18:30 UT, on Feb. 9, the WIND satellite observations show strongly varying solar wind condition with high ram pressure and fluctuating solar wind magnetic field. Under these circumstances the tail is highly extended on the night side. With steady northward IMF observed by WIND between 18:30 UT, Feb. 9 and 1:00 UT, Feb. 10, the tail relaxes and expands in radius in the plane perpendicular to the equator. When the magnetic field in the cusp

region matches the magnitude of the IMF, the field lines reconnect on the night side and peel off thereby establishing a short tail. Finally, the magnetosphere reaches a state of minimum energy. We emphasize that the short tail shown in panel (b) of Figure 3.21 is in dynamical equilibrium. The reconnection, which occurs in the cusp region, adds flux to the dayside magnetosphere and the solar wind grabs the newly reconnected field line on the night side and transports them downstream. The newly added flux on the dayside is convected along the low-latitude boundary layer (LLBL) to the nightside to supplement the tail flux. Therefore, a steady short tail configuration is maintained.

Figure 3.20 shows the comparison between the observed magnetic field by the Geotail Satellite and the modeled magnetic field from our simulation. The black curve is the Geotail satellite observations. The red dotted curve is the modeled magnetic field from our simulation. Both of the observed and simulated magnetic field are in GSE coordinate. The modeled magnetic field is taken from the simulation through interpolation along the trajectory of the Geotail satellite. For B_x and B_z, The agreement between simulation and observation is good. The simulation reproduces the transition of B_x from $B_x \simeq -10$ nT to $B_x \simeq 0$ nT and the transition of B_z from $B_z \simeq 0$ nT to $B_z \simeq 5$ nT. Both the transition slope and the average magnitude of the magnetic field before and after the transition agree well with the observations. Especially for the steady stage between 00:30 UT and 03:00 UT, Feb. 10, the agreement is quite good. The observation shows

small oscillations of on the time scale of several minutes. The simulation however shows a smoothed average trend in the evolution of the magnetic field. We don't expect the MHD model to reproduce the features of minute-scale oscillations, since the spatial resolution in our numerical grid is 1 R_E in the region of interest. There are some mismatches in the magnitude of B_x between the simulation and the observation before 18:00 UT, Feb 9. The simulation shows a larger magnitude than the observations. We speculate that this is due to mismatches in current sheet thickness between the global MHD model and actual situation. Also, the agreement of B_y between the observation and the simulation is not as good as B_x and B_z. Since we are interested in the transition process from a long stretched tail to a short-closed tail during steady northward IMF, these mismatches don't affect our conclusions on the final steady state as well as on the timescale of evolution.

The good agreement between the Geotail satellite observations and our global MHD simulations leads us to conclude that the earth's magnetosphere during the time interval between 00:30 UT, Feb. 10 and 3:00 UT, Feb. 10, is in its steady state with a short tail of 50 R_E long. During steady stage, the magnetic field B_x is nearly zero in the region x<-20 R_E and near the equatorial plane and B_z is comparable to the solar wind magnetic field B_z in the same region. Although a single satellite observation cannot establish the tail size, the good agreement of the simulation results with Geotail's magnetic field data suggests

that the short tail steady-state magnetosphere for long northward turnings (in excess of four hours) observed in the simulations is a possible realistic size.

3.5   The Role of Preconditioning

At this point it is important to note that there is a discrepancy between our results and those of earlier work by *Fedder and Lyon* [1995], where it was claimed that the magnetosphere with identical solar wind plasma parameters extended to 155 R_E. The explanation for the discrepancy with earlier work is the following. In the work of *Fedder and Lyon* [1995], the start-up did not have the initial 50 min of unmagnetized solar wind flow, while the rest of the start-up is the same as that in section 3.2.1. We refer here to our start-up as scenario A and to their start-up as scenario B. Figure 3.22 shows the time histories of the solar wind B_z for scenario A and B. As a consequence, the magnetosphere was preconditioned in a different way for scenario B compared to the run discussed above for scenario A. Figure 3.23 shows the time evolution of the position of the open-closed boundary R_{OC} as a function of time, for scenario A and scenario B. The dashed curve corresponds to scenario A, while the solid curve corresponds to that obtained by Fedder and Lyon (scenario B). Notice that for scenario B, the relaxation time is much longer than that for scenario A. What is clearly seen is that after the initial southward phase during which the open-closed field line boundary R_{OC} is near Earth at around 20 R_E, the boundary expands at the speed of the solar wind to a
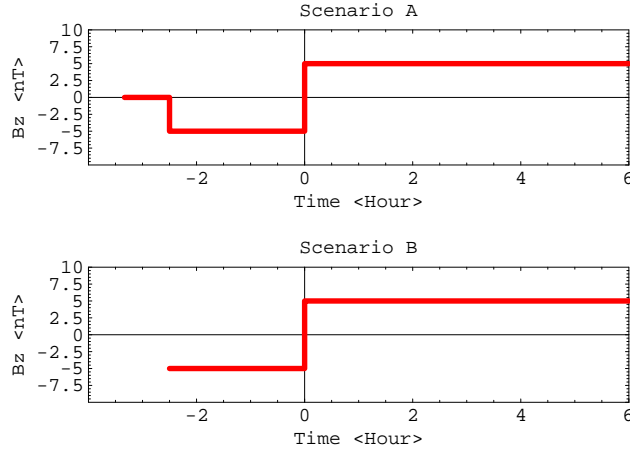
Figure 3.22: Time history of the solar wind B_z for scenario A (top panel) and scenario B (bottom panel).
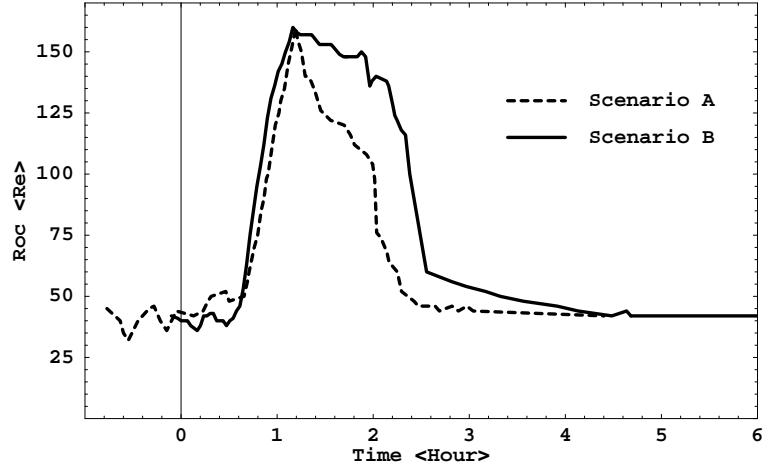
Figure 3.23: Time history of the boundary of the last closed field line for the present study (scenario A) (dashed line) and Fedder-Lyon (scenario B) (solid line).

very long tail. The dynamics following this expansion phase differs markedly for the two different preconditionings of the magnetosphere. A careful examination of the plasma conditions just prior to the northward turning indicates that the plasma pressure in the tail current region is larger for the Fedder-Lyon case

(scenario B) compared to our case (scenario A). This slows down the early phase of the relaxation. As a consequence, a "quasi-steady" state with an extended tail exists for ∼ 30 minutes. The run reported in *Fedder and Lyon* [1995] paper was terminated after 20 min into the "quasi-steady" state. However, using their data, we ran it out for a longer period of time and found that it finally relaxes to a much shorter magnetosphere, similar to the steady state shown in Figure 3.2 a and b. Different preconditionings affect the evolution to reach the steady state, but not the final steady state. The final steady state size of the magnetosphere on the nightside is also in very good agreement with the tail length results for the steady state quiet time magnetosphere obtained by others [*Gombosi et al.*, 1998; *Song et al.*, 1999; *Bargatze et al.*, 1999] for similar solar wind parameters. We believe that such studies are required to address and resolve long-standing issues in the interpretation of global MHD simulations.

3.6   Conclusions

We have investigated the quiet time magnetosphere for northward IMF, assuming that the solar wind density and velocity are constant over a long time period to achieve a steady state. The global MHD simulation shows that the steady state magnetosphere with northward IMF has a short tail ($\sim 40\ R_E$) for the standard case, which is consistent with the results of [*Gombosi et al.*, 1998; *Song et al.*, 1999; *Bargatze et al.*, 1999]. Cusp region reconnection and ionospheric

four-cell convection pattern are clearly seen in our simulations. We observe the concave shape of the steady state magnetosphere in our simulation, which has been predicted by the phenomenological analysis of *Song et al.* [2000]. Our results differ from the long-tail result obtained by simulations of *Berchem et al.* [1995] and *Raeder et al.* [1995].

We find that the size of the magnetosphere is controlled by the value of B_{IMF} and V_{SW}. These two solar wind parameters control the size of the quiet time magnetosphere. The scaling dependences are summarized as following:

1. The cross-equatorial area $A_{CE} \propto 1/B_{\mathrm{IMF}}$. The cross-tail area A_{CT} measured near the cusp region at $x \approx$ -10 R_E is also found to decrease with the increase in B_{IMF}. In that region, since the field in the tail is dominantly the dipole field, our simple model indicates that $A_{CT} \propto 1/B_{\mathrm{IMF}}^{1/3}$.

2. In general, with higher solar wind velocity the radius of the tail cross section is smaller, and the tail length is longer. The cross tail area A_{CT} measured at $x \approx$ -10 R_E is proportional to $V_{SW}^{-0.4}$.

3. The area A_n on the nightside for the newly reconnected flux through the equatorial plane (along the coast of the concave bay) increases with the increase of V_{SW} and decreases with the increase of B_{IMF}. Our model based on the balance between the adding of flux at the dayside and the peeling off of flux on the night side shows that $A_n \propto \frac{\sqrt{\rho}V_{SW}}{B_{IMF}}$, which is consistent with the simulated dependence.

Using simple flux conservation and momentum balance conditions, the nu-

merically observed scaling laws for the size of the closed magnetosphere on the nightside have been qualitatively explained. We also demonstrate that the ionospheric conductance is a minor effect in determining the steady magnetotail size. Only, the transient behavior is influenced by the conductance. Furthermore, we study the structure of the magnetosphere and its dependence to different solar wind conditions. The structures of 1D cuts of various tail plasma and field quantities along X axis and direction of Z axis at x=-10 R_E, y= 0 R_E are analyzed. The steady 3D current sheet profiles as modeled from global MHD simulations are also presented.

We examined one quiet-time northward IMF event, during which the Geotail satellite is inside the tail. The actual event, occurred on Feb. 9, 1995, is simulated and analyzed. The good agreement between our global MHD simulation results and the Geotail satellite observations leads us to conclude that, during steady northward IMF, the Earth's magnetotail relaxes from a long stretched tail configuration to a short closed tail configuration. During steady stage, in the region around x<-20 R_E near the equatorial plane, the magnetic field B_x is nearly zero and B_z is comparable to the solar wind magnetic field B_z. This is consistent with our predictions based on the model we develop with the ideal case. The time for the transition takes several hours.

Thus the global MHD code provides a very reliable comparison of the northward IMF steady state since the final dynamic equilibrium state depends on

104

general global force balance. We have here resolved the difference between the earlier long-tail results of *Fedder and Lyon* [1995] and the short tail observed by various groups [*Gombosi et al.*, 1998; *Song et al.*, 1999; *Bargatze et al.*, 1999].

Part III

Magnetospheric Substorms

Chapter 4

Global MHD Simulation of an Ideal

Magnetospheric Substorm

4.1 Introduction

In the past, global MHD models were used to simulate several actual magneto-spheric substorm events [*Fedder et al.*, 1995; *Wiltberger*, 1998; *Goodrich et al.*, 1998; *Lyon et al.*, 1998; *Lopez et al.*, 1998; *Wiltberger et al.*, 2000; *Papadopoulos et al.*, 1999; *Slinker et al.*, 2001; *Raeder et al.*, 2001] and were quite successful in reproducing the observed substorm activities in both the magnetosphere and the ionosphere. In this chapter, an ideal magnetospheric substorm is simulated with the LFM global MHD model and is analyzed comprehensively. The substorm is initiated by a sudden northward-southward IMF turning. This chapter serves as a pictorial review of the typical behavior of the Earth's magnetosphere and

ionosphere during substorms as seen by the global MHD model.

Several models have been developed [*Kivelson and Russell*, 1995] in order to explain different magnetospheric and ionospheric phenomena during magnetospheric substroms. The most successful ones are Near-Earth Neutral-Line (NENL) model and Current-Disruption (CD) model. A central feature of the near-earth neutral line (NENL) model [*Baker et al.*, 1996] is the formation of an X-line in the magnetic field structure in the mid-tail region of the magnetosphere. The imbalance between the rates of reconnection at the dayside magnetopause and the distant neutral line leads to accumulation of magnetic flux in the tail and its stretching. The formation of the X-line in the mid-tail ($\sim$ 20-50 R_E) impulsively resolves the imbalance. The consequences of the near-Earth neutral line formation are the generation of a plasmoid and its ejection, the sudden shrinking of the earthward part of the tail, the generation of earthward plasma flows and the formation of substorm current wedge, leading to auroral activity. The Current-Disruption (CD) model [*Lui*, 1996] is based on the observation that the substorm often starts with a burst of plasma turbulence and partial disruption of the cross-tail current in the near-Earth ($\sim$ 6-10 R_E) region. The Current-Disruption model has the onset of a non-MHD instability in a thin current sheet in the near-Earth magnetotail. In this model, the global tail reconfiguration, including the formation of the X-line, arises as a marcroscopic consequence of this relatively small-scale process. Both the Near-Earth Neutral-Line model and the

Current-Disruption model strive to explain the close coupling between the near-Earth magnetotail and the mid-tail region. To distinguish and integrate these models is the goal of ongoing studies, including the global MHD simulations.

With the extensive analysis of several actual substorm event simulations, *Wiltberger* [1998], *Wiltberger* [2000] and *Slinker et al.* [2001] conclude that although the MHD code cannot model the detailed local plasma kinetic processes central to both the current-disruption and NENL models, the simulations capture the essential features of the substorm, both those used to support the NENL model and those associated with the Current-Disruption model. The flow channel observed in *Wiltberger* [1998] and *Wiltberger et al.* [2000] indicates a close coupling between the mid-tail region and the near-Earth magnetotail. The simulation results of the ideal substorm presented next support these conclusions. We refer to *Wiltberger* [1998], *Wiltberger et al.* [2000] and *Slinker et al.* [2001] for the analysis of previous studies.

In the following sections, we present the initial solar wind conditions used in our simulation, the arrival of the northward-southward IMF turning at the magnetopause and the subsequent magnetospheric and ionospheric responses for the first twenty minutes. Then, both the magnetospheric and ionospheric responses during the substorm as simulated with the global MHD model are analyzed in detail, and the conclusions are presented.

4.2   Solar Wind Conditions and Simulation Model
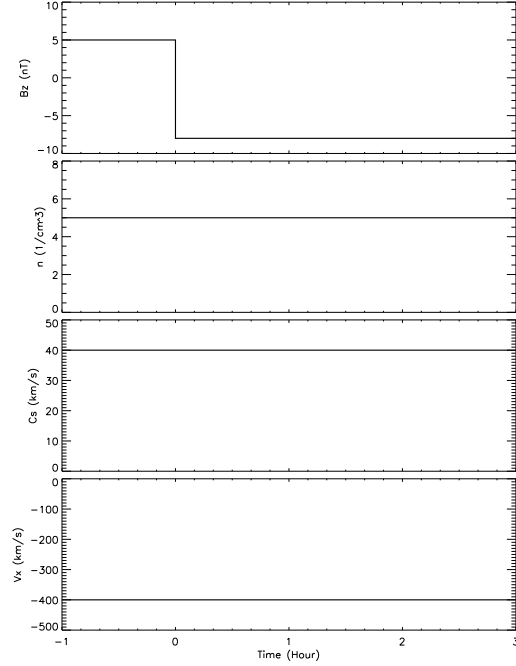
Figure 4.1:   Solar wind condition used in the ideal magnetospheric substorm simulation.

Figure 4.1 shows the solar wind condition for the ideal case simulation. At t = 0 min, the solar wind magnetic field B_Z changed from northward (=5 nT) to southward (=-8 nT). The solar wind condition is recorded at X = 20 R_E sunward along the sun-Earth line. Before t = 0 min, a long period of northward IMF (= 5 nT) was applied to the Earth's magnetosphere and the magnetosphere reached the idealized steady state that we studied in Chapter 3. The solar wind parameters were: density= 5 /cc; velocity V_x = 400 km/s; sound speed C_s = 40 km/s. The y, z components of the solar wind velocity field and the x, y

components of the solar wind magnetic field were zero. The full ionospheric model as described in Chapter 2 was used in the simulation, but the dipole tilt was not included, which is not important for our ideal event.

4.3 Arrival of the Northward-Southward IMF Turning at the Magnetopause

Figure 4.2 illustrates the propagation of the Northward-Southward (NS) transition through the magnetosheath. Contour lines of B_z as a function of position along the SM X axis and time in minutes are shown in Figure 4.2. The positive contours are shown by solid lines and the negative contours by dotted lines. The contour interval is 4 nT starting at 2 nT and -2 nT for positive and negative contours respectively. The dash line marks the contour of $B_z = 0$ nT and represents the propagation of the NS transition along the X axis and in time. At t = 0, the NS transition arrives at X = 20 R_E. In the upper left side, the transition propagates at the solar wind speed. At t = 2 min, it hits the subsolar bow shock at X = 13.5 R_E and slows in the magnetosheath as is indicated by the weak slope of the contours. After an additional 8 min, at t = 10 min, the NS transition reaches the magnetopause at X = 10.5 R_E. The delay time is consistent with the observations of *Ruobonuemi and Greenwald* [1998]. As the transition approaches the magnetopause, the flow nearly stagnates.
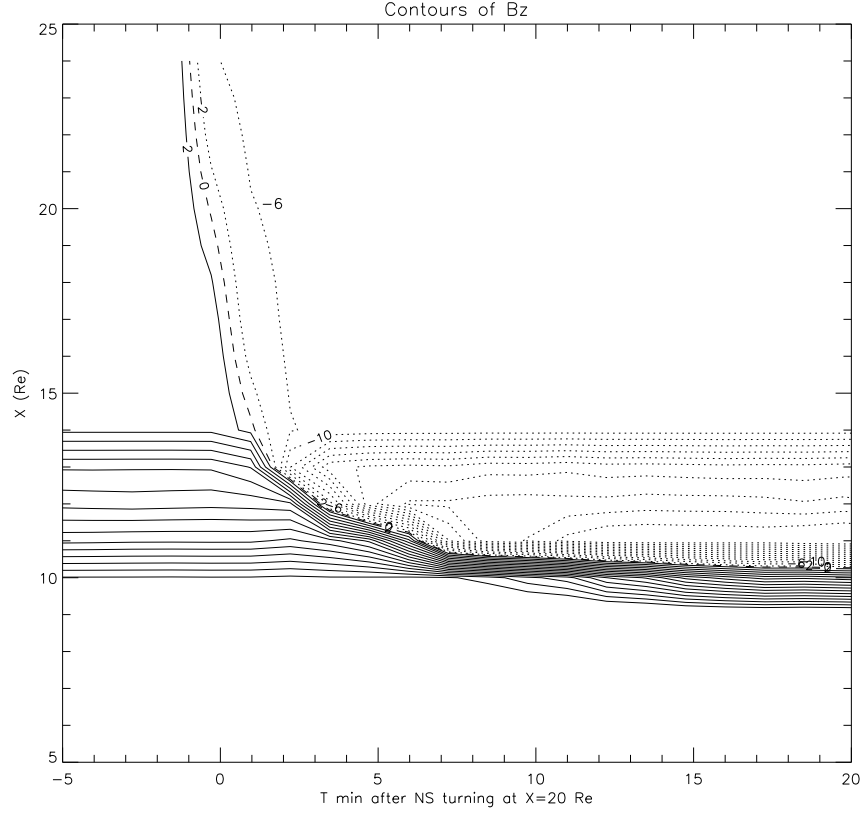
Figure 4.2: Contour lines of B_z as a function of position along the SM X axis and time in minutes. The positive contours are shown by solid lines and the negative contours by dotted lines. The contour interval is 4 nT starting at 2 nT and -2 nT for positive and negative contours repectively. The dash line marks the contour of $B_z = 0$ nT.

Figure 4.3 shows the plasma speed V_x in km/s versus time in minutes for several locations along the SM X axis near the magnetopause. The magnetopause is eroded due to the fast reconnection. The plasma flows toward the reconnection site from both sides. For a fixed point earthward of the eroding magnetopause, the flow is initially positive toward the reconnection site and then becomes negative after the merging region passes. From Figure 4.3, we see that the magnetopause passes X = 10.15 R_E at t = 22.5 min, X = 9.55 R_E at t =

112
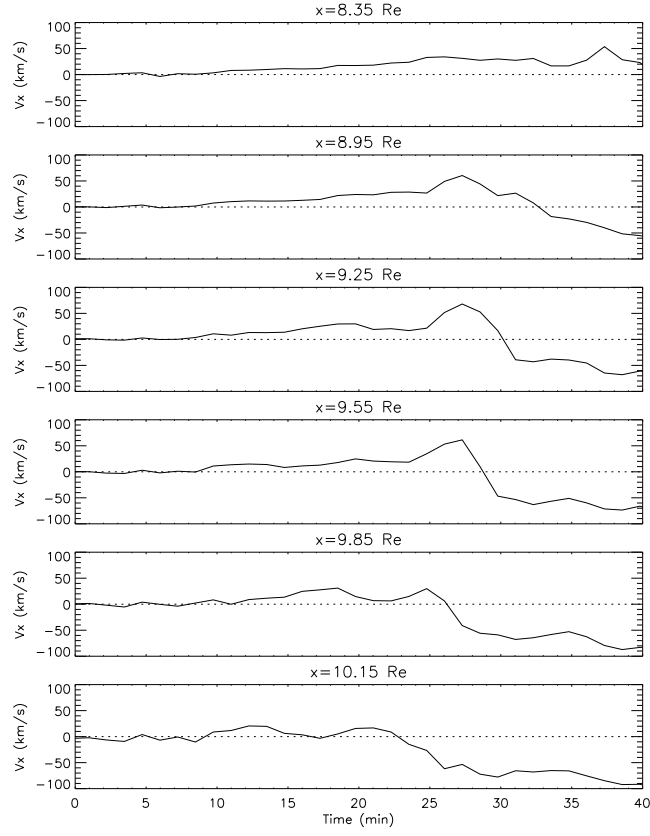
Figure 4.3: The plasma speed V_x in km/s vs. time in minutes for several locations along the SM X axis near the magnetopause.

28.3 min, and X = 8.95 R_E at t = 33 min.

The response in the ionosphere due to the NS transition is observed after t = 10 min. Figure 4.4 shows the simulated ionospheric electric potential contours at 4 instants after the arrival of the NS IMF transition at the magnetopause. The contour interval is 1 kV. The color legend on the left side of each panel represents the positive and negative contour values. At t = 00:08:28, the ionospheric electric potential contours show a four-cell pattern, which is typical of the magnetosphere
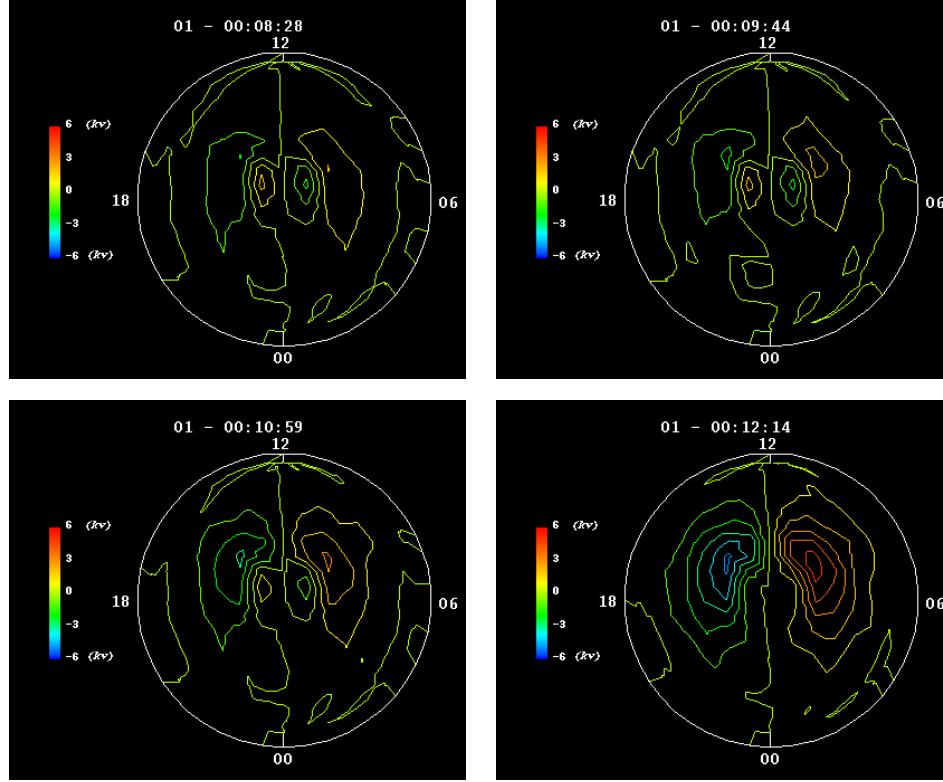
Figure 4.4: The simulated ionospheric electric potential contours at 4 instants after the arrival of the NS IMF transition at the magnetopause. The potential contours are drawn for the northern hemisphere and the view point is above the north pole. Noon and midnight side are labeled with 12 and 00 respectively in each panel, dawn is to the right, and dusk is to left. The contour interval is 1 kV. The time is labeled at the top part of each panel. The frames picked are t = 00:08:28, t = 00:09:44, t = 00:10:59, t = 00:12:14.

with steady northward IMF as studied in Chapter 3. At t = 00:09:44 and t = 00:10:59, the two potential cells close to dayside grow in size and magnitude. Meanwhile, the high-latitude reverse cells driven by post cusp reconnection decay and disappear at t = 00:12:14. The perturbation caused by the NS transition is transmitted from the nose of the magnetosphere as an Alfven wave. At t = 00:12:14, the two reverse cells driven by the dayside reconnection are dominant.

The cross polar cap potential (=12 kV) is small at t = 00:12:14.

Figure 4.5 shows the development of the typical two-cell ionospheric potential pattern and magnetospheric convection at four later instants. In column (a) of Figure 4.5, the ionospheric electric potential contours at four instants are shown. The contour interval is 8 kV. The arrangements in each panel of column (a) are the same as those in Figure 4.4. In column (b), the color maps of the velocity V_x in the YZ plane at X = -5 R_E in the magnetosphere at four instants are shown. The color legend at the bottom right corner of each panel represents the velocity range (from -60 km/s to 60 km/s). Positive velocity is represented using reddish color and points towards the sun. In column (c), similar color maps in the YZ plane at X = -8 R_E as those in column (b) are shown. In twelve minutes (from t = 00:14:44 to t = 00:26:01), the ionospheric cross polar cap potential grows from 24 kV to 90 kV and the two-cell ionospheric potential pattern is fully developed. We can also see the development of magnetospheric sunward convection from the color maps of V_x in column (b) and (c). Large sunward V_x appears several R_E inside the magnetopause after t = 00:18:30 and grows both in space and magnitude. At t = 00:22:16 and t = 00:26:01, large sunward V_x spreads in, above and below the equatorial plane. The shade of sunward V_x is broader in y direction for cut plane at X = -8 R_E than for that at X = -5 R_E. The sunward flow inside the magnetopause appears as a fast magnetosonic refraction wave propagating perpendicular to the closed field lines. It is channeled around

115
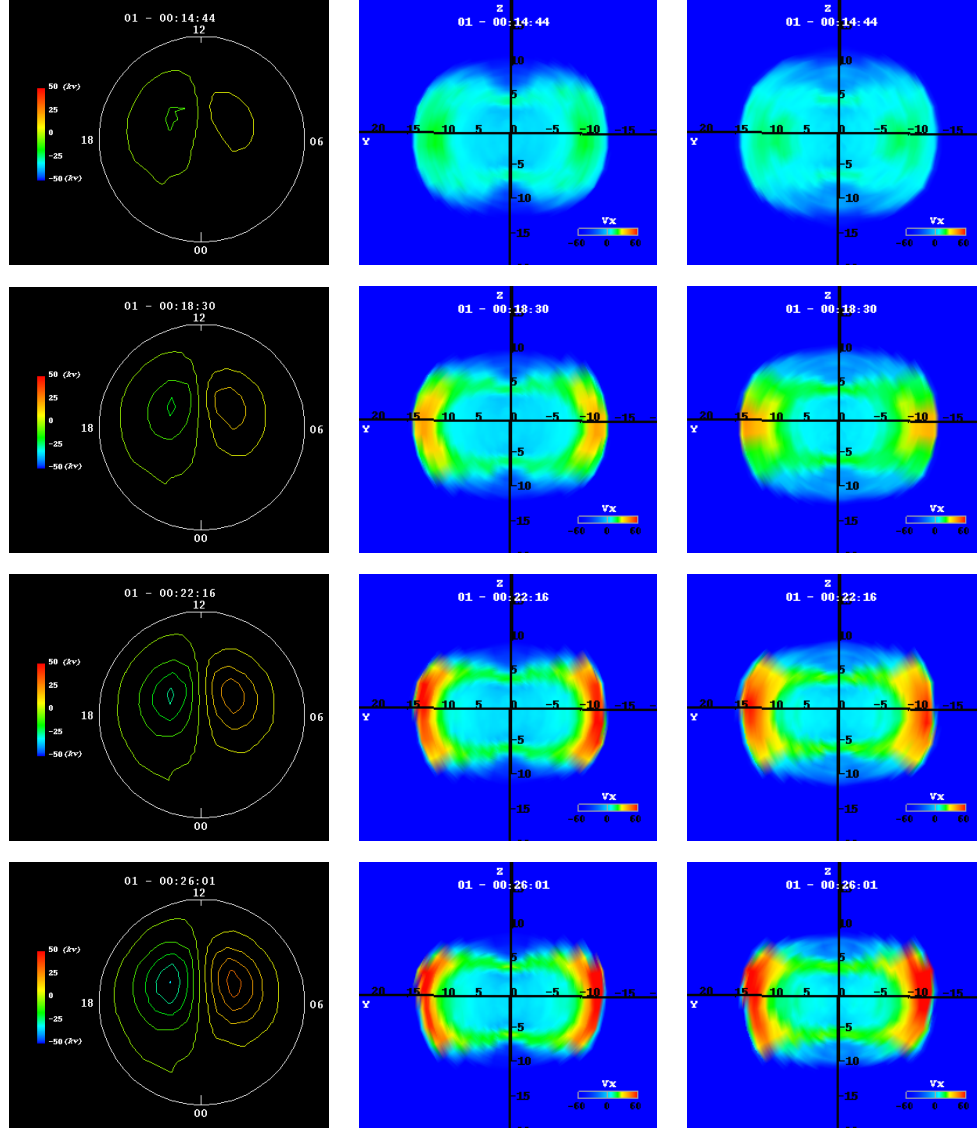
(a) Potential Contours   (b) Vx at x= -5 R_E (c)Vx at x= -8 R_E

Figure 4.5: Column (a): The development of the ionospheric two-cell potential pattern at four instants. The contour interval is 8 kV. The arrangement in each panel of column (a) are the same as those in Figure 4.4. Column (b): Color maps of the velocity V_x in the YZ plane at X = -5 R_E in the magnetosphere at four instants. The color legend at the bottom right corner of each panel represents the velocity range (from -60 km/s to 60 km/s). Positive velocity points towards the sun. Column (c): Color maps of the velocity V_x in the YZ plane at X = -8 R_E in the magnetosphere. The arrangements in each panel of column (c) are the same as those in column (b). From top to bottom, the frames are at t= 00:14:44, t = 00:18:30, t = 00:22:16 and t = 00:26:01.

the Earth and convected towards subsolar region to supply magnetic flux to the reconnection happening there. The sunward convection inside the magnetopause maps to the outer part of the two cell convection pattern in the ionosphere, which also convects sunward.

4.4   Magnetospheric Substorm

4.4.1   Mid-Tail Reconnection

Figure 4.6 shows the evolution of the Earth's magnetosphere in the North-South (XZ) plane. In each panel of Figure 4.6, the view point is from the west side of the Earth. The lines are magnetic field lines in the north-south plane. The X axis points toward the Sun and the Z axis points toward the north. The background is the log of density. At t = -00:07:48, the magnetosphere with steady northward IMF is of the typical short-tail configuration, which we have studied in Chapter 3. At t = 00:47:20, the magnetotail reaches a long and stretched configuration. During southward IMF, the newly reconnected magnetic flux at the dayside magnetopause connects to the IMF and is tranported over the polar cusps by the solar wind, where it is added to the outer portion of the tail lobes. The tail lobe is compressed until a corresponding increase in tail-lobe magnetic pressure balances the external pressure. At t = 00:51:05, we can see that the mid-tail reconnection starts to occur at X = -55 R_E. In the simulation, the growing lobes
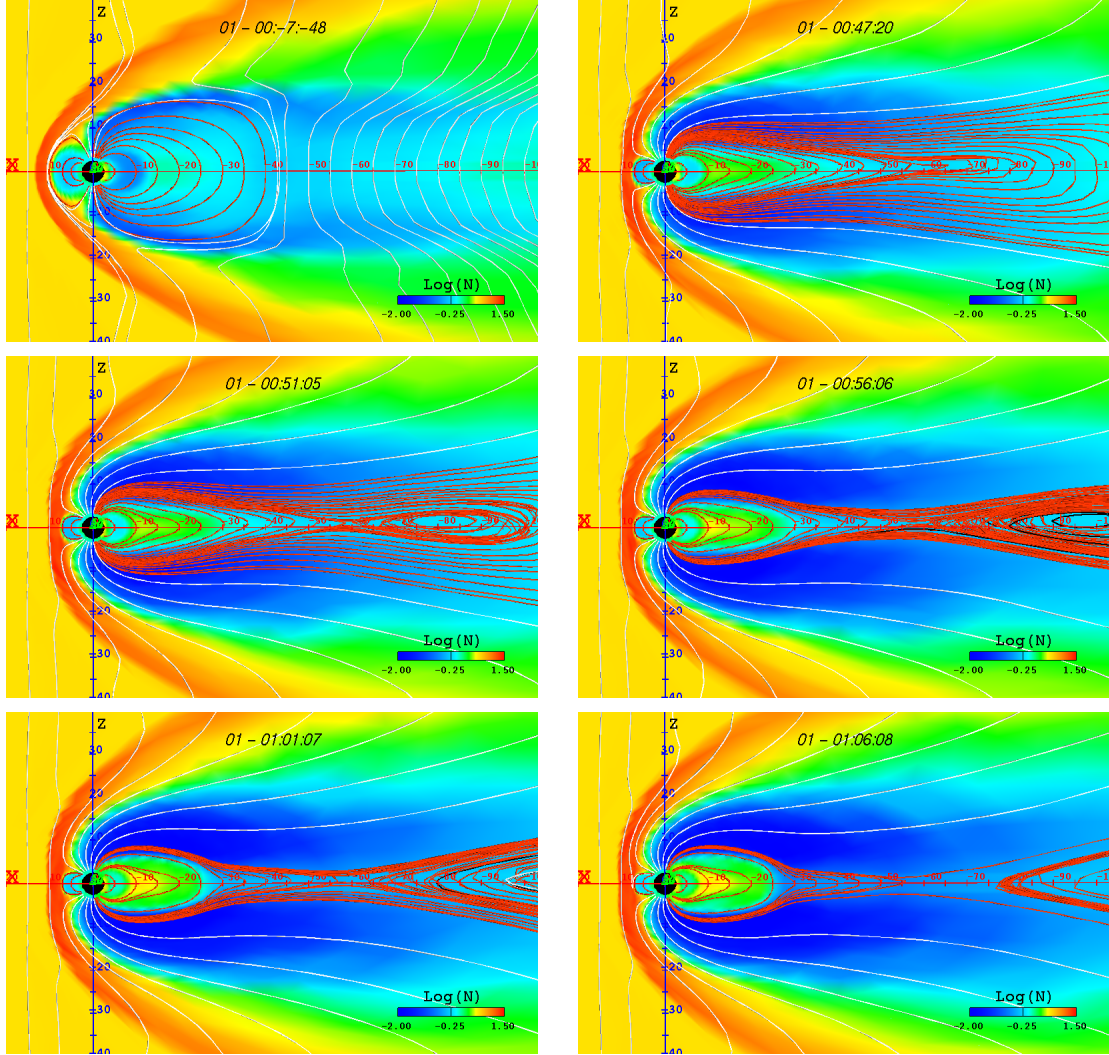
Figure 4.6: The evolution of the Earth's magnetosphere in the North-South (XZ, Y = 0) plane. In each panel, the view point is from the west side of the Earth. The lines are magnetic field lines in the north-south plane. The white lines are field lines outside the magnetopause and the red lines are field lines inside the magnetopause. The X axis points toward the Sun and the Z axis points toward the north. The background is the log of density. The frames picked are at t = -00:07:48, t = 00:47:20, t = 00:51:05, t = 00:56:06, t = 01:01:07 and t= 01:06:08.

of the magnetosphere squeeze and heat the plasma sheet and cause the current sheet to thin. In regions where the plasma density is the smallest the pressure can't be held off, and the equilibrium fails in a sudden increase in reconnection. We believe that the timing and site of the magnetotail reconnection depends on where the magnetic field gradient is sharp enough to break the MHD assumption and not on the nature of the small resistvity responsible for the breakdown. Panels at t = 00:56:06, t = 01:01:07, and t = 01:06:08 show the formation and ejection of the plasmoid (bubble of closed field lines) created by the neutral line.

4.4.2 Magnetospheric Responses

Electric Field and Field Aligned Current Diagnostic

Figures 4.7 and 4.8 show the frames of the evolution of the magnitude of the electric field (|E|) (left column) and field aligned current (FAC) (right column) in the equatorial (XY) plane with the velocity vectors overlaid. In the left column, color maps of the magnitude of the electric field (|E|) are shown. The color legend at the bottom right corner of each panel represents the |E| range (from 0 to 5.0 mV/m). In the right column, color maps of the field aligned current are shown. The color legend in each panel represents the FAC range (from -0.5 nA/m^2 to 0.5 nA/m^2).

At t = 00:00:57, before the NS IMF transition hits the magnetopause, the magnetosphere is quiet and the tail lobe electric field is small. Field aligned
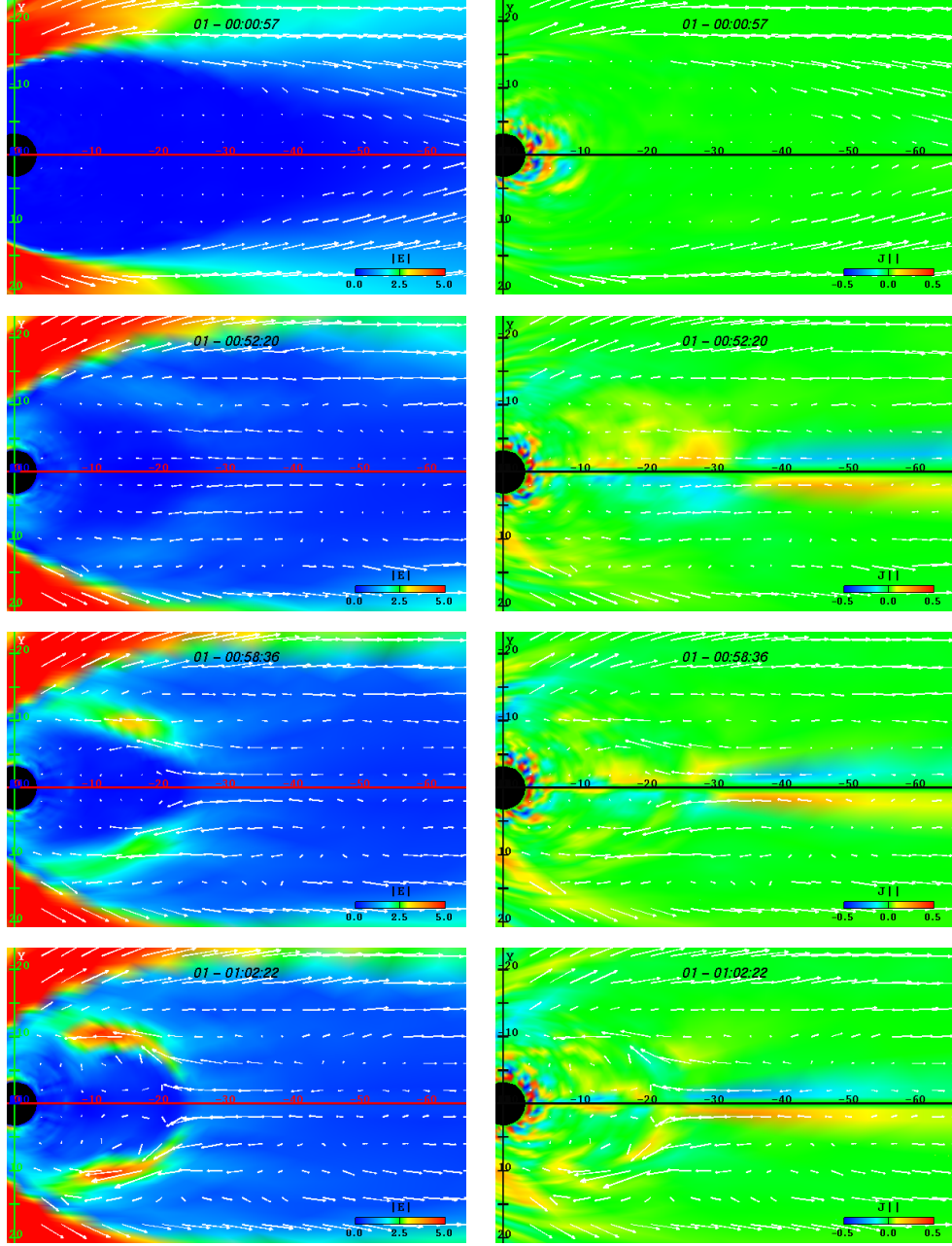
(a) Electric Field (|E|)   (b) Field Aligned Current

Figure 4.7: Frames of the evolution of the electric field magnitude (left column) and field aligned current (right column) in the equatorial (XY) plane. The white arrows are velocity vectors. Left column: Color maps of the magnitude of electric field (|E|). The color legend at the bottom right corner of each panel represents the |E| range (from 0 to 5.0 mV/m). Right column: Color maps of the field aligned current. The color legend at the bottom right corner of each panel represents the FAC range (from -0.5 to 0.5 nA/m^2). From top to bottom, the frames are at t = 00:00:57, t = 00:52:20, t = 00:58:36 and t = 01:02:22, respectively.
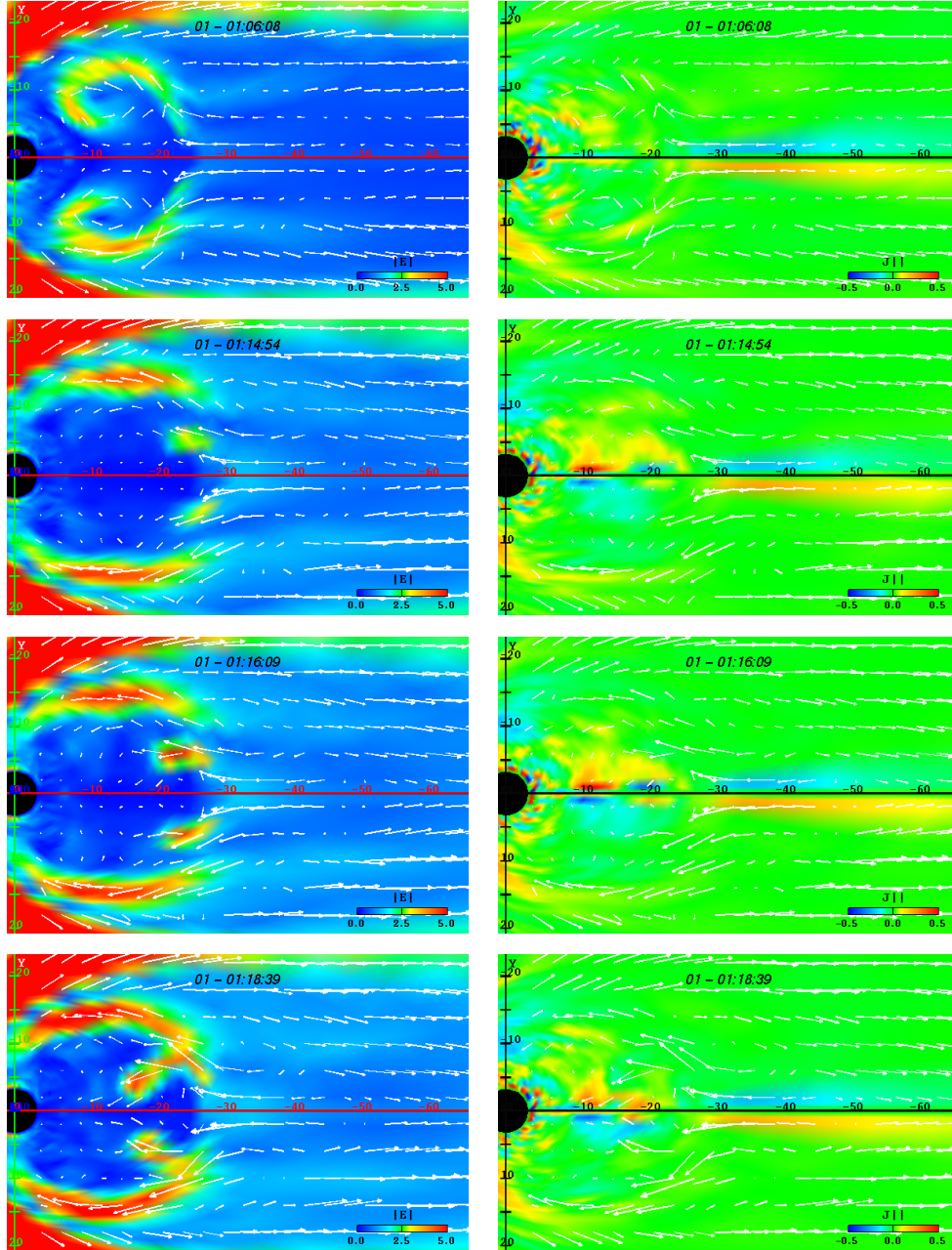
(a) Electric Field (|E|)   (b) Field Aligned Current

Figure 4.8:   Figure 4.7 Continued. From top to bottom are frames at t = 01:06:08, t = 01:14:54, t = 01:16:09 and t = 01:18:39, respectively.

current inside the tail lobe is mainly distributed in the near Earth region (X> -10 R_E). At t = 00:52:20, the tail lobe electric field is still small. The field aligned current in the region X< -35 R_E down the tail does not affect the ionosphere and its formation is due to the variation of B_x in the Y direction. At t = 00:58:36 and t = 01:02:22, the electric field in the near-Earth region starts to increase and appears as two bright arcs in regions around X = -15 R_E, Y = ±10 R_E. This increase is due to the mid-tail reconnection and its resulting shrinking of the earthward part of the tail. The earthward flow coming from the more distant magnetotail diverges around the inner current sheet. At t = 01:02:22, the earthward flow is enhanced. At t = 01:06:08, we can clearly see that two vortices are formed in regions around X = -15 R_E, Y = ±10 R_E. The symmetry of the two vortices is due to the idealized symmetry in our simulation. In an actual event simulation, *Wiltberger et al.* [2000] observed the formation of one vortex close to this location. In the t = 01:06:08 frame, there are flow channels penetrating into the inner magnetosphere and sets of counter-streaming flow near X = -20 R_E. The earthward flow from the mid-tail region encounters the tailward flows near X = -20 R_E, Y = ±7 R_E. At t = 01:14:54, the two vortices subsides. The frames of t = 01:14:54, t = 01:16:00 and t = 01:18:39 show the development of two large finger-like flow-channels penetrating into the inner magnetotail. At t = 01:18:39, the earthward flow penetrates into the region around X = -12 R_E. The frames of t = 01:14:54, t = 01:16:00 and t = 01:18:39 show that the

field aligned currents in the region between X = -10 R_E and X = -20 R_E are significantly enhanced. The field aligned currents appear in pairs of upward and downward current. This corresponds to the formation of the substorm current wedge. Here, we note that significant increase of precipitating electron energy flux in the ionosphere and sharp dip of pseudo-AL index are observed after t = 01:10:00.

Cross-Section of Velocity V_x Diagnostic

Figure 4.9 shows frames of the color map of the velocity V_x in the equatorial (XY) cutplane with overlaid velocity vectors. The color legend at the bottom right corner of each panel represents the V_x range (from -500 km/s to 500 km/s). Again, we can see the development and enhancement of the earthward flow originating from the mid-tail reconnection. The earthward flow diverges at X = -25 R_E. At t = 01:06:08, the two vortices can be seen clearly with their inner part being blue-shaded (V_x is tailward). The frames of t = 01:14:54 and t = 01:18:39 confirm that the penetration of the finger-like structure is due to the formation of strong earthward flow channels.

Figure 4.10 shows the color maps of the velocity V_x in the YZ cutplane at different locations in the magnetosphere at five instants. The color legend at the bottom right corner of each panel represents the velocity range (from -200 km/s to 200 km/s). Positive velocity points towards the sun. From the panels in the
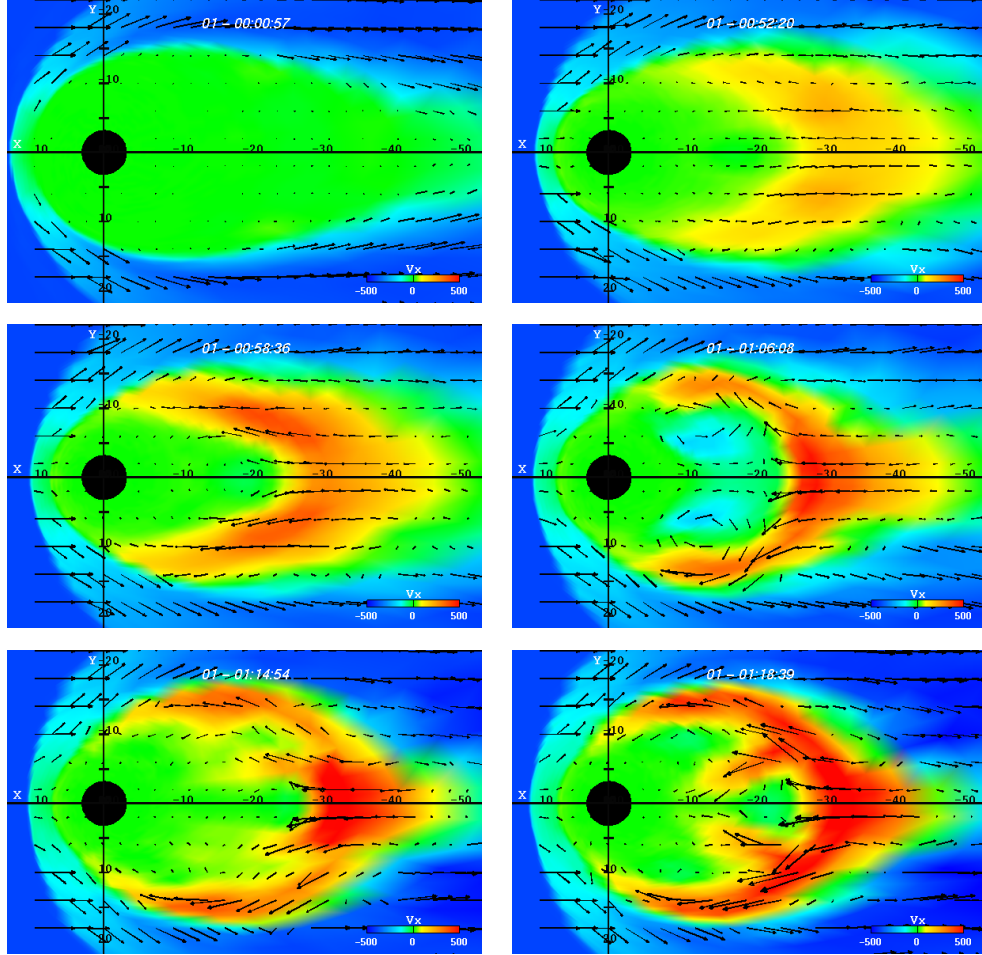
Figure 4.9: Frames of the color map of the velocity V_x in the equatorial (XY) cutplane with overlaid velocity vectors. The color legend at the bottom right corner of each panel represents the V_x range (from -500 km/s to 500 km/s). The frames picked are at t = 00:00:57, t = 00:52:20, t = 00:58:36, t = 01:06:08, t = 01:14:54 and t = 01:18:39.
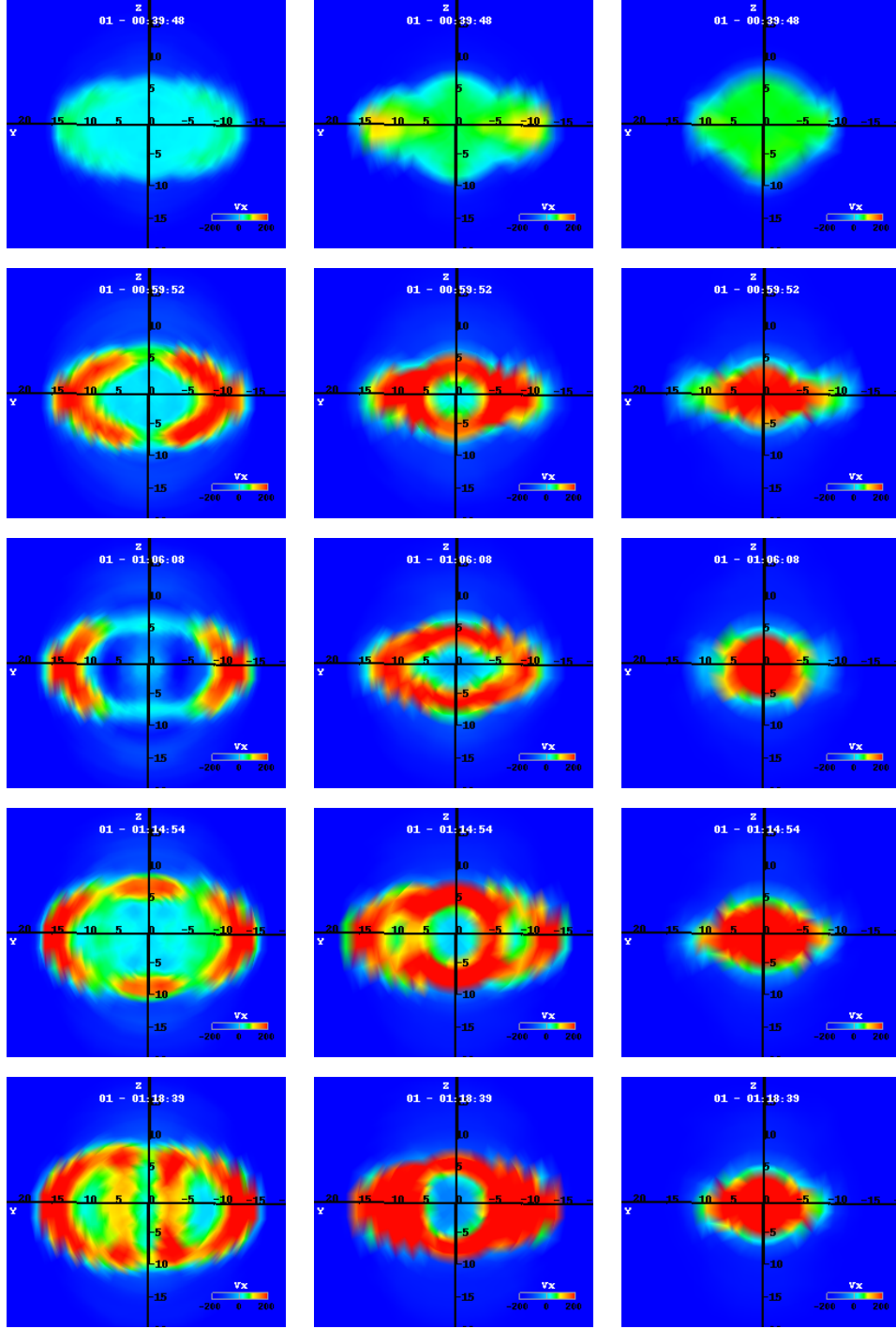
(a) Vx, X = -12 R_E (b) Vx, X = -24 R_E (c) Vx, X = -36 R_E

Figure 4.10:   Color maps of the velocity V_x in the YZ cutplane at different locations in the magnetosphere at five instants. Column (a): Cutplanes at X = -12 R_E; Column (b): Cutplanes at X = -24 R_E; Column (c): Cutplanes at X = -36 R_E. From top to bottom are frames at t = 00:39:48, t = 00:59:52, t = 01:06:08, t = 01:14:54 and t = 01:18:39, respectively.

right column (cutplanes at X = -36 R_E), we see that the earthward flow due to the mid-tail reconnection appears in the frame of t = 00:59:52 and is present in all frames thereafter. From the frames of t = 00:59:52 and t = 01:06:08 in the middle column (cutplanes at X = -24 R_E), we see that the region of strong earthward flow appears as thick red ring. The earthward flow encounters strong resistence from the closed field lines near the X axis and forms a stagnant region in the center by circling around that region. From the frames of t = 00:59:52 and t = 01:06:08 in the left column (cutplanes at X = -12 R_E), we see the formation of the two vortices we discussed previously. In the frame of t = 01:06:08 in the left column, the two blue-shaded regions in the center represent the tailward flows which form the vortices together with earthward flows in the outer red-shaded regions. The earthward flow bifurcates in the Y direction and there are no strong earthward flows near Z=± 5 R_E. The frames of t = 01:14:54 and t = 01:18:39 in the left and middle columns show the penetration of the two flow channels in the YZ cutplanes at X = -12 R_E and X = -24 R_E. We can see that the penetration of the flow channels appear first at t = 01:14:54 in the cutplane at X = -24 R_E and then at t = 01:18:39 in the cutplane at X = -12 R_E. The flow channels appear around Y = ± 5 R_E and spread in the Z direction.

Dipolarization

Figure 4.11 illustrates the evolution of the magnetic field lines traced from X = -6, -10, -14 R_E, Y= 0 R_E, Z= 2 R_E in the North-South meridian plane. The background is the log of the density (in /cc). At t = 01:14:54, the field line is
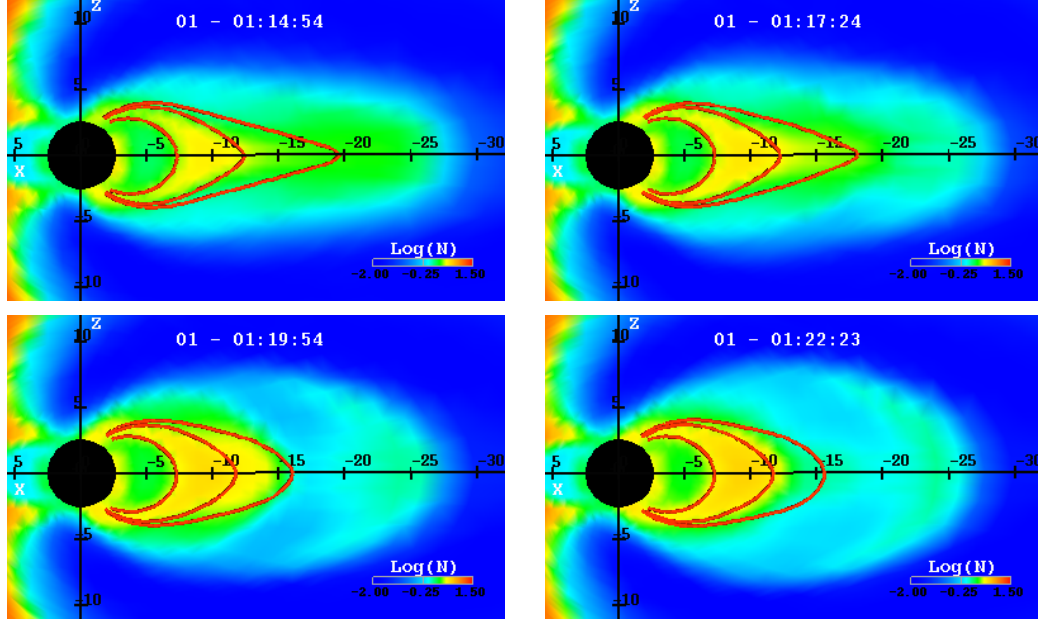
Figure 4.11: Evolution of the magnetic field lines traced from X = -6, -10, -14 R_E, Y= 0 R_E, Z= 2 R_E in the North-South meridian plane. The background is the log of the density (in /cc). The color scale is described by the color legend at the bottom right corner. The frames are picked at t = 01:14:54, t = 01:17:24, t = 01:19:54 and t = 01:22:23.

still stressed. After t= 01:17:24, the field lines relax and dipolarization occurs. The most significant change occurs with the field line traced from the point at X = -14 R_E, Y = 0 R_E and Z = 2 R_E. The signatures of the dipolarization of the magnetic field lines are also present in the measurements of the local magnetic field. Figure 4.12 shows the time history of the plasma and the field quantities
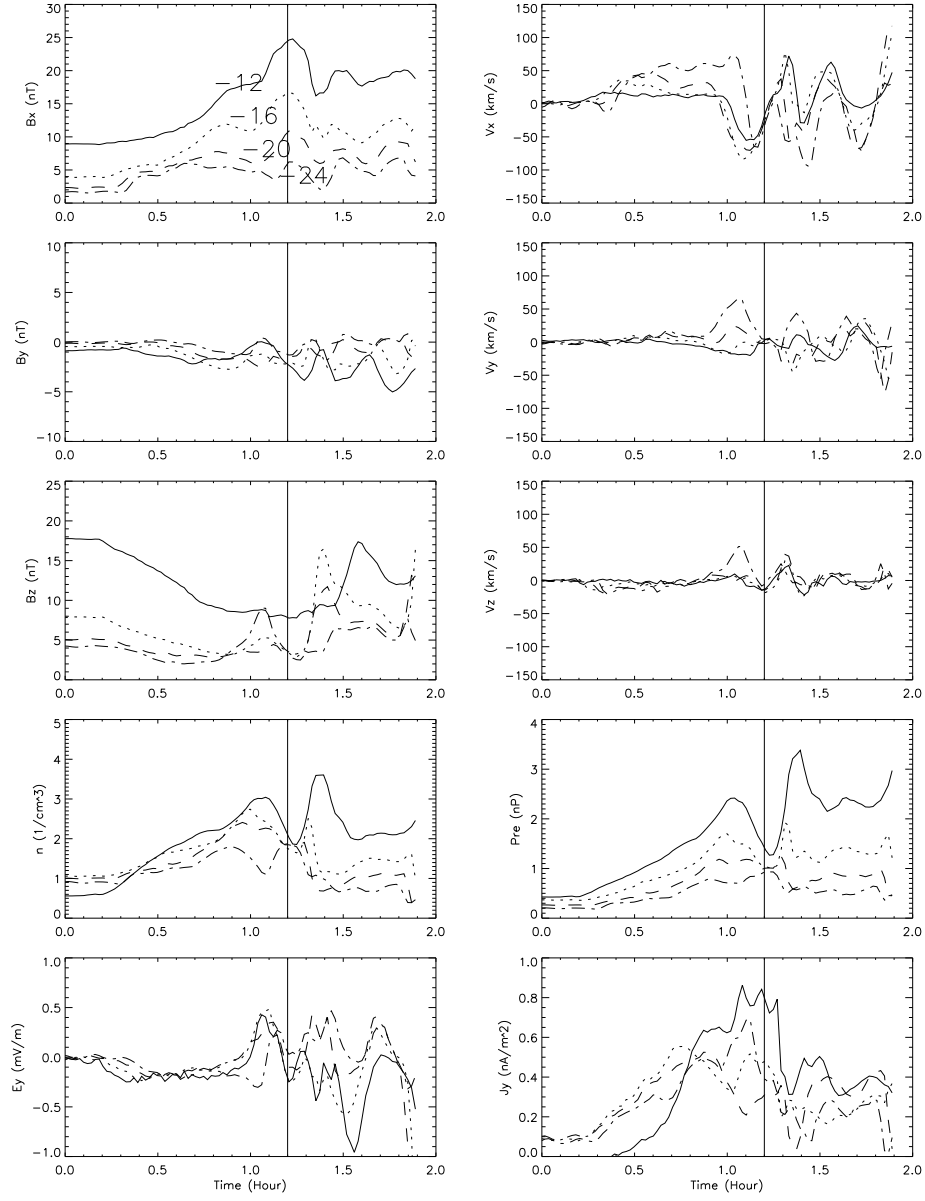
Figure 4.12: Time history of plasma and field quantities at fixed points in the magnetotail. The points are at (Y,Z) = (0 , 1) R_E and four X positions: X = -12 R_E (solid lines), X= -16 R_E (dotted lines), X= -20 R_E (dashed lines) and X= -24 R_E (dash-dotted lines). The vertical line is at t = 70 min.

at fixed points in the magnetotail. The points are at (Y, Z) = (0, 1) R_E and four X positions: X= (-12, -16, -20, -24) R_E. The vertical line is at t = 70 min. Dipolarization is seen in the B_x and B_z graphs of Figure 4.12, where B_x decreases and B_z increases at all the locations after t = 70 min. A surge of sunward flow is seen in the V_x plots.

Current Sheet Disruption
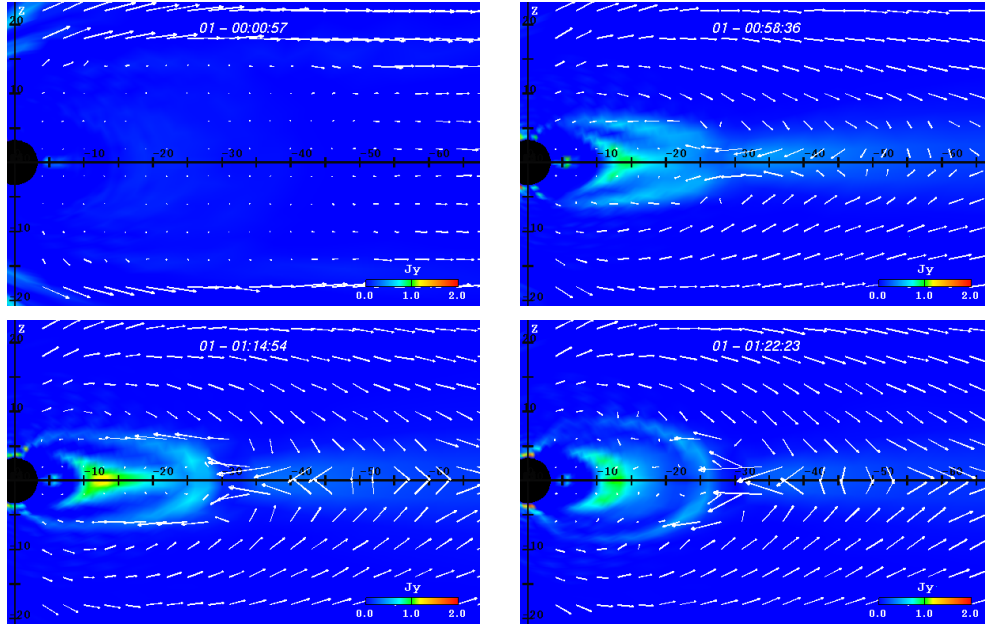
Figure 4.13: Frames showing the evolution of J_y in the North-South (XZ, Y = 0) plane with velocity vector overlaid. The color legend at the bottom right corner represents the range of J_y (from 0 to 2 nA/m^2). The time picked are t = 00:00:57, t = 00:58:36, t = 01:14:54 and t = 01:22:23.

Figure 4.13 shows the evolution of J_y in the North-South (XZ, Y = 0) plane with velocity vector overlaid. J_y is the current density flowing perpendicular to the North-South (XZ, Y = 0) plane. At t = 00:00:57, no current is of significant

129

magnitude. At t= 00:58:36, there are two clear structures within the current sheet. There is an inner current sheet that extends from X = -10 R_E to X = -20 R_E on the XZ cutplane. An outer current sheet extends from the distant tail to X= -30 R_E where it appears to bifurcate and run along the outer edge of the plasma sheet. At t = 01:14:54, the inner current sheet is intensified and extends from X = -10 R_E to X = -25 R_E (longer than that at t = 00:58:36). Both the inner and outer current sheet are thin in the Z direction. At t = 01:22:23, the inner current sheet is disrupted in the sense that the inner sheet is broad and the current density is small. The outer current sheet is also weak and broad in the Z direction. The current sheet disruption occurs around when the penetration of earthward flow channel occurs. The signature of current sheet disruption can also be seen from the local measurements of current density J_y. In Figure 4.12, the J_y graph shows the decreases of J_y at all locations around t = 70 min.

4.4.3 Ionospheric Responses

Auroral Brightening

Figure 4.14 shows the color maps of the simulation output for auroral precipitating electron energy flux in the nightside northern polar cap. The derivation of the electron energy flux from the global MHD model is introduced in chapter 6. Though this is not auroral light output, it is closely related to it [*Fedder et al.*, 1995a; *Slinker et al.*, 2001]. Here, the color range is fixed as from 0 to

130
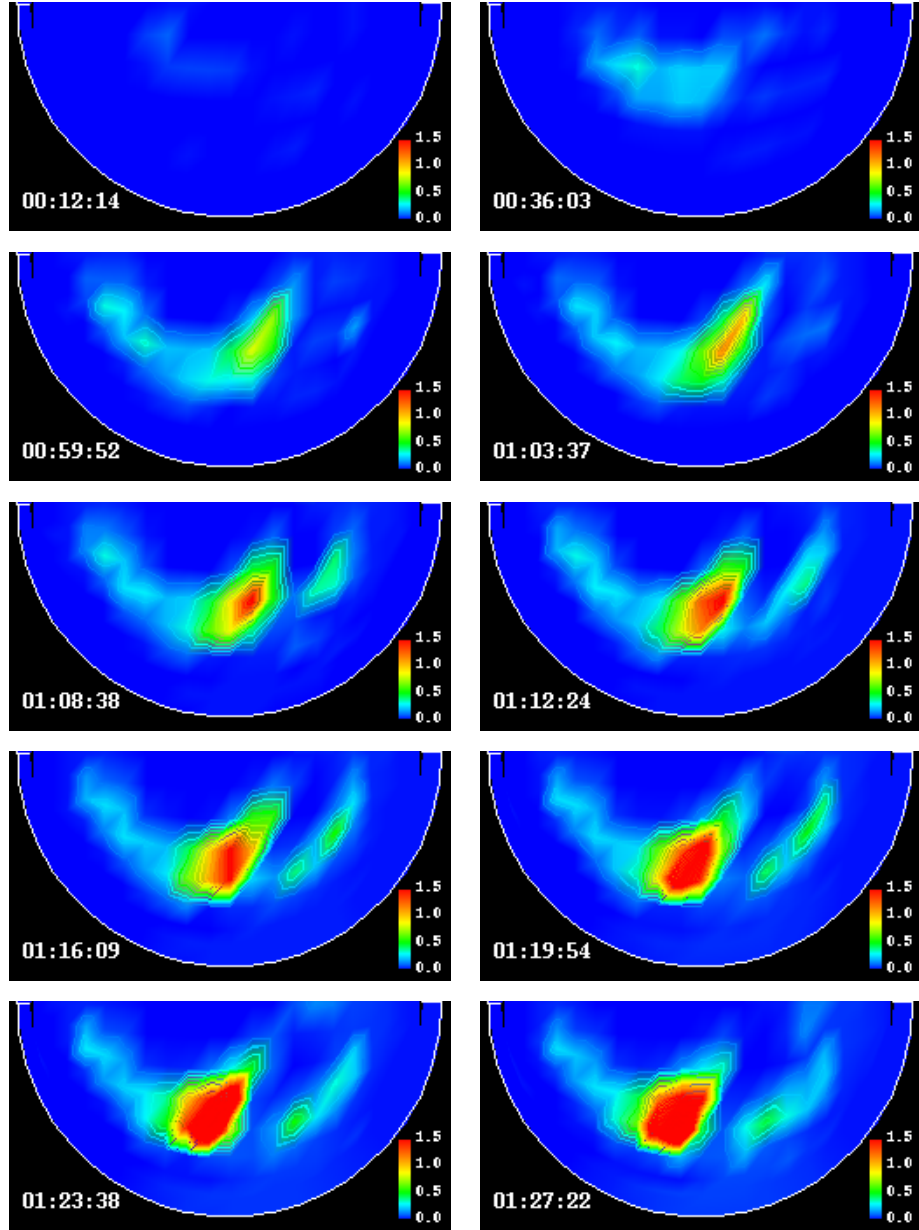
Figure 4.14: Frames showing the color map of the simulation precipitating electron energy flux into the nightside northern polar cap. The color range is from 0 to 1.5*10¹² eV/cm^2s. The image is centered on the magnetic pole and the region is from 60 degree geomagnetic latitude to the pole. Midnight is on the bottom and dawn is on the right. The time is labeled at the bottom left corner.

$1.5*10^{12}$ eV/cm^2s (= 2.4 ergs/cm^2s). The area with precipitating electron energy flux larger than 2.4 ergs/cm^2s is shown as red. Before t = 01:03:37, the activity remains at a low level and experiences slow intensification. Starting from t= 01:08:38, the activity increases rapidly and expands poleward and westward. This is the classical signal of an auroral onset of a substorm and the substorm enters the expansion phase. The aurora brightens in the 2200-2400 MLT (premidnight) sector.

Enhancement of the Field Aligned Currents

Figure 4.15 shows the color maps of the field aligned current streaming into and out of the nightside northern polar cap. Positive field aligned current flows out of the ionosphere and corresponds to the flow of electrons into the ionosphere. Starting from t= 01:08:38, the magnitude of the field aligned current increases rapidly. The region with the largest positive field aligned current is also the same region with the largest precipitating electron energy flux as shown in Figure 4.14.

Evolution of the Pseudo-AL Index and the Cross Polar Cap Potential

Figure 4.16 shows the evolution of the simulated pseudo-AL index. In our model, pseudo-AL index is produced from the minimum east-west (maximum westward in the azimuthal direction) ionospheric Hall current which has been searched throughout the grids on the northern hemisphere. It is known that the AL index
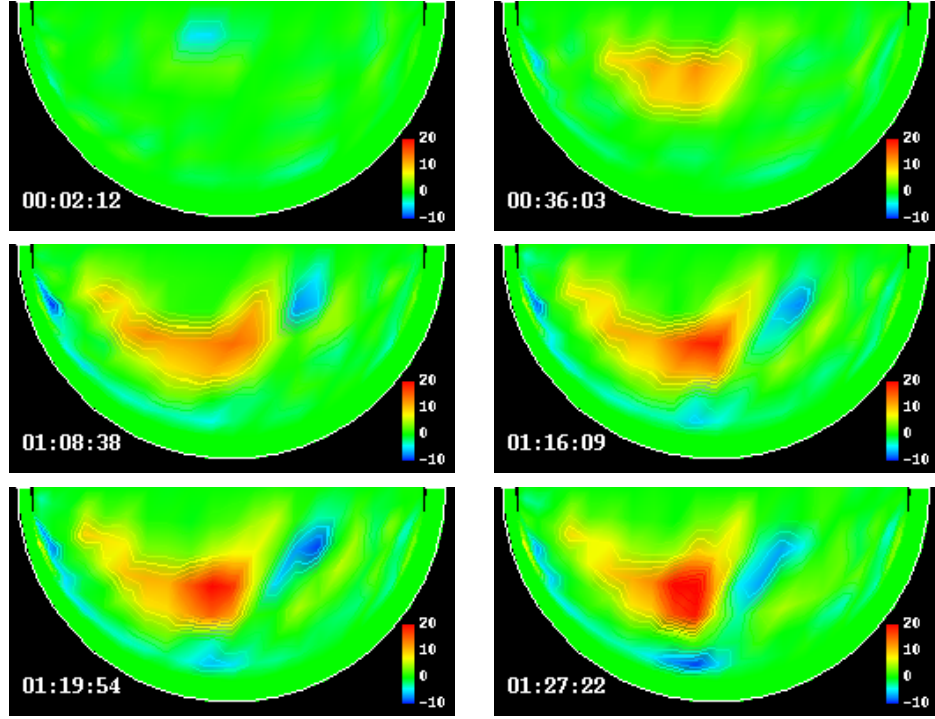
Figure 4.15: Color maps of the field aligned current streaming into and out of the nightside northern polar cap. The region is from 60 degree geomagnetic latitude to the pole. The color range is from -10 uA/m to 20 uA/m. Positive field aligned current flows out of the ionosphere. Midnight is on the bottom and dawn is on the right. The time is labeled at the bottom left corner.

perturbations are mainly produced by the east-west (azimuthal) ionospheric Hall current during magnetospheric substorms [*Kamide and Baumjohann*, 1993]. The pseudo-AL index produced from global MHD models is very close to the observed AL index during substorm event. This is confirmed by the studies of [*Wiltberger*, 1998; *Wiltberger et al.*, 2000; *Fedder et al.*, 1995a].

In Figure 4.16, the two vertical dotted lines are at t = 68 min and t = 95 min and divide the substorm into three phases: growth, expansion and recovery phase. We can see that during the growth phase, there is small decrease in the
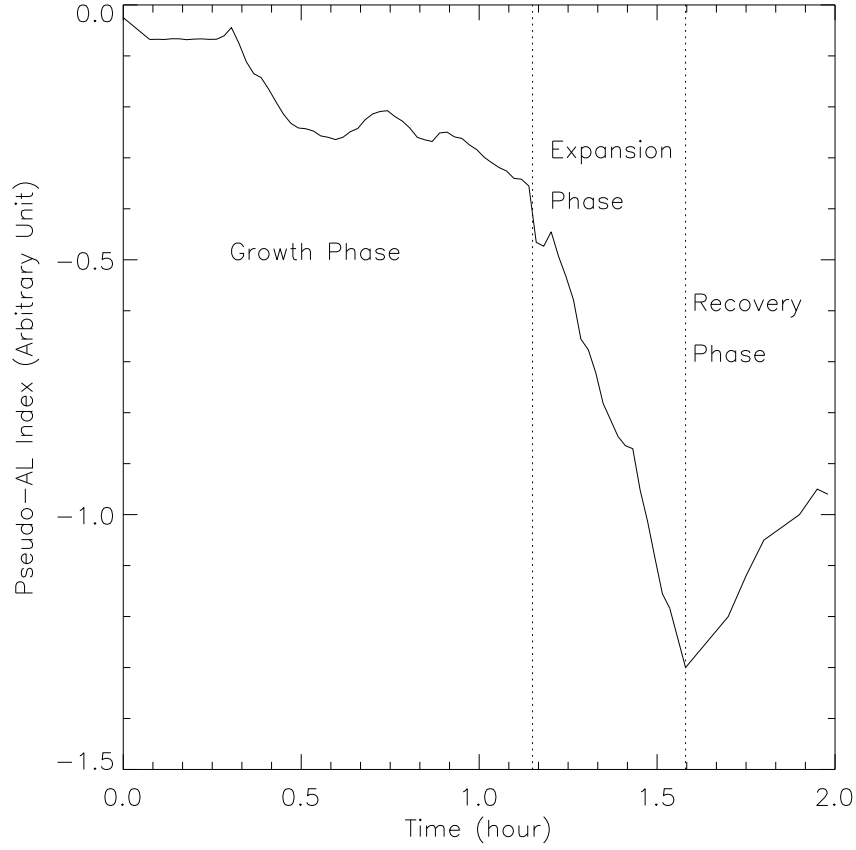
Figure 4.16: Evolution of pseudo-AL index. Pseudo-AL index is calculated from the minimum east-west ionospheric Hall current. The two vertical dotted lines are at t = 68 min and t = 95 min and divide the substorm into three phases: growth, expansion and recovery phase.

pseudo-AL index. At t = 68 min, a sharp decrease occurs with the pseudo-AL index and marks the start of the expansion phase. The auroral expansion occurs after t =68 min. The decrease of the pseudo-AL index stops at t = 95 min and the recovery phase starts. Due to the continuous constant southward IMF applied to the magnetosphere, the pseudo-AL index does not recover fully back to its initial value (nearly 0) and stays at relatively low value. We note that
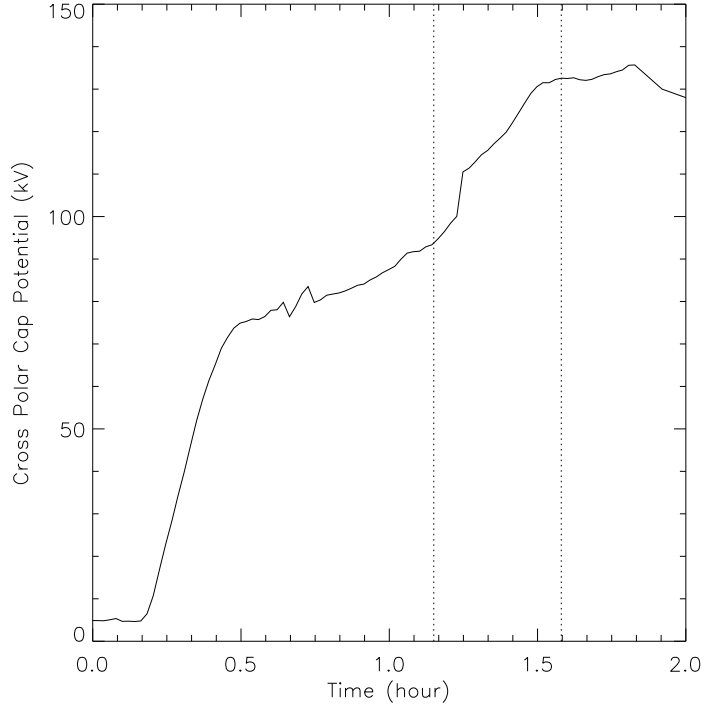
Figure 4.17: Evolution of the cross polar cap potential. Cross polar cap potential are the difference between the maximum and minimum polar cap potential in the northern hemisphere. The two vertical dotted lines are at t = 68 min and t = 95 min and divide the substorm into three phases: growth, expansion and recovery phase.

during actual substorm event, the solar wind conditions are more variable and often with northward IMF turning. Therefore, the AL index recovers back to 0 in most cases and the typical time scale for a substorm event is about 80 minutes.

Figure 4.17 shows the evolution of the cross polar cap potential. Cross polar cap potential are the difference between the maximum and minimum polar cap potential in the northern hemisphere. We can see that during the growth phase, the cross cap potential rises to 80 kV in twenty minutes. This has been discussed in section 4.3. During the expansion phase, the cross polar cap potential

experiences another rapid increase (up to 135 kV). The cross polar cap potential stays around 130 kV during the recovery phase. This is due to the continuous constant southward IMF applied to the magnetosphere.

4.5 Conclusions

In this chapter, an ideal magnetospheric substorm initiated by a sudden northward-southward IMF turning is simulated with the LFM global MHD model and is analyzed comprehensively. This chapter serves as a pictorial review of the typical behavior of the Earth's magnetosphere and ionosphere during substorms. We first studied the arrival of the northward-southward IMF transition at the magnetopause and showed the development of the ionospheric two-cell potential pattern. Then, the results show the key features of the solar wind-magnetosphere coupling, viz. auroral onset and expansion, AL index dipping, dipolarization, current sheet disruption, formation of the substorm current wedge and formation and ejection of plasmoid created by the neutral line. The flow channel penetrating into the inner magnetosphere connects the mid-tail and inner-tail region and supports the observations that auroral activities originate from the inner magnetotail. However, it is not easy to characterize the time sequence of all the events in the inner magnetotail, especially since their occurrence varies with position in the magnetotail. All of the substorm activities in the inner-tail are preceded by magnetic reconnection occurred in the mid-tail. To a large ex-

tent, the simulated substorm supports some tenets of the NENL model. The symmetry of the simulation result is due to the idealized symmetry in our simulation. Situations in actual substorm events are more complicated than what we have discussed in this chapter [*Wiltberger,* 1998; *Wiltberger et al.,* 2000; *Slinker et al.,* 2001]. We maintain that the simulation results are not sufficiently comprehensive or definitive to select between models or to verify the prediction of one over the others. Additional ideal and actual event simulations are needed to draw broader conclusions. This also motivates us to study the characteristic features of substorm dynamics using nonlinear dynamical techniques, which is presented in next chapter.

Chapter 5

Phase Transition-like Behavior of Magnetospheric Substorms: Global MHD Simulation Results

5.1 Introduction

The analysis in chapter 4 is based on the simulation of an idealized substorm. In this chapter, we will study the statistical features of substorm dynamics using nonlinear dynamical techniques.

The global behavior of the magnetosphere in response to the solar wind input is known to be coherent to a large extent [*Sharma*, 1995,*Klimas et al.*, 1996]. The largest substorm phenomena, e.g. global reconfiguration, are in reasonable agreement with low-dimensional magnetospheric models and in particular those of inverse bifurcations. Models of the magnetospheric behavior during sub-

storms, e.g. near-earth neutral line (NENL) model [*Baker et al.*, 1996], imply its global coherence.

At the same time there is growing evidence of hierarchical multi-scale aspect of magnetospheric activity represented first of all in the form of various power-law spectra [*Tsurutani et al.*, 1990; *Takalo et al.*, 1993; *Ohtani et al.*, 1995; 1998; *Lui*, 1998]. This evidence has led to models [*Consolini*, 1997; *Chapman et al.*, 1998; *Lui et al.*, 2000] based on the hypothesis that the magnetosphere is in a state of self-organized criticality (SOC) [*Bak*, 1987]. The original SOC model is based on the model of sandpiles, where the critical state is characterized by power-law fluctuations spectra. Briefly, a system is in a state of SOC when the statistics of the energy release events (avalanches) reveal no characteristic length or timescale and, as a result, the appropriate spectra obey power laws. *Sergeev et al.* [1996] give a detailed review on the multiscale aspects of the substorm activity.

Both the self-organization and SOC model have their limitations. The self-organization model can't explain the multi-scale behavior of the substorms. The typical SOC model is essentially independent of the driver and thus is autonomous, which is not the case with the Earth's magnetosphere. The SOC models are too simplified to capture the global coherent behavior of the magnetosphere. It has been found recently that the global coherent (self-organization) and multi-scale (self-organized criticality) aspects of the magnetospheric behav-

ior can be reconciled in terms of non-equilibrium phase transition [*Sitnov et al.*, 2000], consistent with earlier phenomenological models of substorm activity [*Sergeev et al.*, 1996] and magnetospheric convection [*Chen and Wolf*, 1993]. The global coherent dynamics of substorms can be described as the transition between two states (quiet ground state and active state), and this resembles closely a phase transition. The dynamical evolution of substorms in a phase space reconstructed from observational data can be compared with the characteristic temperature-pressure-density diagram of equilibrium water-steam system [*Sitnov et al.*, 2000]. On the other hand, the multi-scale behavior [*Sergeev et al.*, 1996] may be explained by deviations from this low-dimensional picture close to the critical point, characteristic of second-order phase transitions [*Stanley*, 1971]. Recently, *Sitnov et al.* [2001] have computed a critical exponent of the non-equilibrium transitions in the magnetosphere, which reflects the multi-scale aspect of the substorm activity, different from power-law frequency and the scale spectra of autonomous systems. This exponent relates input and output parameters of the magnetosphere and is consistent with a second-order phase transition.

The introduction of the concept of non-equilibrium phase transition opens a new area in the study of magnetospheric substorms. The phase transition diagram and multi-scale features were obtained by *Sitnov et al.* [2000] from analysis of hundreds of hours of observed input-output data of the coupled solar wind-magnetosphere system,compiled by *Bargatze et al.* [1985] (hereafter referred to

as BBMH). The database contains 34 intervals of correlated measurements of the auroral electrojet index AL and solar wind input, each 1-2 days in length. The phase transition-like behavior of the magnetospheric substorms was discovered by reconstructing the dynamical evolution of large number of events.

In the past, the global MHD studies have been focused on the simulation of individual substorm events and comparison with satellite and ground observational data. In this chapter, we investigate whether the simulated substorms produced by the global MHD model have the non-equilibrium phase transition-like features as revealed by *Sitnov et al.* [2000]. We simulated 6 intervals of total duration of 240 hours from the same BBMH data set with the LFM global MHD model. Using the same phase space reconstruction techniques as in *Sitnov et al.* [2000, 2001], we analyzed the input-output system as obtained from the global MHD model and compared the results to those in *Sitnov et al.* [2000, 2001]. One advantage of the global MHD model is that, within the model, it provides a large amount of information of the magnetospheric and ionospheric response to the solar wind. Therefore, besides the pseudo-AL index, we also analyzed the behavior of the ionospheric cross polar cap potential, the total ionospheric Joule heating, the magnetospheric tail field B_Z, and the field aligned current at selected locations in the magnetotail.

In section 5.2, we introduce the computational model and data processing techniques. In section 5.3, the pseudo-AL index as simulated from the global

MHD model is analyzed and compared with the results from *Sitnov et al.* [2000, 2001]. In section 5.4 and 5.5, the ionospheric and magnetospheric response are analyzed and discussed, respectively. Finally, conclusions are given.

5.2   Input and Output data

The LFM global MHD model was driven with the solar wind conditions observed by the IMP8 satellite (data available at the data center of UCLA) for 6 intervals selected from the BBMH data set, each 1-2 days in length. The original BBMH data set [*Bargatze et al.*, 1985] contains 34 intervals and is divided into 3 subsets (1-15, 16-26, and 27-34) representing different levels of substorm activity. Several studies have been conducted with this data set [*Blanchard and McPherron*, 1993; *Smith and Horton*, 1998] which contains salient features of substorms. The six intervals simulated in this thesis are the 16th, 18th, 19th, 20th, 21st, and 25th intervals, which are chosen from the second BBMH subset associated with medium activity. The total duration of these 6 intervals are around 240 hours.

In other words, the driver we used in the global MHD simulation is the solar wind condition observed during the six intervals which coincide with those in BBMH data set. The solar wind variables are the density, velocity (vector), magnetic field (vector), and thermal pressure. The data gaps are filled with interpolated data. These solar wind variables are propagated to the front boundary of the global MHD model in the usual sense described in chapter 2.

The full ionospheric model is used and dipole tilt is included. The simulations were conducted on the CRAY SV1 at supercomputer center of University of Texas.

The simulated magnetospheric and ionospheric response were saved every minute in SM coordinates. With these data files, we built the database of the coupled input-output system given by the global MHD model. The modeled magnetospheric response are sampled at x=20 R_E, y=0, z=1 R_E upstream, which are regarded as the solar wind input. The solar wind input contains several components. Since the substorm activity is closely related to the southward interplanetary magnetic field, in the analysis of this chapter, the solar wind input is represented by the induced electric field vB_s, where B_s is the southward component of the interplanetary magnetic field (IMF) (B_s=0 when B_z>0; B_s=-B_z when B_z<0) and v is the component of the solar wind velocity along the Earth-Sun axis. The same solar wind input is used by *Sitnov et al.* [2000] and other studies [*Blanchard and McPherron*, 1993; *Smith and Horton*, 1998]. Figure 5.1 shows an example of the relation between vB_s and the observed AL index from the BBMH data set. We note that magnetospheric substorms are influenced by many factors other than vB_s, e.g. solar wind ram pressure and other solar wind magnetic field components, and their physics is still a hotly debated research area. The substorms closely related to the variation of vB_s belong to a major subclass of the whole family of magnetospheric substorms. Understanding
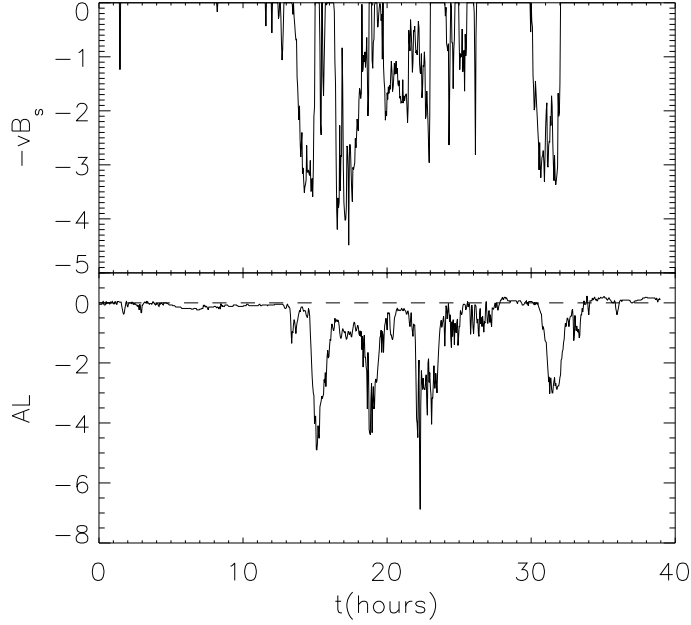
Figure 5.1:   Example of the relation between vB_s and the observed AL index from the BBMH data set.

the vB_s–AL index coupling contributes significantly to the understanding of the magnetospheric substorm physics [*Vassiliadis,* 1996].

For the output data, both ionospheric and magnetospheric response are used. The pseudo-AL index is used as the major measure of the ionospheric response during substorms. As introduced in Chapter 4, the pseudo-AL index is produced from the maximum westward ionospheric Hall current which has been searched throughout the grids in the northern hemisphere. The observational AL index is a measure of the strength of the auroral electrojet and the AL index perturbations are mainly produced by the east-west (azimuthal) ionospheric Hall current during magnetospheric substorms [*Kamide and Baumjohann,* 1993]. The pseudo-AL index produced from global MHD models is very close to the

observed AL index during substorm events. This is confirmed by other studies [*Wiltberger*, 1998; *Wiltberger et al.*, 2000; *Fedder et al.*, 1995a]. Therefore, the coupled vB_s–pseudo-AL index system is analyzed and compared to *Sitnov et al.* [2000, 2001], that are based on the analysis of vB_s–observed-AL index system. As noted, the cross polar cap potential and the total Joule heating are also used as measures of the ionospheric response. The cross polar cap potential is defined as the difference between the maximum and minimum electric potential in the northern polar cap. The total Joule heating is the integrated Ohmic heating due to the ionospheric Pedersen conductance. Both of them show significant activity during substorms.

To monitor the response in the magnetosphere, samples at three locations inside the magneto-tail were used. These three locations are x=-10, -15, -20 R_E with y=0 R_E, z=1 R_E. Since we monitor the substorm activity inside the tail, the tail magnetic field B_z and field-aligned current (FAC) measured at the three locations are used to represent the magnetospheric response. Each of these output data (both magnetospheric and ionospheric response) is coupled to the input vB_s data to form the input-output system.

In the next section, we illustrate the phase space reconstruction technique used to analyze the coupled vB_s–pseudo-AL index data sets.

5.3 Analysis of the Coupled vB_s–Pseudo-AL In-

dex Syetem

5.3.1 Singular Spectrum Analysis

A salient feature of a chaotic dynamical system is that the number of variables needed to describe the dynamics can be much smaller than the number of physical variables [*Takens*, 1981]. An estimate of the actual number of variables can be obtained from singular spectrum analysis. Following the analysis used by *Sitnov et al.* [2000], we use a modified singular spectrum analysis (SSA) or the so-called principle component analysis (PCA) [*Broomhead and King,* 1986] to include both input and output time series. The input is the product vB_s time series, essentially the solar wind induced electric field in the Y direction, which is related to the reconnection rate near the Earth's front magnetopause. The output variable is the pseudo-AL index produced from the global MHD model. The technique is based on the singular value decomposition (SVD) of the so-called trajectory matrix constructed from the time series data by time delay embedding:

$$Y(t_i) = (O(t_i), ..., O(t_i - (m-1)\tau), vB_s(t_i), ..., vB_s(t_i - (m-1)\tau)), \quad (5.1)$$

where i=1,...,N. The time delay τ and the embedding dimension m are chosen from the dynamical properties of the system. The typical value of τ is taken to be

146

2 min and that of the dimension m of the embedding space is 40, which provide a time window of 80 min comparable to the typical substorm scales. The input and output parameters are normalized separately by the corresponding standard deviations to make them more homogeneous.

This matrix $\mathbf{Y}$ contains all the dynamical features of the system embodied in the data and the state space reconstructed by time-delay embedding is quite noisy, mainly due to the randomness of the solar wind driver. Since the essential features of the dynamics may be described by a smaller number of linearly independent vectors, the solar wind noise can be removed by the technique of singular spectrum analysis. The matrix $\mathbf{Y}$ can be represented in the form

$$Y = UWV^T, \tag{5.2}$$

using singular value decomposition (SVD)[*Press et al.*, 1992]. Here $\mathbf{U}$ is an N×2m matrix; $\mathbf{W}$ is a 2m×2m diagonal matrix; and $\mathbf{V}$ is a 2m×2m orthogonal matrix. By construction, $V^T V$ is the identity matrix and $\mathbf{W}$ is a diagonal matrix with the elements w_j, where w_j^2 are the eigenvalues of the semi-positive definite matrix $Y^T Y$. $\mathbf{V}$ contains the SVD eigenvectors, while $\mathbf{U}$ determines the projections of the original trajectory matrix $\mathbf{Y}$ along the eigenvectors $P_j \equiv U_j w_j = (YV)_j$, respectively.

For an ideal system, the number of non-zero eigenvalues of $Y^T Y$ gives the number of variables needed to model the system. For a system with noise, SSA can be used to estimate the effective dimension of the system by selecting

diagonal elements w_j considerably above a particular noise floor w_{fl}. Then, the principle components defined by the eigenvectors P_j which corresponds to these w_j define the corresponding attractor (if it exists) in the embedding space [Ott, 1997]. These linearly independent eigenvectors define the principle directions and thus the principal coordinates in the embedding space, and the time series of these principal variables may be obtained by projecting the given time series onto these directions [$Sharma$, 1993, 1994; $Sharma\ et\ al.$, 1993]. The projected variables may then be used to describe and reconstruct the dynamics. The singular spectrum analysis removes the turbulent or random effects and yields the deterministic dynamical features. However, SSA uses linear techniques and consequently the dimension it gives may be considered only as an estimate. SSA may be regarded as a modification of Fourier or wavelet analysis because of its data-derived basic functions [$Preisendorfer$, 1988].

5.3.2   Singular Spectrum and Effective Dimension

The singular spectrum of the coupled vB_s–pseudo-AL index data were computed for time delays τ=2.0, 4.0, and 6.0 min and for embedding dimensions m=20, 40, and 60. These values are chosen to keep the analysis close to the case studied by $Sitnov\ et\ al.$ [2000], in which τ=2.5, 5.0, and 7.5 min and m=16, 32, and 48 were used. The total time windows (mτ) are in the range 40-120 minutes. Figure 5.2a shows the singular spectrum (eigenvalues w_j) for different time delays τ=2.0, 4.0,
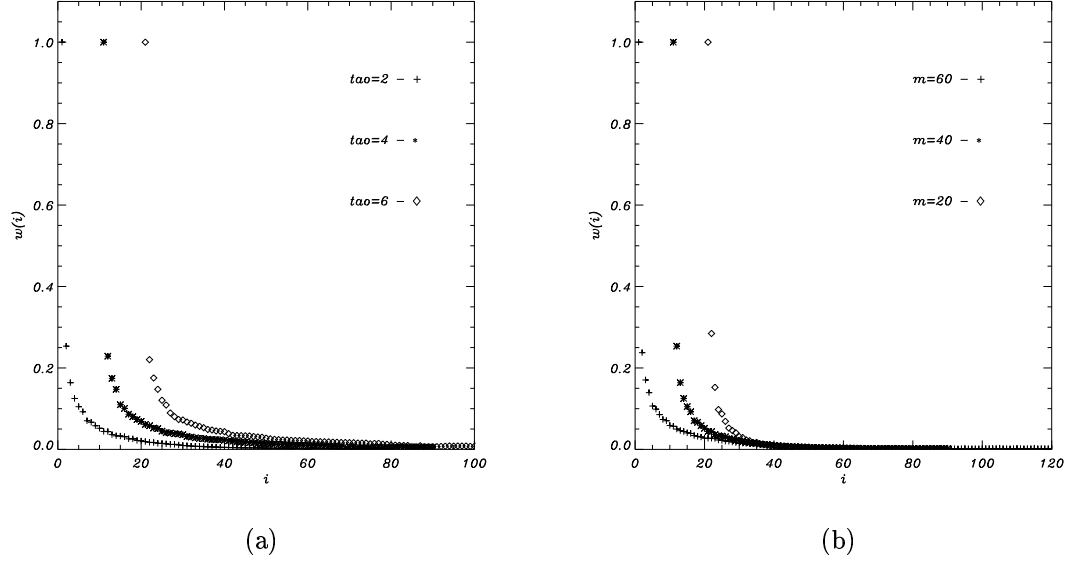
Figure 5.2: Singular spectrum of the coupled vB_s–pseudo-AL index data for (a) different time delay τ=2.0, 4.0, and 6.0 min and m=40; (b) different embedding dimension m=20, 40, and 60 and τ=2.0 min.

and 6.0 min and embedding dimension m=40. Figure 5.2b shows the eigenvalues

for τ=2.0 min and different embedding dimension m=20, 40, and 60. All the

eigenvalues have been normalized to the corresponding maximum eigenvalue.

Figure 5.2 shows that two or three leading eigenvalues dominate over the oth-

ers (the fourth eigenvalue is less than 0.15). This is consistent with the results

based on the analysis of the coupled vB_s–observed-AL index system in *Sitnov et*

al. [2000]. Here, the second largest eigenvalue is less than 0.3, while in *Sitnov*

et al. [2000] the second largest eigenvalue is larger than 0.4. This implies that

the leading eigenvectors of the coupled vB_s–pseudo-AL index system which are

derived from global MHD model are more dominant. This issue is re-addressed

in section 5.3.5 when we discuss the multiscale feature of magnetospheric sub-storms.

In order to assess the fractal dimension of the system trajectory in the embedding space, we calculate the coast-line dimension of the trajectory. The coast-line dimension of the trajectory set in the embedding space [*Abarbanet et al.*, 1993] is given by

$$D_f \approx D(N_p) = log(N_t)/log(N_p), \tag{5.3}$$

where N_p is the number of partitions along each principal component P_j (j=1,...,4 as in our case) and N_t is the number of cubes created because of this partitioning that contain at least one point of the trajectory.

Figure 5.3 shows the coast-line dimension of the coupled vB_s–pseudo-AL index system as a function of the partition N_p along each of the m directions in the m-dimensional embedding space for different m=1, 2 , 3, and 4. Here, the time delay τ is 2 min. Figure 5.3 shows that when the embedding dimension is increased over 2 (m=3, 4), the coast-line dimension converges to D_f=2. This is typical of systems with finite dimension. This implies that the trajectory lies mainly on a two-dimensional manifold in the embedding space. In *Sitnov et al.* [2000], the coast-line dimension of the coupled vB_s–observed-AL index system also converges to D_f=2 for the embedding dimension larger than 2. Therefore, the coast-line dimension of the coupled system derived from the global MHD model is consistent with that of the input-output system based on observations.
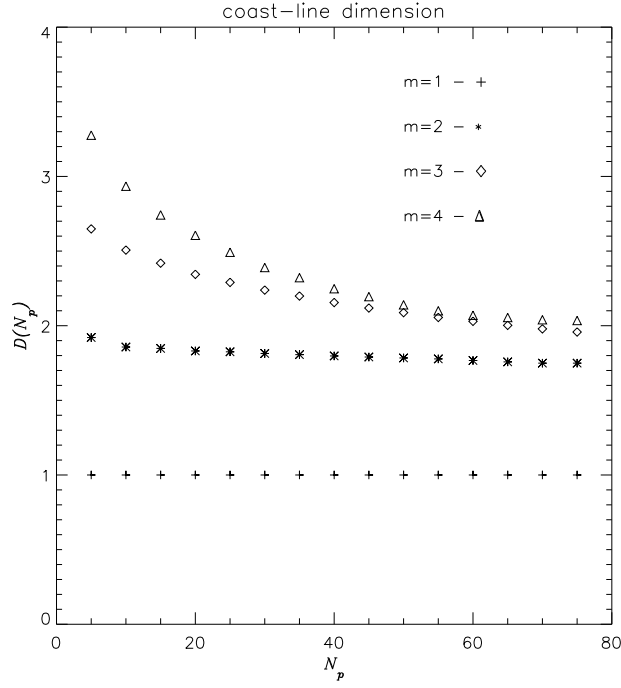
Figure 5.3: Fractal dimension of the coupled vB_s–pseudo-AL index system as a function of the partition N_p. N_p is the number of partitions along each of the m directions in the m-dimensional embedding space for different m=1, 2 , 3, and 4.

Both singular spectrum and fractal dimension analysis show that the manifold on which the trajectory of substorm dynamics lies can be approximated by a two-dimensional surface. This helps us in reducing effectively the noise and capturing the essential dynamical features of the system obtained from the global MHD simulations. Therefore, we proceed to reconstruct the substorm dynamics in the reduced phase space created by the leading eigenvectors. In the following analysis, the main eigenvectors are limited to be 3. The trajectory matrix $\mathbf{Y}$ formed with τ=2 min and m=40 is projected onto the three leading

151

eigenvectors. The manifold in the three-dimensional space is approximated by a two-dimensional surface.

5.3.3 Original and Rotated Eigenvectors

Figure 5.4a-c show the original three leading eigenvectors (the first, second, and third eigenvectors) corresponding to the three largest eigenvalues obtained from the singular spectrum analysis (SSA). Each eigenvector is composed of output and input components. The output component V(j) (j=1–40) is blue-shaded and the input component V(j) (j=41–80) is green-shaded. As we can see, the input and output components are mixed in each eigenvector.

The ratio between the output and input components are not maximized or minimized in the original eigenvector and make it difficult to visualize and understand the manifold. As suggested by *Sitnov et al.* [2000], we rotate the eigenvector as

$$\left\{ \begin{array}{l} V_1 \to V_1 \cos \alpha + V_2 \sin \alpha \\[2mm] V_2 \to -V_1 \sin \alpha + V_2 \cos \alpha \end{array} \right\} \otimes \left\{ \begin{array}{l} V_2 \to V_2 \cos \beta + V_3 \sin \beta \\[2mm] V_3 \to -V_2 \sin \beta + V_3 \cos \beta \end{array} \right\}. \qquad (5.4)$$

The goal of each rotation is to minimize or maximize the ratio between the output (j=1–40) and input (j=41–80) parts so that the resultant variables approach either the control or state parameter of some catastrophe model. During the first rotation, we maximize the the ratio $|\sum_{j=1}^{40} V_1(j) / \sum_{j=41}^{80} V_1(j)|$. While for the second rotation, we minimize the ratio $|\sum_{j=1}^{40} V_2(j) / \sum_{j=41}^{80} V_2(j)|$. In this way,
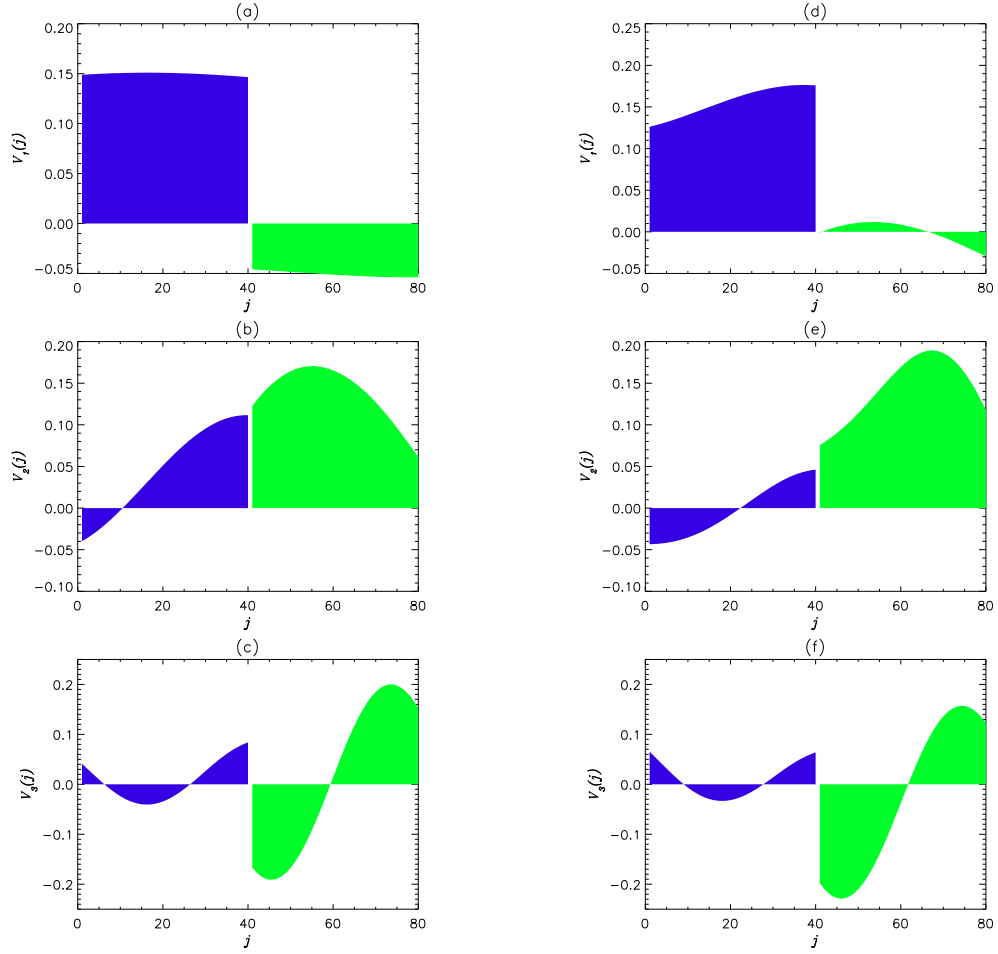
Figure 5.4: (a)-(c) are the original three leading eigenvectors obtained from the singular spectrum analysis (SSA). (a)The first eigenvector; (b)The second eigenvector; (c)The third eigenvector. (d)-(f) are the three leading eigenvectors after the eigenvectors in (a)-(c) are rotated. (d) Obtained from rotating the eigenvector in (a); (e) Obtained from rotating the eigenvector in (b); (f) Obtained from rotating the eigenvector in (c). Each eigenvector is composed of output and input components. The output component V(j) (j=1–40) is blue-shaded and the input component V(j) (j=41–80) is green-shaded.

the first eigenvector is rotated to a direction along which the output component is dominant and the second eigenvector is rotated to a direction along which the input component is dominant. The adjustment is achieved through trial and error and in this case α =0.35 and β =0.30. The rotated three leading eigenvectors (we call them basis eigenvectors) are shown in Figure 5.4d-f. From Figure 5.4d-f, we see that the first vector is dominated by the output part, while the second and the third vector are controlled by the input component. The orthogonality among the three newly obtained basis eigenvectors is maintained.

5.3.4   First-Order Phase Transition-Like Behavior

After obtaining the rotational parameter α and β, the principle components P_j (j=1, 2, 3) are projected onto the newly rotated basis vector (shown in Figure 5.4d-f). In other words, we are studying the trajectory manifold formed by P_j (j= 1, 2, 3) in the 3-D space with axes formed by the newly obtained basis eigenvectors. Since for the first basis eigenvector, the output component (pseudo-AL index) is dominant, we call the corresponding principle component along this eigenvector as P_o, which is closely related to time-averaged output. For the second basis eigenvector, the input component (vB_s) is dominant, and the corresponding principle component is called P_i. For the third basis eigenvector, the input component is dominant and experiences one period of oscillation, and the corresponding principle component is called P_3. P_3 is roughly proportional
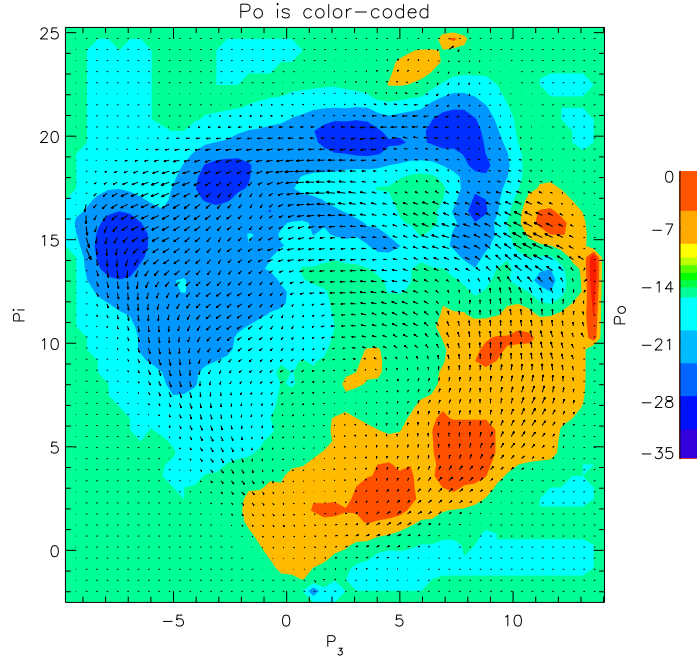
Figure 5.5: The 2D surface approximation of the manifold representing magnetospheric dynamics on the basis plane (P_3, P_i). The principle component P_o is color-coded. The circular flows given by dP_i/dt and dP_o/dt are represented by arrows. The phase transition map is obtained from the coupled vB_s–pseudo-AL index system. The pseudo-AL index is derived from global MHD model.

to the time derivative of the input component.

Figure 5.5 shows the 2D surface approximation of the manifold representing magnetospheric dynamics on the basis plane (P_3, P_i). The principle component P_o is color-coded. Surface approximation is achieved through standard triangulation procedure. The circular flows given by dP_i/dt and dP_o/dt are represented by arrows. This map is derived from the coupled vB_s–pseudo-AL index system.

Figure 5.6, obtained by *Sitnov et al.* [2000], is the similar surface approximation of the manifold to that in Figure 5.5. This map is constructed for the

155
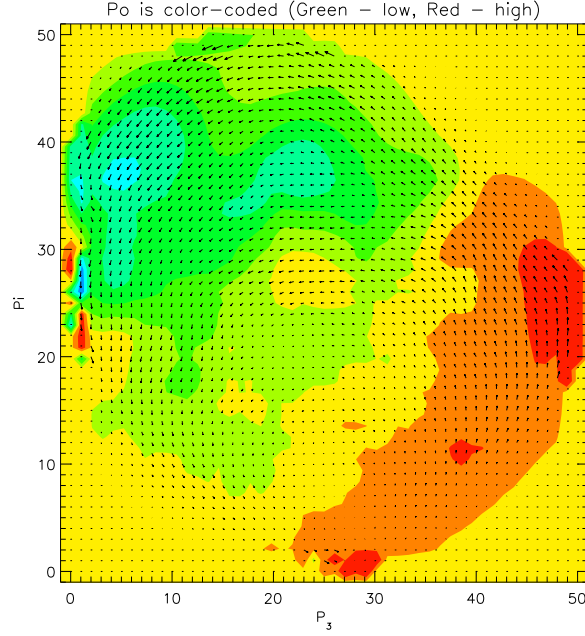
Figure 5.6: The similar map as in Figure 5.5 derived by *Sitnov et al.* [2000] for the coupled vB_s–observed AL index system. This map is constructed with the second subset (16-26) of the BBMH data set.(Courtesy of Dr. Sitnov at University of Maryland)

coupled vB_s–observed AL index system derived from the second subset of the BBMH data set. Figure 5.5 resembles Figure 5.6 in the sense that both of the maps capture the phase transition-like behavior qualitatively.

In Figure 5.5, P_i=0 and P_3=0 mark the start of the substorm cycle. The flow arrows show the trajectory of the substorm cycle. During the substorm cycle, when P_i is increased over zero, P_o remains nearly 0 and experiences some small decreases (changing from red to yellow). During this interval, P_3 is increased first, then remains nearly constant around 10. This phase corresponds to the growth phase in the substorm cycle. Then P_o takes large negative values. The flow arrows are the largest during this transition. This rapid transition and the

156

following intensifications (dark blue shaded area) correspond to the expansion phase. The restoration of the system to the original state involves the decrease of P_i and $-P_o$. This phase corresponds to the motion towards the motion inside left bottom corner and is termed as recovery phase in the substorm cycle. The 'S' shaped feature in the vicinity of $P_i=14$ and $P_3=12$ corresponds to the hysteresis phenomenon.

There have been many discussions regarding the timing of the substorm onset. The coupled input–output system studied here is constructed with the pseudo–AL index and vB_s input. The auroral eletrojet index itself alone is not sufficient to determine the substorm onset, for which combined observations of the auroral image, AL and AE index and tail satellite observations are needed. Furthermore, Figure 5.5 presents the substorm cycle with P_i closely related to time-averaged input and P_o closely related to time averaged output. Therefore, we do not expect that the transition revealed in Figure 5.5 by the large falling down will coincide with the usual substorm onset defined from the combination of all available observations. In any case, Figure 5.5 reconciles the essential features of many substorm cycles revealed by the coupled vB_s–pseudo-AL index on the same map.

Both Figure 5.5 and Figure 5.6 are obtained with the same data processing technique, namely singular spectrum analysis. Figure 5.5 is constructed from the simulated system and Figure 5.6 is constructed from the real system. Both Figure 5.5 and Figure 5.6 show that the evolution of the magnetosphere on the largest

scale is quite regular and resembles the temperature-pressure-density (TPD) diagram of equilibrium phase transition [*Stanley*, 1971]. The fact that Figure 5.5 resembles Figure 5.6 implies that the global MHD model reproduces successfully the phase transition-like behavior which exists in the real substorm cycle. Although, the comparison between observation and individual global MHD simulation may vary, the overall global transition pattern during the substorm cycle revealed by SSA is consistent between simulations and observations. The whole procedure of phase transition analysis using SSA is reliable in the sense that it reveals the qulitative features of global configuration change resides statistically both in the real system and in the global MHD simulation.

As explained in *Sitnov et al.* [2000], both the approximated 2D manifold and the corresponding circulation flows shown in Figure 5.5 are close to a simple low-dimensional scheme of a magnetospheric substorm as a cusp catastrophe (inverse bifurcation) first proposed by *Lewis* [1991]. Figure 5.7 shows the schematic cusp catastrophe manifold that was expected to approximate the substorm dynamics of the magnetosphere according to the model of *Lewis* [1991]. The evolution of an isolated substorms is shown by dashed arrows.

In this model, the dynamics of the magnetosphere is described by the evolution equation for the state parameter z

$$\frac{dz}{dt} = -\frac{\partial U(z, c_1, c_2)}{\partial z},$$

(5.5)
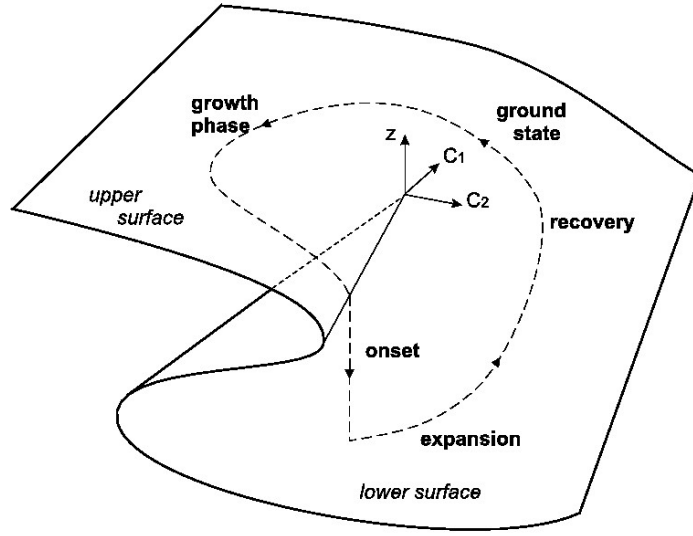
Figure 5.7: Hypothetical cusp catastrophe manifold that was expected to approximate the substorm dynamics of the magnetosphere according to the model of *Lewis* [1991]. The evolution of an isolated substorms is shown by dashed arrows. (Courtesy of Dr. Sitnov at University of Maryland)

where the effective potential is defined as

$$U(z, c_1, c_2) = z^4 + 2c_1 z^2 + 4c_2 z \qquad (5.6)$$

and has two control parameters c_1 and c_2. These parameters control the quasi-static changes of z, which is possible as long as the condition $\frac{\partial U(z, c_1, c_2)}{\partial z} = 0$ is satisfied. The folded surface shown in Figure 5.7 is determined through this condition. In this model, the state parameter z is the nightside magnetic field orientation and the control parameters $c_1 = $ -*(open flux)* + *constant* and c_2=(*nightside - dayside*) *reconnection rate.* The first parameter c_1 resembles the parameter P_i in our model, while the second parameter c_2 is closely related to the parameter

P_3. According to panel f in Figure 5.4, P_3 represents the difference between the immediate dayside reconnection rate, which is proportional to vB_s (negative green bay in Figure 5.4f) and its delayed value (positive green bay). The delay is comparable to the propagation time of the signal from the subsolar magnetopause to the distant neutral line. The delayed component mimics the night side reconnection rate. The potential in Eq. 5.6 may have both one and two minima corresponding to different equilibrium states of the system. The onset of the substorm is represented as a local fold catastrophe arising due to the disappearance of the upper potential minimum. In this way, Figure 5.5 fits into the low-dimensional scheme of magnetospheric substorm as a cusp catastrophe illustrated in Figure 5.7.

Although catastrophe-like picture can explain the global transition revealed in Figure 5.5 and 5.6 on the largest scale, there are still deviations from the ideal catastrophe model. *Sitnov et al.* [2000, 2001] note that the clear first order phase transition structure gradually disappears with the increase of the average activity. They also observe multi-scale features existing with the coupled input-output system. *Sitnov et al.* [2000, 2001] propose another interpretation that accounts for the deviations. The same catastrophe-like picture and multi-scale features may be created by dynamical transitions. The bifurcation/catastrophe picture is associated with first-order dynamical phase transitions, while the deviations from the ideal catastrophe picture may be explained by second-order

phase transitions near the critical point. The first-order phase transition picture suggests the location of the critical point, which can be used to obtain the appropriate critical exponent. It is quite interesting to study whether the results from global MHD have multiscale features or not.

5.3.5 Multi Scale Behavior

The concept of the self-organized criticality (SOC) is based on a simple model of sandpile [*Bak et al.*, 1987] and has been used widely in the interpretation of catastropic processes in open spatially extended systems. The SOC concept has been used to explain substorm activity on the basis of the observation that some spectra obey power laws [*Tsurutani et al.*, 1990; *Takalo et al.*, 1993; *Ohtani et al.*, 1995, 1998; *Lui*, 1998]. *Sitnov et al.* [2000] suggest that scale invariant or multi-scale behavior originates from the second-order phase transitions instead of SOC.

SOC models emphasize that the input is not essential because of the self-tuning properties of the system and provide only one class of critical exponents, which relate some parameter of the system, such as the energy released with the spartial scale or characteristic frequency. While the second-order phase transitions have at least one more class of critical exponents that relate the input parameter of the system, e.g. magnetic field or temperature, with its output, e.g. magnetization or density. In *Sitnov et al.* [2000, 2001], two kinds of crit-

ical exponents are found with the new data-derived image of substorms. The first critical exponent is related to the scale invariant (or power law) behavior of the eigenvalues obtained from SSA as shown in Figure 5.8a. The second critical exponent, which is the primary distinctive feature between second-order phase transition and self-organized criticality (SOC), is derived from the envelope $max(-dP_o/dt)$ of the velocity time series $v(t_i) = dP_o/dt$. In other words, given P_i, which is closely related to the time-averaged input, there is a maximum decreasing rate for P_o and $max(-dP_o/dt)$ scales in power law with P_i. Using an analogy to the dynamical Ising model in the mean-field approximation, the connection between the data-derived exponent of nonequilibrium transitions in the magnetosphere and the standard critical exponent β of equilibrium sencond-order phase transitions is shown to be $\beta = \beta_*/3$. *Sitnov et al.* [2000, 2001] conclude that the substorm dynamics of the magnetosphere resembles more the conventional set of first and second-order phase transitions rather than SOC or catastrophe model. In this section, we investigate these two kinds of critical exponents using the global MHD simulations and compare them to the results of *Sitnov et al.* [2000, 2001].

Figure 5.8a shows the singular spectra of the coupled vB_s–observed-AL index system from *Sitnov et al.* [2000] on log–log plot. Figure 5.8b shows the singular spectra of the coupled vB_s–pseudo-AL index system derived from the global MHD model on log–log plot. Figure 5.8a indicates that the singular spectrum

(a)   (b)
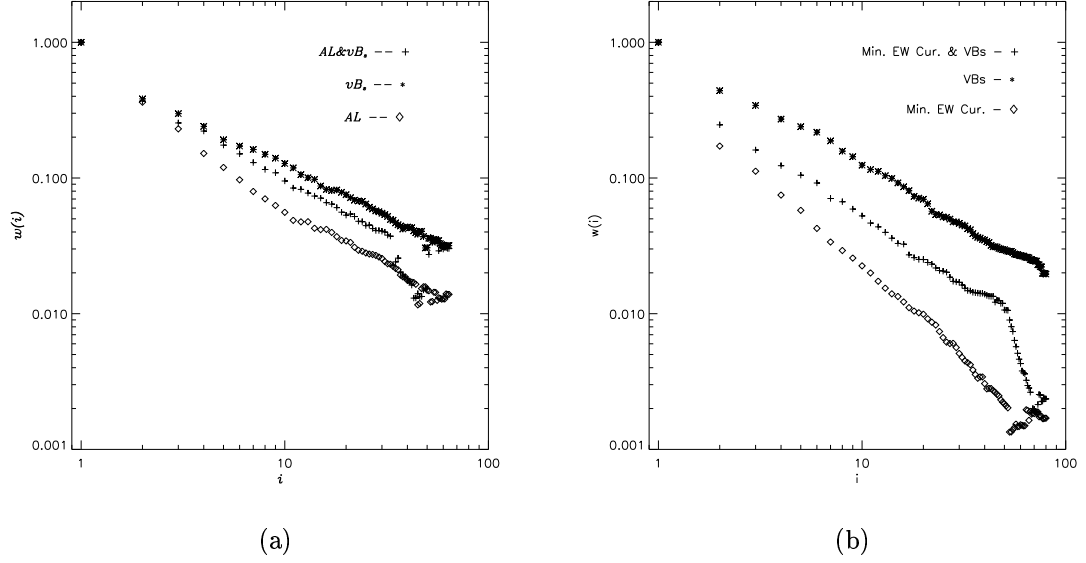
Figure 5.8: Log–Log Plots of SSA eigenvalues for observed-AL or pseudo-AL index and vB_s parameters alone as well as for the combined data in cases of (a) the coupled vB_s–observed-AL index system from *Sitnov et al.*, 2000 (Courtesy of Dr. Sitnov at University of Maryland); $\tau = 2.5$ min, m=32 in the case of combined data, and m= 64 for input and output parameters alone;(b) the coupled vB_s–pseudo-AL index system derived from global MHD model. $\tau = 2$ min, m=40 in the case of combined data, and m= 80 for input and output parameters alone.

of the observed-AL index data alone obeys power law with an exponent around

-1. While Figure 5.8b indicates that the singular spectrum of the pseudo-AL

index data alone also obeys power law with an exponent around -1.5. Both the

observed-AL index and the pseudo-AL index show multi-scale behavior. But, the

pseudo-AL index is much cleaner than the observed-AL index in the sense that

its singular spectrum assumes steeper slope (in log–log plot). This is because the

global MHD model works on large scales and low frequency regions and smoothes

local and high frequency fluctuations. Figure 5.8a also shows that the singular

spectrum of the combined vB_s and observed-AL index data obeys power law and assumes the slope (in log–log plot) in between those of the singular spectra of the vB_s data and the observed-AL index data, separately. In Figure 5.8a, the singular spectrum of the combined data spreads for i>40. While for the singular spectrum of the combined vB_s and pseudo-AL index data, the slope of the singular spectrum changes around i=50. In Figure 5.8b, the slope of the spectrum of the combined data is -1.33 for $i < 50$ and changes to -3 for $i > 50$. For higher SSA components of the combined data derived from the global MHD model, the spectrum decays faster and the corresponding principle component is less important.

Figure 5.9 shows the rate of the positive and negative changes of the parameter P_o as a function of P_i obtained from the analysis of the global MHD model data. The green curve and red curve marks the lower envelope of the changing rate of P_o. We can clearly see that there are two envelopes. For the positive values of dP_o/dt which corresponds to the recovery phase of substorms, the envelope is a straight line. While for the negative values of dP_o/dt, which corresponds to the active period (decrease of pseudo-AL index), the envelope is a curve. With the increase of P_i, the maximum of ($-dP_o/dt$) increases.

Figure 5.10 shows the similar plot of dP_o/dt vs. P_i obtained from the coupled vB_s–obseved-AL index system studied in *Sitnov et al.* [2001]. We can see that Figure 5.9 resembles Figure 5.10 in the sense that both of the plots show similar
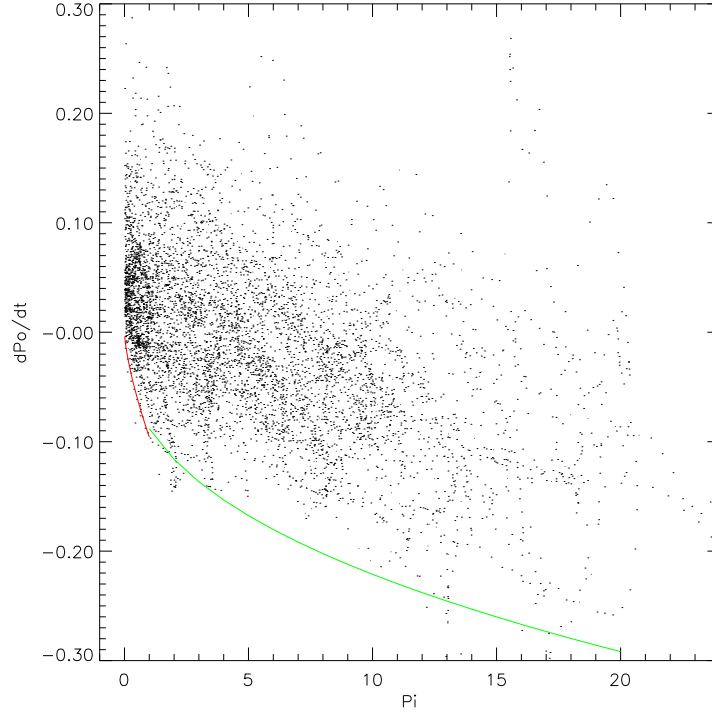
Figure 5.9: Rate of the positive and negative changes of the parameter P_o as a function of P_i obtained from the analysis of the global MHD model data. The green curve and red curve marks the lower envelope of the changing rate of P_o as a function of P_i.

envelopes. The curved envelopes in Figures 5.9 and 5.10 are of interest, since they are related closely to the input and output parameter.

Figure 5.11 (a) and (b) shows the Log–Log plots of the lower (curved) envelopes in Figures 5.9 and 5.10, respectively. In Figure 5.11a, the two lines are of slopes 0.7 and 0.4, separately. They correspond to the red and green curve in Figure 5.9, respectively. While in Figure 5.11a, the dash line is of slope 0.64. We can see that the curved envelope derived from the coupled vB_s –observed-AL index system (in Figure 5.10) obeys a power law that spans four decades.
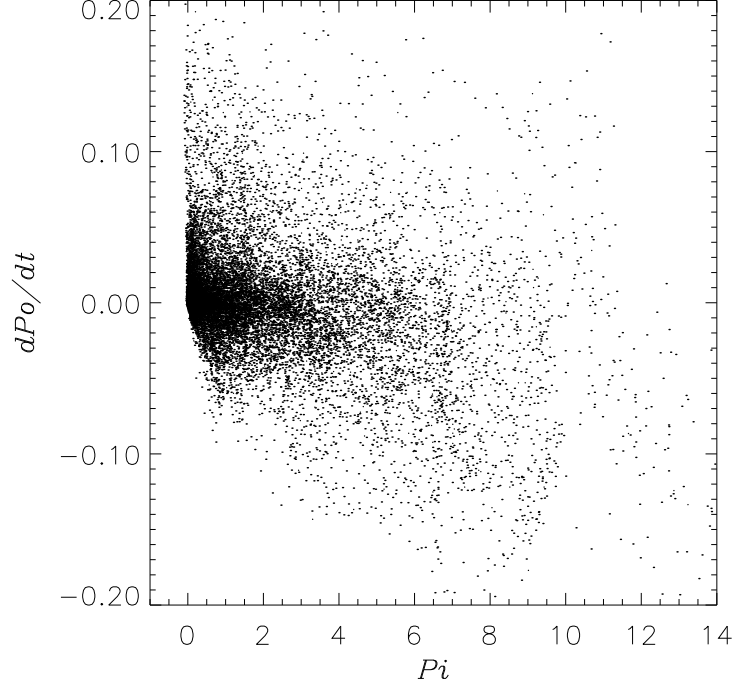
Figure 5.10: Rate of the positive and negative changes of the parameter P_o as a function of P_i obtained from the the coupled vB_s–obseved-AL index system studied in *Sitnov et al.* [2001]. (Courtesy of Dr. Sitnov at University of Maryland)

The curved envelope derived from the coupled vB_s –pseudo-AL index system (in Figure 5.9) shows two slopes. When the parameter P_i is small (< 1.0), the curved envelope in Figure 5.9 scales with a power close to that of the real system. When the parameter P_i is large(> 1.0), the curved envelope in Figure 5.9 scales with another power smaller than that of the real system. With the increase of the input vB_s, the maximum changing rate of (-P_o) doesn't increase as fast as in the case derived from observations. Our explanation is that in the global MHD model, which has only an electro-static model of the ionosphere and

166
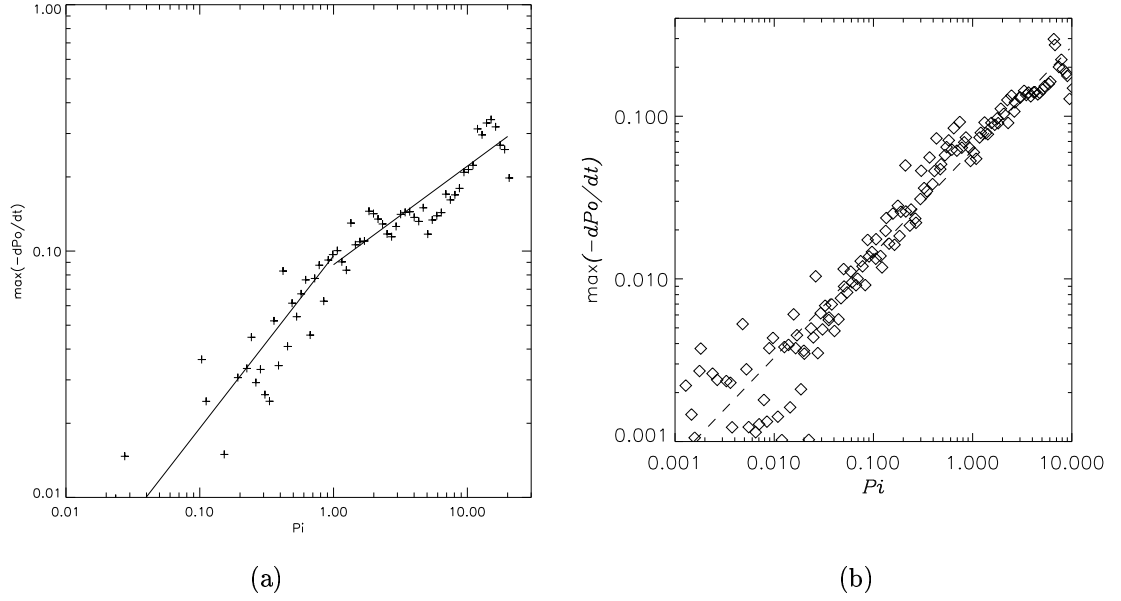
Figure 5.11: (a) Log–Log plots of the lower envelope in Figure 5.9; (b) Log–Log plots of the lower envelope in Figure 5.10.

doesn't have a ring current in the magnetosphere, the ionospheric activity can be underestimated with excessive input.

The global MHD simulation data reveal the curved envelope relation between P_i and max($-dP_o/dt$), as in the real system. P_i and P_o are closely related to input and output parameter. The envelope of max($-dP_o/dt$) scales as P_i with two envelopes. Therefore, to some degree, the global MHD model reveals the multi-scale behavior. Both the analysis of the real system and that of the global MHD model show that the magnetosphere resembles the conventional set of first and second-order phase transition rather than SOC or catastrophe model.

Figure 5.12: The 2D surface approximation of the manifold representing magnetospheric dynamics on the basis plane (P_3, P_i). The principle component P_o is color-coded. The circular flows given by dP_i/dt and dP_o/dt are represented by arrows. The map is obtained from (a) the coupled vB_s–cross polar cap potential system; (b) the coupled vB_s–total Joule heating system.

5.4   Analysis of Other Ionospheric Responses

In the previous section, we analyzed the coupled vB_s–pseudo-AL index system.

Besides pseudo-AL index, the cross polar cap potential and the total Joule heating are often used as measures of the ionospheric response.

Following similar analysis described in section 5.3.1–4 by replacing the output parameter pseudo-AL index with the cross polar cap potential and the total ionospheric Joule heating, respectively, we construct the approximated 2D color surfaces in Figure 5.12. We can clearly see the first-order phase transition pattern in Figure 5.12a, which is constructed for the coupled vB_s–cross polar cap

potential system. Figure 5.12a shows that the initial increase of the the cross polar cap potential during the growth phase is significant (the relative magnitude changes from 10 to 18). This has been discussed in section 4.3. At the substorm onset, there is an abrupt increase in the cross polar cap potential. This abrupt change is shown in Figure 5.12a with the transition from blue to green near ($P_3=5$, $P_i=15$). The resemblance between Figure 5.5 and Figure 5.12a implies that the phase change is of the same origin, namely global change of the magnetospheric configuration.

Figure 5.12b shows that the evolution of the Joule heating during a substorm cycle is more complicated than the phase transition shown in Figure 5.12a. The total Joule heating might experience mixed stages of enhancement during substorm cycles. The total Joule Heating is integrated over the entire ionosphere. *Wiltberger et al.* [2000] showed that for some substorm events, there are strong flow channels formed locally and about twenty minutes later, a global tail reconnection occurs. While the pseudo-AL index can not discern between these two kinds of signatures in the ionosphere, the total Joule heating shows two phases.

5.5 Analysis of Magnetospheric Responses

5.5.1 Signature of Dipolarization

In this section, we search for the signature of dipolarization inside the magneto-sphere during magnetospheric substorm. Following similar analysis described in section 5.3.1–4 by replacing the output parameter pseudo-AL index with local magnetic field B_z, we construct the approximated 2D color surfaces in Figure 5.13 (a) and (b). Figure 5.13a is obtained from the coupled vB_s–B_z at (x=-10 R_e, y=0 R_e and z= 1 R_e) system and Figure 5.13b is obtained from the coupled vB_s–B_z at (x=-15 R_e, y=0 R_e and z= 1 R_e) system.

During a substorm event, the stretched magnetic field lines move back towards the Earth side. This dipolarization is marked by the increase of the local magnetic field B_z. Figure 5.13b clearly shows the phase transition pattern revealed with the increase of the magnetic field B_z at x=-15 R_e. However, Figure 5.13a shows no clear transition pattern. The signature of dipolarization during substorm is stronger in the region of x=-15 R_e than in the region of x=-10 R_e. Actually, the tail field around x= -15 R_e changes from a highly compressed (nearly anti-parallel) configuration during dipolarization. While in the region closer to the Earth (around x=-10 R_e), the field configuration doesn't change dramatically.
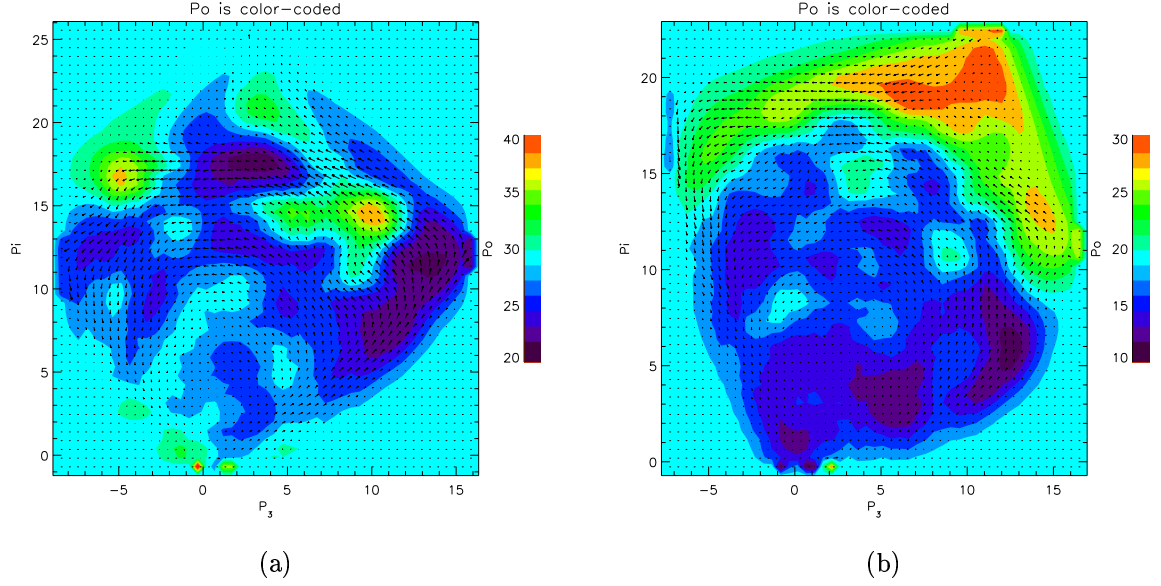
Figure 5.13: The 2D surface approximation of the manifold representing magnetospheric dynamics on the basis plane (P_3, P_i). The principle component P_o is color-coded. The circular flows given by dP_i/dt and dP_o/dt are represented by arrows. The map is obtained from (a) the coupled vB_s–B_z at (x=-10 R_e, y=0 R_e and z= 1 R_e) system; (b) the coupled vB_s–B_z at (x=-15 R_e, y=0 R_e and z= 1 R_e) system.

5.5.2 Intensification of Field Aligned Current

In this section, we search for the signature of intensification of the field aligned current inside the magnetosphere during magnetospheric substorm. Again, following analysis similar to section 5.3.1–4 by replacing the output parameter pseudo-AL index with the local field aligned current (FAC), we construct the approximated 2D color surfaces in Figure 5.14 (a) and (b). Figure 5.14a is obtained from the coupled vB_s–FAC at (x=-10 R_e, y=0 R_e and z= 1 R_e) system and Figure 5.14b is obtained from the coupled vB_s–FAC at (x=-20 R_e, y=0 R_e and z= 1 R_e) system.

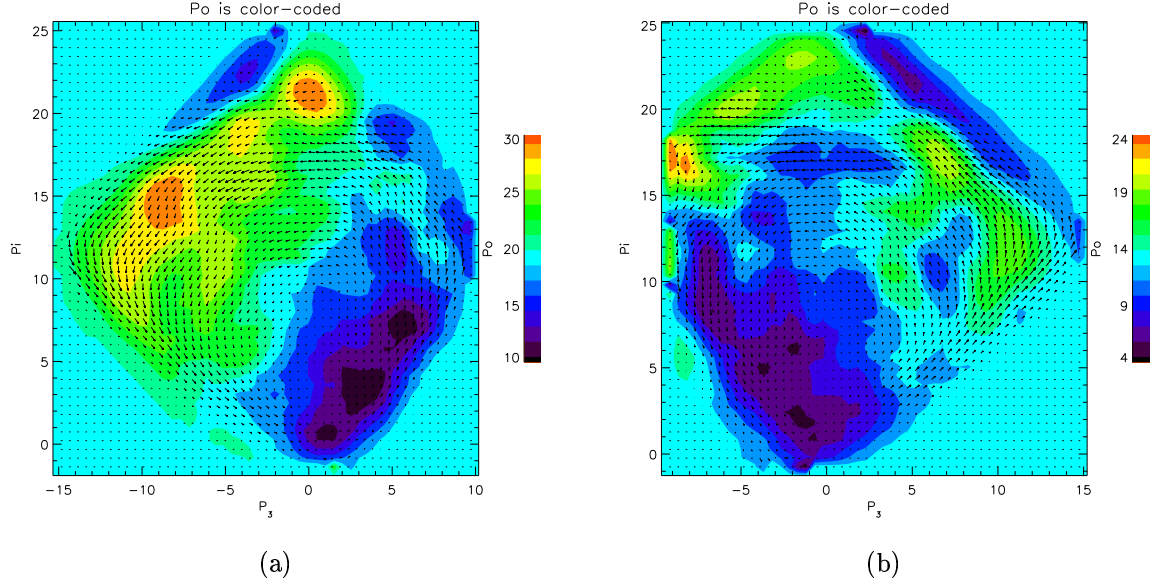(a)   (b)
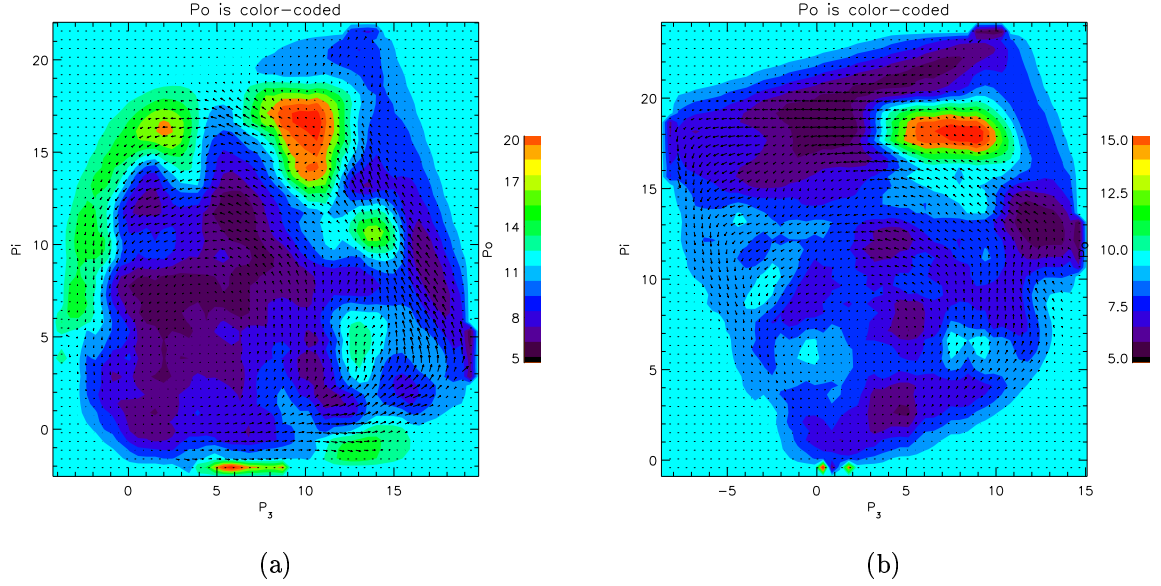
Figure 5.14:   The 2D surface approximation of the manifold representing mag-
netospheric dynamics on the basis plane (P_3, P_i). The principle component P_o
is color-coded. The circular flows given by dP_i/dt and dP_o/dt are represented
by arrows. The map is obtained from (a) the coupled vB_s–field aligned current
at (x=-10 R_e, y=0 R_e and z= 1 R_e) system; (b) the coupled vB_s–field aligned
current at (x=-20 R_e, y=0 R_e and z= 1 R_e) system.
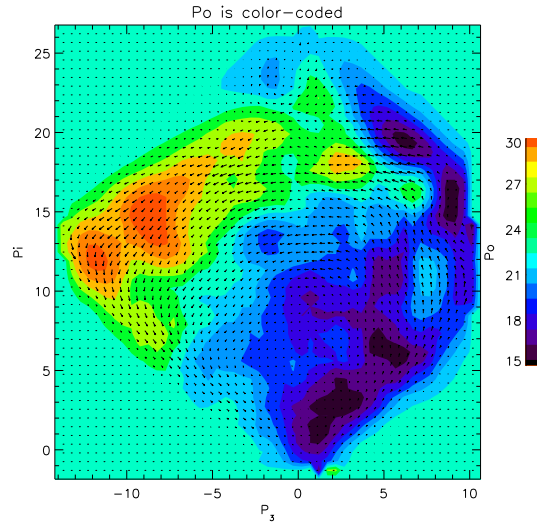
Figure 5.15:   Similar to Figure 5.14 (a) and (b). the map is constructed from the
coupled vB_s–Maximum FAC system. Maximum field aligned current is obtained
at the inner boundary of the magnetosphere model.

Since we are only interested in the intensification of the field aligned current, we use here the absolute value of the field aligned current to construct map. We can see that the maps are complicated for both x=-10 R_E and x=-15 R_E and there is no clear two phase behavior. The map constructed at x=-10 R_e shows some more activities during substorm cycle. But, when we study Figure 15, the scenario is different. Figure 15 is constructed from the coupled vB_s–Maximum FAC system. Maximum field aligned current is obtained at the inner boundary of the magnetosphere model. We can clearly see the phase transition pattern. This is consistent with the analysis of pseudo-AL index, since pseudo-AL index is mainly driven by the field aligned current.

5.6   Conclusions

In this chapter, we use techniques of singular spectrum analysis (SSA) to analyze the coupled input-output system derived from the global MHD simulations and compare the results to those from the analysis of the observations by *Sitnov et al.* [2000, 2001]. We also use similar techniques to analyze other ionospheric and magnetospheric response.

1. The analysis of the coupled vB_s–pseudo-AL index system derived from the global MHD simulations shows the first-order phase transition map, which is consistent with the similar map obtained for the vB_s–observed-AL index system from *Sitnov et al.* [2000, 2001]. The reconstructed surface resembles the

so-called temperature-pressure-density (TPD) diagram for the equilibrium first order phase transitions (e.g., [*Stanley,* 1971]). Although, the comparison between observation and individual global MHD simulation may vary, the overall global transition pattern during the substorm cycle revealed by SSA is consistent between simulations and observations. The procedure of phase transition analysis using SSA has revealed the qualitative features of global configuration change both in the real system and in the global MHD simulations.

2. The bifurcation/catastrophe picture is associated with first-order dynamical phase transitions, while the deviations from the ideal catastrophe picture may be explained by second-order phase transitions near the critical point. The coupled vB_s–pseudo-AL index system derived from global MHD simulations shows multi-scale behavior (scale-invariant power-law dependence) in singular power spectrum. The pseudo-AL index is much cleaner than the observed-AL index in the sense that its singular spectrum assumes more steep slope (in log–log plot).

The global MHD simulation data reveal the curved envelope relation between P_i and $\max(-dP_o/dt)$, as in the real system. P_i and P_o are closely related to the input and output parameter, respectively. The envelope of $\max(-dP_o/dt)$ scales as P_i with two exponents. With the increase of the input vB_s, the maximum changing rate of $(-P_o)$ doesn't increase as fast as in the case derived from observations. Our explanation is that in the global MHD model, which has only an electro-static model of the ionosphere and doesn't have ring current in the

magnetosphere, the ionospheric activity can be underestimated with excessive input. In any case, the curved envelope relation between P_i and $\max(-dP_o/dt)$ is the essential feature which distinguish the second order phase transition model from the SOC model.

3. The analysis of other ionospheric responses during substorm show that the cross polar potential experiences similar phase transition pattern revealed by the coupled vB_s–pseudo-AL index system, while the total Joule Heating experiences mixed stages of enhancement during substorm cycles. The explanation may be that for some substorm events, there are strong flow channel formed locally close to the Earth and about twenty minutes later, a global tail reconnection occurs.

4. The analysis of the signature of dipolarization (increase of local B_z field) indicates that the clear phase transition exist in the region x=-15 R_e. While the analysis of the signature of the intensification of field aligned current shows that the clear phase transition pattern during substorm cycle exists for the maximum FAC at the inner boundary of magnetospheric model. The map is complicated for FAC intensification measured locally and there is no clear transition between two phases.

In summary, the global MHD simulation results show both global coherent and multi-scale behavior, which have been observed in the real system. This affirms that the global MHD model is an invaluable tool in studying magnetospheric science and predicting space weather.

Part IV

Magnetosphere-Ionosphere

Coupling

Chapter 6

Modeling Magnetometer and Riometer Observations from Global MHD Simulations

6.1 Overview

The magnetospheric response to solar wind is often measured in the ionosphere, using networks of magnetometers, riometers, and radars. An extensive database on substorm activities is obtained from ground-based measurements. Modeling magnetosphere-ionosphere coupling and comparison with ionospheric observations plays an important role in understanding how the solar wind drives the magnetosphere and the ionosphere to produce phenomena observed by means of ground measurements.

As introduced in Chapter 2, the global MHD model, which uses the solar

wind data to drive the evolution of the magnetosphere, provides a link between the solar wind and the ionosphere. In the global MHD model, the main LFM code is complemented with extensive output modules that allow comparison with measurements. Figure 7.1 shows the structure of the complete model including subsidiary codes and diagnostic output. An important test of the models is how
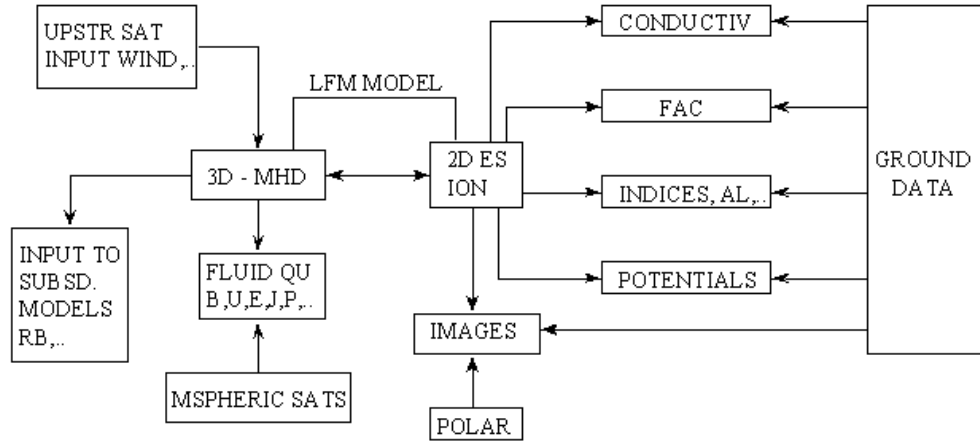
Figure 6.1: LFM model including subsidiary codes and diagnostic output

well they reproduce the ionospheric measurements. In this chapter, we present the models for simulating the observations of riometer and magnetometer from output of the global MHD simulations. The model results are compared with riometer and magnetometer network data for the January 10, 1997 event.

The development of the models for simulating riometer and magnetometer data and comparison with the actual observations guided us to validate and improve our model and achieve better understanding of the magnetosphere-

ionosphere coupling. Riometers measure the changes in the absorption of very high frequency (VHF) radio signals of galactic origin passing through the ionosphere [*Rosenberger et al.*, 1991]. As we will show in section 6.4.2, the preliminary model results of the code was inconsistent with riometer data. This leads us to identify the causes of the discrepancy and improve the appropriate part of the model. We find that turbulent heating due to electrojet instabilities is important in calculating the ionospheric absorption. In view of this, we develop a model that describes the temporally and spatially averaged electron temperature, based on non-linear physics considerations and comparison with available radar observations of the electron heating. The model improved agreement greatly with the riometer observations. In current model, no feedbacks are provided to the global MHD dynamical model.

Magnetometers monitor the perturbations in the ground magnetic field produced by the ionospheric currents and the induced ground current. For the simulation of magnetometer data, we have developed a model using the computed ionospheric current density distribution and the height dependence of the electrojet (determined by the energy of precipitating electrons), to calculate the perturbed magnetic field by implementing Biot-Savart's law. This model including height dependence of the current layer on precipitating electron energy reduces by 10 percent the error compared to the model with fixed current sheet height.

6.2 Physics of Signatures

6.2.1 Riometer Observations

Since its development in the 1950s, the riometer [*Little and Leinbach*, 1958, 1959] has been used primarily to measure the changes in the absorption of cosmic radio noise within the ionization region of the polar atmosphere. During magnetospheric substorms, the density and energy of the precipitating electrons entering the ionosphere are enhanced. These fast precipitating electrons collide with and ionize neutrals. An ionization layer is formed about 110 km above the ground and the electron density within it is enhanced during substorms. The exact altitude of the ionization layer depends on the precipitating electron energy. The enhanced electron density within the ionization region of the polar atmosphere leads to increased attenuation of very high frequency (VHF) radio signals of galactic origin [*Rosenberg et al.*, 1991]. The radio signals used by riometers are typically in the 20–50 MHz range. The absorption of cosmic radio noise in the ionosphere depends on the height integrated electron density and temperature in the lower ionosphere and provides a measure of the ionospheric conductivity. A strong increase in auroral absorption during a substorm is often associated with the intensification of the auroral electrojet [*Hudson et al.*, 1999]. Therefore, riometer observations are a good indicator of substorm activity. Absorption data used in this chapter were measured by an array of imaging

riometers in polar region developed at the University of Maryland [*Detrick and Rosenberg*, 1990]. The VHF signal is of frequency 38 MHz.

6.2.2 Magnetometer Observation

Magnetometers monitor the perturbations in the ground magnetic field which is produced by the ionospheric current and the corresponding induced imaging ground current. During magnetospheric substorms, the ionospheric current is affected in two ways to accommodate the enhanced energy input from the solar wind via increased dissipation [*Kamide and Baumjoham*, 1993]. One is through the increase of the Hall current flow in the covection auroral electrojets, which is directly related to the energy input from the solar wind along with the driven process. Additionally, sporadic unloading of energy previously stored in the magnetotail leads to the formation of a substorm current wedge with strongly enhanced westward current flow in the midnight sector. Therefore, a chain of ground magnetometers is very useful to record the ionospheric response to the substorm activities.

6.3 Introduction to Computational Models

6.3.1 Modeling Riometer Observations

The detailed computational model for simulating riometer observations is developed in Appendix A. Here, we briefly outline the relevant parts. In the model, we consider the ionospheric absorption of VHF signals caused by a thin plasma layer, produced by ionization due to precipitating electrons. The uniform ionospheric layer is with thickness $\triangle z$, electron density n_e, neutral density N_n, and electron temperature T_e. The modeled VHF absorption in dB is given by Eq. (A.3). We repeat here for reference.

$$A = 8.7 \times 10^{-18} n_e (cm^{-3}) N_n (cm^{-3}) \Delta z (km) f (MHz)^{-2} (T_e/300K)^{5/6}. \quad (6.1)$$

The output of the LFM model provides the key local quantities: the characteristic energy ε and the flux Φ of the precipitating electrons along with the electric field $\mathbf{E}$. In order to compare the riometer observations with the LFM output, we need to connect the values of n_e, N_n and T_e with ε, Φ and $\mathbf{E}$. Using the characteristic energy ε and flux Φ of precipitating electrons from the LFM model, we obtain the energy deposition height, the neutral density at this altitude, and total energy flux released by the precipitating electrons. Next, we compute the electron density inside the ionized layer along with the electron-neutral collision frequency for cold electrons. The resulting absorption is given by Eq. (A.11)

and is reproduced here,

$$A(dB) = 8.5\varepsilon_{keV}^{2.25} f_{MHz}^{-2} (\frac{\Phi}{\Phi_0})^{1/2} (\frac{T_e}{300K})^{4/3}.$$ (6.2)

In the preliminary model, we use constant electron temperature $T_e = 350$ K. As we can see in section 6.4.2, for the January 10, 1997 event, the results of the model were totally inconsistent with riometer data. This led to further research to identify the causes of the discrepancy and improve the appropriate part of the model. In examining the times of the discrepancies we realized that they coincided with the times that the electrojet were very large. This led us to hypothesize that instabilities connected with the electrojet might result in turbulent electron heating. The non-linear theory of the modified two-stream instability, also known as the Farley-Buneman instability, was developed by [*Ossakow et al.*, 1975. Later on, *Schlegel and St-Maurice* [1981] using radar observations confirmed that the electron temperature rises significantly (up to 2000–3000 K) in the polar electrojet during substorms. In view of this, using the electric fields **E** in the ionosphere obtained from the LFM model, we develop a model (presented in Appendix A.2) that describes the temporally and spatially averaged electron temperature, based on non-linear physics considerations and comparison with available radar observations of the electron heating. The resulting average electron temperature is calculated using Eq. (A.14). The equation is reproduced here for reference.

$$< T_e > \simeq 1.5 T_0 (E_C/E_{th0}),$$ (6.3)

where T_0 the electron temperature approximately equal to the temperature of neutral particles in the cold (unperturbed) ionosphere, $\mathbf{E_C}$ is the convection electric field and E_{th0}=20 mV/m. The model gives good agreement with the riometer observations.

6.3.2   Modeling Magnetometer Observations

The detailed computational model for simulating magnetometer observations is developed in Appendix B. Here, we briefly outline the relevant parts. In the Lyon-Fedder-Mobbary Global MHD model [*Fedder et al.*, 1995b], at the inner boundary located at $2 - 3R_E$ from the earth, the parallel current density $J_\parallel$ is computed at each time step. This parallel current is mapped into the ionosphere along unperturbed dipole magnetic field lines. The height-integrated current continuity equation yields the perpendicular current density (both Hall and Pedersen) in the ionosphere. *Kisabeth and Rostoker* [1977] had shown how three-dimensional ionospheric current systems associated with magnetospheric substorms can be used to quantitatively evaluate the magnetic field perturbation at any location on the ground by applying Biot-Savart's law. Following a similar approach, we model the perturbations of magnetic field produced at various locations by the 2D ionospheric current system. One important novel feature of our model is to evaluate the instantaneous height of the 2D current system by using the energy of the precipitating electrons to calculate the penetration depth

and hence the position of the auroral electrojet. To account for the contribution of the current induced in the ground, the calculated magnetic field is enhanced by a factor of two. To compare with the observations, the magnetic field is represented in the local coordinate system (H, D, Z), where H is the component that points towards the north magnetic pole, D points eastward and Z points down towards the center of the Earth. We hasten to add that the individual components will be strongly influenced by the local conductivity of the ground which can rotate the polarization of the magnetic field. Thus we have focused on comparing the magnitude of the horizontal component ($\sqrt{H^2 + D^2}$), total field ($\sqrt{H^2 + D^2 + Z^2}$) and Z component with ground-based magnetometer data. Both the model including height dependence of the current layer on precipitating electron energy and the model with fixed current sheet height are applied to the January 10, 1997 event.

6.4 Simulation Results with the January 10, 1997 Magnetospheric Storm Event

6.4.1 January 10, 1997 Magnetospheric Storm Event

On January 10, 1997, a magnetic cloud produced a major geomagnetic storm. This storm was the first solar terrestrial disturbance whose temporal develop-

ment was followed from its solar source and its subsequent effects on the magnetosphere and ionosphere using the entire suite of resources of the International Solar Terrestrial Physics (ISTP) program. The SOHO LASCO experiment observed the CME expanding from the solar surface apparently toward the Earth on January 6. Early on January 10, WIND first observed the (CME associated) magnetic cloud, which produced a complex magnetic storm lasting 22 hours. This storm may have been responsible for the failure of the AT&T Telstar 401 satellite.

Using the LFM global MHD simulations, the group at Maryland (Goodrich, Wiltberger, Lopez and Papadopoulos) in collaboration with J. Lyon from Dartmouth College, simulated the January 10-11, 1997 storm event. The simulation was initialized using upstream WIND satellite data. Forty-eight hours of real time development of the geomagnetic activity in the magnetosphere and ionosphere were simulated. The results of the 3D MHD simulation of this event and its consequence on the magnetosphere and ionosphere have been presented in *Goodrich et al.* [1998a, 1998b]; *Papadopoulos et al.* [1999] and *Lopez et al.* [1999]. The simulation results agreed well with ground-based and geosynchronous satellite observations. They showed that during the period of southward IMF, the ionospheric activity was strongly correlated with the solar wind density variation. It was concluded that both the solar wind magnetic field and ram pressure are important in determining the structure of the magnetosphere

and the activity in the ionosphere during the Jan. 10-11, 1997 magnetic storm.
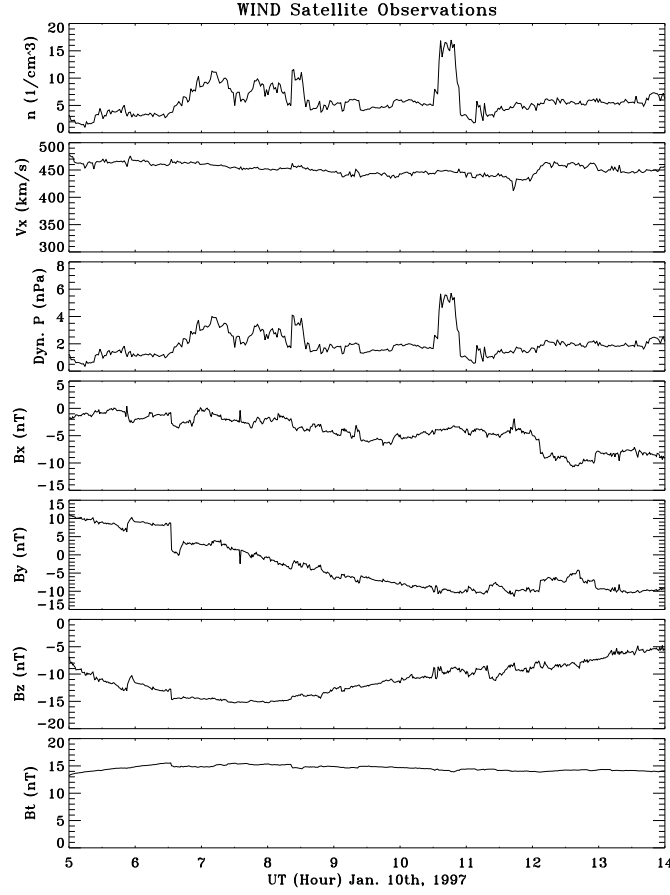
Figure 6.2: Solar wind condition as observed by the WIND satellite on Jan. 10, 1997.

The time period we investigated for modeling riometer and magnetometer observations was from 6:00 UT to 13:00 UT on January 10, 1997. During this interval, the interplanetery magnetic field in the solar wind was mainly southward and quite steady. The ionospheric activity was strongly correlated with the solar wind density variation. Figure 6.2 shows the solar wind condition observed

by the WIND satellite. All the vector components are in GSM coordinates. V_x and V_y are not plotted because they are in the range of -50 km/sec to 50 km/sec. The solar wind velocity is quite steady for the time interval of interest. The solar wind experienced density increases between 6:30 UT and 8:30 UT. There was another large solar wind density pulse around 10:30 UT. Due to the time delay for the solar wind to arrive at the magnetopause from the WIND satellite, and subsequent propagation into the magnetosphere, the two major perturbations observed in the ionosphere triggered by the density pulses occurred in the interval between 7:00 UT and 9:00 UT and around 11:00 UT.

Riometer observations used in comparison are at three high latitude stations: Sondrestrom, Iqaluit and Gakona. Whereas, magnetometer observations used in comparison are at four ground stations: Sondrestrom, Iqaluit, Rankin Inlet and Gakona. The geographic and magnetic coordinates for the four stations used in our comparison are listed in table 6.1.

	Geographic Coordinates		Magnetic Coordinates	
	Lat	Lon	Lat	Lon
Sondrestrom(Greenland)	N67.02	E309.28	N73.35	E41.48
Rankin Inlet (Canada)	N62.82	E267.89	N70.37	E338.92
Iqaluit (Canada)	N63.75	E291.57	N72.09	E14.53
Gakona (Alaska)	N62.41	E214.88	N63.12	E267.25

Table 6.1: Magnetometer Site Coordinates
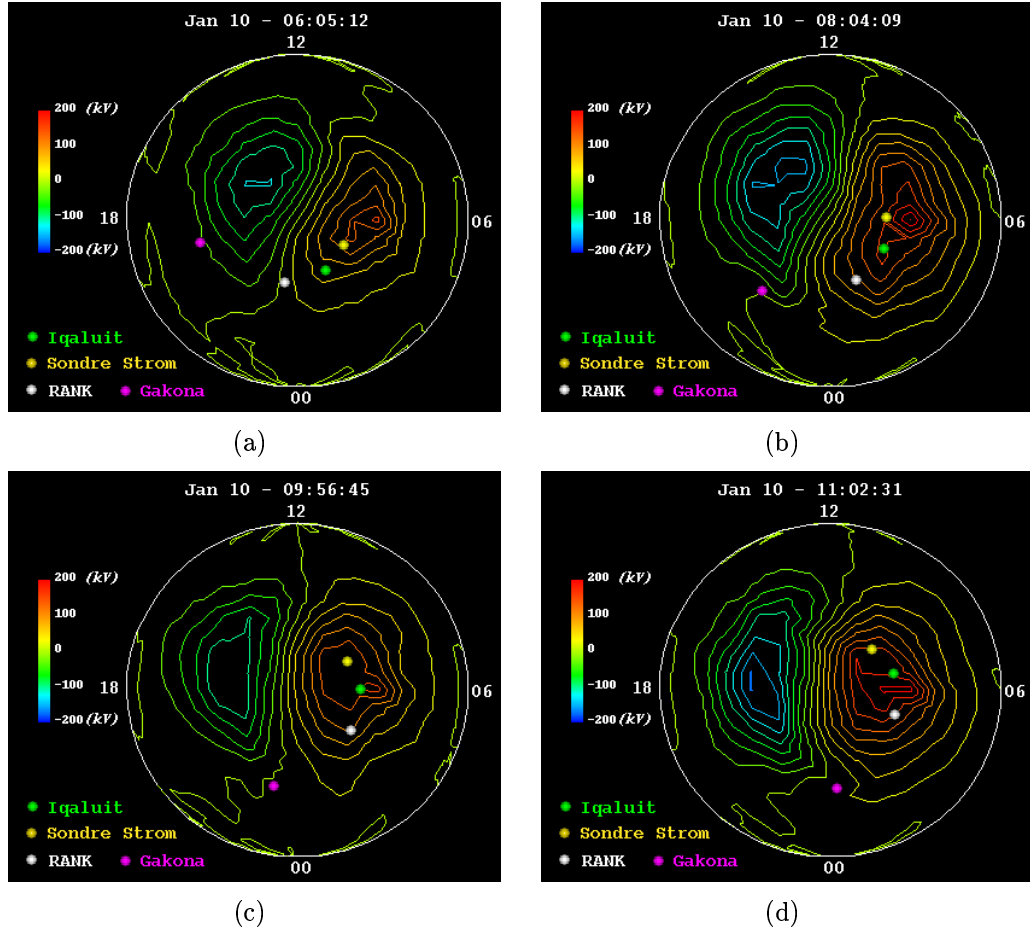
Figure 6.3: Northern polar cap electric potential contours for four time instants from the simulation. The colored ball denotes the location of the four ground stations. The time for each panel is labeled at the top part of the panel. The lower left corner labels the meaning of each colored ball. The adjacent contour is 25 kV apart.

Figure 6.3 shows the northern polar cap potential contour plots obtained from the simulation. The interval between two adjacent potential contours is 25 kV. Since the interplanetary magnetic field is southward, the ionospheric potential contour plots show the characteristic two cells pattern. Four snap shots are picked to present the typical behavior of the ionosphere. The four colored balls

on each panel represents the four ground stations. The color labels at the lower left corner in each panel identifies each ball with one of the four stations. They are Iqualuit (green), Sondrestrom (yellow), Rankin Inlet (white) and Gakona (pink).

As shown in Figure 6.3, at 6:05 UT, due to the long period of southward IMF, the two-cell pattern in the ionospheric is fully developed. The cross polar cap electric potential (Maximum-Minimum) is about 270 kV. AT 8:04 UT, the perturbation due to the increase of solar wind density arrives in the ionosphere. The magnitude of electric potential is enhanced significantly. The cross polar cap potential reaches about 400 kV. The enhancement of ionospheric electric potential lasts until 9:30 UT. At 9:56 UT, the ionosphere electric potential recovers from the perturbation. During this time period, the solar wind conditions are roughly steady for about one hour. The large density pulse at about 10:30 UT observed by WIND satellite has its effects in ionosphere at about 11:00 UT. The panel for 11:02 UT shows the corresponding enhancement of ionospheric potential. For the four magnetometer sites, Gakona is at low SM latitude and remains mainly on the night side sampling the overhead current associated with the negative potential cell and subsequently the positive cell. Also during the entire period, this station is at the boundary of the auroral oval. On the other hand Sondrestrom, Iqaluit and Rankin Inlet sample the current mainly for the positive potential cell.

6.4.2 Comparison with Riometer Observations

Figure 6.4: Temporal evolution of the VHF absorption for f = 38.2 MHz observed during January 10 event at the three locations of interest (solid traces) along with computations made by keeping the electron temperature constant, Te=350 K, (dashed traces).

Figure 6.4 shows the VHF absorption measured by the riometers at the three locations (Sondrestrom, Iqaluit and Gakona) during January 10 1997 (solid trace) along with the model results computed by neglecting the anomalous electron heating and assuming constant electron temperature T_e= 350 K (dashed trace). The two intervals of increases in the VHF absorption are caused by the solar wind density pulses. As we can see, the results of the model were totally inconsistent with riometer data. The discrepancies coincided with the times that the

191

electrojet current was very large. This led us to hypothesize that instabilities connected with the electrojet might result in turbulent electron heating.

In order to validate the model we developed in Appendix A.2 for calculating bulk electron temperature due to turbulent heating using the ionospheric electric field, we compare our results with recent observations by *Schlegel and Collis* [1999], made with the EISCAT facility during the storm of January 10, 1997. The values of T_e and $\mathbf{E_C}$ (convection electric field) presented in the paper were both measured over the EISCAT area.
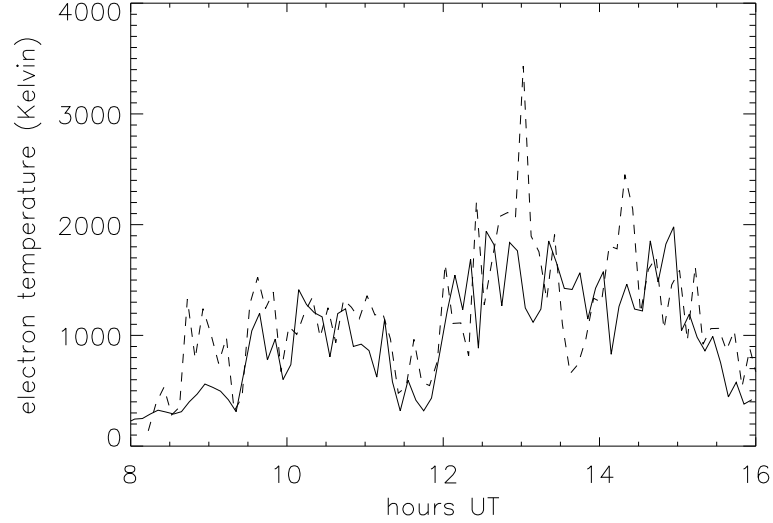
Figure 6.5: Temporal evolution of the modeled electron temperature (dashed line) computed with Eq. (6.3) using the EISCAT measurements for the convective electric field $\mathbf{E_C}$ for the January 10, 1997 substorms along with the electron temperature directly measured by EISCAT (solid line).

Figure 6.5 shows the temporal evolution of the modeled electron temperature $< T_e >$ (dashed curve), computed with Eq. (6.3) using the EISCAT measurements for the convective electric field $\mathbf{E_C}$. This model result is plotted against

the electron temperature directly measured by EISCAT (solid curve). We see
that the linear dependence of $< T_e >$ upon $\mathbf{E_C}$ agrees reasonably with the ob-
servational data, except for the time around 13:00 UT and 14:30 UT when the
strong heating cannot be described by the linear approximation applied. The
radar observations [*Schlegel and St-Maurice*, 1981; *Jones et al.*, 1991] reveal that
the electron temperature can be described by Eq. (6.3) with the numerical co-
efficient ranging between 0.9 and 2.3 for the altitudes 100–120 km. It increases
with the altitude as the collisional losses reduce. In this thesis, we will use the
simple approximation of Eq. (6.3) for the following estimates of the electron
temperature.
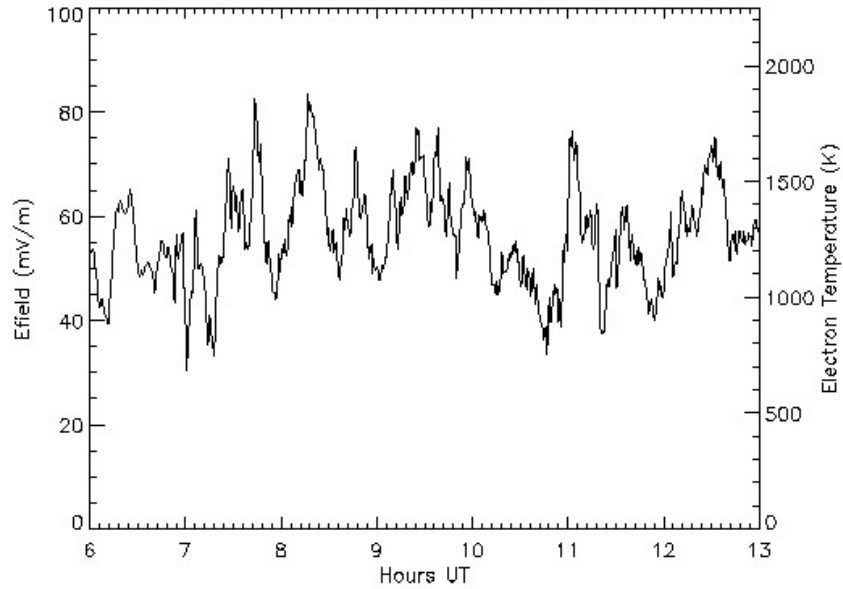
Figure 6.6: Temporal evolution of the electric field and averaged electron tem-
perature computed for Jan. 10 event at Iquluit location.

Figure 6.6 shows an example of the temporal evolution of the electric field computed by the LFM model at Iqaluit during the substorms on Jan. 10, 1997 along with the values of the electron temperature computed by Eq. (6.3).
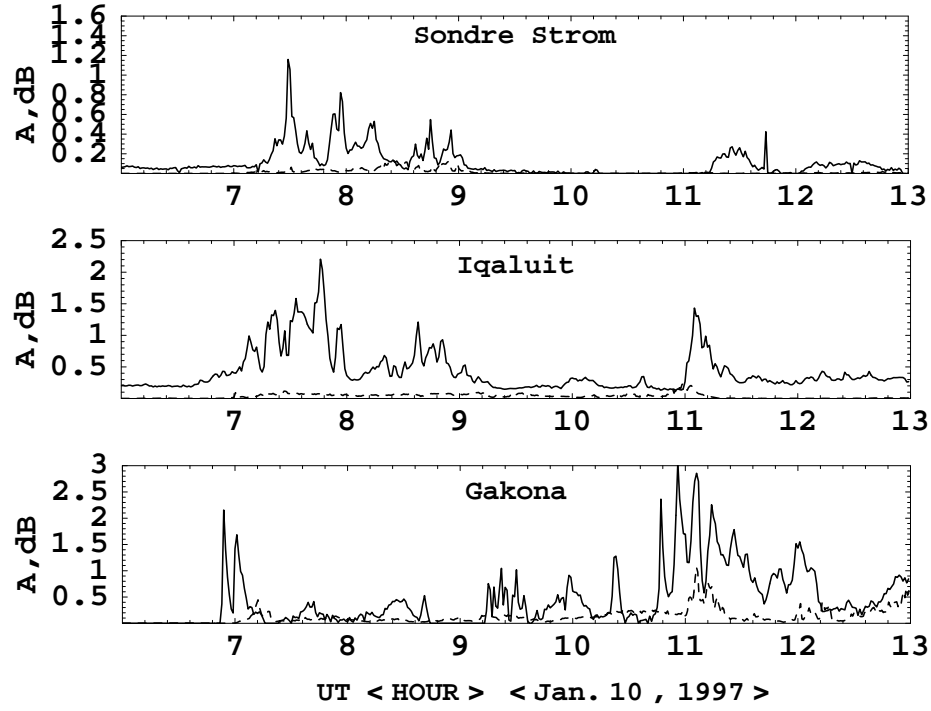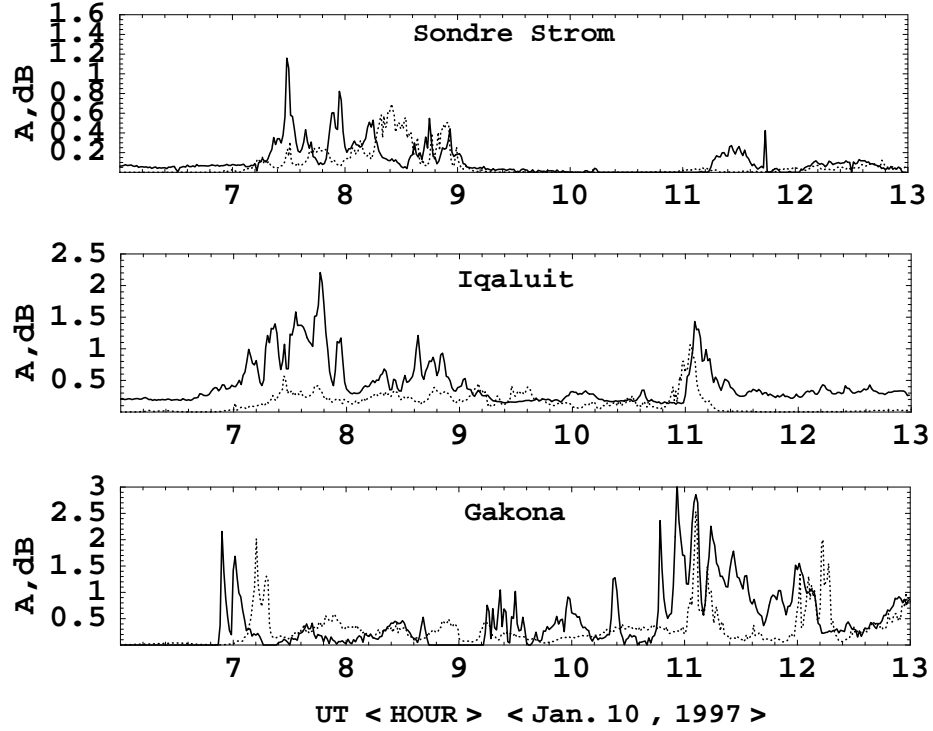

Figure 6.7: Temporal evolution of the VHF absorption for f = 38.2 MHz observed during January 10 event at the three locations of interest (solid traces) along with computations made by considering anomalous heating (dotted traces).

Figure 6.7 shows the measured VHF absorption (solid trace) along with the model results taking into account the anomalous electron heating (dotted trace). When anomalous heating is taken into consideration the agreement between the computed VHF absorption and observations improves considerably.

There are many features of the model that are responsible for the limited agreement of its results with the observations and some of these are as follows.

Many of the observed details of the observations, such as at Gakona at 09:15–10:30 UT could be produced by a local arc, which cannot be obtained by the MHD model with 400 km spatial resolution. In the LFM model the energy of precipitating electrons does not exceed 20 keV, which corresponds to the penetration altitude in excess of 95 km. Thus the model neglects the changes in absorption which occur in the ionosphere below 95 km. This may lead to an underestimate of the total absorption, as is seen in the top two panels of Figure 3 corresponding to the higher latitude stations. During the long period of strong southward IMF, which is the case for the time interval of interest on January 10, realistic ring current model which is absent in global MHD model becomes important. The absence of ring current model also accounts for the underestimate of the total absorption. Also some mismatch in the timing between the model and observations are apparent, especially for the low latitude Gakona case. The spatial resolution of 400×400 km in the model is equivalent to a temporal resolution of 15 min due to the rotation of the Earth, and thus a mismatch of this magnitude is inherent in the model. While the agreement between the model results and observations are not high enough to be usefully quantified in terms of correlation coefficients, it brings out new features such as the role of anomalous electron heating.

6.4.3 Comparison with Magnetometer Observations

In present study we have focused on comparing the time history of the perturbed horizontal, total and Z component of the magnetic field computed using our model, to the data from magnetometers at four high latitude stations: Sondrestrom, Iqaluit, Rankin Inlet and Gakona.
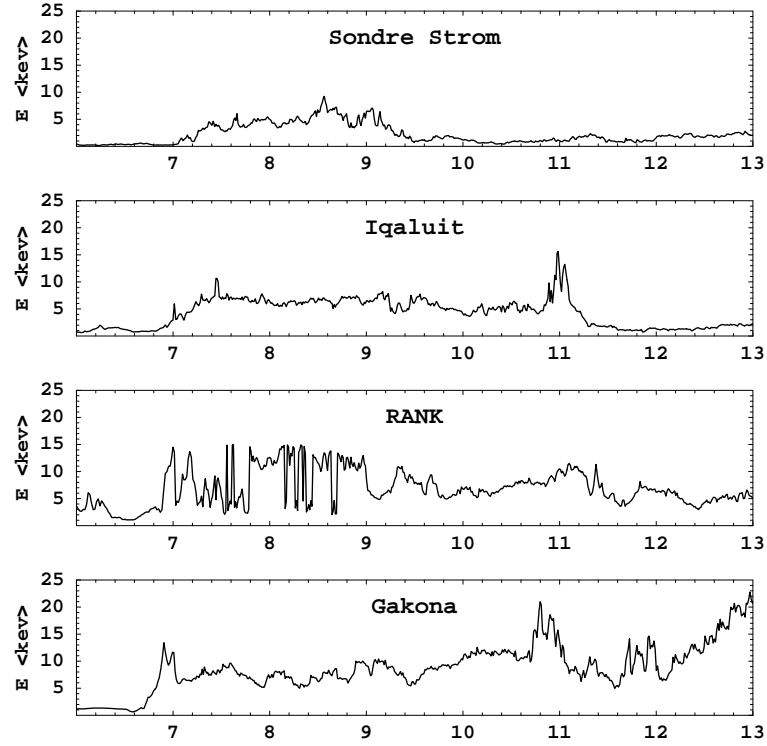
Figure 6.8: Time history of precipitating electron energy as simulated right above the four stations. The horizontal axis is UT (Hour since Jan. 10th, 1997).

Applying the model developed in Appendix B, we calculate the magnetic field perturbations at the four magnetometer sites. Figure 6.8 shows the energy of precipitating electron as simulated from the global MHD model at sites right

above the four locations we are interested. The precipitating electron energy is less than 20 keV. The time interval when the increase in precipitating electron energy is observed is well correlated to the period when the solar wind density pulse occurs. The derived penetration altitude above the four locations is
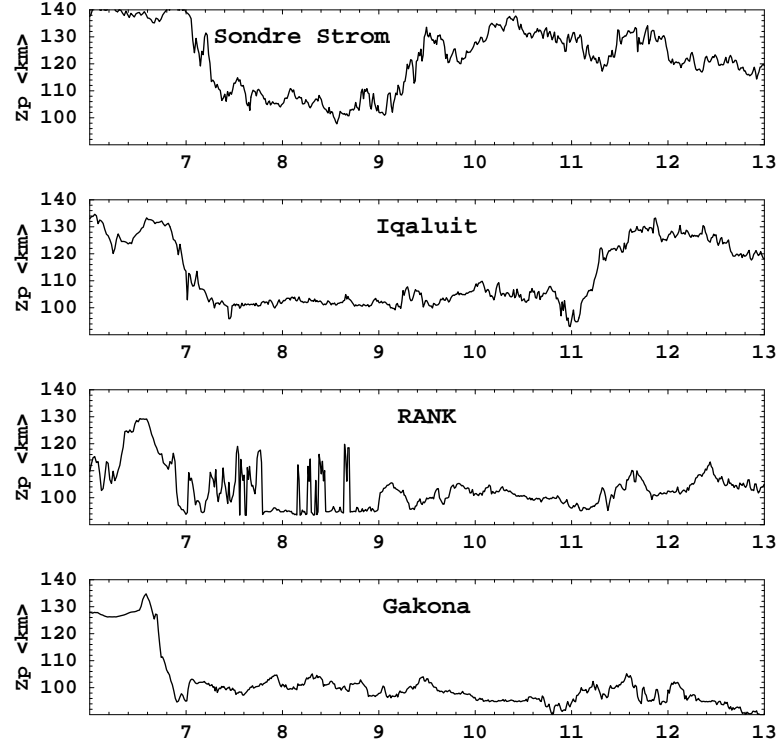
Figure 6.9: Time history of penetration altitude as simulated right above the four stations. The horizontal axis is UT (Hour since Jan. 10th, 1997).

presented in Figure 6.9. During the quiet time, the penetration altitude is around 130 km and for the active time interval, the penetration altitude is around 100 km.

Figures 6.10-6.13 show the comparisons of the magnitude of the horizontal component ($\sqrt{H^2 + D^2}$), total ($\sqrt{H^2 + D^2 + Z^2}$) and Z component perturbed
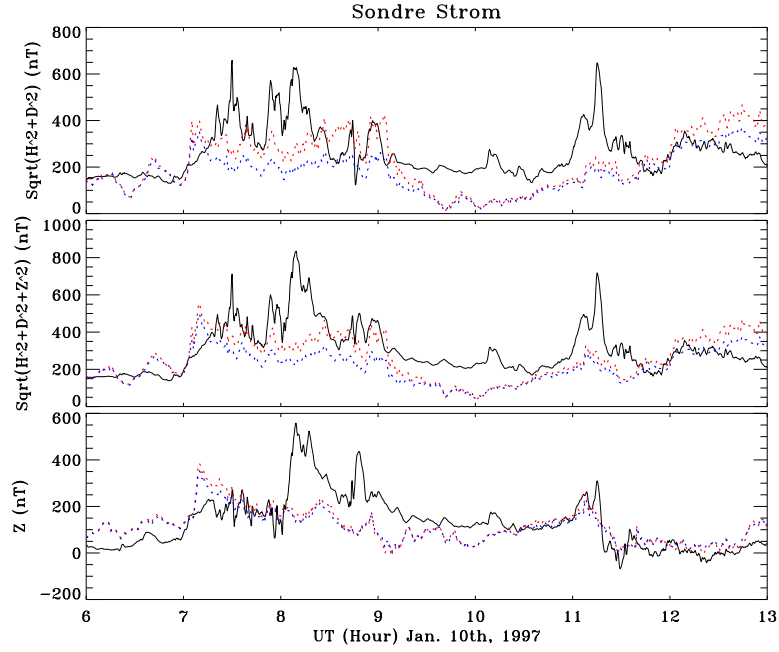
Figure 6.10: Comparison of the horizontal, total and Z component perturbed magnetic field between simulations and observations for Sondre Strom. The black curve is from observation; the red dotted curve is from simulation with current sheet height-dependent model and the blue dotted curve is from simulation with fixed height model.

magnetic field all in nT between observations and simulations for different locations. In each of these figures we show the time history of the magnetometer data (black), the numerically computed data without the time-varying height-dependence of the electrojet current (blue dotted line) and the numerically computed data with the height-dependence included (red dotted line). The original simulated results for Gakona lagged behind the observations for about 15 minutes. We searched inside the 400kmx400km grid cell and Figure 6.13 presents the closest match.

The overall magnitude of computed magnetic fields is in reasonable agree-

198
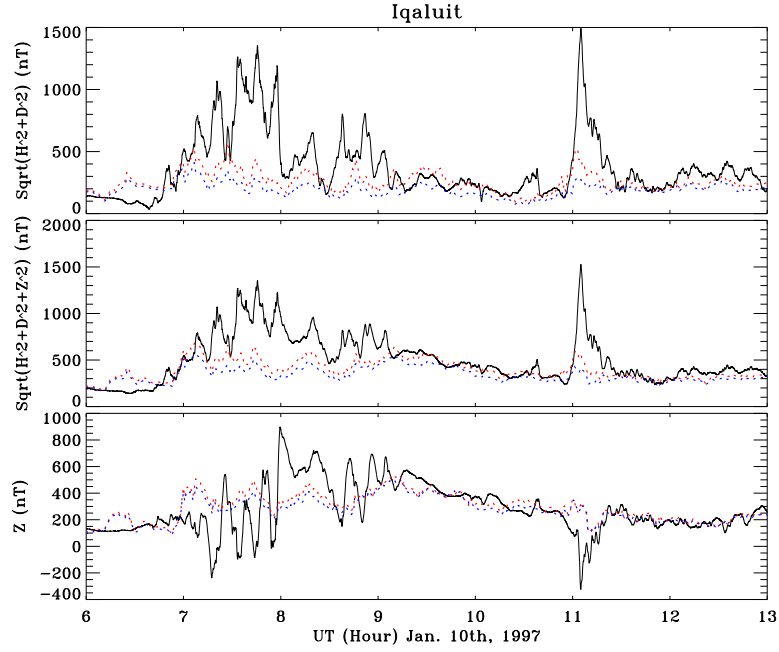
Figure 6.11:   Similar comparison as in Figure 7.6 for Iquluit.

ment with magnetometer data for both horizontal and total perturbed magnetic field. For Sondrestrom, Iqualuit and Rankin Inlet, the comparisons show good agreement with observations for both horizontal and total perturbed magnetic field. The magnetic field perturbations due to the two solar wind density pulses which occurred between 7:00 UT and 9:00 UT and around 11:00 UT are captured at these three sites and agree well with observations. But the calculated magnitude is smaller for these perturbations, especially around 11:00 UT. We speculate that, due to the lack of realistic ring-current model in global MHD code, the region 2 current is not well developed in the model. Thus, the modeled ground magnetic field perturbations isn't large. In other words, the direct
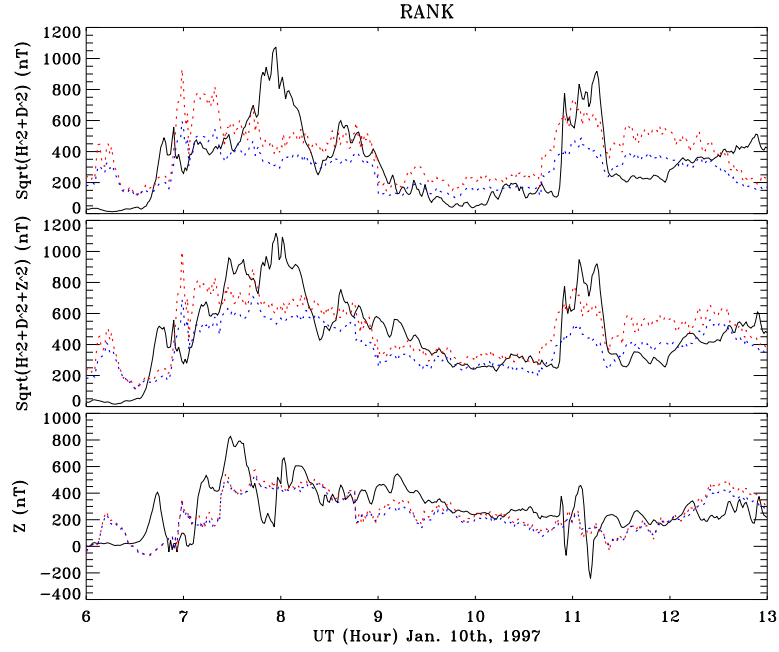
Figure 6.12: Similar comparison as in Figure 7.6 for Rankin Inklet.

effects of the density pulse in the solar wind on the magnetosphere is the enhancement of the day side reconnection, the compression of the magnetosphere and the subsequent enhancement of the tail lobe reconnection. All of these effects contribute to enhance the field aligned current which feeds into ionosphere. This is simulated by the global MHD model. The region 2 current is expected to be enhanced and be closed with ring current in the magnetosphere. But, in global MHD model, the ring-current is not included and region 2 current isn't fully developed. Therefore, the modeled total ionospheric current isn't large enough to produce the observed magnitude of the perturbations.

For the Z component, the model can only capture the average trend of vari-

200
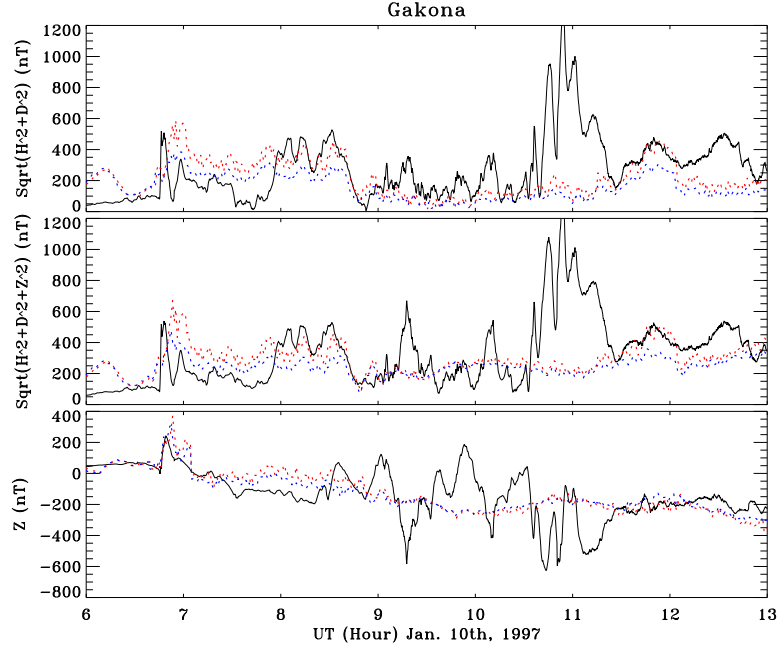
Figure 6.13: Similar comparison as in Figure 7.6 for Gakona.

ation for Sondrestrom, Iqaluit and Rankin Inlet. The simulated Z component

misses the variations shown in the observation for the time interval from 7:00 UT

to 9:00 UT. It captures some signatures of the variation that occurred around

11:00 UT. The comparison for Z component magnetic field doesn't seem to be as

good as that for $\sqrt{H^2 + D^2}$ and $\sqrt{H^2 + D^2 + Z^2}$. This is because the calculation

of the Z component of the magnetic field is affected more by the limited reso-

lution of the ionosphere model than the horizontal component of the magnetic

field. In our calculation, the current in the overhead grid cell produces mainly

horizontal magnetic field perturbations. The Z component of the magnetic field

is produced by the ionospheric currents in the grid cells which are further away

from the ground station. With current resolution of grid size 400km x 400km, assuming uniform current in the overhead grid smoothes the current and excludes any localized feature which may contribute to the perturbation of the Z component of the magnetic field.

There are fine structures of duration 10-15 minutes in the magnetometer data. These spikes are of large magnitude. Global MHD simulation is unable to capture these features. We speculate that they could be produced by local auroral arcs, which are not present in the global MHD ionospheric model. Besides this, some mismatch in the timing between the model and observations is apparent. The agreement is poor for Gakona which is located at a low SM latitude (N63.12). The observed large perturbations occurring around 11:00 UT is totally missed. It could be produced by local auroral arc. Our calculations show a perturbation occurring around 11:40 UT. This is the simulated consequence of the second solar wind density pulse. Gakona is near the lower boundary of the ionospheric model and the non-uniform grid size is larger compared to that at high latitude (see Figure B.2). Thus, the reduced resolution and boundary condition leads to worsening the comparison between the observed and the calculated data.

However in spite of these limitations, the model does reasonably well in predicting the perturbations of the ground magnetic field.

In order to compare the performances of the model including height dependence of the current layer to the model with a fixed current sheet height, we

define the root mean square error (R.M.S.E.) as the error measure of our prediction.

$$R.M.S.E. = \sqrt{\frac{\sum(X_{simu.} - X_{obser.})^2}{N}} \tag{6.4}$$

Here, X is the one of the components of the ground magnetic field perturbations. N is the data points in the interval from 6:00 UT to 13:00 UT on January 10, 1997. The resulting error ratio between these two models is tabulated in Table 6.2.

	Error Ratio for		
Ground Station	$\sqrt{H^2 + D^2}$	$\sqrt{H^2 + D^2 + Z^2}$	Z
Sondre Strom	0.88	0.86	0.99
Rankin Inlet	1.02	0.97	0.99
Iqaluit	0.84	0.83	1.00
Gakona	0.94	0.97	1.05

Table 6.2: Root Mean Square Error (R.M.S.E.) ratio between height-dependent model and fixed-height model for $\sqrt{H^2 + D^2}$, $\sqrt{H^2 + D^2 + Z^2}$ and Z components of the ground magnetic field perturbations.

For Sondre Strom and Iqaluit, the inclusion of the height dependence improves the comparison with the ground data for horizontal and total magnetic field. The error ratio is reduced by more than 10 percent. For Z component, including height dependence doesn't improve the prediction. In our calculation, the Z component of the ground magnetic field perturbation is produced by the

grids which are not right above the station and these grids' distance to the ground station is less affected by the current sheet height. For Rankin Inlet, we note that the poor performance of the height-dependent model mainly appears after 11:30 UT. But neither of the models compares well with observations after 11:30 UT. If we change the time interval to from 6:00 UT to 11:30 UT and calculate the error ratio, then the error ratio between height-dependent model and height-fixed model for Rankin Inlet is 0.98 for $\sqrt{H^2 + D^2}$ component, 0.89 for the total magnetic field and 0.96 for the Z component. The error is reduced by 10 percent with the height-dependent model for the total magnetic field. For Gakona, the comparison itself is poor, we don't expect the height-dependent model to improve the results.

6.5 Conclusions

The comparison between the simulated and observed riometer data for the January 10, 1997 event shows that anormalous electron heating is important in calculating ionospheric absorption. Many features of the temporal variations of computed absorption are consistent with that measured by the riometers. The magnitude for VHF absorption are comparable between model and observations. In many instances the model resolution cannot describe the fine structure of the high frequency radio wave absorption, which could be produced by patchy or arc-like structures of smaller scale. The absence of ring current in MHD model

accounts for the underestimate of the magnitude of the riometer data in the simulation for the January 10, 1997 event.

Currently the MHD model neglects the effect of turbulent electron and collisional ion heating by the ionospheric electric field. However, the inclusion of the turbulent electron heating leads to a much better agreement of the simulations with the actual values of integrated absorption at the three riometer locations. We expect that inclusion of anomalous collision frequency into the ionospheric conductance could improve the model by providing feedback between the model ionosphere, serving as a dynamic boundary condition, and the 3–D global magnetospheric simulations.

The comparison between the simulated and observed magnetometer data shows reasonable agreement between observations and simulations. The model including height dependence of the current layer reduces by 10 percent the error compared to the model with a fixed current sheet height. Due to the lack of realistic ring current model, the modeled magnetic field perturbations during active storm period are of smaller magnitude than the observations. The limitations of the global MHD model in calculating ground observed perturbed magnetic field are also discussed. This model therefore expands the capability of global MHD simulation to simulate individual ground magnetometer observation.In the future, the comparison with magnetometer data will help us to improve the global MHD model and to incorporate a realistic ring current and

ionospheric conductance model.

Part V

Summary

Chapter 7

Summary

Variations in the solar wind plasma density, flow velocity, and, most important, the direction of the interplanetray magnetic field cause significant changes throughout the Earth's magnetosphere, ionosphere and on the ground [*Baker et al.*, 1998]. With more satellites launched in space and more comprehensive networked ground-based measurements, understanding and predicting the geospace environment becomes more and more important and feasible.

With the advent of advanced scientific computing, three-dimensional global magnetohydrodynamic (MHD) model proved to be a powerful approach for the study of the magnetosphere-ionosphere system driven by the solar wind. The objective of this thesis is to use the LFM global MHD model to investigate and understand the physical properties of the Earth's magnetosphere, its coupling with the ionosphere and to further expand the capability of the global MHD model in actual event simulations. Specifically, this thesis studied three topics

in magnetospheric physics:

- **Steady state Earth's magnetosphere with northward IMF**

- **Magnetospheric substorms**

- **Magnetosphere-ionosphere coupling**.

These three topics provide a comprehensive coverage for using global MHD model to study magnetospheric physics. Through extensive studies of the Earth's magnetosphere, the overall conclusion is that the LFM model is an invaluable tool in studying magnetospheric sciences and predicting space weather. In the next, we summarize the conclusions for each topic.

7.1 Steady State Earth's Magnetosphere with Northward IMF

The structure and magnetic topology of the magnetosphere under steady northward IMF is one of the fundamental problems in magnetospheric physics. Global MHD simulations play an important role in this study. There have been longtime arguments in the community of global MHD modeling about whether the Earth's Magnetosphere during steady northward IMF should have a long or short tail for a standard case (reaching steady state with constant solar wind density= 5 1/cc, B_Z= 5 nT and V_{SW}= 400 km/sec). Our present work found a short tail

configuration (tail length $\sim 40~R_E$) for the standard case, which is consistent with the results of *Gombosi et al.*, [1998], *Song et al.*, [1999] and *Bargatze et al.* [1999]. In this thesis, we have focused on understanding the physical properties of the steady state Earth's magnetosphere. We also discussed about the long tail configuration obtained by *Berchem et al.* [1995] and *Raeder et al.* [1995]. The differences between our present work and the earlier results of *Fedder and Lyon* [1995] were clarified by addressing the issue of transients and plasma preconditioning. Furthermore, we studied the three-dimensional configuration of the steady state and ionospheric polar cap potential pattern. Cusp region reconnection and ionospheric four-cell convection pattern were clearly seen in our simulations. We observed the concave shape of the steady state magnetosphere in our simulation, which has been predicted by the phenomenological analysis of *Song et al.* [2000].

To understand the steady magnetosphere with northward IMF and its scaling with input parameters, we varied the solar wind parameters: (1) the magnitude of the interplanetary magnetic field B_{IMF} and (2) the magnitude of the solar wind velocity V_{SW}. We demonstrated that the ionospheric conductance is a minor effect in determining the steady magnetotail size. Only, the transient behavior is influenced by the conductance. We numerically developed the dependence of characteristic magnetospheric spatial scale sizes on the strength of the solar wind and the IMF. Based on conservation of flux and force balance, simple analytical

models were derived to interpret the parametric dependences of the scaling of the tail on solar wind conditions and are summarized as following:

1. The cross-equatorial area $A_{CE} \propto 1/B_{\mathrm{IMF}}$. The cross-tail area A_{CT} measured near the cusp region at $x \approx$ -10 R_E is also found to decrease with the increase in B_{IMF}. In that region, since the field in the tail is dominantly the dipole field, our simple model indicates that $A_{CT} \propto 1/B_{\mathrm{IMF}}^{1/3}$.

2. In general, with higher solar wind velocity the radius of the tail cross section is smaller, and the tail length is longer. The cross tail area A_{CT} measured at $x \approx$ -10 R_E is proportional to $V_{SW}^{-0.4}$.

3. The area A_n on the nightside for the newly reconnected flux through the equatorial plane (along the coast of the concave bay) increases with the increase of V_{SW} and decreases with the increase of B_{IMF}. Our model based on the balance between the adding of flux at the dayside and the peeling off of flux on the night side shows that $A_n \propto \frac{\sqrt{\rho}V_{SW}}{B_{IMF}}$, which is consistent with the simulated dependence.

Furthermore, we studied the structure of the magnetosphere and its dependence on different solar wind conditions. The parametric dependences of 1D cut of various tail plasma and field quantities along X axis and Z direction at x= -10 R_E, y= 0 R_E were analyzed. The simulations show that during the steady state, inside the tail, in the region x<-20 R_E on the equatorial plane, the magnetotail field B_z is comparable to the solar wind magnetic field B_z and the tail field B_x is nearly 0. The steady 3D current sheet profiles as modeled from global MHD

simulations were also presented.

An actual northward IMF event which occurred on Feb. 9, 1995, is simulated and the results are compared with the Geotail satellite observations. We found that the time scale for the temporal evolution and magnitude of the various components of the field from our simulation are in excellent agreement with those observed by the Geotail satellite. This supports our model of the evolution of the magnetosphere to steady state during northward IMF. Thus the global MHD code provides a very reliable comparison of the northward IMF steady state since the final dynamic equilibrium state depends on general global force balance.

7.2   Magnetospheric Substorms

Because of their relevance to massive global energy loading and unloading, lots of observations and studies have been made for magnetic substorm events. In this thesis, we simulated and analyzed an ideal substorm with the LFM global MHD model. The ideal substorm is initiated by a sudden northward-southward IMF turning. This study serves as a pictorial review of the typical behavior of the Earth's magnetosphere and ionosphere during substorms as simulated with the global MHD model. The results showed auroral onset and expansion, AL index dipping, dipolarization, current sheet disruption, formation of the substorm current wedge and formation and ejection of plasmoid created by the neutral

line. There are flow channels penetrating into the inner magnetosphere and connecting the mid-tail and inner-tail region, which supports the observations that auroral activities originate from the inner magnetotail. The simulation captures the essential features of the substorm.

Then, we studied the statistic features of substorm dynamics using nonlinear dynamical techniques. [*Sitnov et al.,* 2000] propose that the global coherent and multi-scale aspects of the magnetospheric behavior during substorms can be reconciled in terms of non-equilibrium phase transition. We investigated whether the simulated substorms produced in global MHD model have the non-equilibrium phase transition-like features as revealed by *Sitnov et al.* [2000]. We used the LFM global MHD model to simulate 6 intervals of total duration of 240 hours from the same data set used in [*Sitnov et al.,* 2000, 2001]. We analyzed the input-output (vB_s–pseudo-AL index) system as obtained from global MHD model and compare the results to those in *Sitnov et al.* [2000, 2001]. The analysis of the coupled vB_s–pseudo-AL index system derived from the global MHD simulations shows the first-order phase transition map, which is consistent with the similar map obtained for real system from *Sitnov et al.* [2000, 2001]. The overall global transition pattern during the substorm cycle revealed by Singular Spectrum Analysis (SSA) is consistent between simulations and observations. The procedure of phase transition analysis using SSA has revealed essentially the same features of global configuration change both in the real system and in

the global MHD simulations.

The coupled vB_s–pseudo-AL index system derived from global MHD simulations shows multi-scale behavior (scale-invarianet power-law dependence) in singular power spectrum. We found critical exponents of the non-equilibrium transitions in the magnetosphere, which reflect the multi-scale aspect of the substorm activity, different from power-law frequency and the scale spectra of autonomous systems. The exponents relate input and output parameters of the magnetosphere and distinguish the second order phase transition model from the self-organized criticality model.

7.3 Magnetosphere-Ionosphere Coupling

We developed models that use the output of the global MHD model to simulate riometer and magnetometer observations, which we applied to the January 10, 1997 magnetospheric storm event.

Riometers measure the changes in the absorption of very high frequency (VHF) radio signals of galactic origin passing through the ionosphere [*Rosenberg et al.*, 1991]. We developed a model to simulate riometer observations using global MHD simulation output. We found that turbulent heating due to electrojet instabilities is important in calculating the ionospheric absorption. In view of this, we developed a model that describes the temporally and spatially averaged electron temperature, based on non-linear physics considerations and compari-

son with available radar observations of the electron heating. The model gives good agreement with the riometer observations.

Magnetometers monitor the perturbations in the ground magnetic field produced by the ionospheric current and the induced ground current. For the simulation of magnetometer data, the model uses the computed ionospheric current density distribution and the height dependence of the electrojet (determined by the energy of precipitating electrons), to calculate the perturbed magnetic field by implementing Biot-Savart's law. The model including height dependence of the current layer on precipitating electron energy reduces by 10 percent the error compared to the model with fixed current sheet height. The limitations of the global MHD model in calculating ground observed perturbed magnetic field were also discussed.

Modeling ionospheric measurements from global MHD simulation and comparison with ionospheric observations plays an important role in understanding magnetosphere-ionosphere coupling and validating and improving the code.

7.4 Implications to Future Work

The ultimate objective of the space weather program is the development of a suit of operational models that can reliably predict, as far in advance as possible, the effect of solar activity on the technological infrastructure. First-principles magnetospheric modeling such as global MHD model constitutes the most ma-

ture aspect of the space weather chain. The advanced state of the art in this area is due to the synergistic theory-observation approach of the International Space Terrestrial Program (ISTP), in which the consortium led by the space physics group at the University of Maryland played a central role. Currently, the global MHD model does not account for plasmasphere, ring current, ionospheric neutral winds and coroation electric field. These processes are expected to have the greatest effect on the inner magnetosphere and will be the focus of out future work. The actual ring current consists of trapped particles. Some of the trapping is due to the co-rotation electric field. The bulk, however, is due to the gradient and curvature drifts of the ring current particles, which are larger than the convective drift. Development of a realistic ring current module and its incorporation in the model will enable the LFM model be the workhorse on the magnetospheric aspects of the space weather project.

Energetic electron fluxes in the outer zone are observed to vary over orders magnitude, and exhibit changes on a variety of time scales. There is considerable evidence that variations in the electron radiation environment of a spacecraft can lead to failure via deep dielectric charging of spacecraft components [*Vampola*, 1987; *Shea et al.*, 1992; *Wrenn*, 1995; *Baker et al.* 1994b, 1998]. Geo-synchronous orbit, an important region for communications and weather satellites, lies at 6.6 R_E and typically well within the outer zone, while the 4.2 R_E, 55 degree inclination orbits of the GPS constellation of spacecraft like-

wise carry them through the heart of the outer radiation zone. It is important to accurately model the radiation environment. At present many static models for the radiation belts do exist e.g., the NASA AE and AP models (*Vette* [1991]), CRRESELE and CRRESPRO (*Albert and Ginet,* 1998a, 1998b; *Meffert and Gussenhoven,* 1994; *Brautigam and Bell,* 1995, etc.), providing useful information regarding the average radiation conditions that might be seen over the lifetime of a spacecraft. However, they are of limited use in predicting the effects of the sometimes drastic temporal variations present in a storm-time magnetosphere, and do not include contributions from solar energetic particles (except perhaps in a temporally-averaged sense). MHD simulations of the magnetosphere provide sufficient temporal resolution to catch the dynamics of a storm. But approximations made in obtaining the MHD equations do not allow specification of energetic particle populations in the magnetosphere or solar wind. To derive a picture of the global evolution of the storm-time radiation belts from global MHD simulations, some work (e.g., *Hudson, [1999]; Elkington, [1999]*) has been done with the test particle method by using global MHD simulations to provide input fields for the particle simulations. Further work will use two kinds of codes to model the radiation belt, viz. test particle code and data-driven or data-assimilation model.

Advances in computational power and numeric techniques will continue to allow us to improve the resolution and incorporate non-MHD physical processes

important in smaller scale. Besides the above mentioned future works regarding overall modeling, we present the specific future work for each of the three topics covered in this thesis as following:

- **Earth's Magnetosphere with Northward IMF**

  In this thesis, we focused on using the global MHD model to study the Earth's magnetosphere with steady northward IMF. The steady state is of short tail. Our next question is that if we perturb this steady state, how the tail will response. Recently [*Huang et al.,* 2000, 2001] reported observations of 40-60 minutes quasi-periodic oscillation in ionospheric velocity, ground magnetic field perturbation and magnetospheric magnetic field observed by GOES-8 satellite for northward IMF. It is of interest to investigate the role of simple time-dependent (e.g. sinusoidally varying) solar wind and IMF on the size and dynamics of the magnetosphere with northward IMF. Driving the global MHD model with sinusoidally varying solar wind V_{SW}, our preliminary results show that the tail oscillates and the largest oscillation magnitude is located in the 30-50 minutes period interval. The magnetosphere behaves like a low frequency filter. It is quite possible that the magnetospheric-ionospheric perturbations originated from the excitation of standing magneto-sonic wave inside the magnetospheric cavity. Further investigations and the development of simple analytical model are needed.

Earth's magnetosphere with more complicated time-dependent solar wind condition during northward IMF is another research topic. This study will focus on actual event simulations and comparisons with Polar, Interball, IMAGE and Geotail satellite observations. This will guide us to achieve better understanding of the cusp region reconnection, the behavior of the tail field and ionospheric response during northward IMF.

- **Magnetospheric Substorms**

More physics-based and actual event simulations using the global MHD model are needed to understand the physics and the consequences of geomagnetic storms and substorms. Further case studies need to be conducted to determine the universality of the substorm response time scale, substorm onset triggers, time sequence of the inner magnetotail and ionospheric acticities. To select among existing substorm models or propose more reasonable model also requires further study.

The phase transition-like behavior of substorm dynamics as revealed by *Sitnov et al.* [2000] for the real system and by our study for the global MHD simulation results, opens a new area in the studies of magnetospheric substorms. In the future, we will simulate and study substorms from other data sets to see how the first order and second order phase transition behavior changes for substorms of different activity level. Other

magnetospheric and ionospheric response, such as the total tail magnetic energy, total energy deposition in the ionosphere, will be derived from the MHD model and used to study the phase transition-like behavior.

The nonlinear dynamical model uses the solar wind variables such as the induced electric field VB_z as the input and predict the auroral electrojet indices AL, AE, and AU for substorms and the Dst index for storms. Comparison of these predictions with those made with global MHD simulations using solar wind input and with the actual AL or Dst will guide us to understand substorm dynamics better and develop data-assimilation model for reliable space weather prediction.

- **Magnetosphere-Ionosphere Coupling**

Ground photometer observes meridional profile of red line emission at wavelength 6300 $\mathring{A}$. The sources of 6300 $\mathring{A}$ emission are [*Rees, 1967, Rees and Jones, 1973, Rees and Luckey, 1974*] direct excitation of atomic oxygen (to the $O(^1D)$ state) by precipitating energetic electrons. [*Samson et al., 1992*] suggested that the location of open-closed field line boundary can be determined from the the measurements of 6300 $\mathring{A}$ emission as a function of latitude. The separatrix is assumed to locate at the poleward boundary of auroral electron precipitation. In the future, we will build a model to calculate the intensity distribution of 6300 $\mathring{A}$ emissions as a function of

invariant latitude and UT as observed by a ground station.

Currently the MHD model neglects the effect of turbulent electron and collisional ion heating by the ionospheric electric field. However, the inclusion of the turbulent electron heating led to a much better agreement of the simulations with the actual values of integrated absorption at the three riometer locations. We expect that inclusion of anomalous collision frequency into the ionospheric conductance could improve the model by providing feedback between the model ionosphere, serving as a dynamic boundary condition, and the 3–D global magnetospheric simulations. More actual event simulations and comparisons with magnetometer data and other ionospheric observations will help us to improve the global MHD model and incorporate realistic ring current model and ionospheric conductance model.

There is still much to be done.

Part VI

Appendices

Appendix A

Computational Model for Simulating

Riometer Observations

The radio signals used by riometers are typically of very high frequency (VHF), in the 20–50 MHz range. The total column integrated changes in the intensity of VHF waves due to the ionospheric absorption is given by

$$A = \frac{1}{2c(2\pi f)^2} \int \omega_{pe}^2 \nu_{en} dz \qquad (A.1)$$

where f is the frequency of the VHF wave, ω_{pe} is the electron plasma frequency, and ν_{en} is the electron-neutral collision frequency. Note that the frequency of the radio waves used in riometers is much greater than both the electron gyrofrequency Ω_e and electron-neutral collision frequency ν_{en}, viz. $2\pi f \gg \Omega_e$, ν_{en}.

In the model below we consider the ionospheric absorption of VHF signals caused by a thin plasma layer, produced by ionization due to precipitating elec-

trons. Furthermore, since the ionospheric absorption strongly depends on the bulk electron temperature, we include anomalous electron heating by strong turbulent electric fields developed at the same time, due to electrojet instabilities [*Ossakow et al.*, 1975; *Stauning*, 1984; *St-Maurice and Laher*, 1985]. Note that electron heating up to 2000–3000 K at the time of a substorm is often inferred by radar observations [*Schlegel and St-Maurice*, 1981; *Schlegel and Collis*, 1999].

A.1 Modeling Ionospheric Absorption of VHF Wave

We consider for simplicity absorption by a uniform ionospheric layer with thickness $\triangle z$, electron density n_e, neutral density N_n, and electron temperature T_e. The apparent absorption measured by a riometer is a logarithm of the ratio of the galactic noise power level during an absorption event to that during quiet ionospheric conditions. Applying Eq. (A.1) with the effective electron-neutral collision frequency ν_{en} given by Gurevich [1978],

$$\nu_{en}(s^{-1}) = 0.6 \times 10^{-8} N_n(cm^{-3})(T_e/300K)^{5/6}, \qquad (A.2)$$

we find that the VHF absorption in dB is given by

$$A = 8.7 \times 10^{-18} n_e(cm^{-3}) N_n(cm^{-3}) \Delta z(km) f(MHz)^{-2}(T_e/300K)^{5/6}. \quad (A.3)$$

It takes into account the dependence of the cross section of electron-neutral inelastic collisions upon the electron temperature.

The output of the LFM model provides the key local quantities: the characteristic energy ε and the flux Φ of the precipitating electrons along with the electric field $\mathbf{E}$. In order to compare the riometer observations with the LFM output, we need to connect the values of n_e, N_n and T_e with ε, Φ and $\mathbf{E}$.

We obtain first the penetration altitude of the fast precipitating electrons, and the neutral density at this altitude. The energy balance of electrons moving downwards in the ionosphere is given by

$$\frac{d\varepsilon}{dz} = -\sigma_{ion}(\varepsilon)\varepsilon_{ion}N_n(z), \tag{A.4}$$

where σ_{ion} is the ionization cross section, while ε_{ion} is the energy spent per ionization, which is usually taken as 35 eV [*Rees*, 1989] and N_n is the neutral density. In the exponential atmosphere, $N_n \sim e^{-z/L}$, where L is the density scale height. Here, we take L=10 km. Eq. (A.4) allows us to obtain the penatration altitude z_p, and the neutral density corresponding to z_p

$$N_n(z_p) \simeq \frac{1}{L\varepsilon_{ion}} \int_{\varepsilon_{ion}}^{\varepsilon} \frac{d\varepsilon}{\sigma_{ion}(\varepsilon)}. \tag{A.5}$$

The ionization cross section of air by electrons in the energy range $\varepsilon < 20 KeV$ is described with sufficient accuracy by the following interpolation formula [*Gurevich et al.*, 1997]

$$\sigma_{ion}(cm^2) \simeq 8.3 \times 10^{-16} \frac{\varepsilon/\varepsilon_m - 0.11}{1 + 1.85(\varepsilon/\varepsilon_m)^{1.75}} \tag{A.6}$$

where $\varepsilon = 110\ eV$ corresponds to the peak of σ_{ion}.

By substituting Eq. (A.6) into Eq. (A.5) and integrating while taking into account that in the energy range provided by the LFM model, 1 keV$\leq \varepsilon \leq$20 keV, $\varepsilon/\varepsilon_m \gg 1$, we find that the air density at the penetration altitude (z_p) is

$$N_n(z_p) = \frac{4 \times 10^9 cm^{-3}}{(L/10km)} (\frac{\varepsilon}{\varepsilon_m})^{1.75}. \tag{A.7}$$

Using the U. S. Standard Atmosphere (1976) we found the penetration altitude for different electron energies and compared them with that found by using the formulas from Rees [1992]. This analysis reveals a consistency between these models at 1 keV $\leq \varepsilon \leq$ 20 keV with an accuracy of a few percent.

We next estimate the electron density in a thin ionized layer created by the absorption of fast electrons. Taking into account that the total energy of fast electrons is absorbed along the scale height L of the pressure gradient, we find that the energy flux $\varepsilon\Phi$ of fast electrons produces thermal electrons inside the column L with the ionization rate

$$q_{ion} = \frac{\varepsilon\Phi}{\varepsilon_{ion}L}. \tag{A.8}$$

The electron density balance equation gives

$$\frac{dn_e}{dt} = q_{ion} - \alpha n_e^2, \tag{A.9}$$

where $\alpha \simeq 2 \times 10^{-7}(300K/T_e)\ cm^3/s$ is the electron-ion recombination rate [Gurevich, 1978]. In a stationary case (d/dt=0) the electron density becomes

$$n_e = \sqrt{\frac{\varepsilon\Phi}{\varepsilon_{ion}L\alpha}} \tag{A.10}$$

Finally, the absorption of the radio noise having frequency f can be found from Eqs. (A.3), (A.7), (A.10), taking into account that the thickness of the ionized layer is $\Delta z \simeq L \simeq 10$ km. Thus we obtain

$$A(dB) = 8.5\varepsilon_{keV}^{2.25} f_{MHz}^{-2} \left(\frac{\Phi}{\Phi_0}\right)^{1/2} \left(\frac{T_e}{300K}\right)^{4/3}. \tag{A.11}$$

Here Φ is given in electron/cm^2s, while $\Phi_0 = 10^9 \ cm^{-2}s^{-1}$. Eq. (A.11) reveals that the absorption strongly depends upon the temperature of the bulk of electrons which increases during magnetic cloud events, as discussed in the next section.

A.2 Anomalous Electron Heating

It is known from numerous radar observations that electron temperature rises significantly in the polar electrojet during substorms [*Schlegel and St-Maurice, 1981; Jones et al., 1991; Schlegel and Collis, 1999*]. Strong anomalous electron heating is predominantly caused by turbulent electric fields developing in the electrojet mostly as a result of the modified two-stream, or Farley-Buneman (F-B) instability driven by the convection electric field $\mathbf{E_C}$. This mechanism was first suggested by *Ossakow et al.* [1972]; *Schlegel and St-Maurice* [1981]; see also *St-Maurice and Laher* [1985] and *Jones et al.* [1991]. However, the existing approximate models cannot interpret satisfactorily the available radar data. Here, we will give a simple and usable recipe for estimates of the temporally-

and spatially-averaged electron temperature, based on physical reasoning and comparison with available radar observations of the heating.

To get the electron temperature under quasi-stationary conditions, we equate the electron Joule heating by the total electric field, $\mathbf{jE}$, to the cooling via inelastic electron-neutral collisions, $\delta_{en}\nu_{en}n_e k_B(T_e - T_0)$, where k_B is the Boltzmann's constant, T_0 is the electron temperature approximately equal to the temperature of neutral particles in the cold (unperturbed) ionosphere and $\delta_{en}(T_e)$ is the average fraction of the electron energy lost in electron-neutral collision. As a result we obtain for the average temperature increment $\Delta T_e = T_e - T_0$,

$$\frac{\Delta T_e}{T_0} \simeq \frac{2m_e}{m_i \delta_{en}}(1 + \frac{<E_\parallel^2>}{<E_\perp^2>}\frac{\Omega_e^2}{\nu_{en}^2})\frac{<E_\perp^2>}{E_{th0}^2}, \tag{A.12}$$

where $E_{\parallel,\perp}$ are the components of the total electric field parallel and perpendicular to the geomagnetic field $\mathbf{B}$, respectively (the angular brackets mean time averaging). The normalization constant $E_{th0} \simeq 20\ mV/m$ represents the minimum F-B threshold field $E_{th}(T_e) = C_S B/c$ ($C_S = [k_B(T_e + T_i)/m_i]^{1/2}$ is the ion acoustic speed) taken for the 'cold' (i.e. unperturbed) ionosphere: $C_S = C_{S0} \approx (2k_B T_0/m_i)^{1/2}$.

Since the nonlinear theory of the F-B instability is still far from complete, here we estimate the electric field energy in the nonlinearly saturated turbulent state based on simple physical reasonings. For the driving field $\mathbf{E_C}$ well above the threshold value $E_{th}(T_e)$, it is natural to assume that the energy level of saturated turbulence is such that the major nonlinear term is of order of the

228

largest linear terms in the appropriate equations. This yields for the turbulent electric field a simple estimate $< E^2 > \approx < E_\perp^2 > \sim E_C^2$, corresponding to several percent of the coupled plasma density perturbations. Strong electron heating is due to parallel turbulent electric field associated with finite parallel components of the wave-vectors $k_\parallel$ [*St-Maurice and Laher*, 1985]. For potential F-B waves we have $E_\parallel / E_\perp = k_\parallel / k_\perp \approx \theta$, where $\theta << 1$ is the aspect angle.

We may anticipate that the bulk of saturated turbulence in the θ-space is spread over a broad range around the linear growth rate maximum, at least up to the boundary of the linearly unstable range, $\psi = \psi_\perp [1 + (\theta \Omega_e / \nu_{en})^2] \simeq E_C / E_{th}(T_e)$, where $\psi_\perp = \nu_{en} \nu_{in} / (\Omega_e \Omega_i)$. The F-B instability is effectively excited at the altitudes where $\psi_\perp \ll 1$. Taking $\psi \approx 1$ as an effective value of ψ responsible for the main contribution to the Joule heating, we obtain $(\theta \Omega_e / \nu_{en})^2 \simeq 1/\psi_\perp \gg 1$ and from Eq. (A.12)

$$\frac{\Delta T_e}{T_0} \simeq \frac{2m_e}{m_i \delta_{en} \psi_\perp} \left(\frac{E_C}{E_{th0}}\right)^2. \tag{A.13}$$

This is an implicit expression for T_e in terms of $\mathbf{E_C}$ since $\psi_\perp \propto \nu_{en}(T_e)$. In the range of interest 800K $< T_e <$ 3,000K, to a good accuracy, the temperature dependence of the electron cooling rate is given by $\delta_{en}(T_e)\nu_{en}(T_e) \propto T_e$ [*Gurevich*,1978]. Thus for $T_e \simeq \Delta T_e \gg T_0$ the estimated electron temperature is roughly proportional to the convection electric field.

To obtain the proper value of T_e used in Eq. (A.11), we should average Eq. (A.13) over the altitude range between 105 and 115 km within the electrojet.

Assuming the exponential height dependence of the neutral atmosphere with the typical e-folding scale for these altitudes L $\simeq$ 10 km, neglecting the spatial dependence of ion composition and $\mathbf{E_C}$, B and T_0 within the range of interest, while adopting the values of δ_{en} from *Gurevich* [1978] we obtain from Eq. (A.13) the average temperature

$$< T_e > \simeq 1.5 T_0 (E_C / E_{th0}). \qquad (A.14)$$

Note that derivation of Eqs. (A.13) and (A.14) required excitation of the F-B instability well above the threshold. The actual threshold electric field increases with temperature, $E_{th}(T_e) \propto C_S \propto (T_e + T_0)^{1/2}$. Thus a strong anomalous electron heating caused by nonlinearly developed turbulence might in principle break this condition. However, as seen from Eq. (A.14), for $E_{th}(T_e) \propto C_S \propto (T_e + T_0)^{1/2}$ the ratio $E_C / E_{th}(T_e) \sim (E_C / E_{th0})^{1/2}$, so that the required condition and, hence Eq. (A.14) remain to be valid.

Appendix B

Computational Model for Simulating Magnetometer Observations

As we have introduced in Chapter 2, in LFM code, the inner boundary condition on the MHD solution is determined from the results of an ionospheric simulation. The solution in the ionosphere is done by solving a 2 dimensional height integrated electrostatic potential equation driven by the field aligned currents within the magnetosphere,

$$\nabla_\perp \bullet \Sigma \bullet \nabla_\perp \Phi = \vec{J}\|$$
(B.1)

with Φ as the ionospheric potential, Σ as the anisotropic conductivity tensor and $\vec{J}\|$ as the field aligned current. The field aligned current $(\vec{J}\|)$ are calculated from the magnetic field data on the inner edge of the MHD model and used in conjunction with Σ to determine the potential Φ. The conductivity tensor has both Petersen and Hall components, whose values contain two parts. The first

part comes from the steady SUV flux and the second from particle precipitation in the auroral region. The 2D height integrated ionospheric current density is

$$\vec{J_\perp} = \Sigma \bullet \nabla_\perp \Phi \tag{B.2}$$

The perpendicular current obtained from Eq. (B.2), is specified on a spherical shell with an angular range from 45 degrees to 90 degrees in latitude (solar-magnetosphere coordinate) for each hemisphere. To calculate the perturbed magnetic field produced by the ionospheric current, we implement the generalized form of Biot-Savart's law [*Kisabeth and Rostoker*, 1977]

$$\vec{B}(\vec{r_0}) = \mu_0/4\pi \int_s \frac{\vec{J}(\vec{r}(\varepsilon)) \times (\vec{r}_0 - \vec{r}(\varepsilon))d^2\vec{r}(\varepsilon)}{|\vec{r}_0 - \vec{r}(\varepsilon)|^3} \tag{B.3}$$

Because the ionospheric current in our case is 2D (since $\vec{J}(\vec{r})$ has been height integrated over the thickness of the current sheet), the integral is calculated on the spherical shell $d^2\vec{r}$ of the current sheet. Here $\vec{r_0}$ is the position of the site in SM coordinates, where the perturbed magnetic field is computed and $\vec{r}(\varepsilon)$ denotes the position of the ionospheric current sheet in SM coordinates. The height of the ionospheric electrojet changes in time and is determined by the energy of the precipitating electrons. The precipitating energetic electrons ionize the neutrals and are finally stopped when they lose all their energy in the ionization process. The more energetic the electrons are, the deeper they penetrate into the atmosphere. Thus $\vec{r}(\varepsilon)$ can be expressed as

$$|r(\varepsilon)| = R_E + h(\varepsilon); \tag{B.4}$$

Here R_E is the radius of the earth and $h(\varepsilon)$ is the energy-dependent height of the electrojet current. From the LFM code we get a time history of the energy of the precipitating electrons at each grid point. Knowing the instantaneous energy of the precipitating electrons we can calculate the desired height of the 2D electrojet current sheet at each grid point.

As presented in Appendix A.1, we find that the air density at the penetration altitude (z_p) is

$$N_n(z_p) = \frac{4 \times 10^9 cm^{-3}}{(L/10km)} (\frac{\varepsilon}{\varepsilon_m})^{1.75}. \tag{B.5}$$
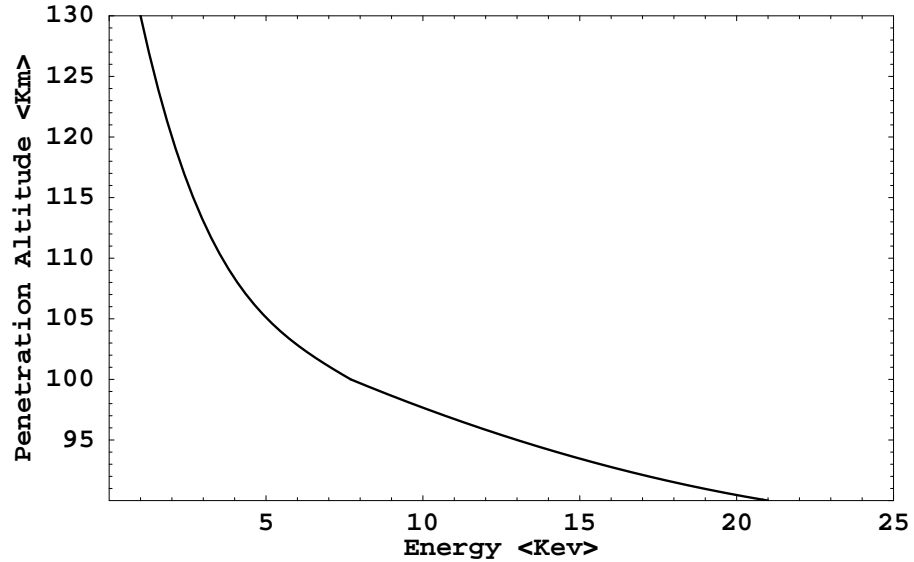
Figure B.1: The electron penetration altitude vs. electron energy (Computed from our model).

Using the U. S. Standard Atmosphere (1976), we have computed the penetration altitude z_p for different electron energies ε. The resulting dependence of

penetration altitude z_p on energy ε is plotted in Figure B.1. After penetration altitude z_p is obtained, the energy-dependent height of the electrojet current $h(\varepsilon)$ is calculated as $h(\varepsilon) = z_p + \delta z/2$, where δz is the thickness of the ionization layer and can be approximated as $\delta z = L = 10$ km.

Thus knowing the height dependence and the current density of the electrojet we can use Eq. (B.3) to compute the magnetic field at any location $\vec{B}(\vec{r_0})$ in the SM coordinate system as a function of time. The integral is discretized into a summation over all the grid points. Figure B.2 shows the grid configuration. The non-uniform grids from global MHD model have been mapped to the

Figure B.2: The grid configuration for the model.

uniform grids in polar coordinate shown in Figure B.2. The adjacent longitudinal

(j, j±1) and azimuthal (i, i±1) lines are two degrees apart, respectively. The longitudinal lines (j, j±1) converge at the northern pole. The points (i±1/2, j±1/2) and (i±1/2, j∓1/2) are at the center of ea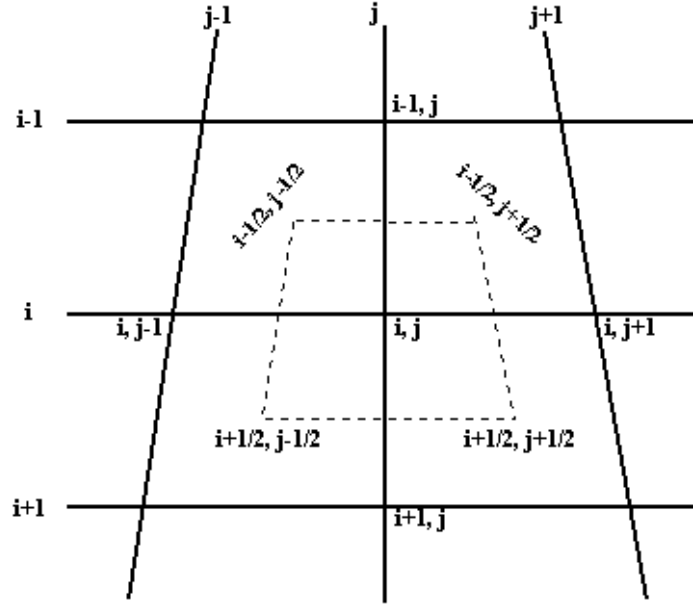ch grid. For grid point (i, j), its contribution to the integral is calculated within the area formed by the dotted lines. We assume same current sheet height and uniform horizontal current inside the area formed by the dotted lines. The integration is evaluated by summing over all the grid points.

We then calculate the magnetic field in the local observational coordinate system, $(\widehat{r}_0, \widehat{\theta}_0, \widehat{\phi}_0)$ of the desired station as $\overrightarrow{B}(\overrightarrow{r_0}) = B_1\widehat{r}_0 + B_2\widehat{\theta}_0 + B_3\widehat{\phi}_0 = -Z\widehat{r}_0 - H\widehat{\theta}_0 + D\widehat{\phi}_0$. Here, H is the component that points towards the north magnetic pole, D points eastward and Z points down towards the center of the Earth. Finally, to account for the contribution of the current induced in the ground, the calculated magnetic field is enhanced by a factor of two. We hasten to add that the individual components will be strongly influenced by the local conductivity of the ground and that would rotate the polarization of the magnetic field. Thus, in Chapter 6, we have focused on comparing the magnitude of the horizontal component ($\sqrt{H^2 + D^2}$), total field ($\sqrt{H^2 + D^2 + Z^2}$) and Z component with ground-based magnetometer data.

References

Abarbanel, H. D., R. Brown, J. J. Sidorovich, and T. S. Tsimring, The analysis of observed chaotic data in physical systems, *Rev. Mod. Phys., 65*, 1331, 1993.

Akasofu, S., The development of the auroral substorm, *Planet. Space. Sci., 12*, 273, 1964.

Axford, W. I., and C. O. Hines, A unifying theory of high latitude geophysical phenomena and geomagnetic storms, *Can. J. Phys., 39*, 1433, 1961.

Bak, P., C. Tang, and K. Wiesenfeld, Self-organized criticality: An explanation of 1/f noise, *Phys. Rev. Lett., 50*, 381-384, 1987.

Baker, D. N., R. D. Belian, P. R. Higbie, R. W. Klebesadel, and J. B. Blake, Deep dielectric charging effects due to high energy electrons inEarth's outer magnetosphere, *J. Electrost, 20*, 3, 1987.

Baker, D. N., S Kanekal, J. B. Blake, B. Klecker, and G. Rostoker, Satellite anomalies linked to electron increase in the magnetosphere, *EOS, 75*, 401, 1994.

Baker, D. N., T. Pulkkinen, V. Angelopoulos, W. Baumjohann, and R. L. McPherron, Neutral line model of substorm: Past results and present view, *J. Geophys. Res., 101*, 12,975, 1996.

Baker, D. N., J. H. Allen, S. G. Kanekal, and G. D. Reeves, Disturbed space environment may have been related to pager satellite failure. *EOS*, page 477, October 6 1998.

Bargatze, L. F., Baker, D. N., McPherron, R. L. et al., Magnetospheric impulse response for many levels of geomagnetic activity, *J. Geophys. Res., 90*, 6387, 1985.

Bargatze, L. F., T. Ogino, R. L. McPherron, and R. J. Walker, Solar wind magnetic field control of magnetospheric response delay and expansion phase onset timing, *J. Geophys. Res.,104*, 14,583, 1999.

Berchem, J., J. Raeder, and M. Ashour-Abdalla, Reconnection at the magnetospheric boundary Results from global MHD simulations, in *Physics of the magnetopause, Geophysical Monogram Series, vol. 90*, edited by B. U. O. Sonnerup, P. Song, and M. Thomsen, 1995.

Berchem, J., M. El Aloui, M. Ashour-Abdalla, J. Raeder, A. Frank, W. R. Petersen, J. B. Sigwarth, S. Kokubun, R. P. Lepping, H. J. Singer, and S. Romanov, Global MHD simulation of January 12 1997, magnetospheric substorm, *SM12A-12*, fall AGU meeting 1998.

Blanchard, G. T., and R. L. McPherron, A bimodal representation of the response function relating the solar wind electric field to the AL index, *Adv. Space Res., 13(4)*, 71, 1993.

Blanchard, G. T., Lyons, L. R., et al., Locating the polar cap boundary from observations of 6300 Å auroral emission, *J. Geophys. Res., 100*, 7855-

7862, 1995.

Broomhead, D. S., and G. P. King, Extracting qualitative dynamics from experimental data, *Physica D, 20* 217, 1986.

Burch, J. L., P. H. Reiff, R. A. Heelis, R. W. Spiro, and S. A. Fields, Cusp region particle precipitation and ion convection for northward interplanetary field, *Geophys. Res. Lett., 7*, 393, 1980.

Burch, J. L., J. D. Menietti, and J. N. Barfield, DE-1 observations of solar wind-magnetosphere coupling processes in the polar cusp, in *Solar Wind Magnetosphere Coupling*, edited by Y. Kamide and J. A. Slavin, p. 441, Terra Scientific, Tokyo, 1986.

Chang, T., Multiscale intermittent turbulence in the magnetotail, in *Substorms-4: International Conference on Substroms-4, Lake Hamana, Japan, March 9-13, 1998*, edited by S. Kokibum and Y. Kamide, 431, Terra Sci., Tokyo, 1998.

Chapman, S. C., N. W. Watkins, R. O. Dendy, PHelander, and G. Rowlands, A simple avalanche model as an analogue for magnetospheric activity, *Geophys. Res. Lett., 25*, 2397, 1998.

Chen, C. X. and Wolf R. A., Interpretation of High-Speed Flows in the Plasma Sheet, *J. Geophys. Res., 98*, 21409, 1993.

Clauer,C. R., and E. Friis-Christensen, High-altitude dayside electric fields and currents during strong northward interplanetary magnetic field: observations and model simulations. *J. Geophys. Res., 93*, 2749, 1988.

Coroniti, F. V., and C. F. Kennel, Can the ionosphere regulate magnetospheric convection ? *J. Geophys. Res., 78*, 2837, 1973.

Consolini, G., Sandpile cellula automata and magnetospheric dynamics in *Proceedings of the 8th GIFCO Conference, Cosmic Physics in the year 2000: Scientific Perspectives and New Instrumentations*, 8-10 April 1997, edited by S. Aiello et al., Soc. Ital. di Fis., Bologna, Italy, 1997.

Detrick, D. L., and T. J. Resenberg, A phased-array radiowave image for studies of cosmic noise absorption, *Radio Science, 25*, 325, 1990.

Dungey, J. W., Interplanetary magnetic field and the auroral zones, *Phys. Rev. Lett., 6*, 47,1961.

Dungey, J. W., The structure of the ionosphere, or adventures in velocity space, in *Geophysics: The Earth's Enviroment*, edited by C. DeWitt, J. Hiebolt, and A. Lebeau, p. 526-536, Gordon and Breach, New York, 1963.

Evans, C. R., and J. F. Hawley, Simulation of magnetohydrodynamic flows: A constrained transport method, *Ap. J., 332*, 659, 1988.

Fairfield, D. H., Solar wind control of the distant magnetotail: ISEE3, *J. Geophys. Res.,98*, 21,265, 1993.

Fedder, J. A., and J. G. Lyon, The solar wind-magnetosphere-ionosphere current-voltage relationship, *Geophys. Res. Lett., 8*, 880, 1987.

Fedder, J. A., C. M. Mobarry, and J. G. Lyon, Reconnection voltage as a function

of imf clock angle *Geophys. Res. Lett., 18*, 1047, 1991.

Fedder, J. A., J. G. Lyon, S. P. Slinker, and C. M. Mobarry, Topological structure of the magnetotail as function of interplanetary magnetic field and with magnetic shear, *J. Geophys. Res., 100*, 3613, 1995a.

Fedder, J. A., and J. G. Lyon, The Earth's magnetosphere is 165 R_E long: Self consistent currents, convection, magnetospheric structure, and processes for northward interpanetary magnetic field,*J. Geophys. Res., 100*, 3623, 1995.

Fedder, J. A., S. P. Slinker, J. G. Lyon, and R. D. Elphinstone, Global numerical simulation of the growth phase and the expansion onset for substorm observed by Viking, *J. Geophys. Res., 100*, 19083, 1995b.

Fukushima, N., Generalized theorem for no ground magnetic effect of vertical currents connected with Pedersen currents in the uniform conducting ionosphere, *Rep. Ionos. Space Res. Jpn., 30*, 35, 1976.

Godunov, S. K., A difference scheme for numerical computation of discontinuous solution of hydrodynamic equations, *Math. Sbornik, 47*, 271, 1959.

Gombosi, T. I., D. L. Dezeeuw, C. P. T. Groth, K. G. Powell, and P. Song, The length of the magnetotail for northward IMF: Results of 3D MHD simulations, in *Physics of Space Plasmas (1998)*, edited by T. Chang, and J. R. Jasperse, vol. 15, p. 121, MIT press, Cambridge, 1998.

Goodrich, C. C., M. Wiltberger, R. E. Lopez, K. Papadopoulos, and J. G. Lyon. An overview of the impact of the january 10-11, 1997 magnetic cloud on the magnetosphere via global mhd simulation, *Geophys. Res. Lett., 25*, 2537–2540, 1998a.

Goodrich, C. C., M. Wiltberger, R. E. Lopez, K. Papadopoulos, and J. G. Lyon. Global MHD Simulations of Actual Magnetospheric Substorm Events *Substorms-4*, edited by Kokubun and Y. Kamide, 645-649, 1998b.

Gurevich, A. V., *Nonlinear Phenomena in the Ionosphere*, New york, Springer-Verlag, 1978.

Gurevich, A. V., N. D. Borisov, and G. M. Milikh, *Physics of Microwave Discharges, Artificially Ionized Regions in the Ionosphere*, United Kindom, Gordon & Breach, 1997.

Guzdar, P. N., X. Shao, M. Wiltberger, C.C. Goodrich, K. Papadopoulos, J. G. Lyon, Three-dimensional MHD simulations of the steady-state magnetosphere with northward interplanetary magnetic field, *J. Geophy. Res., 106*, 275, 2001.

Hain, K., The partial doner method, *J. Comp. Phys., 73*, 131, 1987.

Hones, E. W. Jr., Transient phenomenon in the magnetotail and their relation to substorms, *Space Sci. Rev., 23*, 393, 1979.

Huang, C. S., G. J. Sofko, A. V. Kustov, et al., Quasi-periodic ionospheric disturbances with a 40-min period during prolonged northward interplanetary magnetic field, *Geophys. Res. Lett., 27*, 1795, 2000.

Huang C. S., G. J. Sofko, A. V. Kustov, et al., Long-period magnetospheric-ionospheric perturbations during northward interplanetary magnetic field, *J. Geophys. Res., 106*, 2001.

Hudson, M. K., S. R. Elkington, J. G. Lyon, C. C. Goodrich, and T. J. Rosenberg, Simulation of radiation belt dynamics driven by solar wind variations, *Sun-Earth Plasma Connections, Geophysical Monography, 109*, 171, 1999.

Iijima, T., Field-aligned currents during northward IMF, in magnetospheric currents, *Geophys. Monogr. Ser., vol. 28*,edited by T. A. Potemra, pp. 115-122, AGU, Washington, D.C., 1984.

Johnson, F. J., The gross character of the geomagnetic field in the solar wind, *J. Geophys. Res.,65*, 3049, 1960.

Johnson, F. J., The driving force for magnetospheric convection, *Rev. Geophys., S. Phys., 16*, 161, 1978.

Jones, B., P. J. S. Williams, K. Schlegel, T. Robinson, and I. Haggstrom, Interpretation of enhanced electron temperatures measyred in the auroal E-region during the ERRRIS campaign, *Ann. Geophysicae, 9*, 55, 1991.

Jordanova, V. K., et al., Ring current activity during the early Bz¡0 phase of the January 1997 magnetic cloud, *J. Geophys. Res., 104*, 24,895, 1999.

Jursa, A. S., Handbook of Geophysics and the space environment, *Air Force Geophysics Laboratory*, 1985.

Kamide, Y. and W. Baumjohann, Magnetosphere-Ionosphere Coupling, *Physics and chemistry in space, v. 23*, Springer, 1993.

Kelley, M. C., *The Earth's Ionosphere: Plasma Physics and Electrodynamics*, Academic Press, San Diego, 1989.

Kennel, C. F., Convection and substorms, *International Series on Astronomy and Astrophysics*, Oxford University Press, 1995.

Kisabeth, J. L. and Rostoker, G., Modelling of the three-dimensional current systems associated with magnetospheic substorms, *Geophys. J. R. astr. Soc.*, 49, 655-683, 1977.

Kivelson, M. G. and C. T. Russell, *Introduction to Space Physics*, Cambridge University Press, 1995.

Klimas, A. J., D. N. Baker, D. A. Roberts, D. H. Fairfield and J. Büchner, A nonlinear dynamical model of geomagnetic activity, *J. Geophys. Res.,97*, 12,253, 1992.

Klimas, A. J., D. Vassiliadis, D. N. Baker, and D. A. Roberts, The organized nonlinear dynamics of the magnetosphere, *J. Geophys. Res., 101*, 13089, 1996.

Klimas, A. J., D. Vassiliadis, and D. N. Baker, Data-derived analogues of the magnetospheric dynamics, *J. Geophys. Res., 102*, 26,993, 1997.

Laakso, H., Fairfield, D. H., Russell, C. T., et al., Field-line resonances triggered by a northward IMF turning, *Geophys. Res. Lett., 25*, 2991, 1998.

Lax, P. D., Weak solutions of non-linear hyperbolic equations and their numeric computation, *Comm. Pure and Applied Mathematics, 7*, 159, 1954.

Lewis, Z. V., On the apparent randomness of substorm onset, *Geophys. Res. Lett., 18*, 1627, 1991.

Lopez, R. E., C. C. Goodrich, M. Wiltberger, and J. G. Lyon, Simulation of the march 9, 1995 substorm and initial comparison to data, In J. L. Horowitz, D. L. Gallagher, and W. K. Peterson, editors, *Geospace Mass and Energy Flow: Results from the International Solar-Terrestrial Physics Program*, volume 104 of *Geophysical Monograph*, pages 237–245, AGU, 1998.

Lopez, R. E., M. Wiltberger, and J. G. Lyon, C. C. Goodrich, MHd simulations of the response of high-latitude potential patterns and polar cap boudaries to sudden southward turnings of the interplanetary magnetic field, *Geophys. Res. Lett., 26*, 967–970, 1999.

Lu, G., et al., Global energy deposition during the January 1997 magnetic cloud event, *J. Geophys. Res., 103*, 11,695, 1998.

Lui, A. T. Y., Extended consideration of a synthesis model for magnetospheric substorms, in *Magnetospheric Substorms*, edited by J. R. Kan, T. A. Potemra, A. Kokubun, and T. Iijima, vol. 64 of *Geophysical Monograph*, 43, AGU, 1991.

Lui, A. T. Y., Current disruption in the Earth's magnetosphere: Observations and models, *J. Geophys. Res., 101*, 13067, 1996.

Lui, A. T. Y., Multiscale and intermittent nature of current disruption in the magnetotail, in *Physcis of Space Plasmas*, vol. 15, edited by T. Chang and J. R. Jasperse, 233, Mass. Inst. Technol. Cent. for Geo/Cosmo Plasma Phys. Cambridge, 1998.

Lui, A. T. Y., Chapman S. C., Liou K. et al., Is the dynamic magnetosphere an avalanching system? *Geophys. Res. Lett., 27*, 911, 2000.

Lyon, J. G., K. Hain, and S. T. Zalesak, Hybrid schemes for the transport of solenodial vector fields, *Unpublished NRL memo*, pages 1-26, 1983.

Lyon, J. G., R. E. Lopez, C. Goodrich, M. Wiltberger, and K. Papadopoulos, Simulation of the march 9, 1995 substorm: Auroral brightening and the onset of lobe reconnection, *Geophys. Res. Lett., 25*, 3039–3042, 1998.

Lyon, J. G., C. M. Mobarry, and M. Wiltberger, The discrete interface method, *in preperation*, 1999.

Lyon, J. G., The solar wind-magnetosphere-ionosphere system, *Science, 288*, 1987, 2000.

Makita, k., and C.-I. Meng, The shift of the auroral elctron precipitation boundaries in the dawn-dusk sector in association with geomagnetic activity and interplanetary magnetic field, *J. Geophys. Res., 88*, 7967, 1983.

Milikh, G. M., Y. S. Dimant, X. Shao, P. N. Guzdar, A. S. Sharma, K. Papadopoulos, E. M. Burns, C. C. Goodrich, T. J. Rosenberg, A. T. Weatherwax, M. J. Wilberger, J. G. Lyon, and J. A. Fedder, Modeling Riometer

Observations of Ionospheric Absorption During Substorms, *Geophy. Res. L.*, *28*, 487, 2001.

Mobarry, C.M., J. A. Fedder, and J. G. Lyon, Equatorial plasma convection from global simulations of the Earth's magnetosphere, *J. Geophys. Res.*, *101*, 7859, 1996.

Ogino, T., R. J. Walker, A magnetohydrodynamic simulation of the bifurcation of tail lobes during intervals with a northward interplanetary magnetic field, *Geophys. Res. Lett.*, *11*, 1018, 1984.

Ohtani, S., T. Higuchi, A. T. Y. Lui, and K. Takahashi, Magnetic fluctuations associated with tail current disruption: fractal analysis, *J. Geophys. Res.*, *100*, 19135, 1995.

Ohtani, S., T. Higuchi, A. T. Y. Lui, and K. Takahashi, AMPTE/CCE-SCATHA simultaneous observations of substorm associated magnetic fluctuations, *J. Geophys. Res.*, *103*, 4671, 1998.

Ossakow, S., K. Papadopoulos, J. Orens, and T. Coffey, Parallel propagation effects on the type I electrojet instability, *J. Geophys. Res.*, *80*, 141, 1975.

Ott, E., *Chaos in Dynamical Systems*, Cambridge University Press, Cambridge, 1997.

Papadopoulos, K., Goodrich, C., Wiltberger, M., Lopez, R. and Lyon, J. G., The Physics of Substorms as revealed by ISTP, *Phys. Chem. Earth(C)*, Vol. 24, No. 1-3, pp. 189-202, 1999.

Preisendorfer, R. W., *Principal Component Analysis in Meteorology and Oceanaography*, 425 pp., Elsevier, New York, 1988.

Press, W. H., B. P. Flannery, S. A. Teukolsky, and W. V. Vetterling, *Numerical Recipies: The Art of Scientific Computing*, 2nd ed., Cambridge Univ. Press, New York, 1992.

Pulkkinen, T. I., D. N. Baker, M. Wiltberger, C. C. Goodrich, R. E. Lopez, and J. G. Lyon, Pseudobreakup and substorm onset: observations and mhd simulations compared, *J. Geophys. Res.*, *103*, 14847–14854, 1998.

Raeder, J., Global MHD simulations of the dynamics of the of the magnetosphere: wrak and strong solar wind forcing, in*Proceedings of the Second International Conference on Substorms*, eds. J. R. Kan, J. D. Craven, and S. -I. Akasofu, University of Alaska Press, Fairbanks, pp 561-568, 1994.

Raeder, J., R. J. Walker, and M. Ashour-Abdalla, The structure of the distant geomagnetic tail during long periods of northward IMF, *Geophys. Res. Lett.*, *22*, 349, 1995.

Raeder, J., Modeling the magnetosphere for northward interplanetary magnetic field: Effects of electrical resistivity, *J. Geophys. Res.*, *104*, 17357, 1999.

Raeder, J., R. L. Mcpherron, L. A. Frank, S. Kokubun, G. Lu, T. Mukai, W. R. Paterson, J. B. Sigwarth, H. J. Singer, and J. A. Slavin, Global simula-

tion of the Geospace Evironment Modeling substorm challenge event, *J. Geophys. Res., 106*, 381, 2001.

Rees, M. H., J. C. G. Walker, and A. Dalgarno, Auroral excitation of the forbidden lines of atomic oxygen, *Planet. Space Sci., 15*, 1097, 1967.

Rees, M. H., and R. A. Jones, Time dependent studies of the aurora: II. Spectroscopic morphology, *Planet. Space Sci., 21*, 1213, 1973.

Rees, M. H., and D. Luckey, Auroral emission energy derived from ratios of spectroscopic emissions: I. Model computations, *J. Geophys. Res., 79*, 5181, 1974.

Rees, M. H., *Physics and Chemistry of the Upper Atmosphere*, Cambridge University Press, Cambridge 1989.

Rees, M. H., Auroral energy deposition rate, *Planet. Space Sci., 40*, 299, 1992.

Reiff, P. H., and J. L. Burch, IMF B_y-dependent plasma flow and Birkland currents in the dayside magnetosphere, 2, A global model for northward and southward IMF, *J. Geophys. Res., 90*, 1595, 1985.

Robinson, R. M., R. R. Vondrak, K. Miller, T. Dabbs and D. A. Hardy, On calculating ionospheric conductivities from the flux and energy of precipitating electrons, *J. Geophys. Res., 92*, 2565, 1987.

Rosenberg, T. J., D. L. Detrick, D. Venkatesan, and G. van Bavel, A comparative study of imaging and broad-beam riometer measurements: The effect of spatial structure on the frequency dependence of auroal absorption, *J. Geophys. Res., 96*, 17793, 1991.

Ruohoniemi, J. M., and R. A. Greenwald, The response of high-latitude convection to a sudden southward IMF turning, *Geophys. Res. Lett., 25*, 2913, 1998.

Russell, C. T., J. A. Fedder, S. P. Slinker et al., Entry of the POLAR spacecraft into the polar cusp under northward IMF conditions, Geophys. Res. Lett., 25, 3015, 1998.

Russell, C. T., G. Le, S. M. Petrinec, Cusp observations of high-latitude reconnection for northward IMF: An alternative view, *J. Geophys. Res., 105*, 5489, 2000.

Samson, J. C., L. R. Lyons, B. Xu, F. Creutzberg, and P. Newell, Proron auroral and substorm intensifications, *Geophys. Res. Lett., 19*, 2167,1992.

Schlegel, K. and J. P. St-Maurice, Anormalous Heating of the Polar E region by Unstable Plasma Waves-1: Observations, *J. Geophys. res., 86A*, 1447, 1981.

Schlegel, K., and P. N. Collis, The storm of 10 January 1997: Electrodynamics of the high latitude E region from EISCAT data, *J. Atm. & Solar Terr. Phys., 61*, 217, 1999.

Sergeev, V. A., T. I. Pulkkinen, and R. J. Pellinen, Coupled mode scenario for the magnetospheric dynamics, *J. Geophys. Res., 101*, 13047, 1996.

Shao X., P. N. Guzdar, G. Milikh, K. Papadopoulos, C. Goodrich, A. Sharma,

M. Wiltberger, and J. G. Lyon, Comparing ground magnetic field pertur-
bations from global MHD simulation with magnetometer data for Jan.
10, 1997 magnetic storm event, *J. Geophy. Res.*, in press, 2001.

Shao X., P. N. Guzdar, K. Papadopoulos, C. C. Goodrich, A. S. Sharma, G.
M. Milikh, M. J. Wiltberger, and J. G. Lyon, Three-dimensional MHD
simulations of the Earth's magnetosphere on Feb 9-10 1995 for northward
interplanetary magnetic field and comparison of the lobe field with Geotail
observations, *Geophy. Res. Lett., 28*, 3835, 2001.

Sharma, A. S., Nonlinear dynamics of space plasmas and predictive modeling,
in Recent Trends in Nonlinear Space Plasmas, edited by R. Z. Sagdeev,
Am. Ins. Phys., p. 141, 1993.

Sharma, A. S., Reconstruction of phase space from time series data by singular
spectrum analysis, in *Physics of Space Plasmas*, vol. 13, edited by T.
Chang and J. R. Jasperse, p. 423, Mass. Inst. Technol. Cent. for Theor.
Geo/Cosmo Plasma Phys., Cambridge, 1994.

Sharma, A. S., Assessing the magnetosphe's nonlinear behavior: It's dimension
is low, it's predictability is high, *Rev. Geophys., 33*, supp., 645, 1995.

Sharma, A. S., D. Vassiliadis, and K. Papadopoulos, Reconstruction of low-
dimensional magnetospheric dynamics by singular spectrum analysis, *Geo-
phys. Res. Lett., 20*, 335, 1993.

Sitnov, M. I., A. S. Sharma, K. Papadopoulos, D. Vassiliadis, J. A. Valdivia,
A. J. Klimas, and D. N. Baker, Phase transition-like behavior of the
magnetosphere during substorms, *J. Geophys. Res., 105*, 12955, 2000.

Sitnov, M. I., A. S. Sharma, K. Papadopoulos, and D. Vassiliadis, Modeling
substorm dynamics of the magnetosphere: From self-organization and
self-organized criticality to nonequilibrium phase transitions, submitted
to Phys. Rev., 2001.

Slinker, S. P., J. A. Fedder, and J. G. Lyon, Plasmoid formation and evolutiion
in a numerical simulation of a substorm, *Geophys. Res. Lett., 22*, 859,
1995.

Slinker, S. P., J. A. Fedder, J. M. Ruohoniemi, and J. G. Lyon, Global MHD sim-
ulation of the magnetosphere for November 24, 1996, *J. Geophys. Res.,
106*, 361, 2001.

Smith, J. P., and W. Horton, Analysis of the bimodal nature of solar wind-
magnetosphere coupling, *J. Geophys. Res., 103*, 14.917, 1998.

Song P. and C. T. Russell, Model of the formation of the low-latitude boundary
layer for strongly northward interplanetary magnetic field. *J. Geophys.
Res., 97*, 1411, 1992.

Song P., D. L. De Zeeuw, T. Gombosi, C. P. Groth and K. G. Powell, A numerical
study of solar wind-magnetoaphere interaction for northward interplane-
tary magnetic field. *J. Geophys. Res., 104*, 28361, 1999.

Song P., T.I. Gombosi, D.L. Dezeeuw, K.G. Powell, C.P.T. Groth, A model of

solar wind-magnetosphere-ionosphere coupling for due northward IMF. *Planetary and space science, 48*, Jan, 2000.

Sonnerup, B. U. O., Theory of the low latitude boundary layer, *J. Geophys. Res., 85*, 2017, 1980.

St-Maurice, J. P., and R. Laher, Are observed broadband plasma wave amplitude large enough to explain the eng]hanced temperatures in the igh-latitude E-region?, *J. Geophys. Res., 90*, 2,843, 1985.

Stanley, H. E., *Introduction to Phase Transition and Critical Phenomena*, Oxford Univ. Press, New York, 1971.

Stauning, P., Absorption of cosmic moise in the E-region during electron heating events: A new class of riometer absorption events, *Geophys. Res. Lett., 11*, 1184, 1984.

Stone, J. M. and M. L. Norman, ZEUS-2D: A radiation magnetohydrodynamic code for astrophysical flows in space dimensions. II The magnetohydrodynamic algorithms and tests, *Ap. J. Supp., 80*, 791, 1992.

Takalo, J., J. Timonen, and H. Koskinen, Correlation dimension and affinity of AE data and bicoloered noise, *Geophys. Res. Lett., 20*, 1527, 1993.

Takens, F., Detecting strange attractors in turbulence, in *Dynamical Systems and Turbulence*, Springer, Berlin, 1981.

Tsurutani, B., M. Sugiura, T. Iyemori, B. E. Goldstein, W. D. Gonzalez, S-I Akasofu, and E. J. Smith, The nonlinear response of AE to the IMF Bs, *Geophys. Lett., 17*, 279, 1990.

Usadi, A., A. Kageyama, K. Watanabe, and T. Sato, A global simulation of the magnetosphere with a long tail tail: Southward and Northward interplanetary magnetic field, *J. Geophys. Res., 98*, 7503, 1993.

Vassiliadis, D., A. J. Klimas, D. N. Baker, and D. A. Roberts, The nonlinearity of models of the $vB_{South}-AL$ coupling, *J. Geophys. Res., 101*, 19,779, 1996.

Wiltberger, M., Global magnetohydrodynamic simulations of magnetospheric substorms, *Ph.D. Dissertation*, University of Maryland, College Park, 1998.

Wiltberger, M., T. I. Pulkkinen, J. G. Lyon, and C. C. Goodrich, MHD simulation of the magnetotail during the december 10, 1996, substorm, *J. Geophys. Res., 105*, 27,649, 2000.

Winglee, R. M., V. O. Papitashvili, and D. R. Weimer, Comparison of t he high-latitude ionospheric electrodynamics inferred from global simulations and semiempirical models for the January 1992 GEM campaign, *J. Geophys. Res., 1 02*, 26961, 1997.

Wu, C. C., The effects of northward IMF on the structure of the magnetosphere, *Geophys. Res. Lett., 12*, 839, 1985.

Yee, K. S., Numerical solution of initial boundary value problems involving Maxwell's equations in isotropic media, *IEEE Trans. Antennas and Prop-*

agat., *14*, 302, 1966.

Zalesak, S. T., Fully multidimensional flux-corrected transport algorithms for fluids, *J. Comput. Phys., 31*, 335, 1979.

Zanetti, L. J., and T. A. Potemra, The relationship of Birkland and ionospheric current systems to the interplanetary magnetic field in *Solar Wind - Magnetosphere Coupling*, edited by Y. Kamide and J. A. Slavin, pp. 547-562, Terra Scientific, Tokyo, 1986.

Zhou, X. W.,C. T. Russell, G. Le et al., Solar wind control of the polar cusp at high latitude, *J. Geophys. Res., 105*, 245, 2000.